From precise date to process rate: a high-precision zircon U-Pb geochronology perspective on the timing, rates and durations of geological processes

Wotzlaw, Joern Frederik

UNIVERSITÉ DE GENÈVE
Département des sciences de la Terre

FACULTÉ DES SCIENCES
Prof. Urs Schaltegger

From precise date to process rate:

A high-precision zircon U-Pb geochronology perspective on the timing, rates and durations of geological processes

THÈSE

présentée à la Faculté des sciences de l'Université de Genève
pour obtenir le grade de Docteur ès sciences,
mention sciences de la Terre

par
Jörn-Frederik Wotzlaw

de
Göttingen, Allemagne

Thèse N° 4621

Genève
2013

UNIVERSITÉ DE GENÈVE

FACULTÉ DES SCIENCES

Doctorat ès sciences
Mention sciences de la Terre

Thèse de *Monsieur Jörn Frederik WOTZLAW*

intitulée :

**" From Precise Date to Process Rate :
A High-precision Zircon U-Pb Geochronology Perspective
on the Timing, Rates and Durations of Geological Processes "**

La Faculté des sciences, sur le préavis de Messieurs U. SCHALTEGGER, professeur ordinaire et directeur de thèse (Département des sciences de la Terre), I. BINDEMAN, professeur (Department of Geological Sciences, University of Oregon, United States of America), F. HILGEN, professeur (Department of Earth Sciences, University of Utrecht, The Netherlands) et O. MÜNTENER, professeur (Institut des sciences de la Terre, Université de Lausanne, Suisse), autorise l'impression de la présente thèse, sans exprimer d'opinion sur les propositions qui y sont énoncées.

Genève, le 2 décembre 2013

Thèse - 4621 -

Le Doyen, Jean-Marc TRISCONE

N.B. - La thèse doit porter la déclaration précédente et remplir les conditions énumérées dans les "Informations relatives aux thèses de doctorat à l'Université de Genève".

From precise date to process rate:

A high-precision zircon U-Pb geochronology perspective on the timing, rates and durations of geological processes

Jörn-Frederik Wotzlaw

Genève
2013

The research presented in this thesis was accomplished with financial support through the European Community's Seventh Framework Program (FP7/2007-2013) under grant agreement no. [215458] and the Swiss National Science Foundation (SNSF). The research was carried out in the Department of Earth Sciences, University of Geneva, within the framework of the Marie Curie Initial Training Network *GTSnext* and the *Doctoral Program in Mineral Sciences (DPMS)*.

Thesis director:

Prof. Dr. Urs Schaltegger
Department of Earth Sciences,
University of Geneva, Switzerland

Members of the Dissertation committee:

Prof. Dr. Ilya N. Bindeman
Department of Geological Sciences,
University of Oregon, USA

Dr. Frederik J. Hilgen
Department of Earth Sciences,
University of Utrecht, The Netherlands

Prof. Dr. Othmar Müntener
Institute of Earth Sciences,
University of Lausanne, Switzerland

Content

Prologue

Arthur Holmes (1911), in what is now considered the first real geochronology paper, argued that accumulation of lead in uranium-rich minerals would be the most reliable way to determine the formation ages of rocks. Two years later, he published his now famous book *"The age of the Earth"* (Fig. 1), in which he summarized underlying principles and early applications of uranium-lead (U-Pb) geochronology to calibrate Earth history. More than a century later, U-Pb geochronology by isotope dilution – thermal ionization mass spectrometry (ID-TIMS) is widely regarded as the most accurate radioisotope geochronometer and is often referred to as the *gold standard* of geochronology. This stems from the unique dual decay of ^{238}U and ^{235}U aiding evaluation of closed system behaviour, precisely and accurately determined decay constants (Jaffey et al., 1971), gravimetrically calibrated reference and tracer solutions (Condon et al., submitted) as well as decades of progressive improvements of analytical protocols leading to reduced laboratory contamination (e.g., Krogh, 1973 ; Bowring et al., 2006) and developments of sample pre-treatment methods reducing the affects of post-crystallization Pb-loss in the most commonly dated mineral zircon (Krogh, 1982; Mattinson, 2005).

The unprecedented precision and accuracy achievable by ID-TIMS U-Pb geochronology made it the method of choice for assessing the timing, durations and rates of a diverse range of processes and events, such as the formation of the first solids in the protoplanetary disk

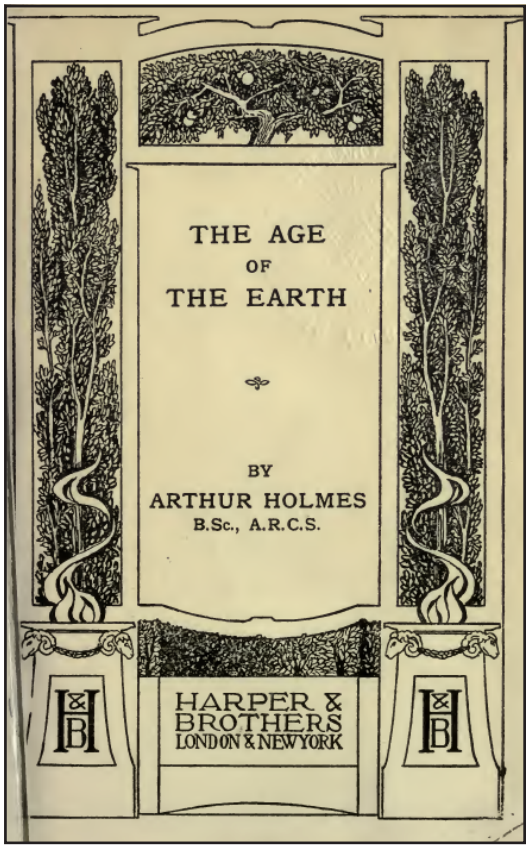

FIGURE 1. Front cover of Arthur Holmes' classic book *The age of the Earth* published in 1913. It contains a detailed comparison of different approaches to estimate geologic time, a careful documentations of the underlying principles of U-Pb geochronology, a discussion of suitable minerals, and a summary of some of the earliest U-Pb data.

(e.g., Amelin et al., 2002; Connelly et al., 2012), the timing and causes of some of the most devastating mass extinction events in Earth history (e.g., Bowring et al., 1998; Schoene et al., 2010; Blackburn et al., 2013), the time-scales of pluton emplacement (e.g., Schaltegger et al., 2009; Schoene et al., 2012) and the rates of processes preceeding some of the largest volcanic eruption on Earth (e.g., Crowley et al., 2007; Wotzlaw et al., 2013). In this thesis, ID-TIMS U-Pb geochronology of the accessory mineral zircon, is extensively employed to gain quantitative insights into the time scales of magmatic processes, to improve our understanding of U-Pb systematics by intercalibration with independent geochronometers and to calibrate stratigraphic records in sedimentary basins (Fig. 2).

HIGH-PRECISION ZIRCON U-PB GEOCHRONOLOGY AS A TOOL IN IGNEOUS PETROLOGY

U-Pb and U-series geochronology of accessory minerals is an important tool to understand the time scales of magmatic processes. In situ techniques, such as secondary ion mass spectrometry (SIMS), offer superb spatial resolution (Fig. 3A) and the relative analytical precision on the order of several % is sufficient to resolve magmatic processes operating on the 10,000 to 100,000 years time-scale in Pleistocene magmatic systems. Most notably, ion microprobe based U-Th disequilibria dating of U- and Th-rich accessory minerals (especially zircon) proved remarkably useful to understand the life-times of a plethora of Pleistocene magmatic systems (e.g., Cooper and Reid, 2008; Schmitt, 2011). However, due to the relatively short ^{230}Th half-life of 75,400 years, U-Th dating is limited to crystals younger than ~300,000 years, making it applicable only to *active* volcanic systems (*sensu* Schmitt, 2011). However, some of the most remarkable features of crustal magmatism are only known from fossil magmatic system. For instance, the youngest exposed granitoid pluton is older than one million years and the most voluminous eruption occured some twenty-eight million years ago. Accessory minerals in these magmatic rocks are in secular equilibrium with respect to the uranium decay series and can not be dated employing U-Th meth-

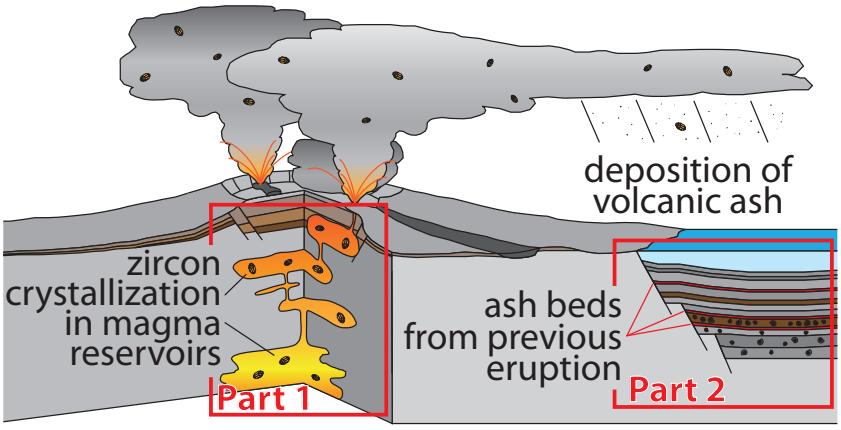

FIGURE 2. Illustration of the applications of zircon U-Pb geochronology presented in the two parts of this thesis. *Part 1* comprises applications of zircon U-Pb geochronology to understand the time scales of processes in magma reservoirs. *Part 2* employs zircon U-Pb geochronology to date ash beds in sedimentary basins to intercalibrate geochronometers and to calibrate the sedimentary records.

ods, but the same minerals can be dated employing the U-Pb method. However, the percent-level precision attainable by in situ techniques is not sufficient to resolve the time scales of magma chamber processes in such fossil magmatic systems (Fig. 3B). In contrary, ID-TIMS techniques allow the determination of U-Pb dates of accessory zircon with approximately an order of magnitude smaller relative analytical uncertainties that translate into absolute uncertainties of several thousands to tens of thousands of years when dating Cenozoic zircons. Such high temporal resolution may result in complex zircon age populations (Fig. 3B), reflecting prolonged zircon growth and magma residence, previously only resolvable by in-situ U-Th dating in much younger magmatic systems (e.g., Schmitt, 2011). The potential of resolving the time-scales and rates of magmatic processes in pre-Pleistocene volcanic deposits and exhumed plutons, recently made ID-TIMS based zircon U-Pb geochronology a widely used tool in igneous petrology (e.g., Crowley et al., 2007; Schaltegger et al., 2009; Schoene et al., 2012; Wotzlaw et al., 2013). Common in many of these applications is that the

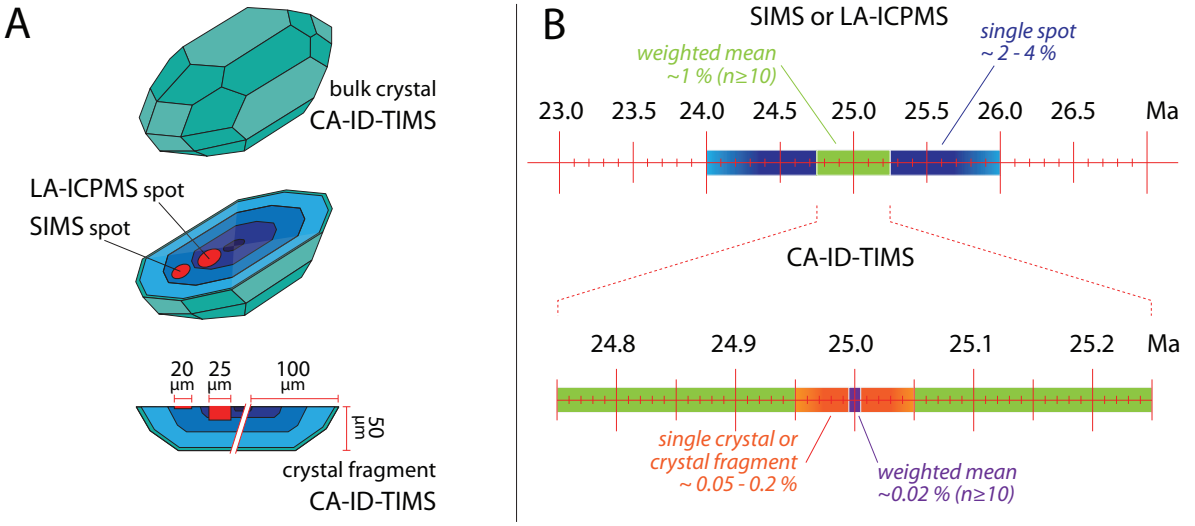

FIGURE 3. Schematic illustration comparing the spatial resolution (A) and the precision (B) achievable by in situ techiques and by ID-TIMS. (A) Comparison of the sample volumes consumed during in situ and ID-TIMS analysis. Traditionally ID-TIMS uses bulk zircon crystals thereby averaging over multiple growth zones. In contrary, the high spatial resolution of in situ techniques allows to date individual growth zones. Microsampling of crystal fragments for ID-TIMS becomes increasingly popular and reduces the sample volume of ID-TIMS analyses by a factor of about 2 to 10. The higher spatial resolution of in situ techniques comes at the expense of significantly lower analytical precision. (B) Comparison of the precision achievable by in situ techniques and by ID-TIMS for a 25 Ma volcanic rock. Shown are uncertainties for single spot and single crystal analyses as well as uncertainties for weighted mean dates of statistically eqivalent populations consisting of ≥ 10 dates. The higher precision of ID-TIMS allows to resolve the time scales of magmatic processes in such young rocks In contrary, the high precision of ID-TIMS techniques, allows to resolve these age differences. SIMS - Secondary ion mass spectromery; LA-ICPMS - Laser Ablation-Inductively Coupled Plasma Mass Spectrometry.

analytical precision largely exceeds the ability to interpret U-Pb dates in the context of magmatic processes. Closing this gap is currently one of the big challenges in high-precision U-Pb geochronology and one of the main themes of the first part (Chapters 1 to 3) of this thesis. Recently developed analytical protocols (e.g., Schoene et al., 2010b) that allow the analysis of oxygen and hafnium isotopic ratios as well as trace element concentrations in tandem with ID-TIMS are employed to link zircon crystallization to specific episodes during the life-times of investigated magmatic systems and ultimately to quantify the durations and rates of underlying processes.

INTERCALIBRATION OF GEOCHRONOMETERS AND THE CALIBRATION OF SEDIMENTARY RECORDS

The high accuracy and precision achievable by ID-TIMS U-Pb geochronology also made it one of the preferred methods for the numerical calibration of the Geologic Time Scale (GTS; e.g., Gradstein et al., 2012). U-Pb dating of zircons from volcanic ash beds intercalated with fossiliferous marine sediments underpins much of the Paleozoic and Mesozoic time-scales. The prolonged crystallization history recorded by zircons has been considered to significantly compromise chronostratigraphic applications, where the desired age information is that of ash bed deposition (e.g., Simon et al., 2008). This potential bias of ash bed deposition ages derived from zircon U-Pb dates was also considered to contribute to systematic offsets between the U-Pb and other radioisotopic systems (e.g., Renne et al., 2010). The second part of this thesis addresses the accuracy, potential and limitations of high-precision zircon U-Pb geochronology for calibrating sedimentary records of Earth history. This technique is then applied to place quantitative constraints on the duration of the Late Triassic Rhaetian stage and the rates of processes during this time interval that culminated in the end-Triassic mass extinction.

REFERENCES CITED

Amelin, Y., Krot, A.N., Hutcheon, I.D., and Ulyanov, A.A., 2002. Lead isotopic ages of chondrules and calcium-aluminium-rich inclusions. Science, v. 297, p. 1678–1683.

Blackburn, T.J., Olsen, P.E., Bowring, S.A., McLean, N.M., Kent, D.V., Puffer, J., McHone, G., Rasbury, E.T., and Et-Touhami, M., 2013. Zircon U-Pb geochronology links the End-Triassic extinction with the Central Atlantic Magmatic Province. Science, v. 340, p. 941–945.

Bowring, S. A., Schoene, B., Crowley, J.L., Ramezani, J., and Condon, D.J., 2006. High-precision U-Pb zircon geochronology and the stratigraphic record: progress and promise. The Paleontological Society Papers, v. 12, p. 25–46.

Condon, D.J., Schoene, B., McLean, N.M., Bowring, S.A., and Parrish, R.R., submitted. Metrology and traceability of U-Pb isotope dilution geochronology (EARTHTIME Tracer Calibration Part I). Submitted to Geochem. Geophys. Geosyst.

Connelly, J.C., Bizzarro, M., Krot, A.N., Nordlund, A., Wielandt, D., and Ivanova, M., 2012. The absolute chronology and thermal processing of solids in the solar protoplanetary disk. Science, v. 338, p.

651–655.

Cooper, K.M., and Reid, M.R., 2008. Uranium-series crystal ages, in Putirka, K.D., and Tepley III, F.J.., eds., Minerals, inclusions and volcanic processes. Rev. Mineral. Geochem., v. 69, p. 479–544.

Crowley, J.L., Schoene, B., and Bowring, S.A., 2007. U-Pb dating of zircon in the Bishop Tuff at the millennial scale. Geology, v. 35, p. 1123–1126.

Gradstein, F.M, Ogg, J.G., Schmitz, M.D., and Ogg, G.M., (eds.), 2012. The Geologic Time Scale 2012. Elsevier, Oxford-Amsterdam-Waltham, 1144 pp.

Holmes, A., 1911. The association of lead with uranium in rock-minerals, and its application to the measurement of geologic time. Proc. Roy. Soc. London, v. 85A, p. 248–256.

Jaffey, A.H., Flynn, K.F., Glendenin, L.E., Bentley, W.C., and Essling, A.M., 1971. Precision measurement of half-lives and specific activities of ^{235}U and ^{238}U. Phys. Rev., v. C4 (5), p. 1889–1906.

Krogh, T.E., 1973. A low contamination method for hydrothermal decomposition of zircon and extraction of U and Pb for isotopic age determination. Geochim. Cosmochim. Acta, v. 37, p. 485–494.

Krogh, T. E., 1982. Improved accuracy of U-Pb zircon ages by the creation of more concordant zircon systems using an air abrasion technique. Geochim. Cosmochim. Acta, v. 46, p. 637–649.

Mattinson, J.M., 2005. Zircon U-Pb chemical abrasion ("CA-TIMS") method: combined annealing and multi-step partial dissolution analysis for improved precision and accuracy of zircon ages. Chem. Geol., v. 200, p. 47–66.

Renne, P.R., Mundil, R., Balco, G., Min, K.W., and Ludwig, K.R., 2010. Joint determination of ^{40}K decay constants and $^{40}Ar^*/^{40}K$ for the Fish Canyon sanidine standard, and improved accuracy for $^{40}Ar/^{39}Ar$ geochronology. Geochim. Cosmochim. Acta, v. 74, p. 5349–5367.

Schaltegger, U., Brack, P., Ovtcharova, M., Peytcheva, I., Schoene, B., Stracke, A., Marocchi, M., and Bargossi, G.M., 2009. Zircon and titanite recording 1.5 million years of magma accretion, crystallization and initial cooling in a composite pluton (southern Adamello batholith, northern Italy). Earth Planet. Sci. Lett., v. 286, p. 208–218.

Schmitt, A.K., 2011. Uranium series accessory crystal dating of magmatic processes. Ann. Rev. Earth Planet. Sci., v. 39, p. 321–349.

Schoene, B., Guex, J., Bartolini, A., Schaltegger, U., and Blackburn, T.J., 2010. Correlating the end-Triassic mass extinction and flood basalt volcanism at the 100 ka level. Geology, v. 38, p. 387–390.

Schoene, B., Latkoczy, C., Schaltegger, U., and Günther, D., 2010. A new method integrating high-precision U-Pb geochronology with zircon trace element analysis (U-Pb TIMS-TEA). Geochim. Cosmochim. Acta, v. 74, p. 7144–7159, doi:10.1016/j.gca.2010.09.016.

Schoene, B., Schaltegger, U., Brack, P., Latkoczy, C., Stracke, A., and Günther, D., 2012. Rates of magma differentiation and emplacement in a ballooning pluton recorded by U-Pb TIMS-TEA, Adamello batholith, Italy. Earth Planet. Sci. Lett., v. 355–356, p. 162–173.

Simon, J.I., Renne, P.R., and Mundil, R., 2008. Implications of pre-eruptive magmatic histories of zircons for U-Pb geochronology of silicic extrusions. Earth Planet. Sci. Lett., v. 266, p. 182–194.

Wotzlaw, J.F., Schaltegger, U., Frick, D.A., Dungan, M.A., Gerdes, A., Günther, D., 2013. Tracking the evolution of large-volume silicic magma reservoirs from assembly to supereruption. Geology, v. 41, p. 867–870.

Summary

This thesis, entitled *"From precise date to process rate: A high-precision zircon U-Pb geochronology perspective on the timing, rates and durations of geological processes"*, comprises a series of papers addressing the potential and limitations of accurate and precise uranium-lead geochronology of accessory minerals for quantifying the time-scales of a variety of geologic processes. The thesis is subdivided into two parts and five chapters.

PART I consists of three papers focusing on quantifying the time-scales of magmatic processes in some well characterised magmatic systems. By integrating high precision U-Pb geochronology with trace element, oxygen and hafnium isotopic data, we place quantitative constraints on the durations and rates of some important processes in these magmatic systems.

CHAPTER 1. This paper presents a new high-precision zircon U-Pb geochronological view on the crystallization and assembly process of one of the most important and intensely studied intrusive bodies on Earth – the Skaergaard intrusion in East Greenland. With analytical uncertainties of a few tens of thousands of years, we were able to resolve several important events during cooling of this intrusion. Initial cooling of the shallowly intruded ~300 km^3 of tholeiitic basaltic magma from liquidus to zircon saturation at ~1000°C is recorded by a precise zircon crystallization age of 55.960 ± 0.018 Ma of an intercumulus gabbroic pegmatite in the lower portion of the intrusion. Based on this zircon crystallization age and a published cooling model we estimate the "true" age of emplacement to be ~56.02 Ma. The last portions of Skaergaard appear to crystallize completely ~100 ka after emplacement as recorded by abundant ~55.91-55.93 Ma zircons in the Sandwich Horizon (SH), where lower and upper solidification fronts met. Intrusion of an isotopically distinct new magma batch, the ~600 m thick Basistoppen Sill, into the solidified upper portion of Skaergaard, happened at 55.895 ± 0.018 Ma, suggesting close timing between crystallization of evolved rocks around the SH and intrusion of the Basistoppen Sill. The novel result of this work is the demonstration that zircons in the SH, >100 m below the Basistoppen contact, have a bimodal age distribution, with the youngest population of 55.838 ± 0.019 Ma postdating intrusion of the Basistoppen Sill by 57 ± 37 ka. Oxygen isotope analyses reveal that SH zircons are low and heterogeneous with respect to $\delta^{18}O$. These results support the proposed conclusion that the SH crystallized twice: it was fully crystalline, then hydrothermally-altered by low-$\delta^{18}O$ surface waters and subsequently partially remelted, trig-

gered by heat of the Basistoppen Sill. The low-degree partial melt generated during remelting partially migrated upward by intergranular compaction-driven flow, explaining the existence of the most incompatible trace element rich horizon, ~100 m above SH. As the Skaergaard intrusion is also the most classic example of a shallow meteoric hydrothermal system, this work documents the alternating processes in a life of an intrusion with periods of hydrothermal cooling, heating by new intrusions, and related remelting events, which cause the generation of low-$\delta^{18}O$ magmas.

Our precise temporal framework for intrusion crystallization also provides constraints for the timing of coeval flood basalt volcanism and its synchronicity with the Paleocene-Eocene-Thermal-Maximum. This chapter is published in *Earth and Planetary Science Letters*.

CHAPTER 2. A novel approach to quantify the chemical, thermal and rheological evolution of large volume silicic magma reservoirs is presented in this chapter and applied to study processes preceeding the most voluminous silicic eruption known from the geologic record; the erution of the Fish Canyon Tuff. Such large-volume eruptions are fed by gigantic silicic magma reservoirs. The thermal evolution of these sub-caldera magma reservoirs controls the volume of eruptible magma and eruptive style. Here we combine high-precision zircon U-Pb geochronology, trace element analyses of the same mineral grains, and mass balance modeling of zircon trace element compositions allowing us to track the thermal and chemical evolution of the Oligocene Fish Canyon Tuff magma reservoir (Colorado, USA), as a function of absolute time. Systematic compositional variations in U-Pb dated zircons record ~440 k.y. of magma evolution. An early phase of volumetric growth was followed by a period of cooling and crystallization, during which the Fish Canyon magma approached complete solidification. Subsequent remelting, due to underplated andesitic recharge magmas, began 219 ± 45 ka prior to eruption and led to the generation of ~5000 km^3 of eruptible crystal-rich (~45 vol.%) dacite. Age-equivalent, but compositionally different, zircons in an andesite enclave from late-erupted Fish Canyon Tuff tie the growth and thermal evolution of the upper crustal reservoir to a lower crustal magma processing zone.

Our results demonstrate that the combination of high-precision dating and trace element analyses of accessory zircons can reveal invaluable information about the chemical and thermal histories of silicic magmatic systems and provides critical input parameters for fluid dynamic modeling. This chapter is published in *Geology*.

CHAPTER 3. In this chapter we investigate the time scales and mechanisms of reservoir build-up and evolution beneath large silicic caldera volcanoes. Such volcanoes produce extremely large-volume eruptions, often referred to as *supererruptions*, that are some of the most devastating natural disasters. The most voluminous eruption ever experienced by modern civilizations, the 1815 Tambora eruption, was more than an order of mag-

nitude smaller than the largest-volume eruptions known from the geological record. Perhaps nowhere on Earth are deposits of supereruptions more prominent than in the Snake River Plain-Yellowstone Plateau (SRP-YP) volcanic province. The Heise volcanic field in eastern Idaho contains the youngest complete caldera cycle in the SRP-YP and culminated about 4.5 million years ago in the eruption of the low-$\delta^{18}O$, 1800 km^3 Kilgore Tuff. Accessory zircon crystals in the Kilgore Tuff display remarkable inter- and intracrystalline oxygen isotopic heterogeneity with a total range of 8 ‰ in $\delta^{18}O$ suggesting that they crystallized from isotopically distinct and isolated reservoirs that were assembled and homogenized prior to eruption. In contrary to the oxygen isotopic heterogeneity, twenty-four of these zircons yielded indistinguishable crystallization ages with a Th-corrected weighted mean $^{206}Pb/^{238}U$ date of 4.4876 ± 0.0023 Ma that is indistinguishable from the eruption age. This requires that shallow magma generation and subsequent assembly of isolated magma batches occured within the resolution of our geochronology and thus is an extremely rapid process. This crystal scale image of the configuration of the pre-eruption resevoir, with several isolated magma batches, is very similar to the resevoir configuration imaged seismically beneath active supervolcanoes. The assembly of magma batches vertically distributed over several kilometers would cause a substantial increase in buoyancy, providing a eruption trigger mechanism which is the direct consequence of the reservoir assembly process.

PART II comprises two chapters addressing the potential but also the limitations of high-precision zircon U-Pb geochronology as a tool for calibrating sedimentary records.

CHAPTER 4. Several orbitally tuned Miocene sedimentary sequences around the Mediterranean contain abundant intercalated volcanic ash beds. These sequences provide the rare opportunity to intercalibrate radioisotopic dating methods with independent and accurate deposition ages derived from astrochronology. We present a large data set (N=17, n=175) of high precision zircon U-Pb dates for ash beds from an almost continuous orbitally tuned Messinian to Langhian (~15.4 - 6.2 Ma) sedimentary sequence exposed along the Adriatic coast south of Ancona, Italy. We use this unique data set to evaluate (1) the accuracy of zircon U-Pb dates, (2) the significance of initial intermediate daughter product disequilibria for zircon U-Pb geochronology of young rocks, (3) the effect of prolonged pre-eruption zircon crystallization and zircon recycling on U-Pb derived ash bed deposition ages, and (4) discuss the implications for the intercalibration of radioisotope geochronometers and the calibration of the Geologic Time Scale.

CHAPTER 5. The numerical calibration of the geologic time scale (GTS) has long been one of the most important applications of precise and accurate U-Pb geochronology. In this chapter we report biochronologic and U-Pb geochronologic data from the Late Triassic of Northern Peru and discuss the importance for

global correlations and the calibration of the Late Triassic stages. The numerical calibration of the Late Triassic stages is arguably the most controversial issue in Mesozoic stratigraphy despite their importance for assessing mechanisms of environmental perturbations and associated biologic consequences preceding the end-Triassic mass extinction. Here we report new CA-TIMS zircon U-Pb dates for volcanic ash beds within the Aramachay Formation of the Pucara Group in Northern Peru that place precise constraints on the maximum age of the Norian-Rhaetian boundary. Sampled ash beds are closely associated with a characteristic uppermost Norian bivalve assemblages comprising the last occurence of large flat clam Monotis subcircularis as well as thin shelled Otapiria aff. O. norica and Oxytoma cf. O. inaequivalvis. Zircon U-Pb dates of sampled ash beds constrain the deposition age of this interval to be between 205.70 ± 0.15 Ma and 205.30 ± 0.14 Ma. We further recalibrate previously published zircon U-Pb dates for ash beds bracketing the Triassic-Jurassic boundary employing the most recent calibration of the EARTHTIME tracer solution resulting in a maximum duration of ~4 m.y. for the Rhaetian. This ends a prolonged controversy about the duration of this stage and has fundamental implications for the rates of paleoenvironmental deterioration inferred for the Late Triassic, culminating in the end-Triassic mass extinction and provides an absolute tie-point for magnetostratigraphic and cyclostratigraphic correlations of marine and continental Late Triassic sedimentary sections.

Resumé

Ce manuscrit de thèse, intitulé *"Datation haute précision et vitesse de processus: Perspective de la géochronologie U-Pb haute précision sur zircon pour le timing, la vitesse et la durée des processus géologiques"*, comporte une série d'articles s'adressant au potentiel et aux limitations de la géochronologie précise et exacte par la méthode uranium-plomb sur minéraux accessoires, pour quantifier les échelles de temps de divers processus géologiques. La thèse est divisée en deux parties et cinq chapitres.

La partie I consiste en trois articles se focalisant sur la quantification de durées de processus magmatiques dans des systèmes magmatiques bien caractérisées. En intégrant la géochronologie de haute précision U-Pb avec des données d'éléments traces et isotopiques d'oxygène et hafnium, nous apportons des contraintes quantitatives sur les durées et les taux de certains processus importants dans ces systèmes magmatiques.

Chapitre 1. Ce chapitre présente une nouvelle vue géochronologique de haute précision U-Pb sur zircon, sur les processus de cristallisation et d'assemblage d'un des corps intrusifs les plus étudiés et les plus importants sur Terre : l'intrusion de Skaergaard dans l'Est du Groenland. Avec des incertitudes analytiques de quelques dizaines de milliers d'années, nous fûmes capables de résoudre plusieurs évènements importants pendant le refroidissement de cette intrusion. Le refroidissement initial des ~300 km^3 de magma tholéiitique basaltique mis en place à faible profondeur, du liquidus vers la saturation du zircon vers ~1000°C, est enregistré par un âge de cristallisation précis de 55.960 ± 0.018 Ma pour une pegmatite gabbroique dans la partie inférieure de l'intrusion. En se basant sur cet âge et un modèle de refroidissement publié, nous estimons l'âge réel à ~56.02 Ma. Les dernières portions de Skaergaard paraissent avoir cristallisé complètement ~100 ka après la mise en place, comme suggéré par de nombreux zircons de ~55.91-55.93 Ma dans le Sandwich Horizon (SH) à l'interface entre les fronts de solidification inférieur et supérieur. Une série de magmas isotopiquement distincts sous forme du Basistoppen Sill de ~600 m d'épaisseur, se mit en place dans la partie supérieure solidifiée de Skaergaard a 55.895 ± 0.018 Ma, peu de temps après la cristallisation des roches évoluées du SH. Le résultat novateur de ce travail est la démonstration que les zircons du SH, à plus de 100 m sous le contact avec le Basistoppen, ont une distribution d'âge bimodale, dont la population la plus jeune de 55.838 ± 0.019 Ma postdate l'intrusion du Basistoppen Sill de 57 ± 37 ka. Les analyses d'isotopes

d'oxygène révèlent que les zircons du SH sont faibles et hétérogènes en matière de $\delta^{18}O$. Ces résultats soutiennent la conclusion que le SH cristallisa deux fois : après une première cristallisation, il fut altéré par des eaux de surface de faible $\delta^{18}O$ avant d'être partiellement refondu par la chaleur apportée par le Basistoppen Sill. Les produits du faible degré de fusion migrèrent partiellement vers le haut par un écoulement intergranulaire dû à la compaction, ce qui explique l'existence du niveau le plus enrichi en éléments traces incompatibles à environ 100 m au-dessus du SH. Vu que l'intrusion du Skaergaard est également l'exemple le plus classique d'un système hydrothermal météorique, ce travail documente les processus alternants dans la vie d'une intrusion avec des periodes de refroidissement hydrothermal, de réchauffement par nouveaux apports magmatiques et la fusion associée, qui provoque la genèse de magmas de faible $\delta^{18}O$.

Notre cadre temporel précis pour la cristallisation de l'intrusion apporte également des contraintes temporelles pour le volcanisme de trapp associé et sa simultanéité avec le Maximum Thermique Paléocène-Eocène.

Chapitre 2. Une nouvelle approche pour quantifier l'évolution chimique, thermique et rhéologique de grand réservoirs de magma siliceux est présentée dans ce chapitre et est appliquée à l'études des processus magmatique précédent la plus volumineuse éruption connues dans l'enregistrement géologiques, l'éruption du Fish Canyon Tuff. De telles éruptions sont alimentées par de gigantesques réservoirs magmatiques. L'évolution thermique de ces réservoirs magmatiques, localisés sous les calderas, contrôle le volume de magma éruptible et le style de d'éruption. Ici, nous combinons la géochronologie de haute précision U-Pb sur zircons, l'analyse des éléments en traces de ces mêmes zircons et la modélisation de balance de masse des éléments traces sur les zircons afin de contraindre l'évolution thermique et chimique du réservoir magmatique Oligocène du Fish Canyon (Colorado, USA) en fonction du temps. Les variations systématiques de compositions dans les zircons datés par U-Pb, enregistrent ~440 ka d'évolution magmatique. Une augmentation de volume précoce a été suivi d'une période de refroidissement et de cristallisation durant laquelle le magma du Fish Canyon était proche de la solidification complète. Un évènement de refonte à lieu plus tardivement dû à une recharge de magma andésitique, commençant à 219 ± 45 ka avant l'éruption et conduisant à la génération de ~5000 km^3 de dacite éruptible riche en cristaux (~45 vol.%). D'âges équivalents mais de compositions différentes, les zircons dans les enclaves d'andésites provenant de la précédente éruption du Fish Canyon Tuff font le lien entre la croissance et l'évolution thermique du réservoir de la croûte supérieure avec la croûte inférieure, zone de genèse du magma.

Nos résultats démontrent que la combinaison de la datation de haute précision avec l'analyse des éléments en trace dans les zircons révèle des informations précieuses dans la caractérisation de l'évolution chimique et thermique des

systèmes magmatiques siliceux, et elle fournit des informations cruciales sur les paramètres importants relatifs à la modélisation de la dynamique des fluides.

Chapitre 3. Dans ce chapitre nous avons étudié les échelles de temps, et les mécanismes de développement et d'évolution de réservoir magmatique sous de grandes calderas siliceuses. De tels volcans produisent des éruptions d'un volume extrêmement grand, souvent nommés super éruptions, qui sont en général à l'origine des plus grandes catastrophes naturelles. La plus grande éruption déjà vécu (subi) par les civilisations modernes, l'éruption de Tambora en 1815, était plus d'un ordre de grandeur plus petite que les plus importantes éruptions connues dans l'enregistrement géologiques. Les gigantesques dépôts volcaniques des super éruptions de la province de Snake River Plain-Yellowstone (SRP-YP), n'ont probablement pas d'autre équivalent sur Terre. Le champ volcanique de Heise dans l'est de l'Idaho représente le plus jeune cycle complet de calderas de la province de SRP-YP, et s'est terminé il y a environ 4.5 Ma avec l'éruption du Kilgore Tuff caractérisé par son faible $\delta^{18}O$ et son volume de 1800 km^3. Les zircons dans les tuffs de Kilgore montrent une remarquable hétérogénéité inter- et intra-cristalline dans les signatures isotopiques de l'oxygène, avec une gamme totale de 8 ‰ en $\delta^{18}O$ suggérant qu'ils ont cristallisé depuis des réservoirs isotopiquement distincts et isolés et qui ont successivement été assemblé et homogénéisé avant l'éruption. A l'inverse de l'hétérogénéité des signatures isotopiques de l'oxygène, vingt-quatre de ces zircons ont donné des âges de cristallisation similaires avec une moyenne pondéré d'âge $^{206}Pb/^{238}U$, de 4.4876 ± 0.0023 Ma, ce qui est indissociable de l'âge de l'éruption. Cela exige que la génération du magma peu profond et l'assemblage successif des poches de magmas isolées se sont produit en un temps similaire à la précision de nos datations géochronologiques, ce qui implique un processus extrêmement rapide. La configuration du réservoir pré-éruptif avec plusieurs poches de magmas isolées imagée à l'échelle du cristal (zircons) est très similaire à la configuration des réservoirs révélée par les études sismiques sous les supervolcans actifs. L'assemblage des poches de magmas distribuées verticalement jusqu'à plusieurs kilomètres de profondeurs pourrait causer une hausse de la flottabilité qui serait le mécanisme à l'origine de l'éruption, qui serait donc une conséquence directe de l'assemblage des différents réservoirs.

La partie II inclut deux chapitres traitant du potentiel mais aussi des limites de la géochronologie de haute précision sur zircons comme un outil de calibration de l'enregistrement sédimentaire.

Chapitre 4. Plusieurs séquences sédimentaires Miocène autour de la méditerranée pour lesquels des datations l'astrochronologiques existent contiennent des dépôts de cendres volcaniques intercalés. Ces séquences fournissent une rare opportunité d'inter-calibrer des méthodes de datations radio-isotopiques avec des âges de dépositions indépendant et ex-

act dérivés de l'astro-chronologie. Nous présentons un grand ensemble de données (N=17, n=175) d'âge de haute précision U-Pb sur zircons pour les dépôts de cendres volcaniques d'une séquence sédimentaire exposée le long de la côte Adriatique, dans le sud d'Ancona en Italie, pour laquelle les âges astro-chronologiques vont du Messinien au Langhien (6.2-15.4 Ma). Nous utilisons cet ensemble de données unique dans le but d'évaluer (1) la l'exactitude des âges U-Pb sur zircons, (2) l'importance du déséquilibre initial de l'isotope fils intermédiaire pour la géochronologie U-Pb sur zircons de roches jeunes, (3) l'effet d'une cristallisation et d'un recyclage prolongés des zircons avant l'éruption sur les âges de dépôt des cendres volcaniques dérivés par la méthode U-Pb et (4) les implications concernant l'inter-calibration des géochronomètres radio-isotopiques et de la calibration de l'échelle des temps géologiques

Chapitre 5. La calibration numérique de l'échelle des temps géologiques a longtemps été l'une des plus importantes applications de la géochronologie U-Pb. Dans ce chapitre, nous présentons des données bio-chronologique et géochronologique U-Pb du Trias supérieur dans le nord du Pérou, et nous discutons de l'importance d'une corrélation et d'une calibration globale des étages stratigraphiques du Trias supérieur. La calibration numérique des étages du Trias Supérieur est probablement le problème le plus controversé de la stratigraphie du Mésosoïque malgré leurs importances pour comprendre les mécanismes de perturbations environnementaux associés aux conséquences biologiques précédent l'extinction de masse à la fin du Trias. Ici, nous présentons de nouveaux âges CA-TIMS sur zircons pour les dépôts de cendres volcaniques dans la formation de Aramachay du groupe de Pucara dans le nord du Pérou qui fixent des contraintes précises sur l'âge maximal de la limite géologique Norien-Rhétien. Les dépôts de cendres échantillonnés sont associés de près à des assemblages caractéristiques de bivalve du Norien supérieur, incluant la dernière occurrence de grand mollusques plats Monotis subcircularis ainsi que des coquillages fins de Otapiria aff. O. norica et Oxytoma cf. O. inaequivalvis. Les âges U-Pb sur zircons des dépôts de cendres échantillonnés contraignent l'âge de déposition de cet intervalle entre 205.70 ± 0.15 et 205.30 ± 0.14 Ma. Nous avons recalibré les âges U-Pb sur zircons publiés précédemment pour les dépôts de cendres qui contraignent la limite Trias-Jurassique en utilisant la calibration la plus récente du traceur isotopique EARTHTIME, et obtenons une durée maximale de ~4 Ma pour le Rhétien. Ceci mettant fin à une longue controverse concernant la durée de cet étage stratigraphique et ayant une implication fondamentale pour le taux de détérioration paléo-environnemental déduit pour le Trias supérieur, culminant à la fin du Trias lors de l'extinction de masse. Enfin, cela fournit un point d'ancrage absolu pour les corrélations magnéto-stratigraphiques and cyclo-stratigraphiques des coupes sédimentaires marines et continentales du Trias supérieur.

Chapter 1

High-resolution insights into episodes of crystallization, hydrothermal alteration and remelting in the Skaergaard intrusive complex*

J.F. Wotzlaw, I.N. Bindeman, U. Schaltegger, C.K. Brooks, H.R. Naslund

Keywords:
Skaergaard
zircon
oxygen isotopes
U-Pb geochronology
flood basalts
PETM

ABSTRACT

This paper presents a new high-precision zircon U-Pb geochronological view on the crystallization and assembly process of one of the most important and intensely studied intrusive bodies on Earth – the Skaergaard intrusion in East Greenland. With analytical uncertainties of a few tens of thousands of years, we were able to resolve several important events during cooling of this intrusion.

Initial cooling of the shallowly intruded ~300 km^3 of tholeiitic basaltic magma from liquidus to zircon saturation at ~1000°C is recorded by a precise zircon crystallization age of 55.960 ± 0.018 Ma of an intercumulus gabbroic pegmatite in the lower portion of the intrusion. Based on this zircon crystallization age and a published cooling model we estimate the "true" age of emplacement to be ~56.02 Ma. The last portions of Skaergaard appear to crystallize completely ~100 ka after emplacement as recorded by abundant ~55.91-55.93 Ma zircons in the Sandwich Horizon (SH), where lower and upper solidification fronts met. Intrusion of an isotopically distinct new magma batch, the ~600 m thick Basistoppen Sill, into the solidified upper portion of Skaergaard, happened at 55.895 ± 0.018 Ma, suggesting close timing between crystallization of evolved rocks around the SH and intrusion of the Basistop-

*this chapter is equivalent to the paper "High-resolution insights into episodes of crystallization, hydrothermal alteration and remelting in the Skaergaard intrusive complex" published in *Earth and Planetary Science Letters* (v. 355-356, p. 199-212) and co-authored by J.F. Wotzlaw, I.N. Bindeman, U. Schaltegger, C.K. Brooks and H.R. Naslund.

pen Sill. The novel result of this work is the demonstration that zircons in the SH, >100 m below the Basistoppen contact, have a bimodal age distribution, with the youngest population of 55.838 ± 0.019 Ma postdating intrusion of the Basistoppen Sill by 57 ± 37 ka. Oxygen isotope analyses reveal that SH zircons are low and heterogeneous with respect to $\delta^{18}O$. These results support the proposed conclusion that the SH crystallized twice: it was fully crystalline, then hydrothermally-altered by low-$\delta^{18}O$ surface waters and subsequently partially remelted, triggered by heat of the Basistoppen Sill. The low-degree partial melt generated during remelting partially migrated upward by intergranular compaction-driven flow, explaining the existence of the most incompatible trace element rich horizon, ~100 m above SH.

As the Skaergaard intrusion is also the most classic example of a shallow meteoric hydrothermal system, this work documents the alternating processes in a life of an intrusion with periods of hydrothermal cooling, heating by new intrusions, and related remelting events, which cause the generation of low-$\delta^{18}O$ magmas.

Our precise temporal framework for intrusion crystallization also provides constraints for the timing of coeval flood basalt volcanism and its synchronicity with the Paleocene-Eocene-Thermal-Maximum.

1.1 INTRODUCTION

Chemically-zoned plutons have been the subject of intense research aiming to model the physical mechanisms of igneous differentiation (McBirney and Noyes, 1979; McBirney, 1995; Boudreau and McBirney, 1997; McKenzie, 2011). Most of these models concentrate on the efficiency of crystal-melt separation, the role of convection, and recently silicate liquid immiscibility (Jakobsen et al., 2005; 2010a; Veksler et al., 2007; Humphreys, 2011; Holness et al., 2011). When dealing with now solid plutonic bodies it is important to realize that there are many other time-integrated processes that are possible to unravel with new tools. It is particularly important to realize that even the simplest examples of igneous bodies may contain records of multiple refilling events and events of remelting of preexisting rocks that may be traced by radiogenic and/or stable isotopes and the timing of such events can be quantified using precise geochronological methods. In this study we investigate the late-stage evolution of the Skaergaard intrusion aiming to test proposed petrogenetic models and quantify time-scales of late-stage shallow crustal remelting and

generation of low-$\delta^{18}O$ magmas (Bindeman et al., 2008).

Since its discovery in 1930, the Skaergaard intrusion has been a classic locality for the study of closed-system igneous differentiation (e.g. Wager and Deer, 1939; Wager and Brown, 1968; Brooks et al., 1991; McBirney, 1995; Irvine et al., 1998). After emplacement in the unconformity between the Precambrian basement and overlying Cenozoic basaltic lavas (Fig. 1.1), it evolved by fractional crystallization from primitive olivine gabbro to Fe-rich ferrodiorite with interstitial granophyre. Progressive crystallization from the floor, walls and roof of the intrusion produced the Layered Series (LS), the Marginal Border Series (MBS) and the Upper Border Series (UBS), respectively (Wager and Deer, 1939). The LS comprises the bulk of the volume and is further subdivided into zones and subzones (Fig. 1.1C) reflecting the appearance and disappearance of fractionating cumulus phases (Wager and Deer, 1939; Wager and Brown, 1968; Lindsley et al., 1969; Irvine et al., 1998). The upper and lower crystallization fronts coalesced around what is known as the Sandwich Horizon (SH), which contains the most

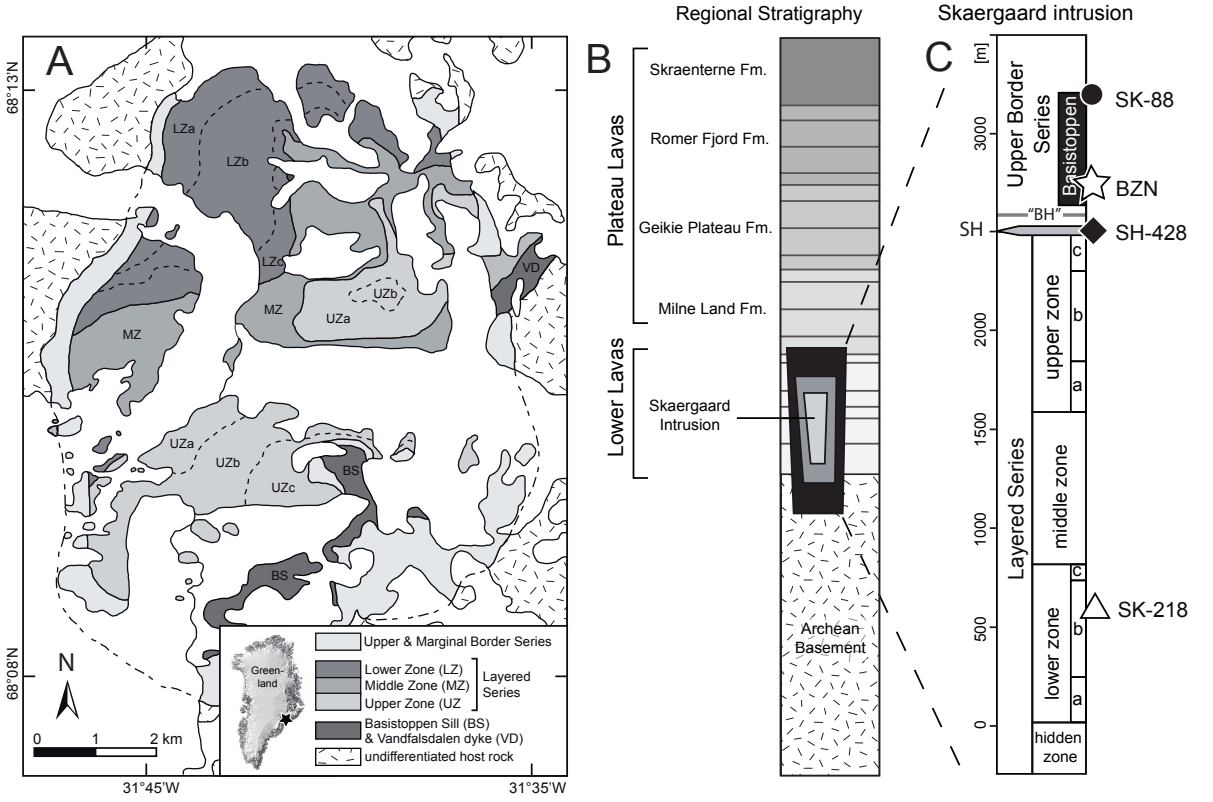

FIGURE 1.1 (A) Geological map of the Skaergaard intrusive complex (McBirney, 1989), (B) regional stratigraphy showing stratigraphic relationship between the Skaergaard intrusion, the Precambrian basement and overlying basalts (after Jakobsen et al., 2010) and (C) stratigraphic column of the Skaergaard intrusion (Wager and Brown, 1968) showing stratigraphic position of analyzed samples. Abbreviations: SH – Sandwich Horizon, BH – Brooks Horizon.

evolved major element differentiation indices (e.g., highest Fe/Mg ratios). However, the highest incompatible trace element concentrations occur tens of meters above the SH, a layer called the secondary SH (McBirney, 2002), or following Bindeman et al. (2008), the "Brooks" Horizon, labeled after the paper by C.K. Brooks (1969) who first discovered this enrichment.

The Skaergaard intrusion is perhaps the simplest layered igneous body on Earth in the sense that ~300 km3 of tholeiitic basaltic magma formed and intruded in a single event into a shallow (ca. 1-2 km) rift zone during ~56 Ma North Atlantic extension, and then differentiated from bottom and top by a closed system differentiation process without much mass loss to the surface, and without much assimilation of highly radiogenic Archean country rocks. Recent work has addressed the importance of crystal compaction vs. convective differentiation (Tegner et al. 2009; McKenzie, 2011), the role of igneous layering, and the role of liquid immiscibility (Jakobsen et al., 2005; 2010a; Veksler et al., 2007; Humphreys, 2011; Holness et al., 2011), but does not attempt to challenge the original views of Wager and Deer (1939) about top to bottom, and bottom to top, liquidus to solidus crystallization of Skaergaard.

1.2 PREVIOUS STABLE ISOTOPE STUDIES AND GEOCHRONOLOGY OF THE SKAERGAARD INTRUSION

These canonical differentiation trends observed in Skaergaard were the initial driving force to empirically understand changes of oxygen and hydrogen isotopic fractionation during magmatic differentiation (Taylor and Epstein, 1963). Subsequent studies, however, found that primary magmatic values were nearly completely overprinted by exchange with low-$\delta^{18}O$ meteoric hydrothermal fluids (Taylor, 1968; Taylor and Forester, 1979; Norton et al., 1984) and that the Skaergaard intrusion drove its own shallow meteoric hydrothermal system in the waning stages of intrusion crystallization and during subsolidus cooling. This high temperature hydrothermal alteration of Skaergaard rocks resulted in highly diverse $\delta^{18}O$ and δD values of feldspars, secondary micas and other minerals, forming a characteristic bulls-eye pattern of greater alteration centered around the upper portion of the intrusion, where water-rock ratios were the greatest (Taylor and Forester, 1979). Norton and Taylor (1979) numerically modeled this process and estimated that the hydrothermal system lasted ~130 ka, and this estimate remains the best in terms of duration of magmatic-hydrothermal events in Skaergaard.

Recently, Bindeman et al. (2008) re-examined oxygen isotope systematics across the Skaergaard intrusion aiming to identify primary magmatic signatures by laser fluorination analyses of small multigrain fractions, individual phenocrysts and refractory accessory minerals. They confirmed the suggestion by Taylor and Forester (1979) that Skaergaard was initially a normal-$\delta^{18}O$ 5.7 ‰ magma but convincingly demonstrated that late-stage differentiates (ferrodiorites) found

around the Sandwich Horizon have crystallized from low-$\delta^{18}O$ magmas as they contain diverse low-$\delta^{18}O$ populations of zircon, sphene, amphibole and other minerals. As generation of low-$\delta^{18}O$ magma in a closed system igneous fractionation is impossible, incorporation of meteoric water derived oxygen into these late state differentiates is required. Bindeman et al. (2008) suggested that generation of these ^{18}O-depleted magmas could involve sequestration of low-$\delta^{18}O$ melt/fluid from dehydration of hydrothermally altered low-$\delta^{18}O$ fallen blocks into the main volume of the intrusion, but favored partial remelting of already solidified and hydrothermally-altered (and thus low-$\delta^{18}O$) rocks, which happened under the Basistoppen intrusion. Complementing these published oxygen isotope data (Bindeman et al., 2008), we here report zircon oxygen isotope ratios measured by ion microprobe to better constrain the magnitude and related mechanisms of ^{18}O depletion of late-stage differentiates. In contrast to numerous petrologic, geochemical and isotopic studies, surprisingly few geochronological data have been published for the Skaergaard intrusion. Brooks and Gleadow (1977) reported a zircon fission track date of 54.6 ± 1.7 Ma that was later confirmed by biotite and hornblende $^{40}Ar/^{39}Ar$ dates from transgressive granophyres of 55.40 ± 0.14 and 55.48 ± 0.30 Ma, respectively (Hirschmann et al., 1997). Recently, Hamilton and Brooks (2004) reported an ion microprobe (SHRIMP) zircon $^{206}Pb/^{238}U$ date of 55.59 ± 0.13 Ma. While these consistent dates appear to constrain the age of emplacement reasonably precisely and put Skaergaard in the broader context of North Atlantic rift opening, they do not yield information about time scales of intraplutonic crystallization and petrologic evolution of the Skaergaard intrusion.

Recent advances in U-Pb geochronology by isotope dilution–thermal ionization mass spectrometry (ID-TIMS), resulting in analytical uncertainties and external reproducibility at the permil level (e.g. Schoene et al., 2006; Slama et al. 2008), allow the evolution of Cenozoic magmatic systems to be tracked at unprecedented temporal resolution and absolute time constraints to be added to thermal and petrogenetic models (e.g. Schaltegger et al. 2009; von Quadt et al., 2011). Given superb exposure and the young ~56 Ma age of Skaergaard, the ID-TIMS method should in theory permit recognition of individual episodes during ~130 ka duration of Skaergaard crystallization. This work employs chemical abrasion ID-TIMS techniques to obtain the best absolute age for emplacement of the Skaergaard intrusion, to determine the age of its most important coeval magma batch, the tholeiitic Basistoppen sill, and to explore in detail the crystallization and remelting history of the Sandwich Horizon, as well as the petrogenesis of the Brooks Horizon. In particular, we discuss how late intrusion of the Basistoppen Sill lead to remelting of already crystallized Skaergaard differentiates that resulted in the appearance of low-$\delta^{18}O$ magmas around SH. We also model how intergranular melt flow during the proposed remelting event could have generated the Brooks Horizon, the

most incompatible trace element rich horizon in Skaergaard. We further discuss the bearing of our temporal framework of intrusion crystallization on the timing of intimately linked flood basalt volcanism and the temporal relationship with environmental perturbations at the Paleocene-Eocene boundary.

1.3 MATERIALS AND METHODS

Zircons were earlier separated from ferrodiorites of the Sandwich Horizon (SH-428; Hamilton and Brooks, 2004), a podiform gabbroic pegmatite from lower zone b of the layered series (SK-218; Larsen and Brooks, 1994), the post-Skaergaard tholeiitic Basistoppen Sill (BZN) and the related Sydtoppen granophyre (SK-88; Naslund, 1989). A total of 32 zircon crystals from samples SK-218, SH-428, and BZN were analyzed as single grains by ID-TIMS at the University of Geneva following procedures of Schoene et al. (2010). Prior to dissolution, all crystals were annealed by heating to 900 °C for 48 h in a muffle furnace, transferred into 3 ml Savillex beakers and chemically abraded in HF + trace HNO_3 at 180 °C for 15 h in Parr bombs (Mattinson, 2005). Subsequently, zircons were rinsed with water, fluxed for several hours in 6N HCl and ultrasonically cleaned with water, acetone and 3N HNO3. Single crystals were loaded in 200 μl Savillex capsules, spiked with ~3-5 mg of the EARTHTIME ($\pm^{202}$Pb)-^{205}Pb-^{233}U-^{235}U tracer solution (http://www.earth-time.org/) and dissolved in ~70 μl HF at 210 °C for 48 h in Parr bombs. After dissolution, samples were dried down and redissolved in 6N HCl at 180 °C overnight, dried down again and redissolved in 3N HCl. U and Pb were separated using a modified HCl-based single-column anion exchange chemistry (Krogh, 1973). The Zr, Hf, and trace element fraction ("wash") was collected for Hf isotope analyses (see below). The U-Pb fraction was loaded on outgassed Re filaments with a Si-Gel emitter modified from Gerstenberger and Haase (1997). U and Pb isotopic measurements were performed on a Thermo TRITON thermal ionization mass spectrometer. Pb was measured in dynamic mode on a MasCom secondary electron multiplier. Analyses employing the ET2535 tracer were corrected using the fractionation factor derived from the measured ^{202}Pb/^{205}Pb ratio assuming a true value of 0.99924. Measurements employing the ET535 tracer were corrected for 0.13 ± 0.02 %/amu mass fractionation based on >200 analyses using the ^{202}Pb-^{205}Pb double spike performed during the course of this study. U was measured as U-oxide in static mode on Faraday cups equipped with 10^{12} Ω resistors. Measured isotopic ratios were corrected for interferences of $^{233}U^{18}O^{16}O$ on $^{235}U^{16}O_2$ using an $^{18}O/^{16}O$ of 0.00205, measured on large U500 loads, and for mass fractionation using the measured $^{233}U/^{235}U$ ratio relative to a value of 0.99506 for both tracers. All common Pb in the zircon analyses (average: 0.62 ± 0.14 pg) was assumed to be procedural blank. U-Pb ratios and dates were calculated relative to a $^{235}U/^{205}Pb$ ratio of 100.23 ± 0.023% (1σ) and raw data were reduced using Tripoli and U-Pb_Redux software (Bowring et al., 2011) that employs algorithms of McLean et al. (2011).

All uncertainties are reported at the 95% confidence level and exclude systematic uncertainties associated with tracer calibration and decay constants unless otherwise indicated.

Lutetium-Hafnium isotopes of selected U-Pb dated zircons were analyzed employing a Thermo NEPTUNE multi collector–inductively coupled plasma mass spectrometer (MC-ICPMS) at Goethe University Frankfurt. After column chemistry, the washes were dried down, redissolved in 250-400 μl 0.5 M HNO_3 + 0.1 M HF and transferred into pre-cleaned auto sampler microtubes. Solutions were introduced into the plasma employing an Aridus desolvation nebulizer with a nominal uptake rate of 100 μl/min. Isotopic ratios were measured in static mode on Faraday detectors equipped with 1010 (for mass 180) or 10^{11} Ω (all other masses) resistors. ^{172}Yb, ^{173}Yb and ^{175}Lu were measured to correct for isobaric interferences of Yb and Lu on mass 176 assuming a ^{176}Yb/^{173}Yb ratio of 0.79502 and a ^{176}Lu/^{175}Lu ratio of 0.02656. Yb and Hf isotopic ratios were corrected for mass fractionation by normalizing to ^{172}Yb/^{173}Yb of 1.35351 and ^{179}Hf/^{177}Hf of 0.7325 using an exponential law. Mass fractionation of Lu was assumed to follow that of Yb (see Gerdes and Zeh, 2006). Accuracy and reproducibility of this protocol were assessed by repeat analyses of 10 ppb JMC 475 standard solutions (^{176}Hf/^{177}Hf=0.282148 ± 5, 2SD, n=21) bracketing unknowns. Initial ^{176}Hf/^{177}Hf ratios and εHf were calculated using the ^{206}Pb/^{238}U date of the respective crystal and the CHUR parameters of Bouvier et al. (2008; ^{176}Lu/^{177}Hf=0.0336; ^{176}Hf/^{177}Hf=0.282785). All uncertainties are given at the 2σ level and include the reproducibility of the JMC 475 solution propagated by quadratic addition.

For in-situ oxygen isotope analyses, zircon crystals were available from samples SK-218, SH-428 and SK-88. Sam-

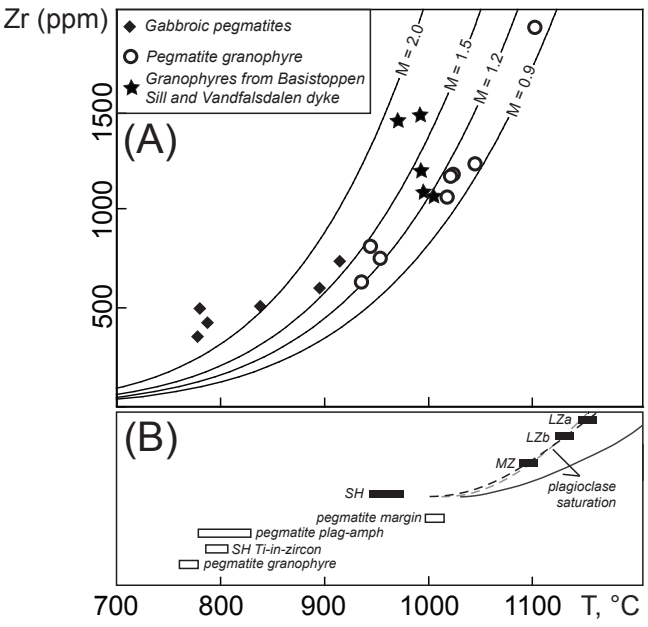

FIGURE 1.2 Zircon saturation temperatures and crystallization temperatures of late-stage pegmatites and related granophyres. (A) Zr concentrations plotted against zircon saturation temperatures calculated according to Watson and Harrison (1983) using whole rock compositions published by McBirney (1989) and Larsen and Brooks (1994). (B) Independent constraints for the crystallization temperature of Layered Series gabbros (closed symbols and curves of plagioclase saturation temperature), late-stage pegmatites and related granophyres (open symbols; see text for details and references).

ple BZN only yielded ~10 zircons that we preferred to use for geochronology. Zircon crystals were mounted in epoxy resin, polished to expose grain interiors and gold coated. Cathodoluminescence imaging prior to analyses did not reveal distinct cores and rims (Appendix C). A subset of three individual zircons were pressed in indium metal and only lightly polished (~2-4 μm) to achieve required flatness and analyze outermost rims. Exposed zircon cores and lightly polished zircon faces were analyzed for oxygen isotopes employing a CAMECA ims 1270 secondary ion mass spectrometer (SIMS) at the University of California, Los Angeles (UCLA). Instrumental calibration and analytical methods were identical to those of Bindeman et al. (2010). Uncertainties were estimated from the reproducibility of repeat analyses of standard zircon AS3 measured during the respective analytical session.

1.4 ZIRCON CRYSTALLIZATION IN THE SKAERGAARD INTRUSION

As zircon has only recently been employed in study of Skaergaard (and other similar mafic intrusions), we here provide a discussion of zircon saturation and its time (and temperature) of appearance during crystallization. At crystallization temperatures of 1200-1000°C and low zirconium concentrations (10-130 ppm; Brooks, 1969; McBirney, 2002), zircon unlikely was a cumulus phase during crystallization of LS gabbros. However, throughout the Skaergaard intrusion, the final stages of crystallization are characterized by granophyric accumulations occurring either as segregations of primary gabbroic pegmatites throughout the intrusion, or as interstitial granophyre that comprises up to 50% of late-stage differentiates around the SH (Wager and Brown, 1968; Larsen and Brooks, 1994; Larsen and Tegner, 2006). Late-stage silica enrichment, achieved either by fractional crystallization or liquid immiscibility (e.g. Jakobsen et al., 2005; Holness et al., 2011), is accompanied by progressive Zr enrichment with concentrations of 300-800 ppm in evolved gabbroic pegmatites and up to 2000 ppm in related granophyres (Brooks, 1969; Larsen and Brooks, 1994; McBirney, 1989; Fig. 1.2), represented by our sample SK-218. Bulk SH ferrodiorites (similar to our sample SH-428) have 250-350 ppm Zr (Brooks, 1969; McBirney, 1989; McBirney, 2002) but interstitial granophyres are likely to be similar in composition to pegmatitic granophyres. We thus argue, that gabbroic pegmatites and evolved granophyres provide a good estimate for the range of compositions of zircon crystallizing interstitial liquids. Application of the zircon solubility model of Watson and Harrison (1983) returns apparent zircon saturation temperatures of 778-915°C and 935-1102°C for gabbroic pegmatites and related granophyres, respectively (Fig. 1.2). These zircon saturation temperatures have to be interpreted in the context of independent estimates for the formation temperatures of the respective mineral assemblages: gabbroic pegmatites experienced prolonged crystallization over a temperature interval from 1000 to 800°C (Larsen and Brooks, 1994) and the granophyric assemblage crystal-

lized close to the thermal minimum of the quartz-albite-orthoclase system (660-690°C; Larsen and Tegner, 2006). Watson et al. (2006) reported Ti-in-zircon temperatures for zircons from the SH of 787-806°C that are likely minimum temperatures due to undersaturation of these magmas in rutile. These data support that zircon was not a main cumulus phase but crystallized from silica enriched interstitial liquids. These late-stage silica enriched magmas formed at ~1000°C and had near-liquidus zircon that crystallized over a narrow temperature interval from the time of zircon saturation until eutectic crystallization of the main granophyric assemblage.

The ~600 m thick Basistoppen Sill, a small layered intrusion in itself, had similar bottom to top crystallization and zircon saturation histories to Skaergaard. Upon differentiation, the Basistoppen Sill and related dykes (e.g. Vandfalsdalen dyke; White et al., 1989) achieved granophyric accumulations in the middle and towards the top, similar in composition to pegmatitic granophyres in the Skaergaard intrusion (Naslund, 1989; White et al., 1989). The main granophyric body related to crystallization of the Basistoppen Sill is the Sydtoppen granophyre on top of Basistoppen, which has high radiogenic isotope ratios related to assimilation of Archean crust (Leeman and Dasch, 1978). Zr concentrations and calculated zircon saturation temperatures are similar to Skaergaard granophyres (Fig. 1.2; Naslund, 1989) indicating that zircon crystallization in the Basistoppen Sill is also associated with late-stage silica enrichment.

Table 1.1 *Ion microprobe zircon oxygen isotope data. All $\delta^{18}O$ values are reported relative to Vienna Standard Mean Ocean Water (VSMOW).*

Crystal/Spot	core/face	$\delta^{18}O$ [‰], VSMOW	±1SD*
Sandwich Horizon (SH-428; 13 crystals; 21 spots)			
SH428 1.1	c	4.82	0.47
SH428 1.2	c	4.11	0.47
SH428 2.1	c	4.62	0.47
SH428 2.2	c	5.34	0.47
SH428 3.1	c	4.76	0.47
SH428 3.2	c	4.33	0.47
SH428 3.3	c	4.12	0.47
SH428 3.4	c	4.11	0.47
SH428 3.5	c	4.02	0.47
SH428 4.1	c	5.38	0.47
SH428 4.2	c	4.29	0.47
SH428 4.3	c	4.90	0.47
SH428 5.1	c	5.38	0.47
SH428 6.1	c	4.20	0.47
SH428 7.1	c	4.83	0.22
SH428 8.1	c	4.95	0.22
SH428 9.1	c	4.61	0.22
SH428 10.1	c	4.72	0.22
SH428 11.1	f	3.80	0.36
SH428 12.1	f	3.97	0.36
SH428 13.1	f	3.64	0.36
Pegmatite in LZb (SK-218; 6 crystals; 8 spots)			
SK218 1.1	c	4.31	0.47
SK218 1.2	c	4.62	0.47
SK218 2.1	c	4.03	0.47
SK218 2.2	c	5.05	0.47
SK218 3.1	c	5.05	0.47
SK218 4.1	c	4.81	0.47
SK218 5.1	c	4.39	0.47
SK218 6.1	c	4.03	0.47
Sydtoppen granophyre (SK-88; 5 crystals; 5 spots)			
SK88 1.1	c	4.64	0.22
SK88 2.1	c	5.18	0.22
SK88 3.1	c	5.21	0.22
SK88 4.1	c	5.51	0.22
SK88 5.1	c	5.06	0.22

*1 SD corresponds to the reproducibility of zircon standards analyzed during the same analytical session. Glass standards analyzed in the beginning of each session were reproducible to within 0.2-0.3 ‰.

1.5 OXYGEN ISOTOPE ANATOMY OF THE SKAERGAARD INTRUSION

Multitudes of bulk (whole rocks, bulk minerals) isotope analyses of oxygen and

hydrogen isotopes are presented by Taylor and Forester (1979) and demonstrated profound and pervasive hydrothermal alteration by heated meteoric (rain and snow) water throughout the crystallization history of the intrusion. Plagioclase is particularly strongly altered and was used by Norton and Taylor (1979) to model time-integrated water-rock ratios for each volume of rock. Clinopyroxene shows less isotopic alteration where mineralogically unaltered and uninverted, and appears to indicate mantle-like values for the parental Skaergaard magma (Taylor and Forester, 1979). Clinopyroxene in more evolved rocks is extremely Fe-enriched (nearly pure hedenbergitic end-member; Brown and Vincent, 1963; McBirney, 2006), and is structurally and crystallographically represented by inverted ferrobustamite. It possesses consistently lower $\delta^{18}O$ values relative to coexisting plagioclase that were attributed to subsolidus inversion of magmatic ferrobustamite to a fine-grained mosaic of hedenbergitic clinopyroxenes, making them more susceptible to hydrothermal alteration. In order to circumvent these problems, Bindeman et al. (2008) performed single crystal analysis of least altered selected Skaergaard rocks with near magmatic $\Delta^{18}O_{plag\text{-}cpx}$, and also targeted refractory alteration resistant accessory phases (ferroamphibole, sphene, and zircon) that preserved primary magmatic $\delta^{18}O$ values and maintained $\delta^{18}O_{mineral\text{-}mineral}$ equilibrium characteristic of magmatic temperatures. These authors demonstrated that Skaergaard magma, coeval basalts, and the Basistoppen Sill initially were undoubtedly MORB-like, normal-$\delta^{18}O$ magmas, but evolved Skaergaard ferrodioritic rocks in the interior around SH crystallized from a low-$\delta^{18}O$ melt that was heterogeneously depleted by ~1 to 3‰ with respect to oxygen. However, the "$\delta^{18}O$ equilibrium" zircon value in the Sandwich Horizon is a less certain parameter. If we assume that large and unaltered sphene ($\delta^{18}O = 2.99 \pm 0.03$‰) represents the "true" solidus assemblage (and not high-T hydrothermal) as is texturally apparent, then using the fractionation factor $\delta^{18}O_{zircon\text{-}sphene} = 1.02$‰ (Valley et al. 2003), requires zircon to be 3.88‰ at 800°C; if a 3‰ ferroamphibole is taken as a reference point, then the equilibrium zircon value is to be 3.28‰, similar to the bulk zircon measured. These $\delta^{18}O$ relationships suggest isotopic heterogeneities and motivated us to conduct a zircon oxygen isotope survey by ion-microprobe.

Individual ion microprobe oxygen isotope analyses of zircon cores and lightly polished crystal faces are given in Table 1.1 and are plotted in Figure 1.3 together with previously published data (Taylor and Forester, 1979; Bindeman et al., 2008) against their stratigraphic position in the Skaergaard intrusion. Ion microprobe analyses revealed the presence of normal-$\delta^{18}O$ zircon cores throughout the Skaergaard intrusion. Note that because of the cooling and fractionation effects, the intercumulus or pegmatitic zircons are expected to be slightly lower in $\delta^{18}O$ than a canonical 5.3 ± 0.3‰ mantle zircon (e.g. Valley, 2003). This systematic shift to lower values is also consistent with slightly lower average clinopyroxene $\delta^{18}O$ values in Skaergaard (Fig. 1.3).

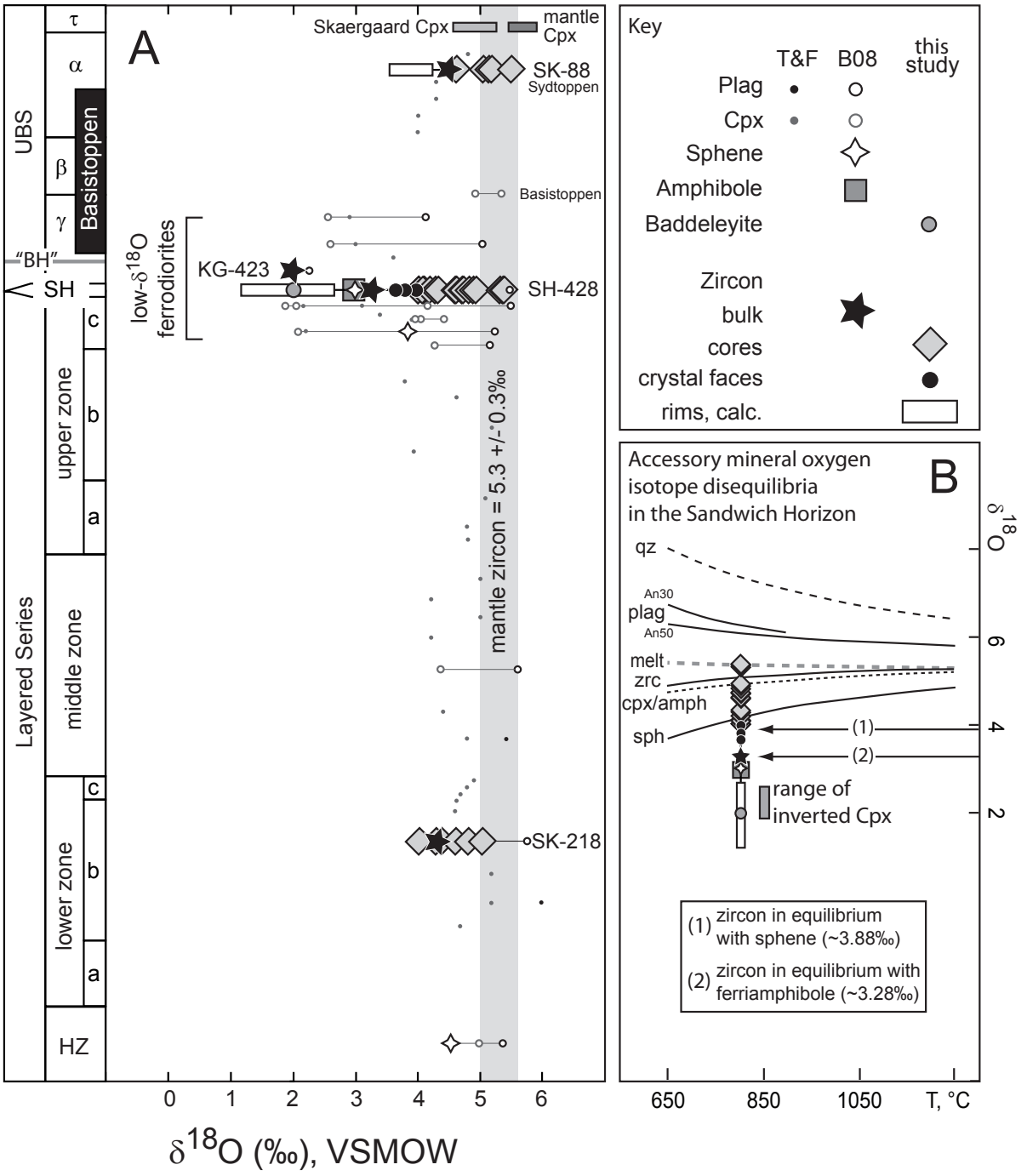
A
Skaergaard Cpx
mantle Cpx
SK-88
Sydtoppen
Basistoppen
KG-423
SH-428
low-δ18O ferrodiorites
mantle zircon = 5.3 +/-0.3‰
SK-218
UBS
Layered Series
τ
α
β
γ
Basistoppen
"BH"
SH
upper zone
middle zone
lower zone
HZ
a
b
c
0
1
2
3
4
5
6
δ18O (‰), VSMOW
Key
T&F
B08
this study
Plag
Cpx
Sphene
Amphibole
Baddeleyite
Zircon
bulk
cores
crystal faces
rims, calc.
Accessory mineral oxygen isotope disequilibria in the Sandwich Horizon
B
qz
An30
plag
An50
melt
zrc
cpx/amph
sph
(1)
(2)
range of inverted Cpx
(1) zircon in equilibrium with sphene (~3.88‰)
(2) zircon in equilibrium with ferriamphibole (~3.28‰)
650
850
1050
T, °C
δ18O
2
4
6

FIGURE 1.3 (previous page) Oxygen isotope anatomy of the Skaergaard intrusion. (A) $\delta^{18}O$ values of zircon cores and crystal faces analyzed by ion microprobe are plotted together with previously published oxygen isotope data of Taylor and Forester (1979) and Bindeman et al. (2008) against their stratigraphic position in the Skaergaard intrusion. (B) Illustration of accessory mineral oxygen isotope disequilibria in the Sandwich Horizon. Equilibrium oxygen isotope fractionation factors are plotted as a function of temperature for various minerals. $\delta^{18}O$ values of accessory minerals from the Sandwich Horizon are plotted at a plausible crystallization temperature of ~800°C showing that ^{18}O depletion exceeds the magnitude of depletion expected from equilibrium fractionation. Horizontal arrows show $\delta^{18}O$ values of zircon in equilibrium with sphene and ferroamphibole.

The newly observed differences between zircon core $\delta^{18}O$ values and those of bulk zircon fractions analyzed by laser fluorination (Bindeman et al., 2008) is interpreted to reflect inter- and intracrystalline heterogeneity and additional presence of isotopically light (~2‰) baddeleyite in bulk zircon fractions[1]. In the case of the pegmatite from LZb, zircon core and bulk zircon $\delta^{18}O$ values overlap suggesting that zircons are isotopically homogeneous within the resolution of SIMS analyses. Zircons from the Sydtoppen granophyre (SK-88) have average core $\delta^{18}O$ values that are ~0.5‰ higher than those of bulk zircon fractions. Isotopic heterogeneity is more pronounced in the most evolved part of the intrusion around the SH (sample SH-428). Ion microprobe analyses of zircon cores yielded $\delta^{18}O$ values ranging from 4.02-5.38‰ and lightly polished zircon crystal faces yielded $\delta^{18}O$ values of 3.64 to 3.97‰, similar to the lowest measured zircon core values, suggesting >1‰ inter- and/or intracrystal variation with respect to $\delta^{18}O$. If baddeleyite contribution to bulk zircon analysis is ignored, then mass balance of 3.25‰ bulk zircon requires that individual (small) zircons or outermost several microns of some zircons had $\delta^{18}O$ values in ~1 to 2.5‰ range (Fig. 1.3B). These calculated rim values are similar to the 2‰ bulk zircons in sample KG-423 (Fig. 1.3), 30 m above SH. The ~2‰ $\delta^{18}O$ values are also in apparent isotopic equilibrium with many individual inverted clinopyroxenes around the Sandwich Horizon (Bindeman et al., 2008), but are lower than is required by sphene and ferroamphibole in the same sample (Fig. 1.3B).

Figure 1.4 represents our view of the textural evolution and magmatic-hydrothermal history of the SH that demonstrates that this assemblage is better viewed as "metamorphic", in a sense that it never achieved 100% remelting, chemical, and isotopic equilibration. Samples 30 m apart (i.e. KG-423 and SH-428) have zircons that are different by 1.3‰ in $\delta^{18}O$. Instead we speculate below that the melting degree upon reheating by Basistoppen was significantly less than 50% and that $\delta^{18}O$ was equilibrated only locally.

---

[1]Baddeleyite in Skaergaard rocks appears as individual irregular shaped crystals and as inclusion within zircons (e.g. Fig. 4e in Bindeman et al., 2008). Small quantity of baddeleyite (0.12 mg) was analyzed as a mix with garnet standard by laser fluorination (see details in Appendix D) and yielded ~2.04 ± 1.12‰ value.

A - Original crystallization of the Sandwich Horizon

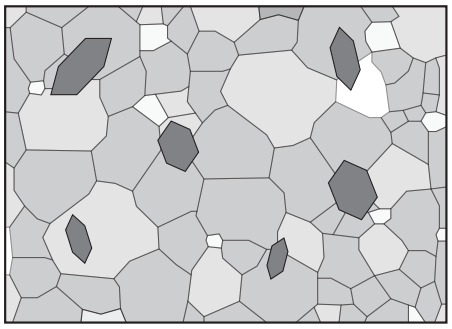

Original crystallization of the Sandwich Horizon with ~5‰ zircon

zircons are isotopically homogeneous

unaltered normal-$\delta^{18}O$ rock and minerals

B - Hydrothermal alteration of SH

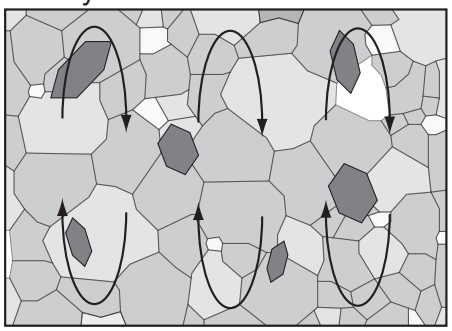

Original ~5‰ zircon unaffected by hydrothermal alteration

Alteration of main phenocryst assemblage (particularly plagioclase)

variably low-$\delta^{18}O$ rock

C - Reheating/remelting

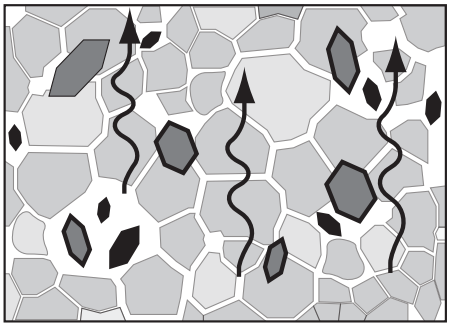

Original zircon rims equilibrate diffusively with low-$\delta^{18}O$ melt.

Original zircon cores unaffected.

Newly crystallized low-$\delta^{18}O$ zircon (rims), sphene and ferro-amphibole.

Low-$\delta^{18}O$ partial melt migrates upward by intergranular compaction driven flow

D - Slow plutonic cooling and renewed hydrothermal alteration

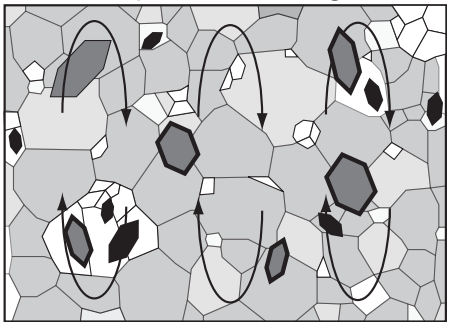

original zircon ($\delta^{18}O$ = 5‰)

original core with equilibrated or newly crystallized rim

newly crystallized upon remelting ($\delta^{18}O$ = 1-4‰)

hydrothermal circulation/alteration

compaction-driven upward percolation of partial melt

FIGURE 1.4 (previous page) Conceptual cartoon of accessory mineral behavior during crystallization and remelting of the Sandwich Horizon based on oxygen isotope heterogeneity. (A) Late-stage zircon crystallization from normal-$\delta^{18}O$ melt. (B) Variable hydrothermal alteration of main phenocryst assemblage leading to low-$\delta^{18}O$ whole rock, plagioclase and clinopyroxene values, while zircons are unaffected. (C) Reheating and partial remelting of hydrothermally altered Skaergaard differentiates leading to the formation of heterogeneously ^{18}O depleted magma, from which low-$\delta^{18}O$ zircon, sphene and ferroamphibole crystallize. Low-$\delta^{18}O$ melt is partially lost upwards by intergranular compaction driven flow. (D) Renewed hydrothermal alteration during slow plutonic cooling leaving low-$\delta^{18}O$ refractory minerals unaffected.

1.6 ID-TIMS ZIRCON U-PB GEOCHRONOLOGY

Zircon U-Pb results are listed in Table 1.2 and Figure 1.5A displays $^{206}Pb/^{238}U$ dates corrected for initial ^{230}Th disequilibrium in comparison to previously published dates for the Skaergaard intrusion. Additionally, Lu-Hf isotopic data of selected dated zircons are listed in appendix A (Tab. A1.1) and Figures 1.5B-D show εHf values plotted against the Th/U ratio of the respective zircon and previously published whole rock Nd and Sr isotope ratios (McBirney and Creaser, 2003). These measurements of Hf isotopic composition were performed on the same zircons, allowing additional fingerprinting of sources. They demonstrate that dated zircons of the LS pegmatite and SH of Skaergaard overlap in isotopic composition, while Basistoppen zircons require a more radiogenic, likely crustally contaminated parental magma.

Seven out of eight $^{206}Pb/^{238}U$ zircon dates of the gabbroic pegmatite from lower zone b of the layered series (SK-218) are equivalent with a weighted mean date of 55.960 ± 0.018 Ma (mean square of weighted deviates, MSWD = 1.4). We interpret this date to reflect rapid crystallization of the pegmatite after accumulation of intercumulus melt. We also consider this oldest age as the closest approximation of Skaergaard intrusion. Norton and Taylor (1979) modeled the thermal evolution of the Skaergaard intrusion and estimated that cooling from 1200-1250°C at the time of emplacement to 800-1000°C, corresponding to the temperature of zircon saturation, took some 60 ka. Considering this model, the "true" intrusion age of Skaergaard can be estimated to be ~56.02 Ma. One SK-218 zircon yielded a significantly older $^{206}Pb/^{238}U$ date of 56.920 ± 0.085 Ma indicating minor xenocrystic or antecrystic contamination.

All analyzed zircons from the Basistoppen Sill (BZN; n=8) yielded statistically equivalent $^{206}Pb/^{238}U$ dates with a weighted mean of 55.895 ± 0.018 Ma (MSWD=0.51). As the sample was taken close to the contact with the Skaergaard intrusion, we consider this zircon crystallization age to approximate injection of the Basistoppen Sill. Notably, zircons from the Basistoppen Sill have distinctly higher Th/U ratios and are less radiogenic with respect to $^{176}Hf/^{177}Hf$ than Skaergaard zircons, which coincides with elevated whole rock $^{87}Sr/^{86}Sr$ and less radiogenic Nd isotopic composition (Fig. 1.5B-D), indicating that they are autocrystic zircons and not antecrysts

Table 1.2 *Zircon U-Pb isotopic results and calculated dates for samples from the Skaergaard intrusive complex*

	Composition				Isotopic Ratios								Dates (Ma)					
Fraction*	Th/U (a)	Pb* (pg) (b)	Pb_c (pg) (c)	Pb*/Pb_c (d)	$^{206}Pb/^{204}Pb$ (e)	$^{206}Pb/^{238}U$ (f,g)	±2σ %	$^{207}Pb/^{235}U$ (f)	±2σ %	$^{207}Pb/^{206}Pb$ (f,g)	±2σ %	Corr. coef.	$^{206}Pb/^{238}U$ (g,h)	±2σ abs	$^{207}Pb/^{235}U$ (h)	±2σ abs	$^{207}Pb/^{206}Pb$ (g,h)	±2σ abs
Basistoppen Sill (BZN)																		
z1	1.77	2.60	0.73	3.5	177	0.008707	0.19	0.0571	2.7	0.047579	2.6	0.753	55.89	0.10	56.4	1.5	78	61
z2	1.49	6.46	0.49	13.1	644	0.008710	0.12	0.05679	1.1	0.047288	0.99	0.694	55.903	0.065	56.08	0.58	64	23
z3	2.27	23.1	0.78	29.6	1230	0.008707	0.086	0.05667	0.42	0.047206	0.39	0.456	55.887	0.048	55.97	0.23	59.7	9.2
z4	1.35	2.49	0.45	5.5	290	0.008700	0.21	0.0567	2.9	0.047308	2.7	0.777	55.84	0.12	56.0	1.6	65	65
z5†	2.16	22.0	0.86	25.6	1090	0.008711	0.087	0.05718	0.51	0.047603	0.46	0.648	55.914	0.049	56.46	0.28	80	11
z6†	1.70	6.86	0.60	11.4	540	0.008706	0.097	0.05697	1.0	0.047462	0.97	0.333	55.879	0.054	56.26	0.55	73	23
z7†	1.82	10.8	0.50	21.7	979	0.008706	0.062	0.05662	0.52	0.047169	0.49	0.589	55.879	0.035	55.92	0.28	58	12
z8†	1.61	19.1	0.48	39.7	1866	0.008712	0.066	0.05672	0.36	0.047218	0.33	0.536	55.917	0.037	56.02	0.20	60.3	7.9
Sandwich Horizon (SH-428)																		
z1	1.08	3.90	0.63	6.2	341	0.008739	0.22	0.0570	2.0	0.047317	1.9	0.660	56.09	0.12	56.3	1.1	65	44
z2	0.55	8.94	0.58	15.4	936	0.008713	0.064	0.05676	0.44	0.047249	0.41	0.614	55.926	0.035	56.06	0.24	61.8	9.7
z3	1.33	7.42	0.85	8.8	451	0.008722	0.096	0.05637	1.0	0.046871	0.97	0.579	55.983	0.053	55.68	0.56	43	23
z4	0.71	3.08	0.60	5.1	309	0.008701	0.098	0.05712	1.4	0.047614	1.3	0.757	55.846	0.055	56.40	0.76	80	31
z5	0.64	7.98	0.49	16.4	970	0.008721	0.066	0.05704	0.45	0.047439	0.43	0.454	55.974	0.037	56.33	0.25	71	10
z6	0.63	2.50	0.53	4.7	288	0.008699	0.10	0.05767	1.6	0.048076	1.5	0.795	55.837	0.058	56.93	0.88	103	36
z7	0.46	7.83	0.59	13.2	821	0.008713	0.061	0.05708	0.50	0.047510	0.47	0.565	55.924	0.034	56.36	0.27	75	11
z8†	0.96	2.30	0.56	4.1	239	0.008714	0.13	0.0577	2.1	0.048061	2.0	0.810	55.932	0.071	57.0	1.1	102	46
z9†	0.96	21.4	0.41	51.9	2807	0.008714	0.036	0.05666	0.20	0.047153	0.17	0.717	55.932	0.020	55.96	0.11	57.0	4.2
z10†	0.45	7.79	0.39	19.9	1240	0.008700	0.042	0.05674	0.36	0.047303	0.36	0.233	55.839	0.023	56.04	0.20	64.5	8.5
z11†	0.74	8.38	0.42	20.1	1157	0.008715	0.049	0.05713	0.41	0.047542	0.37	0.764	55.937	0.027	56.41	0.22	76.6	8.9
z12	0.82	2.22	0.63	3.5	213	0.008697	0.12	0.0574	1.9	0.047875	1.8	0.833	55.820	0.064	56.7	1.1	93	44
z13	0.46	4.97	0.46	10.8	675	0.008712	0.076	0.05651	0.80	0.047040	0.75	0.677	55.918	0.042	55.81	0.43	51	18
z14	0.86	3.85	0.57	6.8	389	0.008713	0.082	0.05716	1.1	0.047575	1.0	0.755	55.925	0.046	56.44	0.58	78	24
z15	1.15	6.64	0.51	13.1	692	0.008711	0.075	0.05660	0.67	0.047122	0.63	0.527	55.914	0.042	55.90	0.36	55	15
z16	1.14	2.01	0.74	2.7	158	0.008699	0.17	0.0577	2.8	0.048142	2.7	0.858	55.837	0.093	57.0	1.6	106	63
Pegmatite in LZb (SK-218)																		
z1	0.79	13.5	0.85	15.8	902	0.008721	0.067	0.05728	0.56	0.047636	0.52	0.666	55.977	0.038	56.56	0.31	81	12
z2	1.19	3.00	0.74	4.0	223	0.008725	0.17	0.0564	2.3	0.046855	2.2	0.779	55.998	0.094	55.7	1.2	42	51
z3	0.79	19.3	0.82	23.6	1341	0.008715	0.062	0.05681	0.32	0.047278	0.30	0.491	55.940	0.035	56.11	0.18	63.3	7.0
z4	0.74	6.86	0.73	9.3	548	0.008717	0.094	0.05723	0.84	0.047619	0.79	0.556	55.950	0.052	56.51	0.46	80	19
z5	0.63	10.8	0.80	13.5	804	0.008723	0.071	0.05707	0.61	0.047450	0.57	0.600	55.988	0.040	56.35	0.33	72	14
z6	0.47	7.48	0.80	9.3	584	0.008710	0.11	0.05689	0.82	0.047375	0.77	0.573	55.903	0.059	56.18	0.45	68	18
z7	0.40	1.87	0.50	3.7	248	0.008719	0.12	0.0573	1.8	0.047654	1.7	0.839	55.965	0.065	56.57	0.99	82	40
z8	0.52	5.52	2.05	2.7	179	0.008869	0.15	0.0589	2.4	0.048127	2.3	0.853	56.920	0.085	58.1	1.4	106	54

*Fractions are single crystals or fragments chemically abraded after Mattinson (2005); †sample measured with ET2535 tracer
(a) Th contents calculated from radiogenic ^{208}Pb assuming concordance between U-Th and Pb systems.
(b) Total mass of radiogenic Pb.
(c) Total mass of common Pb.
(d) Ratio of radiogenic Pb (including ^{208}Pb) to common Pb.
(e) Measured ratio corrected for fractionation and spike contribution only.
(f) Measured ratios corrected for fractionation, tracer and blank.
(g) Corrected for initial Th/U disequilibrium using radiogenic ^{208}Pb and Th/U[magma]=4 ± 1 (2σ).
(h) Isotopic dates calculated using the decay constants λ238 = 1.55125E-10 and λ235 = 9.8485E-10 (Jaffey et al., 1971).

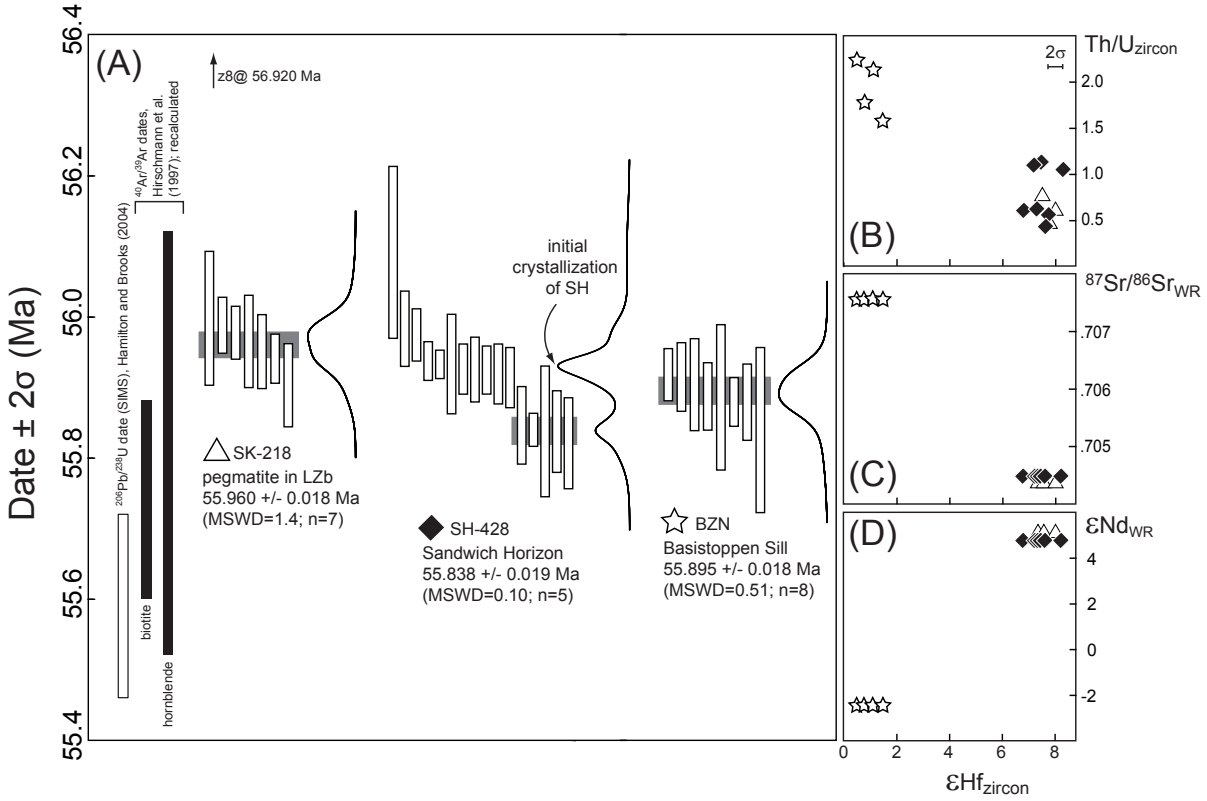

FIGURE 1.5 Geochronology of the Skaergaard intrusive complex. (A) Previously published ion microprobe U-Pb and $^{40}Ar/^{39}Ar$ dates of Hamilton and Brooks (2004) and Hirschmann et al. (1997), respectively and CA-ID-TIMS zircon dates for samples analyzed in this study, displayed as ranked ^{230}Th disequilibrium corrected $^{206}Pb/^{238}U$ dates with the weighted mean dates of the youngest populations and probability density distributions. (B-D) Hafnium isotope data of selected U-Pb dated zircons plotted against their Th/U ratio and whole rock Nd and Sr isotope data of McBirney and Creaser (2003). Note that $^{40}Ar/^{39}Ar$ dates of Hirschman et al. (1997) were recalculated using the age of Kuiper et al. (2008) for the Fish Canyon sanidine standard and the ^{40}K decay constant of Min et al. (2000). All uncertainties are shown at the 95% confidence level.

from the surrounding Skaergaard differentiates.

$^{206}Pb/^{238}U$ dates of zircons from the Sandwich Horizon (SH-428) range from 55.820 ± 0.064 to 56.09 ± 0.12 Ma. Many single grain dates do not overlap at the 95% confidence level (MSWD=6.6; n=16), precluding the calculation of a single weighted mean date for the population. We consider each single grain date to be accurate within the quoted uncertainty and regard the excess scatter to reflect protracted zircon growth. The oldest three zircon $^{206}Pb/^{238}U$ dates are slightly older than the crystallization age of the pegmatite from LZb. Another eight zircons define a subpopulation with $^{206}Pb/^{238}U$ dates that are younger than the pegmatite but older than the Basistoppen Sill. The remaining five zircons define

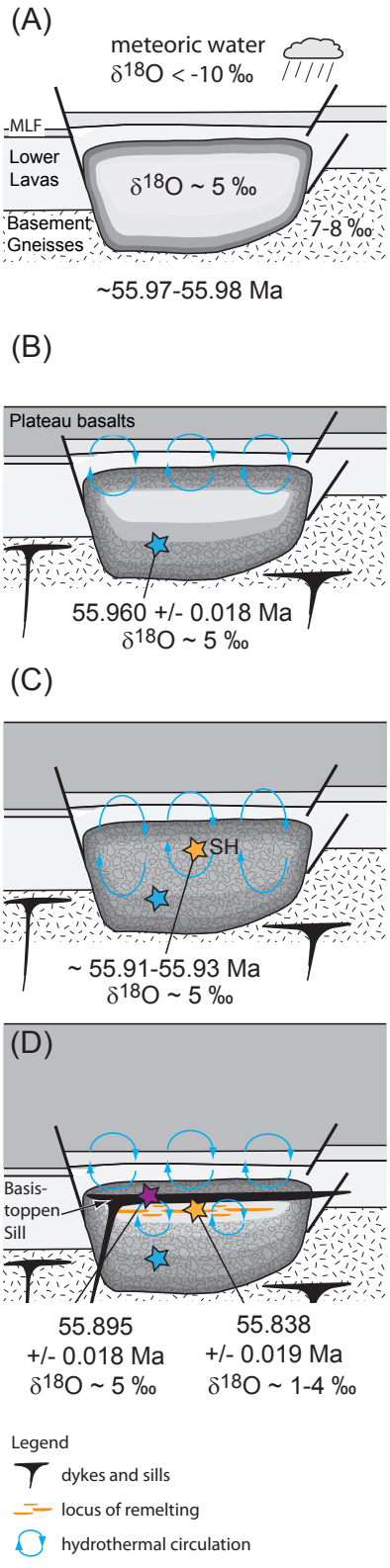

FIGURE 1.6 Cartoon summarizing the evolution of the Skaergaard intrusive complex. (A) Shallow emplacement of the Skaergaard intrusion into the unconformity between basement and overlying basalts. Estimated $\delta^{18}O$ of meteoric water (-14‰) is from Taylor and Forester (1979). (B) Progressive crystallization of the Skaergaard layered series (including pegmatite SK-218) from normal-$\delta^{18}O$ magma and initiation of a meteoric-hydrothermal system that primarily affects the Upper Border Series (UBS). (C) Initial crystallization of the Sandwich Horizon marks the complete solidification of the Skaergaard intrusion. The meteoric-hydrothermal system leads to alteration of most of the intrusion. (D) Intrusion of the Basistoppen Sill into UBS leads to reheating and partial remelting of surrounding Skaergaard differentiates. During these late stages of crystallization the Skaergaard intrusion is progressively buried by outpouring of the East Greenland flood basalts. Note that the thickness of basalts is not to scale.

a subpopulation with a weighted mean $^{206}Pb/^{238}U$ date of 55.838 ± 0.019 Ma that is 57 ± 37 ka younger than the intrusion age of the Basistoppen Sill (see discussion below).

1.7 DISCUSSION

1.7.1 In situ isotopic and geochronologic architecture of Skaergaard reveals partial remelting episode in its lifetime

Our new ion microprobe zircon oxygen isotope analyses and the high-resolution temporal framework derived from chemical abrasion ID-TIMS zircon geochronology provide critical new evidence that late-stage Skaergaard rocks became fully crystalline, hydrothermally altered, and subsequently partially remelted, induced by intrusion of the Basistoppen Sill (Fig. 1.6A-D). Ion microprobe analyses

of zircon cores and zircon crystal faces from the Sandwich Horizon yielded $\delta^{18}O$ values, that are systematically higher than bulk zircon fractions, indicating that zircons in the most evolved part of the intrusion are zoned and isotopically heterogeneous in $\delta^{18}O$. Furthermore, isotopic disequilibria between refractory minerals in this assemblage (zircon, sphene and ferroamphibole) suggest (1) heterogeneous hydrothermal depletion with respect to ^{18}O by ~1-4‰ relative to the initial mantle derived magma, consistent with centimeter scale $\delta^{18}O$ heterogeneity in other meteoric hydrothermal systems (e.g. Mora et al., 1999) and (2) incomplete reequilibration during partial remelting of these variably hydrothermally altered precursor rocks. Calculated minimum values of zircon rims or individual low-$\delta^{18}O$ zircons are also in apparent isotopic equilibrium with many inverted clinopyroxenes (fine grained hedenbergite mosaic; Lindsley et al., 1969) of the same or adjacent samples. Bindeman et al. (2008) speculated that these inverted low-$\delta^{18}O$ clinopyroxenes could be the result of remelting with high melt/solid ratios, whereupon these clinopyroxenes went through the crystallization cycle a second time, equilibrated with the low-$\delta^{18}O$ magma and inverted during cooling. Partial melting with low melt/solid ratios and solid-state recrystallization, in contrast, would result in large individual hedenbergite grains without the characteristic inversion textures (Bindeman et al., 2008). Isotopic equilibrium between some low-$\delta^{18}O$ zircons or zircon rims and inverted clinopyroxenes support this hypothesis and thus support models of remelting after subsolidus hydrothermal alteration.

Such a remelting event requires a proximal heat source and our new geochronological data contribute temporal relationships between late-stage crystallization of Skaergaard differentiates and emplacement of the Basistoppen Sill. Zircon crystallization ages for a normal-$\delta^{18}O$ pegmatite within LZb of the Layered Series and the Basistoppen Sill bracket initial solidification of the Skaergaard intrusion. The majority of zircons from the low-$\delta^{18}O$ SH is older than the crystallization age of the Basistoppen Sill (Fig. 1.5). We interpret this main population to record initial crystallization of the SH from a normal-$\delta^{18}O$ magma before intrusion of the Basistoppen Sill. The youngest five zircons define a population that is 57 ± 37 ka younger than the Basistoppen Sill (Fig. 1.5) suggesting that final solidification of the SH post-dates sill emplacement. This requires that the SH was remelted after subsolidus hydrothermal alteration by the Basistoppen Sill, in line with the oxygen isotope record. Together with our oxygen isotope results, these data suggest that remelting operated over quite some distance (>100 m) and not just along the contacts which is evident from the textural observation of local back-veining and hybridization (Naslund, 1989). Taking into account the possibility that the younger zircon population in the SH might correspond to zircons with post-Basistoppen overgrowth around older (i.e., >55.90 Ma) cores, the lag-time between intrusion of the Basistoppen Sill and crystallization of the youngest dated zircons from the SH may

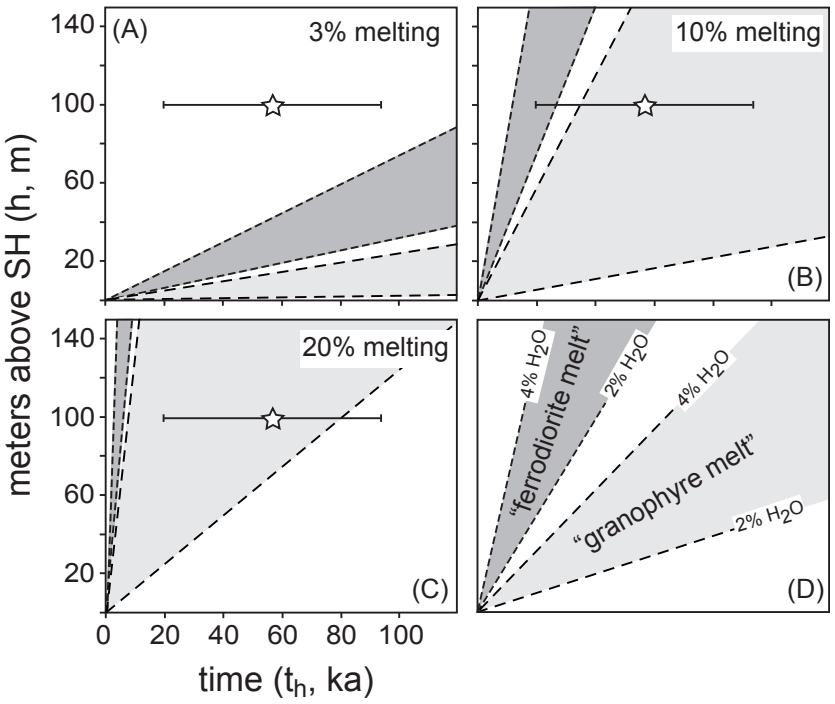

FIGURE 1.7 Calculated time scales for melt migration from the Sandwich Horizon to the Brooks Horizon by compaction driven flow. (A-C) Calculations for various degrees of melting and different magma compositions with various H_2O contents. The star with uncertainty denotes the duration of the proposed remelting event derived from our geochronological data. (D) Graphical explanation for (A-C).

be regarded as a minimum time remelted SH spent above solidus. Considering the volumetric importance of zircon rims in bulk grain analyses and the relatively large uncertainty, we consider this lag-time as our best estimate for the duration of the remelting event (57 ± 37 ka).

1.7.2 Remelting and petrogenesis of the "Brooks" Horizon

The remelting model proposed for generation of late-stage Skaergaard differentiates (low-$\delta^{18}O$ magmas) might also provide an explanation for the petrogenesis of the so-called Brooks Horizon (or "secondary Sandwich Horizon", SHs, of McBirney, 2002), the most incompatible trace element-rich horizon in Skaergaard. The Brooks Horizon is located in UBSγ, approximately 100 m above SH and roughly coincides with the most 18O depleted horizon in Skaergaard (Fig. 1.3). Partial remelting of hydrothermally altered rocks would produce ^{18}O depleted and trace element enriched melts. Accumulation of such melt at the Brooks Horizon requires upward percolation through the porous matrix during the remelting event, a process originally discussed by Irvine (1980). We calculated time scales of melt extraction from the partially molten porous matrix between the SH and the Brooks Horizon by compaction using algorithms of McKenzie (1984). Details of the calculation are given in Appendix B. As results of these calculations are most sensitive to the viscosity of the melt (e.g. Bachmann and Bergantz, 2004), which itself is a function of melt composition, we calculated two end-member scenarios: (1) for a melt equivalent in composition to SH ferrodiorites ("ferrodiorite melt") and (2) for a melt equivalent in composition to granitic gra-

nophyres ("granophyre melt"). For each melt composition, water content was varied between 2 and 4 wt.%. Corresponding viscosities were computed using the model of Giordano et al. (2008). Figure 1.7 shows the results of our calculations for various degrees of melting and compares computed time scales with the duration of the remelting event suggested by our geochronological data (i.e. 57 ± 37 ka). The calculations predict that low degrees of melting (e.g. 3%; Fig. 1.7A) are insufficient, as it would require >100 ka for melt migration from the SH to the Brooks Horizon. However, at higher degrees of melting (e.g. 10%; Fig. 1.7B), migration velocities are sufficiently high, except for the "dry granophyre melt", for melt migration by >100 m upwards from the SH during the remelting event. At ~20% melting (Fig. 1.7C), computed time scales are shorter or within error of the duration of the remelting event, irrespective of melt composition. Even higher degrees of remelting would be plausible around the SH where interstitial granophyre makes up to 50% of the rock. These simple calculations thus suggest that redistribution of trace elements by upward percolation of the most trace element rich melt formed during remelting is a plausible mechanism for explaining the petrogenesis of the Brooks Horizon.

1.7.3 Evolution of the Skaergaard intrusion and timing of related flood basalt volcanism

The Skaergaard intrusion is intimately linked to the East Greenland flood basalt province that was erupted during initial opening of the North Atlantic. It was always accepted that Skaergaard intruded into a very shallow rift, as is dictated by low-$\delta^{18}O$ altering waters, and was independently confirmed by pressure estimates based on coexisting SiO2 polymorphs (tridymite and quartz) and ferrobustamite within Skaergaard that indicate pressures of 0.6 ± 0.1 kbar at ~950-980°C (Lindsley et al., 1969). These pressure estimates, however, are likely minimum values (Lindsley et al., 1969) and strongly depend on the identification of tridymite (see discussion in Larsen and Tegner, 2006). These constraints nevertheless indicate that Skaergaard was emplaced prior to the main phase of flood basalt volcanism that produced a >6 km thick sequence of volcanic overburden. Geochemical correlations of the Skaergaard intrusion and lavas of the flood basalt sequence yield additional constraints for the relative timing of intrusion emplacement and basalt eruption. Andreasen et al. (2004) and Nielsen (2004) suggested that the Skaergaard intrusion is correlative with the upper Geikie Plateau Formation or the lower Skraenterne Formation (see Fig. 1.1). More recently, Jakobsen et al. (2010b) showed that the composition of plagioclase-hosted melt inclusions in troctolitic blocks, corresponding to the unexposed most primitive Skaergaard cumulates, is equivalent to basalts of the Milne Land Formation (MLF, see Fig. 1.1) suggesting that they were emplaced contemporaneously, consistent with shallow emplacement of Skaergaard. Furthermore, Larsen and Tegner (2006) used quartz-hosted fluid inclusions in granophyres to show that the Skaergaard intrusion underwent con-

tinuous burial during late stages of crystallization due to thickening of the volcanic overburden. Granophyres in LZa formed at pressures equivalent to 2.4 ± 1.5 km of volcanic overburden above the roof of the intrusion, corresponding to the Lower Lavas and the Skaergaard-like MLF. Granophyres higher up in the Skaergaard intrusion (LZb, MZ and SH) formed at pressures corresponding to >6 km of volcanic overburden above the intrusion, suggesting that the bulk of the East Greenland flood basalt sequence was erupted during the late stages of crystallization of the Skaergaard intrusion. Our zircon crystallization ages record the timing of granophyre formation in LZb (SK-218) and the SH (SH-428) and allow us to scale the pressure increase reported by Larsen and Tegner (2006) to the temporal framework of intrusion crystallization (Fig. 1.8). Granophyres in LZb already record elevated pressures. Assuming accuracy of the relative pressure estimates (see Larsen and Tegner, 2006), this suggests that our zircon crystallization age for pegmatite SK-218 (55.960 ± 0.064 Ma, including systematic uncertainties) is a precise minimum age for the onset of flood basalt volcanism.

1.7.4 Skaergaard intrusion, related flood basalt volcanism and the Paleocene-Eocene Thermal Maximum

Flood basalt volcanism during opening of the North Atlantic has been suggested as a potential trigger mechanism for early Eocene environmental perturbations referred to as the Paleocene-Eocene Thermal Maximum (PETM). The PETM corresponds to a significant negative carbon isotope excursion (3.5-4.5‰) recorded in marine and terrestrial sediments that is associated with pronounced global warming and mass extinction among benthic organisms (e.g. Sluijs et al., 2007). Despite considerable effort to correlate magmatic activity in the Northeast Atlantic and the PETM (Storey et al., 2007; Svensen et al., 2010), uncertainties on the order of ± 300 ka for lava flows, intrusions and sills are insufficient to confidently test synchronicity. In contrast, the onset of the PETM appears to be precisely constrained by cyclostratigraphy, although numerous tuning options have been proposed (Fig. 1.8). Recently, Charles et al. (2011) presented two options for the onset of the PETM based on orbital tuning relative to a $^{206}Pb/^{238}U$ zircon age of an ash bed within the PETM CIE. The youngest five zircons analyzed by Charles et al. (2011) yield a weighted mean $^{206}Pb/^{238}U$ date of 55.785 ± 0.034 Ma. This ash bed post-dates the onset of the PETM CIE by 40-80 ka, depending on the cyclostratigraphic interpretation. Consequently, Charles et al. (2011) derive ages of 55.829 ± 0.101 Ma or 55.866 ± 0.098 Ma (including systematic uncertainties) for the onset of the PETM. These estimates for the timing of the onset of the PETM overlap within uncertainty with our minimum estimate for the timing of flood basalt volcanism (55.960 ± 0.064 Ma, including systematic uncertainties; Fig. 1.8). We conclude that flood basalt volcanism associated with opening of the North Atlantic and the onset of the PETM are correlative at the <100 ka level, strengthening models suggesting a causal link.

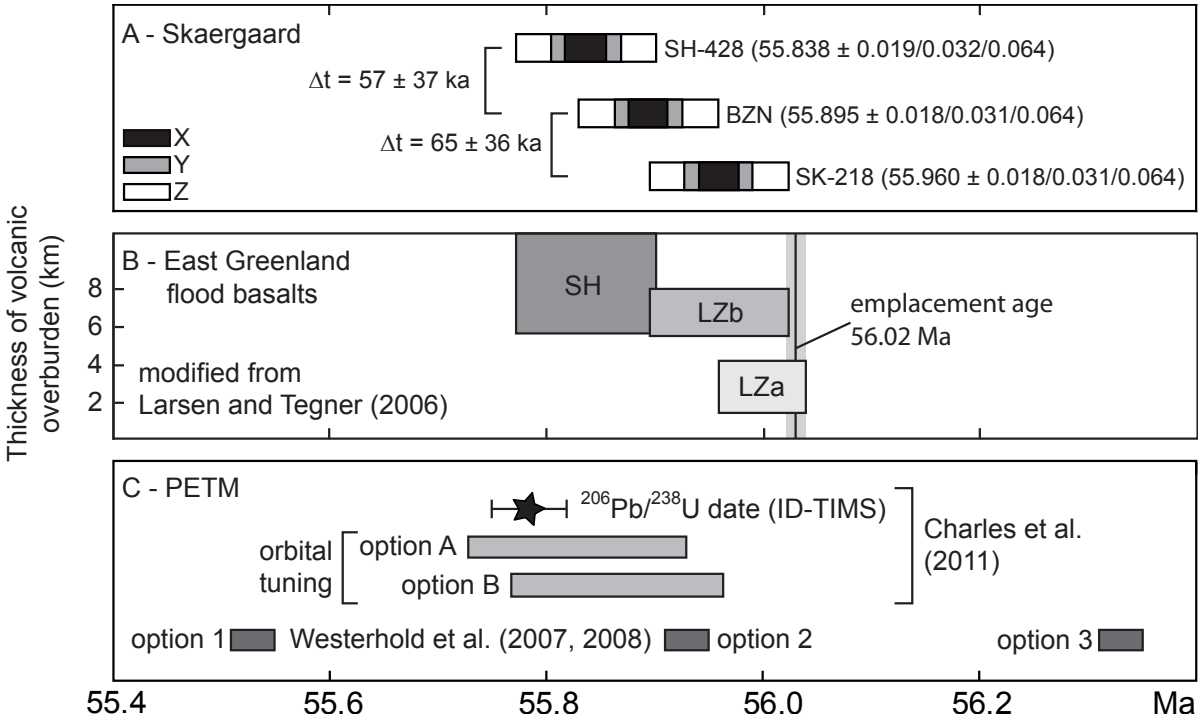

FIGURE 1.8 Summary of Skaergaard geochronology and relation to the East Greenland flood basalts and the Paleocene-Eocene Thermal Maximum (PETM). (A) Weighted mean $^{206}Pb/^{238}U$ dates of analyzed samples from the Skaergaard intrusive complex. Dates are shown at different levels of uncertainty propagation: X – internal (analytical) uncertainty; Y – includes X and tracer calibration uncertainty; Z – includes X, Y and decay constant uncertainty. (B) thickness of volcanic overburden covering the Skaergaard intrusion from Larsen and Tegner (2006) schematically scaled to our Skaergaard zircon crystallization ages and (C) compilation of age estimates for the onset of the Paleocene-Eocene Thermal Maximum (Westerhold et al., 2007; 2008; Charles et al., 2010).

1.8 SUMMARY & CONCLUSIONS

[1] Based on our geochronology and a published cooling model we estimate the emplacement age of the Skaergaard intrusion to be ~56.02 Ma. Interstitial melt within the lower part of the intrusion reached zircon saturation by 55.960 ± 0.018 Ma and the final portions around the Sandwich Horizon crystallized at ~55.91-55.93 Ma (age of oldest peak in SH, see Fig. 1.4) suggesting that crystallization of ~300 km3 of tholeiitic magma took some 100 ka.

[2] Intrusion of the Basistoppen Sill at 55.895 ± 0.018 Ma caused remelting of neighboring Skaergaard differentiates. The lag-time between intrusion of the Basistoppen Sill and subsequent crystallization of neighboring Skaergaard differentiates at 55.838 ± 0.019 suggests a duration of 57 ± 37 ka for the remelting event.

[3] The Skaergaard intrusion initially crystallized from a normal-$\delta^{18}O$ MORB-like magma. Oxygen isotope geochemistry of refractory accessory minerals, particularly zircon, reveal that late-stage differentiates of the Skaergaard intrusion

crystallized from a low-$\delta^{18}O$ melt that was heterogeneously depleted by 1-4‰ with respect to ^{18}O relative to the mantle derived precursor. Our high-precision zircon U-Pb geochronology suggest that shortly after initial solidification and subsequent meteoric-hydrothermal alteration, the newly intruded and hot Basistoppen Sill triggered partial remelting of the hydrothermally altered Skaergaard differentiates leading to the formation of low-$\delta^{18}O$ melts.

[4] This proposed remelting event may have also caused intergranular melt flow and redistribution of trace elements. Our simple calculations permit derivation of the Brooks Horizon, the most incompatible element-rich horizon in Skaergaard, by upward percolation of incompatible element-rich melt through the partially molten matrix during the remelting event.

[5] Our high-precision temporal framework for late-stage crystallization of the Skaergaard intrusion also provide time constraints for the eruption of intimately linked flood basalts, suggesting that flood basalt volcanism associated with opening of the North Atlantic is correlative with the Paleocene-Eocene Thermal Maximum at the <100 ka level.

APPENDIX

APPENDIX A: *Hf isotopic data of U-Pb dated zircons (see Table A1.1)*

APPENDIX B: *Calculation of melt extraction between SH and "Brooks" Horizon*

The theory of compaction of partially molten rocks is discussed in detail elsewhere (e.g. McKenzie, 1984). We used algorithms of McKenzie (1984) to calculate time scales of melt extraction from the partially molten porous matrix between the SH and the "Brooks" Horizon during the proposed remelting event. All input parameters are given in Tab. A1.2 and calculations are described below. The permeability of the partially molten matrix has been calculated employing the Blake-Kozeny-Carman equation (e.g. McKenzie, 1984),

$$k_\phi = \frac{\phi^3 r^2}{K(1-\phi^2)} \qquad \text{(Eq. B.1)}$$

where k_ϕ is the porosity dependent permeability, ϕ is the porosity (i.e. the degree of melting in our case), r is the the grain size (radius) and K is a constant. The relative velocity, ω_0, between crystal matrix and partial melt is defined as

$$\omega_0 = \frac{k_\phi}{\mu}\frac{(1-\phi)}{\phi}(\rho_s - \rho_l)g \qquad \text{(Eq. B.2)}$$

where μ is the viscosity of the melt, ρ_s and ρ_l are the densities of the crystalline matrix and the interstitial melt, respectively, and g is the acceleration due to gravity. ω_0 is a useful measure of the compaction rate as it can directly be compared with the duration of the remelting event derived from our geochronological data. The time required to reduce the amount of interstitial melt in the partially molten layer by a factor of e, t_h, is defined as

$$t_h = \frac{h}{\omega_0(1-\phi)} \qquad \text{(Eq. B.3)}$$

where h is the thickness of the partially molten layer, in our case the distance be-

Table A1.1 *MC-ICPMS Lu-Hf isotope data of selected U-Pb dated zircons*

	$^{176}Yb/^{177}Hf$ (a)	±2σ	$^{176}Lu/^{177}Hf$ (a)	±2σ	$^{178}Hf/^{177}Hf$	$^{180}Hf/^{177}Hf$	SigHf [V] (b)	$^{176}Hf/^{177}Hf$	±2σ (c)	$^{176}Hf/^{177}Hf_t$ (d)	εHf_t (d)	±2σ (c)
Basistoppen Sill (BZN)												
z3	0.0802	64	0.00190	11	1.46718	1.88673	27	0.282761	7	0.282759	0.34	0.24
z5	0.1032	83	0.00246	15	1.46718	1.88671	17	0.282783	8	0.282781	1.10	0.29
z7	0.0722	58	0.00165	10	1.46719	1.88670	19	0.282774	7	0.282772	0.78	0.26
z8	0.0778	62	0.00154	9	1.46718	1.88669	28	0.282792	6	0.282791	1.45	0.22
Sandwich Horizon (SH-428)												
z1	0.1259	101	0.00281	17	1.46717	1.88660	27	0.282986	8	0.282983	8.24	0.28
z2	0.0862	69	0.00201	12	1.46717	1.88654	68	0.282969	6	0.282967	7.66	0.21
z4	0.0681	54	0.00180	11	1.46717	1.88665	36	0.282956	7	0.282954	7.24	0.24
z5	0.0616	49	0.00140	8	1.46718	1.88661	41	0.282944	7	0.282942	6.80	0.23
z6	0.0367	29	0.00096	6	1.46718	1.88660	61	0.282963	6	0.282962	7.50	0.21
z15	0.1521	122	0.00297	18	1.46718	1.88659	22	0.282961	8	0.282958	7.37	0.29
z16	0.0777	62	0.00160	10	1.46719	1.88657	11	0.282956	8	0.282954	7.22	0.30
Pegmatite in LZb (SK-218)												
z1	0.0936	75	0.00290	17	1.46719	1.88673	46	0.282966	6	0.282963	7.52	0.23
z3	0.0881	70	0.00294	18	1.46719	1.88672	53	0.282965	6	0.282962	7.50	0.20
z5	0.0916	73	0.00311	19	1.46719	1.88670	33	0.282977	6	0.282974	7.92	0.23
z6	0.0534	43	0.00143	9	1.46720	1.88677	42	0.282969	6	0.282969	7.76	0.23
JMC475 (n=21)	-	-	-	-	1.46718	1.88666	10	0.282148	5	0.282148	-22.52	0.18

Quoted uncertainties (absolute) relate to the last quoted figure. Accuracy and reproducibilty was checked by repeated analyses (n = 21) of 10 ppb solutions of JMC475.

(a) $^{176}Yb/^{177}Hf = (^{176}Yb/^{173}Yb)$true x $(^{173}Yb/^{177}Hf)$meas x (M173(Yb)/M177(Hf))b(Hf), b(Hf) = $\ln(^{179}Hf/^{177}Hf)$true / $(^{179}Hf/^{177}Hf)_{meas}$ / ln (M179(Hf)/M177(Hf)), M=mass of respective isotope. The $^{176}Lu/^{177}Hf$ were calculated in a similar way by using the $^{175}Lu/^{177}Hf$ and b(Yb).

(b) Mean Hf signal in volt.

(c) Uncertainties are quadratic additions of the within-run precision and the daily reproducibility of the 10ppb-JMC475 solution. Uncertainties for the JMC475 quoted at 2SD (2 standard deviation).

(d) Initial $^{176}Hf/^{177}Hf$ and eHf calculated using the apparent U-Pb age determined by ID-TIMS (see Tab. 2), and the CHUR parameters: $^{176}Lu/^{177}Hf = 0.0336$, and $^{176}Hf/^{177}Hf = 0.282785$ (Bouvier et al., 2008).

Table A1.2 *Units, constants and variables used in calculations*

Symbol	Description	Value/unit
k_ϕ	Permeability	m^2
ϕ	Porosity	0.03-0.2
r	Grain size (radius)	$2x10^{-3}$ m
K	Constant in permeability relationship	200
ω_0	Relative velocity between matrix and melt	m/s
μ	Viscosity of melt	Pa s (1)
ρ_s	Density of crystal matrix	2900 kg/m^3
ρ_l	Density of melt	kg/m^3 (2)
g	Accelaeration due to gravity	9.81 m/s^2
t_h	Time scale of melt extraction	s
h	Thickness of partially molten layer	m

(1) Viscosity of melt calculated using the composition of Skaergaard granophyres and bulk ferrodiorites, respectively, employing the model of Giordano et al. (2008) and varying H2O content between 2 and 4 wt.%. These calculations yielded values of 773 and 1828 Pa s for the "ferrodiorite melt" and 14365 and 149774 Pa s for the "granophyre melt".

(2) Density of "granophyre melt" is 2300 kg m-3 and density of "ferrodiorite melt" is 2700 kg m-3

tween the SH and the "Brooks" Horizon (~100 m). This equation allows the calculation of time as a function of height above SH (h), which is displayed in Fig. 1.7.

APPENDIX C: *Cathodoluminescence images of zircons analyzed by ion microprobe (see Fig. A1.1)*

APPENDIX D: *Baddeleyite oxygen isotope analyses by Laser Fluorination Isotope Ratio Mass Spectrometry*

As baddeleyite is an uncalibrated phase for ion microprobe oxygen isotopic determination (and no good homogeneous standards are available to our knowledge), we choose to analyze the small extracted quantities by laser fluorination.

The amount of 0.12 mg of irregular baddeleyite grains was extracted under the microscope and mixed with our standard UOG garnet. The purpose of mixing was two-fold: 1) to prevent jumping (unpowdered baddeleyites and zircons jump early during the laser heating) and 2) adding garnet aimed at creating "flux" to maximize the oxygen yield (baddeleyite and zircons often do not yield 100% due to high melting temperature). Note that laser fluorination is good for ~0.4-0.5 mg of material.

The mixed analysis (baddeleyite+garnet) was $\delta^{18}O$=6.66‰, and pure garnet run after was 7.07‰. By mass balance, and assuming different oxygen yields from each phase (8.2 μmol/mg baddeleyite vs. 14.2 μmol/mg garnet), the computed $\delta^{18}O$ of baddeleyite is 2.04‰. Given typical laser fluorination error of 0.1‰ on garnet determination, the propagated error of such determination for baddeleyite is ±1.12‰.

REFERENCES CITED

Andreasen, R., Peate, D.W., and Brooks, C.K., 2004. Magma plumbing systems in large igneous provinces: Inferences from cyclical variations in Palaeogene East Greenland basalts. Contrib. Mineral. Petrol., v. 147, p. 438–452.

Bachmann, O., and Bergantz, G.W., 2004. On the origin of crystal-poor rhyolites: Extracted from batholithic crystal mushes. J. Petrol., v. 45, p. 1565–1582.

Bindeman, I.N., Brooks, C.K., McBirney, A.R., and Taylor, H.P., 2008. The low-$\delta^{18}O$ late-stage ferrodiorite magmas in the Skaergaard Intrusion: Result of liquid immiscibility, thermal metamorphism, or meteoric water incorporation into magma? J. Geol. v. 116, p. 571–586.

Bindeman, I.N., Schmitt, A.K., and Evans, D.A.D., 2010. Limits of hydrosphere-lithosphere interaction: origin of the lowest $\delta^{18}O$ rocks on Earth in the Paleoproterozoic Karelian rift. Geology, v. 38, p. 631–634.

Boudreau, A.E., and McBirney, A.R., 1997. The Skaergaard Layered Series. Part III. Non-dynamic layering. J. Petrol., v. 38, p. 1003–1020.

Bouvier, A., Vervoort, J.D., and Patchett, P.J., 2008. The Lu-Hf and Sm-Nd isotopic composition of CHUR: Constraints from unequilibrated chondrites and implications for the bulk composition of terrestrial planets. Earth Planet. Sci. Lett, v. 273, p. 48–57.

Bowring, J.F., McLean, N.M., and Bowring, S.A., 2011. Engineering cyber infrastructure for U-Pb geochronology: Tripoli and U-Pb_Redux. Geochem. Geophys. Geosyst., v. 12 (6), doi:

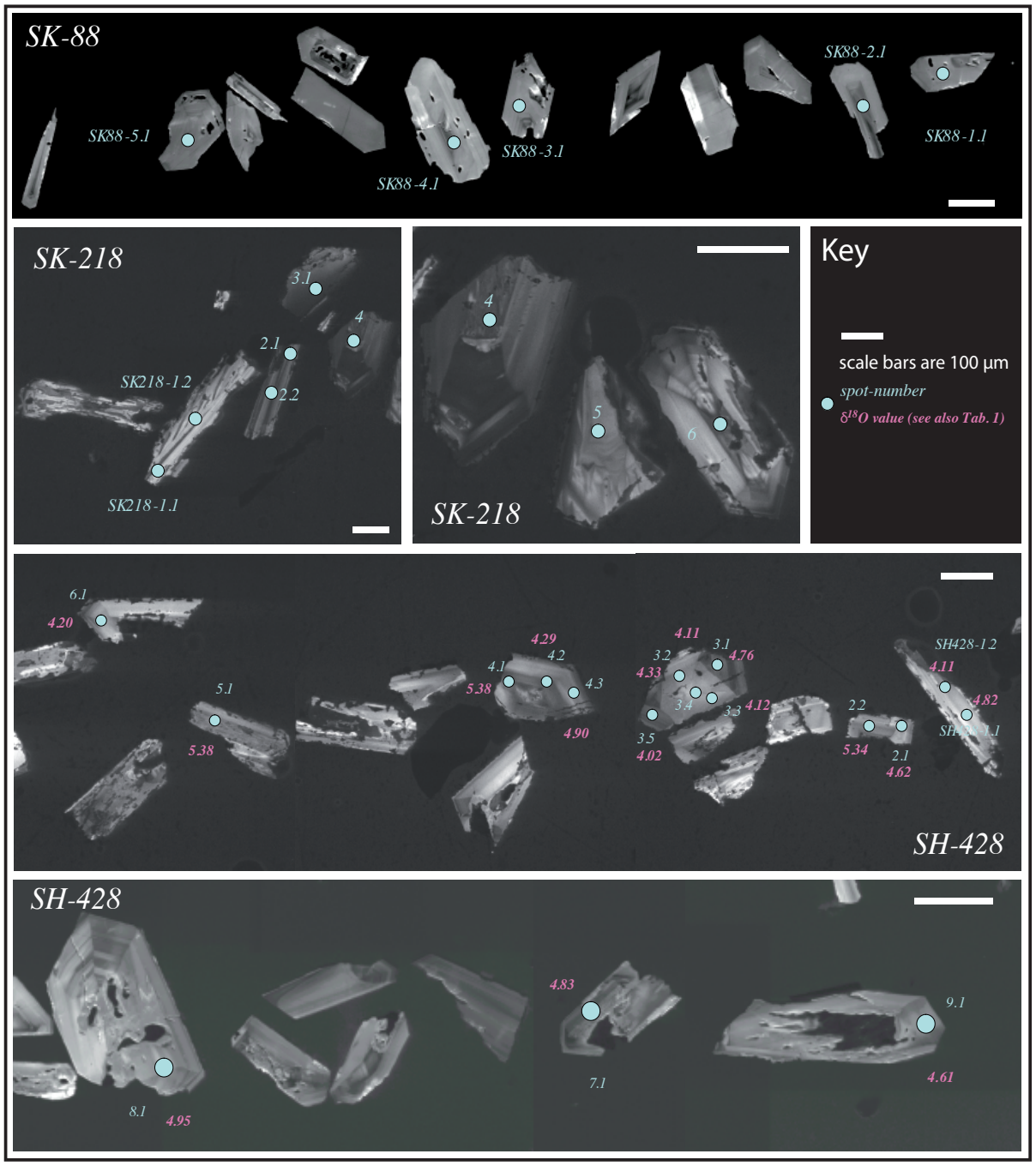

FIGURE A1.1 Cathodoluminescence images of zircons analyzed by ion microprobe for their oxygen isotopic composition. Locations of ion microprobe spot analyses are indicated by the blue dot. Blue numbers indicate the spot number for all samples; red numbers indicate $\delta^{18}O$ value (SH-428 only). Most crystals do not show clear core-rim relationships with respect to CL intensity and oxygen isotopic composition. Some SH-428 zircons tend to have lower-$\delta^{18}O$ rims relative to cores. See main text for further details.

10.1029/2010GC003479.
Brooks, C.K., 1969. On the distribution of zirconium and hafnium in the Skaergaard intrusion, East Greenland. Geochim. Cosmochim. Acta, v. 33, p. 357–374.
Brooks, C.K., and Gleadow, A.J.W., 1977. A fission-track age for the Skaergaard intrusion and the age of the East Greenland basalts. Geology, v. 5, p. 539–540.
Brooks, C.K., Larsen, L.M., and Nielsen, T.F.D., 1991. Importance of iron-rich tholeiitic magmas at divergent plate margins: a reappraisal. Geology, v. 19, p. 269–272.
Brown, G.M., and Vincent, E.A., 1963. Pyroxenes from the late stages of fractionation of the Skaergaard intrusion, East Greenland. J. Petrol., v. 4, p. 175–197.
Charles, A.J., Condon, D.C., Harding, I.C., Pälike, H., Marshall, J.E.A., Cui, Y., Kump, L., and Croudance, I.W., 2011. Constraints on the numerical age of the Paleocene-Eocene boundary. Geochem. Geophys. Geosyst., v. 12 (6), doi: 10.1029/2010GC003426.
Gerdes, A., and Zeh, A., 2006. Combined U-Pb and Hf isotope LA-(MC-) ICP-MS analyses of detrital zircons: Comparison with SHRIMP and new constraints for the provenance and age of an Armorican metasediment in Central Germany. Earth Planet. Sci. Lett., v. 249, p. 47–62.
Gerstenberger, H., and Haase, G., 1997. A highly effective emitter substance for mass spectrometric Pb isotope ratio determinations. Chem. Geol., v. 136, p. 309–312.
Giordano, D., Russell, J.K., and Dingwell, D.B., 2008. Viscosity of magmatic liquids: a model. Earth Planet. Sci. Lett., v. 271, p. 123–134.
Hamilton, M.A., and Brooks, C.K., 2004. A precise U-Pb zircon age for the Skaergaard intrusion. Geochim. Cosmochim. Acta, v. 68, p. A587.
Hirschmann, M., Renne, P.R., and McBirney, A.R., 1997. $^{40}Ar/^{39}Ar$ dating of the Skaergaard intrusion. Earth Planet. Sci. Lett., v. 146, p. 645–658.
Holness, M.B., Stripp, G., Humphreys, M.C.S., Veksler, I.V., Nielsen, T.F.D., and Tegner, C., 2011. Silicate liquid immiscibility within the crystal mush: Late-stage magmatic microstructures in the Skaergaard intrusion, East Greenland. J. Petrol., v. 52, p. 175–222.
Humphreys, M.C.S., 2011. Silicate liquid immiscibility within the crystal mush: Evidence from Ti in plagioclase from the Skaergaard intrusion. J. Petrol., v. 52, p. 147–174.
Irvine, T.N., 1980. Magmatic infiltration metasomatism, double diffusive fractional crystallization, and adcumulus growth in the Muskox intrusion and other layered intrusions, in: Hargreaves, R.B. (ed.), Physics of Magmatic Processes. Princeton University Press, Princeton. N.J., p. 325–383.
Irvine, T.N., Andersen, J.C.O., and Brooks, C.K., 1998. Included blocks (and blocks within blocks) in the Skaergaard intrusion: geologic relations and the origins of rhythmic modally graded layers. Geol. Soc. Am. Bull., v. 110, p. 1398–1447.
Jaffey, A.H., Flynn, K.F., Glendenin, L.E., Bentley, W.C., and Essling, A.M., 1971. Precision measurement of half-lives and specific activities of ^{235}U and ^{238}U. Phys. Rev., v. C4 (5), p. 1889–1906.
Jakobsen, J.K., Veksler, I.V., Tegner, C., and Brooks, C.K., 2005. Immiscible iron- and silica-rich melts in basalt petrogenesis documented in the Skaergaard intrusion. Geology, v. 33, p. 885–888.
Jakobsen, J.K., Veksler, I.V., Tegner, C., and Brooks, C.K., 2010a. Crystallization of the Skaergaard intrusion from an emulsion of immiscible iron- and silica-rich liquids: evidence from melt inclusions in plagioclase. J. Petrol., v. 52, p. 345–375.
Jakobsen, J.K., Tegner, C., Brooks, C.K.,

Kent, A.J.R., Lesher, C.E., Nielsen, T.F.D., and Wiedenbeck, M., 2010b. Parental magma of the Skaergaard intrusion: constraints from melt inclusions in primitive troctolite blocks and FG-1 dykes. Contrib. Mineral. Petrol., v. 159, p. 61–79.

Krogh, T.E., 1973. A low contamination method for hydrothermal decomposition of zircon and extraction of U and Pb for isotopic age determination. Geochim. Cosmochim. Acta, v. 37, p. 485–494.

Kuiper, K.F., Deino, A., Hilgen, F.J., Krijgsman, W., Renne, P.R., and Wijbrans, J.R., 2008. Synchronizing rock clocks of Earth history. Science, v. 320, p. 500–504.

Larsen, R.B., and Brooks, C.K., 1994. Origin and evolution of gabbroic pegmatites in the Skaergaard intrusion, East Greenland. J. Petrol., v. 35, p. 1651–1679.

Larsen, R.B., and Tegner, C., 2006. Pressure conditions for the solidification of the Skaergaard intrusion: eruption of East Greenland flood basalts in less than 300,000 years. Lithos, v. 92, p. 181–197.

Leeman, W.P., and Dasch, E.J., 1978. Strontium, lead, and oxygen isotope investigation of the Skaergaard intrusion, East Greenland, Earth Planet. Sci. Lett., v. 41, p. 47–59.

Lindsley, D.H., Brown, G.M., and Muir, I.D., 1969. Conditions of the ferrowollastonite-ferrohedenbergite inversion in the Skaergaard intrusion, East Greenland. Mineral. Soc. Am. Spec. Publ., v. 2, p. 193–201.

Mattinson, J.M., 2005. Zircon U-Pb chemical abrasion ("CA-TIMS") method: combined annealing and multi-step partial dissolution analysis for improved precision and accuracy of zircon ages. Chem. Geol., v. 200, p. 47–66.

McBirney, A.R., 1989. The Skaergaard Layered Series: I. Structure and average composition. J. Petrol., v. 30, p. 363–397.

McBirney, A.R., 1995. Mechanisms of differentiation in the Skaergaard intrusion. J. Geol. Soc. Lond., v. 152, p. 421–435.

McBirney, A.R., 2002. The Skaergaard Layered Series, Part VI: Excluded trace elements. J. Petrol., v. 43, p. 535–556.

McBirney, A.R., 2006. Igneous petrology (3rd ed.). Sudbury, MA, Jones and Bartlett, 550 p.

McBirney, A.R., and Creaser, R.A., 2003. The Skaergaard Layered Series, Part VII: Sr and Nd isotopes. J. Petrol., v. 44, p. 757–771.

McBirney, A.R., and Noyes, R.M., 1979. Crystallization and layering of the Skaergaard intrusion. J. Petrol., v. 20, p. 487–554

McKenzie, D., 1984. The generation and compaction of partially molten rock. J. Petrol., v. 25, p. 713–765.

McKenzie, D., 2011. Compaction and crystallization in magma chambers: Towards a model of the Skaergaard intrusion. J. Petrol., v. 52, p. 905–930.

McLean, N.M., Bowring, J.F., and Bowring, S.A., 2011. An algorithm for U-Pb isotope dilution data reduction and uncertainty propagation.Geochem.Geophys.Geosyst., v. 12 (6), doi: 10.1029/2010GC003478.

Min, K., Mundil, R., Renne, P.R., and Ludwig, K.R., 2000. A test for systematic errors in $^{40}Ar/^{39}Ar$ geochronology through comparison with U-Pb analysis of a 1.1-Ga rhyolite. Geochim. Cosmochim. Acta, v. 64, p. 73–98.

Mora, C.I., Riciputi, L.R., and Cole, D.R., 1999. Short-lived oxygen diffusion during hot, deep-seated meteoric alteration of anorthosite. Science, v. 286, p. 2323–2325.

Naslund, H.R., 1989. Petrology of the Basistoppen Sill, East Greenland: A calculated magma differentiation trend. J. Petrol., v. 30, p. 299–320.

Nielsen, T.F.D., 2004. The shape and volume of the Skaergaard intrusion, Greenland: Implications for mass balance and bulk composition. J. Petrol., v. 45, p. 507–530.

Norton, D., and Taylor, H.P., Jr., 1979. Quantitative simulation of the hydrothermal systems of crystallizing magmas on the basis of transport theory and oxygen isotope data; an analysis of the Skaergaard intrusion. J. Petrol., v. 20, p. 421–486.

Norton, D., Taylor, H.P., Jr., and Bird, D.K., 1984. The geometry and high-temperature brittle deformation of the Skaergaard intrusion. J. Geophys. Res., v. 89B, p. 10178–10192.

Schaltegger, U., Brack, P., Ovtcharova, M., Peytcheva, I., Schoene, B., Stracke, A., Marocchi, M., and Bargossi, G.M., 2009. Zircon and titanite recording 1.5 million years of magma accretion, crystallization and initial cooling in a composite pluton (southern Adamello batholith, northern Italy). Earth Planet. Sci. Lett., v. 286, p. 208–218.

Schoene, B., Crowley, J.L., Condon, D.C., Schmitz, M.D., and Bowring, S.A., 2006. Reassessing the uranium decay constants for geochronology using ID-TIMS U-Pb data. Geochim. Cosmochim. Acta, v. 70, p. 426–445.

Schoene, B., Guex, J., Bartolini, A., Schaltegger, U., and Blackburn, T.J., 2010. Correlating the end-Triassic mass extinction and flood basalt volcanism at the 100 ka level. Geology, v. 38, p. 387–390.

Sláma, J., Košler, J., Condon, D.J., Crowley, J.L., Gerdes, A., Hanchar, J.M., Horstwood, M.S.A., Morris, G.A., Nasdala, L., Norberg, N., Schaltegger, U., Schoene, B., Tubrett, M.N., and Whitehouse, M.J., 2008. Plešovice zircon – a new natural reference material for U–Pb and Hf isotopic microanalysis. Chem. Geol., v. 249, p. 1–35.

Sluijs, A., Bowen, G.J., Brinkhuis, H., Lourens, L.J., and Thomas, 2007. The Palaeocene-Eocene Thermal Maximum super greenhouse: Biotic and geochemical signatures, age models and mechanisms of global change, in: M. Williams et al. (eds), Deep-Time Perspectives on Climate Change: Marrying the Signal from Computer Models and Biological Proxies. Micropalaeo. Soc. Spec. Publ., p. 323–349.

Storey, M., Duncan, R.A., and Swisher, C.C., 2007. Paleocene-Eocene Thermal Maximum and the opening of the northeast Atlantic. Science, v. 316, p. 587–589.

Svensen, H., Planke, S., and Corfu, F., 2010. Zircon dating ties NE Atlantic sill emplacement to initial Eocene global warming, J. Geol. Soc., v. 167, p. 433–436.

Taylor, H.P., Jr., 1968. The oxygen isotope geochemistry of igneous rocks. Contrib. Mineral. Petrol., v. 19, p. 1–71.

Taylor, H.P., Jr., and Epstein, S., 1963. $^{18}O/^{16}O$ ratios in rocks and coexisting minerals of the Skaergaard intrusion. J. Petrol., v. 4, p. 51–74.

Taylor, H.P., Jr., and Forester, R.W., 1979. An oxygen and hydrogen isotopic study of the Skaergaard intrusion and its country rocks: a description of a 55-Ma fossil hydrothermal system. J. Petrol., v. 20, p. 355–419.

Tegner, C., Thy, P., Holness, M.B., Jakobsen, J.K., and Lesher, C.E., 2009. Differentiation and compaction in the Skaergaard intrusion. J. Petrol., v. 50, p. 813–840.

Valley, J.W., 2003. Oxygen isotopes in zircon. Rev. Mineral. Geochem., v. 53, p. 343–385.

Valley, J.W., Bindeman, I.N., and Peck, W.H., 2003. Empirical calibration of oxygen isotope fractionation in zircon. Geochim. Cosmochim. Acta, v. 67, p. 3257–3266.

Veksler, I.V., Dorfman, A.M., Borisov, A.A., Wirth, R., and Dingwell, D.B., 2007. Liquid immiscibility and the evolution of basaltic magmas. J. Petrol., v. 48, p. 2187–2210.

von Quadt, A., Erni, M., Martinek, K., Moll, M., Peytcheva, I., and Heinrich, C.A., 2011. Zircon crystallization and

the lifetimes of ore-forming magmatic-hydrothermal systems. Geology, v. 39, p. 731–734.

Wager, L.R., and Brown, G.M., 1968. Layered igneous rocks. W.H. Freeman, San Francisco, 588 p.

Wager, L.R., and Deer, W.A., 1939. Geological investigations in East Greenland. III. The petrology of the Skaergaard intrusion, Kangerdlugssuaq, East Greenland. Medd. Gronl., v. 105, p. 352.

Watson, E.B., and Harrison, T.M., 1983. Zircon saturation revisited: temperature and composition effects in a variety of crustal magma types. Earth Planet. Sci. Lett., v. 64, p. 295–304.

Watson, E.B., Wark, D.A., and Thomas, J.B., 2006. Crystallization thermometers for zircon and rutile. Contrib. Mineral. Petrol., v. 151, p. 413–433.

Westerhold, T., Röhl, U., Laskar, J., Raffi, I., Bowles, J., Lourens, L.J., and Zachos, J.C., 2007. On the duration of magnetochrons C24r and C25n and the timing of early Eocene global warming events: Implications from the Ocean Drilling Program Leg 208 Walvis Ridge depth transect. Paleoceanography, v. 22, doi: 10.1029/2006PA001322.

Westerhold, T., Röhl, U., Raffi, I., Fornaciari, E., Monechi, S., Reale, V., Bowles, J., and Evans, H.F., 2008. Astronomical calibration of Paleocene time, Palaeogeogr. Palaeoclimatol. Palaeoecol., v. 257, p. 377–403.

White, C.M., Geist, D.J., Frost, C.D., and Verwoerd, W.J., 1989. Petrology of the Vandfalsdalen Macrodike, Skaergaard Region, East Greenland. J. Petrol., v. 30, p. 271–298.

***

Chapter 2

Tracking the evolution of large-volume silicic magma reservoirs from assembly to supereruption†

J.F. Wotzlaw, U. Schaltegger, D.A. Frick, M.A. Dungan, A. Gerdes, D. Günther

Keywords:
Fish Canyon Tuff
zircon
geochronology
trace elements
supereruption
magma evolution

ABSTRACT

The most voluminous silicic volcanic eruptions in the geological past were associated with caldera collapses above giant silicic magma reservoirs. The thermal evolution of these subcaldera magma reservoirs controls the volume of eruptible magma and eruptive style. Here we combine high-precision zircon U-Pb geochronology, trace element analyses of the same mineral grains, and mass balance modeling of zircon trace element compositions allowing us to track the thermal and chemical evolution of the Oligocene Fish Canyon Tuff magma reservoir (Colorado, USA), as a function of absolute time. Systematic compositional variations in U-Pb dated zircons record ~440 k.y. of magma evolution. An early phase of volumetric growth was followed by a period of cooling and crystallization, during which the Fish Canyon magma approached complete solidification. Subsequent remelting, due to underplated andesitic recharge magmas, began 219 ± 45 ka prior to eruption and led to the generation of ~5000 km^3 of eruptible crystal-rich (~45 vol.%) dacite. Age-equivalent, but compositionally different, zircons in an andesite enclave from late-erupted Fish Canyon Tuff tie the growth and thermal evolution of the upper crustal reservoir to a lower crustal magma processing zone. Our results demonstrate that the combination of high-precision dating

†*this chapter is equivalent to the paper "Tracking the evolution of large-volume silicic magma reservoirs from assembly to supereruption" published in Geology (v. 41, p. 867-870) and co-authored by J.F. Wotzlaw, U. Schaltegger, D.A. Frick, M.A. Dungan, A. Gerdes and D. Günther. Reproduced with permission of the Geological Society of America.*

and trace element analyses of accessory zircons can reveal invaluable information about the chemical and thermal histories of silicic magmatic systems and provides critical input parameters for fluid dynamic modeling.

2.1 INTRODUCTION

The volume, composition, crystallinity and duration of assembly of a large magma body, as well as the character and spatial organization of its heterogeneities prior to eruption, are inter-related consequences of the balance between the rate of magma influx and the rate of cooling. The products of caldera-related silicic supereruptions (5×10^2 - 5×10^3 km^3) are particularly useful for placing constraints on these processes because large volumes of magma are rapidly quenched, thereby preserving information about the thermal and chemical states of the system at the moment of magma evacuation. Groundbreaking studies of the Bishop Tuff (Long Valley caldera; e.g., Halliday et al., 1989; Christensen and DePaolo, 1993), have established a framework for integrating petrologic, geochronologic, and isotopic data as a means for addressing time scales of magma system evolution. These studies triggered an ongoing discussion concerning the residence times of large silicic magma bodies in the upper crust that was accompanied by the emergence of new concepts and the development of new geochemical and geochronologic tools (Mahood, 1990; Reid and Coath, 2000; Vazquez and Reid, 2004; Reid, 2008).

We present a novel approach for tracking the chemical, thermal and rheological evolution of large silicic magma reservoirs as a function of time by integrating high-precision zircon U-Pb geochronology, trace element analyses of the same mineral grains, and mass balance modeling of systematic compositional variations in U-Pb dated zircons. Previous studies have used in-situ zircon U-Th and U-Pb geochronology in concert with trace elements (e.g., Claiborne et al., 2010; Klemetti et al., 2011), which provides high-spatial resolution but is limited to young magmatic systems, where in-situ techniques provide sufficient age resolution. To demonstrate the applicability of our approach to older volcanic deposits, we present a case study from the Oligocene Fish Canyon magmatic system. The Fish Canyon Tuff (5000 km^3; San Juan Volcanic Field, Colorado, USA) and related eruptive products of the La Garita caldera have served as a basis for addressing the origin and evolution of large-volume crystal-rich magmas (e.g., Bachmann et al., 2002; Bachmann and Bergantz, 2003). In the context of independent petrologic and geochronologic constraints, we discuss our results with respect to (1) the petrologic evolution of the Fish Canyon magmatic system and similar large-volume crystal-rich magmas, (2) their relationship to granodiorite plutons, (3) mechanisms that trigger rejuvenation and subsequent eruption of highly crystalline magmas, (4) the control of lower crustal magma processing zones

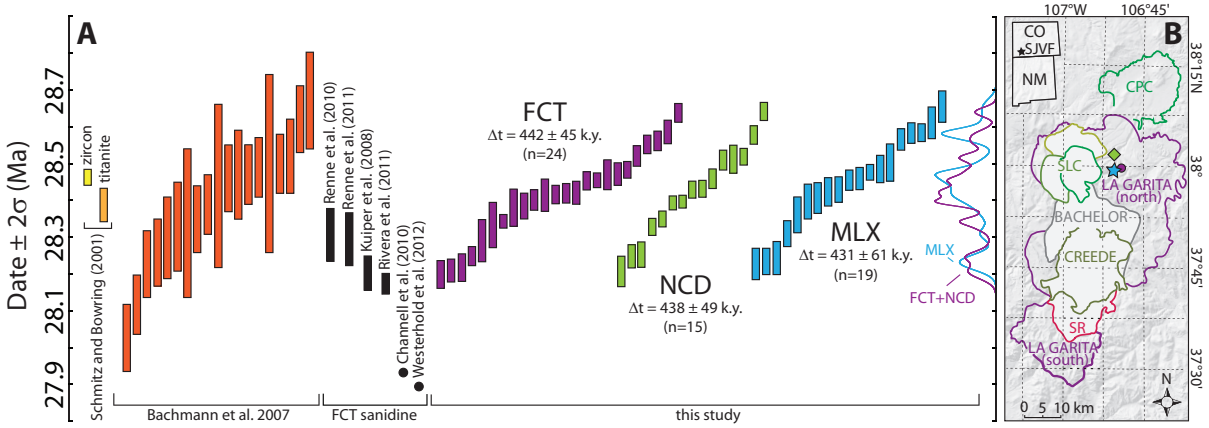

FIGURE 2.1 Geochronology of the Fish Canyon magmatic system. (A) Comparison of previously published zircon and titanite U-Pb and sanidine $^{40}Ar/^{39}Ar$ dates with zircon U-Pb dates obtained in this study. All U-Pb dates are $^{206}Pb/^{238}U$ dates corrected for initial ^{238}U-^{230}Th disequilibrium using Th/U_{melt} of 2.2 (Schmitz and Bowring, 2001). Δt denotes the age difference between the oldest and youngest zircon date of each sample. Probability density functions show the distribution of $^{206}Pb/^{238}U$ dates. (B) Caldera map of the Central San Juan caldera cluster showing locations of samples analyzed in this study; inset map (top left) shows location of the SJVF within the state of Colorado. Abbreviations: FCT – Fish Canyon Tuff, NCD – Nutras Creek Dacite, MLX – Andesite enclave, SJVF – San Juan Volcanic Field, CPC – Cochetopa Park Caldera, SLC – San Luis Complex, SR – South River Caldera.

on the thermal evolution of upper crustal silicic magma reservoirs, and (5) the age of the Fish Canyon Tuff eruption.

2.2 ZIRCON AS A RECORDER OF PRE-ERUPTION EVOLUTION OF THE FISH CANYON MAGMATIC SYSTEM

The presence of zircon in all eruptive products of the Fish Canyon magmatic system, including andesitic enclaves entrained in the waning stage of the eruption, makes it an ideal case for applying high-resolution geochronologic control on the thermal evolution of a magmatic system by using the trace element chemistry of U-Pb dated zircons as a proxy for magma crystallinity and melt composition. New analytical protocols allow us to obtain age, chemical and isotopic information from the exact same volume of single zircon crystals (Schoene et al., 2010; 2012; see Appendix for analytical details). We performed combined high-precision U-Pb geochronology and trace element analyses on 58 single zircons from three samples of the Fish Canyon magmatic system: (1) intracaldera Fish Canyon Tuff, (2) post-caldera Nutras Creek Dacite, and (3) an andesitic enclave. 29 of these zircons have also been analyzed for Hf isotopic compositions (see Tables A2.1, A2.2, A2.3).

Zircon $^{206}Pb/^{238}U$ dates document a growing and evolving magma chamber during 28.642 ± 0.025 – 28.196 ± 0.038 Ma (Fig. 2.1; ~440,000 yrs). Our high-n (n = 58) data set highlights a prominent mode at ~28.4 Ma that coincides with the weighted mean zircon and titanite $^{206}Pb/^{238}U$ dates of Schmitz and Bowring (2001). A second mode at ~28.2 Ma is

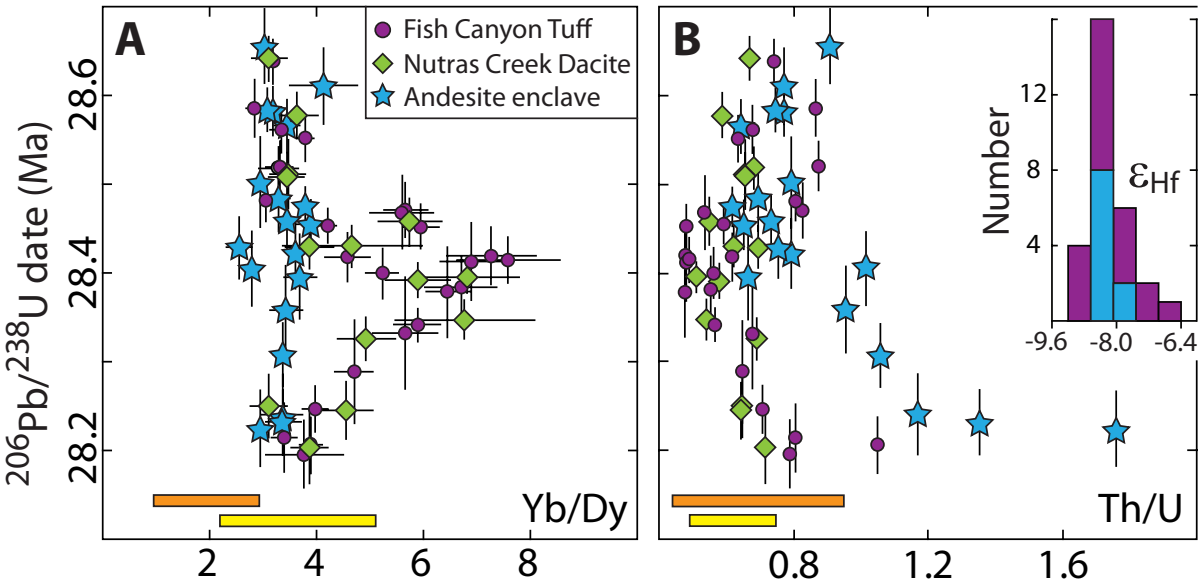

FIGURE 2.2 Trace element and Hf-isotopic compositions of U-Pb dated zircons. Yb/Dy (A) and Th/U (B) of U-Pb dated zircons are plotted against their $^{206}Pb/^{238}U$ date. Uncertainties are shown at the 2σ confidence level. Inset in (B) shows histogram of Hf isotopic compositions for Fish Canyon and andesite enclave zircons. Yellow and orange bars are the calculated compositional ranges of zircons in equilibrium with interstitial glass and whole rocks, respectively, on the basis of experimentally determined partition coefficients (Rubatto and Hermann, 2007) and published glass and whole-rock analyses (Bachmann et al., 2002; 2005).

FIGURE 2.3 Trace element budget of the Fish Canyon magmatic system. Chondrite-normalized trace element concentrations of major and accessory minerals are weighted by their modal abundances. Numbers in brackets denote the relative modal abundance of the respective mineral. The trace element concentrations in the bulk fractionating assemblage correspond to the weighted sum of the concentrations in the minerals. Trace element concentrations are from Bachmann et al. (2005) except for zircon (average composition of zircons analyzed in this study) and modal abundances are based on granodiorite xenoliths (Bachmann et al., 2002). Note the dominant role of titanite in controlling the trace element budget in the bulk fractionating assemblage.

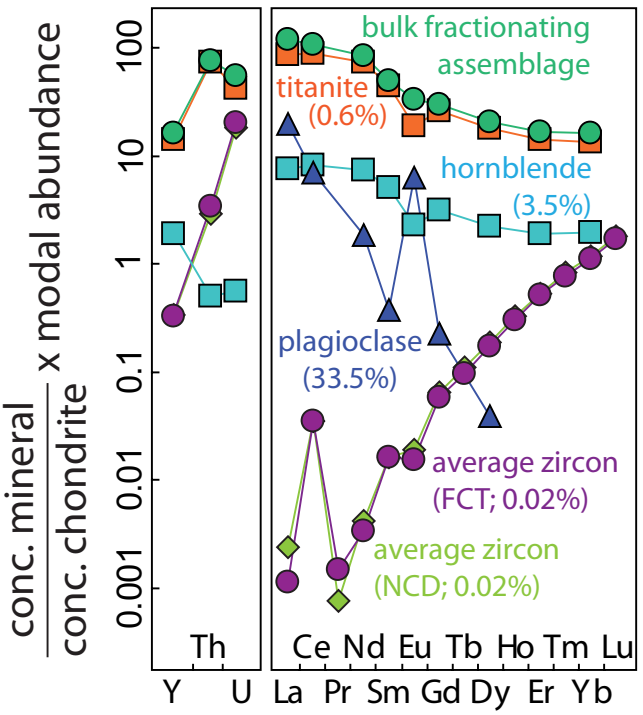

equivalent to recent sanidine $^{40}Ar/^{39}Ar$ dates (Kuiper et al., 2008; Rivera et al., 2011). These zircons display large and systematic variations in trace element chemistry as a function of time (Fig. 2.2) that are taken to indicate that: (1) zircons are reliable recorders of melt composition, (2) zircon grains crystallized over short times in comparison to the duration of the magmatic system, and (3) they persisted as closed systems.

The trace element budget of the Fish Canyon magma is largely controlled by volumetrically minor titanite (≤1 vol.%; Fig. 2.3). The extreme compatibilities of various trace elements (REE, Y, Th) in titanite render small absolute changes in its modal abundance during crystallization, or remelting, the critical factor in controlling their concentrations and ratios in coexisting melt (e.g., $D_{Dy} > D_{Yb}$; Fig. 2.3). These compositional changes in residual melts have been preserved in co-crystallizing zircons, allowing us to use trace element concentrations in zircon as proxies for melt compositions (Fig. 2.2). The parabolic Yb/Dy trend and sympathetic decrease/increase in Th/U in zircon through time is interpreted as: (1) a decrease in temperature and increasing crystallization from ~28.7–28.6 Ma to ~28.4 Ma, hence increasing titanite and zircon abundances, followed by (2) reheating and remelting from ~28.4 Ma to eruption.

2.3 FROM ZIRCON TRACE ELEMENT GEOCHEMISTRY TO MAGMA CRYSTALLINITY

Mass-balance modeling of the observed compositional trends implies that the Fish Canyon magma was perilously close to complete solidification prior to late reheating (Fig. 2.4). The modeling involves calculation of evolving melt composition in response to fractional crystallization followed by inversion of melt compositions to the composition of zircons in equilibrium with the modeled melt. The starting melt composition was taken to be the melt in equilibrium with the zircon with lowest Yb/Dy (maximum melt fraction; experimentally determined partition coefficients of Rubatto and Hermann, 2007). The trace element composition of the bulk fractionating assemblage was calculated from published trace element data of major and accessory minerals (Bachmann et al., 2005) and modal abundances (Bachmann et al., 2002), in which titanite plays the key role (Fig. 2.3 and 2.4). The bulk partition coefficient, defined as the ratio of the bulk fractionating assemblage to initial melt composition, has been held constant throughout the model calculation due to the small temperature interval between zircon saturation (~760 °C) and the solidus (~690 °C), in conjunction with the limited major element variation during crystallization of a granitic near-minimum melt. Using these input parameters, we modeled evolving melt compositions in response to fractional crystallization. Finally, evolving melt compositions were inverted back to zircon compositions using zircon-melt partition coefficients for direct comparison with measured zircon compositions. According to these model calculations (Fig. 2.4), compositional variations in zircons with ages ~28.6–28.4 Ma require 50–75% crystallization

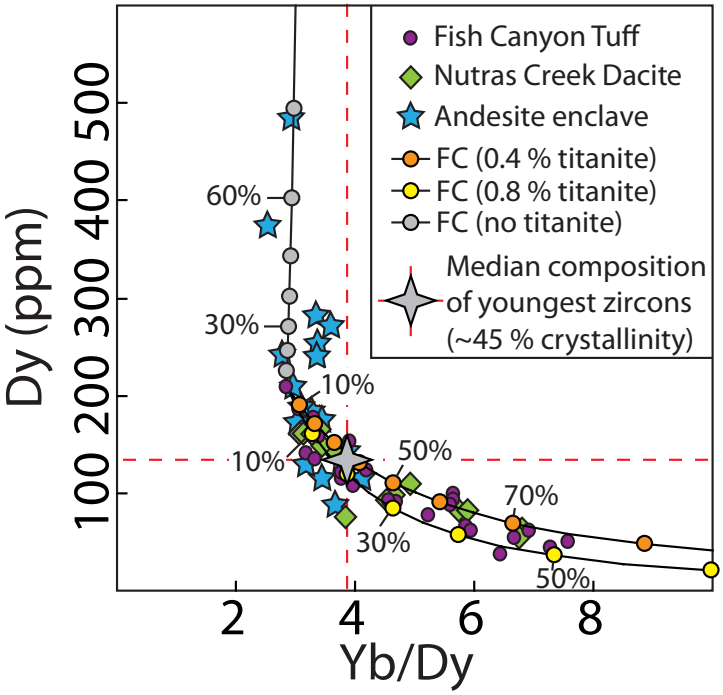

FIGURE 2.4 Middle and heavy rare earth element variations in U-Pb dated zircons modeled as a result of fractional crystallization (FC; see text for details). The gray star and dashed red lines represent the median composition of the youngest dated zircons corresponding to an absolute crystallinity of ~45% (Bachmann et al., 2002; see text for details). The modeled compositional trend for a titanite-free fractionating assemblage is shown for comparison. The model is significantly more sensitive to variations in titanite modal abundance than to minor changes in zircon-melt partition coefficients.

of a fractionating assemblage containing 0.4–0.8% titanite to produce the trend of decreasing Dy concentration and increasing Yb/Dy (Fig. 2.4).

The initial crystallinity (~28.6–28.7 Ma) is unknown, but crystallinity at the time of eruption was ~45 vol.% (Bachmann et al., 2002). If the youngest zircons crystallized close to eruption, their trace element compositions (median Yb/Dy ~3.8; Fig. 2.4) correspond to a crystallinity of ~45%. The average composition of the youngest zircons is the reference point for scaling our model to absolute crystallinity. This framework leads to the conclusion that the magma in which the zircons with the highest Yb/Dy crystallized at ~28.4 Ma had a crystallinity of 75–80% (Fig. 2.4). Large changes in total crystallinity were driven primarily by changes in the modal abundances of near-solidus quartz and sanidine, as demonstrated by mineral modes in completely solidified autoliths with bulk Fish Canyon magma composition (Bachmann et al., 2002). The proximity of the Fish Canyon magma to complete solidification can be taken as indirect evidence for a "volcanic-plutonic connection" between crystal-rich monotonous intermediates and compositionally equivalent granodiorite plutons.

2.4 THE DURATION OF REJUVENATION OF A HIGHLY CRYSTALLINE MAGMA RESERVOIR

Durations or process rates are commonly the primary output parameters in many fluid mechanical models of magmatic processes. Our approach to calibrating the duration of the pre-eruptive remelting event by tracking magma crystallinity as a function of time yields independent constraints that may serve as

input parameters for fluid dynamic modeling, or be used to test competing models. An estimated duration of 219 ± 45 ka for an inferred pre-eruptive remelting event is based on the age difference between the zircon with the highest Yb/Dy and the youngest zircon. With reference to the erupted volume of ~5000 km^3 and a decrease in crystallinity from 75–80% to 45% during this period, we calculate a remelting rate of ~0.01 km3/a. The duration and rate for the reactivation of the rheologically stiff crystal mush are important for assessing related thermal and mechanical mechanisms that ultimately trigger eruption. Our estimates are in excellent agreement with those derived from numerical modeling of remelting by upward percolation of a hot gas-phase plus entrained melt derived from underplated mafic magma (gas sparging; Bachmann and Bergantz, 2003). Similar time scales are also achievable by thermo-mechanical reactivation, a process that involves melting-induced internal fracturing and self-assimilation (Huber et al., 2011). Time scales predicted for buoyancy driven overturn of crystal mush triggered by formation of a low density mobile layer at the base of the mush (unzipping; Burgisser and Bergantz, 2011), are significantly shorter.

2.5 ENCLAVE ZIRCONS AS A WINDOW INTO THE DEEP-CRUSTAL MAGMA PROCESSING ZONE

Zircons from andesitic enclaves record the same age range and similar age distribution to those in the Fish Canyon Tuff and post-caldera Nutras Creek Dacite, but the compositional excursion in Yb/Dy that is recorded by Fish Canyon zircons is not present. This strongly suggests that enclave zircons are not due to mixing with resident Fish Canyon magma during magma recharge and entrapment of the enclaves. The differences in trace element compositions and the similarity of the age distributions of these zircon populations is consistent with evolution of the andesitic magma in a separate reservoir that experienced similar thermal oscillations but at higher absolute temperature without titanite crystallization. We infer that the enclave zircons represent products of the deep-crustal magma processing zone (Hildreth and Moorbath, 1988; Annen et al., 2006) in which the Fish Canyon dacite magma was generated. A common source of dacitic and andesitic magmas is consistent with the limited and overlapping range in Hf isotopic compositions of andesite and FCT zircons (see inset in Fig. 2.2B). This is independent evidence that Fish Canyon magma was generated in a deep zone of mafic magma injection, melting, assimilation, fractionation, and homogenization prior to ascent to the shallow pre-eruptive reservoir (e.g., Lipman et al., 1978). We speculate that such deep-crustal magma processing zones control the thermal evolution of the upper-crustal reservoir by varying rates of magma production and influx, implying an important thermal link between deep and shallow magma reservoirs in continental caldera settings.

2.6 THE ERUPTION AGE OF THE FISH CANYON TUFF

Fish Canyon Tuff sanidine (FCs) is

the most frequently used neutron fluence monitor for $^{40}Ar/^{39}Ar$ geochronology. A valid fluence monitor requires an accurate, precise, and independent determination of it's age (i.e., the eruption age of a volcanic unit). Despite its widespread use, the age of FCs is still under debate. Several recent studies have attempted to improve accuracy and precision of the FCs age using various approaches (Kuiper et al., 2008; Renne et al., 2010; 2011; Channell et al., 2010; Rivera et al., 2011; Westerhold et al., 2012). The results of these investigations range from 27.89 to 28.305 Ma (see Fig. 2.1). Considering the crystallization/remelting history recorded by zircons, we are confident that the youngest dated zircons crystallized close to eruption and thus provide constraints on the eruption age of the FCT. This is further supported by the a lack of resorption-features at the surfaces of analyzed zircons, suggesting that the melt was zircon saturated prior to eruption. Using the crystallization age of our youngest dated zircon (28.196 ± 0.038 Ma) to estimate the eruption age, is most consistent with the calibration of Kuiper et al. (2008) of 28.201 ± 0.046 Ma. This excellent agreement between $^{40}Ar/^{39}Ar$ and U-Pb dates has profound implications for the intercalibration of these geochronometers and the calibration of the Cenozoic time-scale.

2.7 SUMMARY & CONCLUSIONS

We present a new approach that allows us to quantify the chemical and thermal evolution of large silicic magmatic systems as a function of time and apply this approach to the Oligocene Fish Canyon Tuff. The trace element compositions of U-Pb dated zircons record the thermal evolution of this giant magmatic system at previously unattainable temporal resolution. The ~440,000 years of magma evolution recorded by zircons is marked by an early phase of volumetric growth, plutonic cooling to 75–80% crystallinity and a 219 ± 45 ka long period of thermal rejuvenation and remelting. Furthermore, our results provide a concrete link between a deep-crustal magma processing zone in which andesitic recharge magmas evolved and the shallow pre-eruption Fish Canyon magma reservoir. Large-scale thermal oscillations as recorded by Fish Canyon zircons may be common features of many silicic plutonic and volcanic systems reflecting the thermal response to incremental growth, magma recharge and mafic underplating. Our results demonstrate that we can resolve such features over 10^5 years timescales placing unprecedented quantitative constraints on the pre-eruption evolution of supervolcano magma reservoirs such as the Fish Canyon. This approach is widely applicable to evolved volcanic deposits and their plutonic equivalents and provides critical input parameters for fluid dynamic modeling of large silicic magma reservoirs.

APPENDIX

ANALYTICAL METHODS

CA-ID-TIMS U-Pb geochronology: A total of 58 zircon crystals were analyzed as single grains by isotope-dilution-thermal ionization mass spectrometry (ID-TIMS) at the University of Geneva (Tab.

Table A2.1 *U-Pb isotopic data*

	Composition				Isotopic Ratios								Dates (Ma)					
Fraction	Th/U (a)	Pb* (pg) (b)	Pb_c (pg) (c)	Pb*/Pb_c (d)	$^{206}Pb/^{204}Pb$ (e)	$^{206}Pb/^{238}U$ (f,g)	±2σ %	$^{207}Pb/^{235}U$ (f)	±2σ %	$^{207}Pb/^{206}Pb$ (f,g)	±2σ %	Corr. coef.	$^{206}Pb/^{238}U$ (g,h)	±2σ abs	$^{207}Pb/^{235}U$ (h)	±2σ abs	$^{207}Pb/^{206}Pb$ (g,h)	±2σ abs
Fish Canyon Tuff (FCT)																		
z1	0.65	1.68	0.78	2.1	143	0.004398	0.20	0.028488	3.3	0.047002	3.2	0.848	28.289	0.058	28.52	0.94	48	76
z2	0.56	3.45	0.64	5.4	341	0.004415	0.10	0.028750	1.3	0.047247	1.3	0.858	28.400	0.028	28.78	0.38	61	30
z3	0.79	2.45	0.72	3.4	211	0.004383	0.14	0.028063	2.3	0.046453	2.1	0.874	28.196	0.038	28.10	0.62	20	52
z4	0.81	2.23	0.60	3.7	225	0.004386	0.14	0.028513	2.1	0.047167	2.0	0.889	28.215	0.038	28.55	0.59	57	47
z5	0.55	2.69	0.64	4.2	271	0.004413	0.12	0.028737	1.8	0.047254	1.7	0.801	28.383	0.035	28.77	0.50	61	40
z6	0.68	2.02	1.09	1.8	125	0.004405	0.22	0.028776	4.1	0.047403	3.9	0.917	28.332	0.063	28.8	1.2	69	92
z7	0.48	9.96	1.39	7.1	452	0.004423	0.089	0.028550	0.97	0.046832	0.91	0.766	28.452	0.025	28.58	0.27	40	22
z8	0.48	2.34	1.05	2.2	153	0.004412	0.18	0.028945	3.0	0.047602	2.9	0.864	28.379	0.051	28.97	0.86	78	68
z9	0.74	6.47	0.55	11.7	684	0.004452	0.089	0.028743	0.69	0.046842	0.64	0.725	28.638	0.025	28.77	0.20	40	15
z10	0.68	2.09	0.32	6.6	398	0.004440	0.093	0.028770	1.2	0.047012	1.2	0.858	28.561	0.026	28.80	0.35	49	28
z11	0.87	5.34	0.65	8.2	470	0.004434	0.098	0.028506	0.97	0.046648	0.91	0.781	28.520	0.028	28.54	0.27	30	22
z12	1.05	3.30	0.55	6.0	337	0.004385	0.11	0.028015	1.1	0.046356	1.0	0.695	28.206	0.031	28.06	0.30	15	25
z13	0.59	7.98	0.54	14.9	897	0.004424	0.069	0.028652	0.55	0.046998	0.51	0.644	28.454	0.020	28.68	0.15	48	12
z14	0.81	10.3	0.56	18.5	1050	0.004428	0.080	0.028317	0.49	0.046402	0.48	0.427	28.482	0.023	28.35	0.14	17	12
z15	0.57	6.51	0.79	8.2	505	0.004406	0.066	0.028344	0.91	0.046676	0.89	0.539	28.341	0.019	28.38	0.26	32	21
z16	0.71	3.02	0.52	5.7	346	0.004391	0.093	0.028127	1.4	0.046475	1.3	0.796	28.246	0.026	28.17	0.38	21	32
z17	0.64	6.70	0.59	11.3	679	0.004439	0.089	0.028574	0.81	0.046708	0.77	0.659	28.551	0.025	28.61	0.23	33	18
z18	0.83	6.96	0.93	7.5	434	0.004426	0.11	0.028536	1.1	0.046779	1.1	0.689	28.471	0.031	28.57	0.32	37	26
z19	0.48	3.09	0.80	3.9	254	0.004418	0.11	0.028786	1.8	0.047273	1.7	0.898	28.420	0.032	28.82	0.51	62	41
z20	0.54	4.06	0.60	6.8	423	0.004426	0.14	0.028380	1.4	0.046527	1.3	0.926	28.468	0.041	28.42	0.40	24	31
z21	0.62	5.24	0.44	11.8	709	0.004418	0.095	0.028606	0.76	0.046981	0.70	0.697	28.418	0.027	28.64	0.21	47	17
z22	0.87	2.68	0.51	5.2	307	0.004444	0.11	0.029122	1.5	0.047547	1.4	0.878	28.586	0.032	29.15	0.44	76	34
z23	0.48	2.26	0.74	3.1	205	0.004417	0.16	0.028991	2.4	0.047621	2.3	0.894	28.413	0.044	29.02	0.69	79	54
z24	0.49	3.73	0.51	7.3	460	0.004418	0.090	0.028481	1.1	0.046781	1.1	0.725	28.415	0.025	28.52	0.32	37	26
Nutras Creek Dacite (NCD)																		
z1	0.64	3.00	0.40	7.4	449	0.004391	0.11	0.027992	1.3	0.046253	1.2	0.853	28.245	0.032	28.03	0.35	10	28
z2	0.59	2.96	0.49	6.1	376	0.004443	0.089	0.029041	1.2	0.047429	1.2	0.824	28.577	0.025	29.07	0.36	70	28
z3	0.68	4.71	0.49	9.5	567	0.004434	0.081	0.028642	0.81	0.046873	0.77	0.789	28.518	0.023	28.67	0.23	42	18
z4	0.51	6.56	0.45	14.7	906	0.004415	0.062	0.028345	0.56	0.046589	0.52	0.737	28.395	0.018	28.38	0.16	27	13
z5	0.67	4.66	0.54	8.6	518	0.004453	0.087	0.028838	0.89	0.046991	0.84	0.775	28.642	0.025	28.87	0.25	48	20
z6	0.58	8.47	0.50	17.0	1025	0.004414	0.069	0.028403	0.50	0.046690	0.47	0.636	28.392	0.019	28.44	0.14	32	11
z7	0.72	2.96	1.16	2.6	164	0.004385	0.15	0.028201	2.6	0.046668	2.5	0.879	28.204	0.042	28.24	0.72	31	59
z8	0.65	2.25	0.43	5.2	318	0.004392	0.12	0.028438	1.6	0.046983	1.5	0.841	28.250	0.035	28.47	0.44	47	36
z9	0.62	2.97	0.40	7.4	449	0.004420	0.082	0.028496	1.0	0.046781	0.98	0.778	28.430	0.023	28.53	0.29	37	24
z10	0.55	4.28	0.70	6.2	385	0.004424	0.094	0.028923	1.2	0.047435	1.1	0.804	28.458	0.027	28.95	0.33	70	26
z11	0.66	2.54	0.73	3.5	221	0.004433	0.14	0.028648	2.1	0.046896	2.0	0.788	28.511	0.039	28.68	0.59	43	48

(Table A2.1 continued)

z12	0.54	6.03	0.47	12.8	782	0.004407	0.078	0.028346	0.68	0.046670	0.63	0.716	28.347	0.022	28.38	0.19	31	15
z13	0.69	4.32	0.42	10.4	617	0.004404	0.083	0.028328	0.80	0.046675	0.75	0.790	28.326	0.023	28.36	0.22	32	18
z14	0.65	5.45	0.41	13.2	786	0.004432	0.095	0.028439	0.73	0.046558	0.67	0.774	28.509	0.027	28.47	0.21	26	16
z15	0.70	4.01	0.40	10.1	597	0.004420	0.083	0.028545	0.81	0.046863	0.76	0.780	28.428	0.024	28.58	0.23	41	18
Andesite enclave (MLX)																		
z1	0.66	2.08	0.82	2.6	166	0.004415	0.17	0.029116	2.8	0.047834	2.7	0.918	28.395	0.047	29.14	0.81	91	63
z2	1.06	5.87	0.54	10.9	591	0.004401	0.13	0.028549	1.1	0.047070	1.0	0.758	28.308	0.035	28.58	0.30	52	24
z3	1.76	32.3	0.71	45.3	2065	0.004388	0.15	0.028212	0.28	0.046652	0.28	0.625	28.224	0.043	28.249	0.079	30.4	6.9
z4	0.79	2.65	0.80	3.3	204	0.004431	0.18	0.028809	2.4	0.047173	2.3	0.889	28.502	0.051	28.84	0.69	57	55
z5	0.73	3.68	0.44	8.4	498	0.004424	0.11	0.028735	1.3	0.047126	1.3	0.742	28.458	0.030	28.77	0.38	55	30
z6	1.02	2.44	0.41	6.0	338	0.004416	0.15	0.028857	1.7	0.047415	1.6	0.826	28.405	0.042	28.89	0.50	69	39
z7	0.77	2.27	0.29	7.9	461	0.004444	0.098	0.029166	1.0	0.047624	0.99	0.799	28.582	0.028	29.19	0.30	80	24
z8	0.91	1.93	0.57	3.4	202	0.004455	0.15	0.029234	2.3	0.047614	2.1	0.896	28.655	0.043	29.26	0.65	79	51
z9	0.75	5.09	0.51	9.9	581	0.004444	0.085	0.028832	0.81	0.047076	0.77	0.674	28.584	0.024	28.86	0.23	52	18
z10	0.62	11.5	0.67	17.2	1029	0.004427	0.077	0.028625	0.46	0.046918	0.42	0.642	28.475	0.022	28.66	0.13	44	10
z11	0.64	4.58	0.73	6.3	386	0.004441	0.10	0.028734	1.2	0.046946	1.1	0.732	28.565	0.030	28.76	0.34	45	27
z12	0.79	2.34	0.65	3.6	219	0.004419	0.14	0.028942	2.1	0.047525	2.0	0.888	28.422	0.039	28.97	0.61	75	48
z13	0.96	1.85	0.67	2.7	166	0.004409	0.17	0.028749	2.9	0.047314	2.7	0.893	28.359	0.049	28.78	0.81	64	65
z14	0.70	9.22	1.78	5.2	315	0.004428	0.13	0.028626	1.5	0.046903	1.4	0.642	28.485	0.037	28.66	0.42	43	34
z15	0.65	6.64	0.71	9.3	558	0.004424	0.098	0.028799	0.84	0.047237	0.79	0.659	28.454	0.028	28.83	0.24	60	19
z16	0.77	1.84	0.57	3.2	199	0.004448	0.15	0.029078	2.5	0.047433	2.4	0.894	28.611	0.043	29.10	0.71	70	56
z17	0.76	2.24	0.52	4.3	264	0.004420	0.12	0.028516	1.8	0.046816	1.7	0.862	28.428	0.035	28.55	0.51	39	41
z18	1.17	2.43	0.71	3.4	193	0.004390	0.16	0.028479	2.4	0.047067	2.3	0.841	28.241	0.046	28.51	0.68	52	55
z19	1.35	7.21	0.48	15.2	765	0.004389	0.13	0.028184	0.71	0.046594	0.67	0.671	28.232	0.036	28.22	0.20	27	16

(a) Th contents calculated from radiogenic 208Pb and the 207Pb/206Pb date of the sample, assuming concordance between U-Th and Pb systems.
(b) Total mass of radiogenic Pb.
(c) Total mass of common Pb.
(d) Ratio of radiogenic Pb (including 208Pb) to common Pb.
(e) Measured ratio corrected for fractionation and spike contribution only.
(f) Measured ratios corrected for fractionation, tracer and blank. Laboratory blanks were corrected using the average measured composition of 29 total procedural blanks analyzed during the course of this study: $^{206}Pb/^{204}Pb = 18.512 \pm 0.172$, $^{207}Pb/^{204}Pb = 15.473 \pm 0.164$, $^{208}Pb/^{204}Pb = 37.676 \pm 0.382$ (2 S.D.)
(g) Corrected for initial Th/U disequilibrium using radiogenic ^{208}Pb and Th/U[magma] = 2.2 ± 0.5.
(h) Isotopic dates calculated using the decay constants $\lambda 238 = 1.55125E\text{-}10$ and $\lambda 235 = 9.8485E\text{-}10$ (Jaffey et al., 1971).

Table A2.2 *Zircon trace element geochemical data measured by solution ICP-SF-MS*

Zr+Hf-normalized conc. (a,b,c)	Y		Zr		La		Ce		Pr		Nd		Sm		Eu		Gd		Tb		Dy		Ho		Er		Tm		Yb		Lu		Hf		Th	
	ppm	2σ	‰	2σ	ppm	2σ	ppm	2σ	ppm	2σ	ppm	2σ	ppm	2σ	ppm	2s	ppm	2σ	ppm	2σ	ppm	2σ	ppm	2σ	ppm	2σ	ppm	2σ	ppm	2σ	ppm	2σ	ppm	2σ	ppm	2σ
Fish Canyon Tuff (FCT)																																				
z1	1238	40	488	13	0.6	1.0	29.5	2.3	0.8	1.0	3.4	1.9	5.2	2.0	2.6	1.2	23.8	4.3	7.5	1.4	89.9	5.4	36.2	2.7	183.5	9.9	44.5	2.9	423	19	100.7	4.5	10487	229	176.4	7.0
z2	1095	39	487	12	0.18	0.66	40.0	2.3	0.19	0.67	2.1	1.2	4.3	1.6	1.7	0.9	20.0	2.9	6.6	0.9	77.3	3.7	31.6	2.2	166.3	5.8	40.4	2.2	404	13	97.9	3.6	10853	190	217.0	8.7
z3	1443	49	488	11	0.5	1.2	50.0	3.0	0.9	1.4	5.4	2.3	8.2	2.9	3.7	1.6	37.2	4.8	10.7	1.7	120.4	9.4	45.1	3.6	211	10	48.3	2.9	455	25	107.1	5.0	9412	238	324	12
z4	1808	64	488	14	2.5	6.4	56.5	3.2	0.9	1.2	7.4	2.3	11.2	2.9	4.4	1.4	48.3	5.7	14.0	1.8	157.1	8.5	56.6	3.1	266	12	59.0	3.2	534	23	117.7	5.5	9611	238	288	13
z5	851	28	487	12	0.9	1.3	43.3	2.9	0.3	1.2	1.6	1.5	2.4	1.6	1.1	1.1	11.7	3.4	4.1	1.3	54.5	5.0	23.5	2.6	135.1	8.3	34.9	2.9	365	16	94.4	3.3	11031	199	274	11
z6	1378	41	487	12	0.1	2.6	55.1	6.2	0.7	3.4	2.4	3.3	4.9	3.6	1.5	2.3	23.8	6.8	7.6	3.1	94.9	9.1	39.5	5.0	210	12	53.0	5.2	537	24	134.6	7.7	11126	228	394	17
z7	918	28	486	15	0.30	0.35	44.7	1.8	0.17	0.34	1.1	0.5	2.3	0.7	0.8	0.4	13.6	1.7	4.6	0.5	61.6	2.9	26.5	1.3	144.1	4.5	36.6	1.5	367	10	89.3	2.3	11832	257	217.5	5.6
z8	559	12	486	10	1.13	0.81	25.5	1.8	0.14	0.71	1.2	1.0	1.7	1.1	0.7	0.7	9.6	2.0	3.0	0.9	37.1	2.1	15.8	1.4	88.0	3.9	22.5	1.8	239.8	7.1	60.8	2.1	11707	207	111.1	3.6
z9	1580	29	489	10	0.42	0.21	41.8	1.1	0.37	0.21	5.3	0.6	8.3	0.8	3.0	0.4	39.8	1.7	12.2	0.5	140.5	3.4	52.3	1.3	239.8	4.5	51.4	1.3	447	10	92.9	2.0	9117	159	138.5	2.6
z10	1530	40	487	11	0.09	0.57	49.1	2.1	0.24	0.59	4.0	1.3	7.7	1.8	2.7	0.8	37.9	3.4	11.7	1.1	133.9	6.2	49.6	2.1	233.3	8.6	51.0	2.1	446	14	95.2	2.9	10165	214	177.7	5.5
z11	2044	207	488	49	0.93	0.92	82.7	6.2	0.50	0.74	6.6	1.9	10.9	2.4	4.1	1.2	50.8	4.9	15.2	1.7	177	10	65.4	4.3	299	13	65.2	2.5	584	25	126.6	5.6	10033	295	359	20
z12	1877	44	489	11	0.39	0.92	76.0	3.5	0.41	0.86	8.1	2.4	11.3	2.6	4.1	1.3	47.6	4.5	13.4	1.4	152.3	7.4	57.4	3.0	280	11	63.4	2.7	592	16	132.7	3.5	8945	177	371	11
z13	1550	23	486	9	0.71	0.50	54.8	1.9	0.31	0.43	4.0	1.1	6.0	1.3	2.2	0.6	32.5	2.8	10.1	0.8	122.1	4.0	47.6	1.7	238.1	5.9	55.2	2.0	512.9	8.6	116.1	3.0	11307	184	271.7	8.2
z14	2041	43	488	13	0.09	0.29	59.9	1.8	0.38	0.35	6.5	1.1	10.7	1.3	4.3	0.5	53.5	2.6	15.9	0.7	185.8	5.2	67.6	2.3	308.4	7.9	66.0	2.2	567	14	117.3	3.1	9349	222	240.7	6.1
z15	975	19	486	8	0.84	0.85	40.4	2.2	0.11	0.73	2.1	1.2	3.2	1.5	1.0	0.8	16.3	2.8	5.1	1.1	67.2	4.7	28.2	1.7	151.8	5.2	38.6	1.8	395	11	98.9	2.8	11450	210	238.2	5.7
z16	1300	30	487	11	-	-	47.6	2.9	0.06	0.90	4.2	1.9	6.4	2.0	2.3	1.1	32.5	3.6	9.3	1.4	107.0	5.6	40.3	2.5	195.5	7.7	45.2	2.3	425	14	97.2	4.0	10313	199	260.3	7.2
z17	1379	29	487	10	0.21	0.37	52.6	1.5	0.17	0.36	3.3	0.8	5.7	1.1	1.8	0.6	29.4	2.3	9.4	0.8	115.0	4.1	44.1	1.3	214.6	6.1	48.1	1.4	434.6	9.0	94.1	2.5	10212	159	174.0	3.8
z18	1183	64	486	27	3.1	1.2	98.4	5.0	0.4	1.0	5.1	2.1	5.6	2.1	1.0	0.9	24.9	4.1	7.6	1.3	99.4	5.9	40.9	3.3	221	12	56.1	3.0	563	23	134.9	6.3	12073	495	281	31
z19	596	37	486	27	-	-	39.8	3.8	-	-	1.1	1.9	1.7	1.9	0.2	1.1	10.6	3.7	3.3	1.8	43.9	4.6	18.9	2.7	111.5	7.7	29.7	3.1	319	14	79.0	5.9	11857	436	180.5	9.0
z20	1084	52	485	25	0.8	2.0	67.2	6.0	0.3	1.9	3.3	2.9	4.6	2.9	1.2	1.7	20.5	4.6	6.6	2.4	87.1	7.8	37.2	3.8	202	15	50.6	4.6	487	28	113.8	8.7	12782	713	278	17
z21	1019	52	486	30	0.06	0.83	58.1	4.0	0.20	0.84	2.8	1.5	4.9	1.8	1.5	1.0	23.0	3.5	7.1	1.4	92.0	6.6	36.8	2.9	186	11	44.2	3.5	420	24	97.8	6.4	11201	618	252	12
z22	1866	91	488	11	0.0	1.1	77.2	4.4	0.6	1.1	7.7	2.5	13.0	2.6	5.1	1.6	58.1	4.9	17.5	2.4	209.3	5.4	76.1	4.2	340	14	71.4	4.8	596	29	119.1	7.3	9879	393	195	11
z23	1009	37	486	19	1.51	0.79	53.3	3.5	0.54	0.67	2.2	1.0	2.7	1.1	0.9	0.7	13.6	2.1	4.9	1.0	61.6	4.1	27.6	2.4	157.8	9.2	41.5	3.0	425	22	108.6	5.8	11425	411	297	18
z24	711	48	485	37	0.8	1.6	46.8	4.9	0.1	1.4	1.9	2.0	2.4	2.1	0.5	1.2	11.9	3.7	3.6	1.6	50.0	5.5	22.6	2.8	135	13	36.7	3.9	379	24	97.0	6.7	12394	259	226	18
Nutras Creek Dacite (NCD																																				
z1	1017	67	487	36	0.8	1.1	29.7	4.5	0.16	0.86	3.8	2.0	4.6	2.3	2.5	1.1	25.9	5.7	8.1	1.6	91.5	8.5	36.6	3.8	179	12	45.0	3.7	416	26	101.4	6.4	10615	624	139.3	7.8
z2	1676	117	487	33	0.15	0.77	66.5	4.6	0.11	0.69	3.5	1.7	6.5	2.5	2.7	1.1	39.5	5.3	12.6	1.9	144	11	56.4	5.0	259	17	60.6	4.7	523	40	115.9	6.6	10212	508	197	16
z3	1669	124	487	31	0.14	0.42	55.7	4.7	0.22	0.43	4.8	1.4	8.7	1.7	3.6	0.9	44.0	4.4	14.0	1.6	160	13	60.5	5.2	269	25	61.1	5.2	523	40	115.2	8.9	10269	763	184	15
z4	904	59	487	30	4.5	2.0	55.2	5.3	0.7	1.0	4.4	2.3	2.2	1.7	1.1	1.0	13.9	3.7	4.8	1.5	63.3	8.5	27.4	2.4	157	12	42.2	5.0	431	24	113.1	6.6	11129	517	239	19
z5	1674	108	488	31	1.10	0.64	64.4	4.5	0.54	0.57	5.7	1.4	8.1	1.6	3.2	0.8	44.3	3.9	13.8	1.3	160	15	61.0	4.5	269	20	60.2	4.1	499	30	108.1	6.6	9327	536	175	10
z6	1108	52	486	28	1.97	0.86	58.0	4.2	0.32	0.59	2.8	1.4	2.8	1.3	1.4	0.7	19.1	3.0	6.4	0.9	82.0	7.5	35.2	2.5	183	11	48.6	3.4	484	22	121.5	5.9	11326	459	271	16
z7	798	52	488	25	-	-	22.3	2.2	0.03	0.53	3.1	1.4	4.9	1.3	2.4	0.9	23.6	4.3	6.8	1.3	74.3	5.6	27.4	2.5	128.0	8.0	31.2	3.0	287	14	67.6	3.2	9525	426	101.4	6.7
z8	1727	85	487	22	0.3	1.1	59.0	5.7	0.2	1.0	6.3	3.0	10.4	3.3	4.6	1.6	52.8	8.1	14.7	2.1	162	15	57.7	4.5	256	14	56.9	3.5	504	28	115.2	6.8	10838	472	246	11
z9	1061	84	487	29	-	-	28	11	-	-	7	11	5.8	7.9	3.9	5.5	28	15	8.6	7.0	97	25	35	11	196	26	45	12	452	47	113	18	11063	463	112	23
z10	1117	56	486	25	6.3	1.6	71.7	6.0	1.19	0.89	6.5	2.4	4.3	1.8	1.6	0.9	20.9	3.7	6.9	1.2	82.0	7.4	33.8	3.5	175	15	46.9	3.4	471	24	117.6	6.4	11836	592	294	24
z11	1661	78	488	23	0.5	1.0	75.2	5.9	0.11	0.76	4.5	1.7	7.3	2.3	2.6	1.2	39.8	5.7	12.4	1.8	147	13	56.4	4.8	265	14	59.7	4.5	511	19	111.9	5.9	10048	406	221	12
z12	744	38	486	32	3.9	2.7	44.9	5.7	0.4	1.8	4.4	3.7	2.0	2.3	1.3	1.6	12.5	5.4	4.3	2.2	54.6	9.5	22.8	3.6	133	12	35.6	4.4	370	30	98.3	8.6	11446	604	169	14

(Table A2.2 continued)

z13	1425	80	487	28	0.29	0.70	56.7	4.9	0.02	0.55	3.0	1.3	4.7	1.7	2.2	0.9	30.1	5.3	9.4	1.7	108.3	9.2	43.9	3.3	230	15	56.4	4.1	534	36	129.4	8.5	10835	564	318	20
z14	1748	107	487	29	0.04	0.48	65.7	5.3	0.23	0.48	5.6	1.7	9.3	2.3	3.6	0.8	47.1	4.5	14.4	1.5	164	14	61.4	4.3	283	18	65.2	4.7	566	26	128.2	6.0	10181	486	241	17
z15	1560	105	487	34	1.15	0.87	64.3	5.7	0.45	0.63	6.3	1.7	8.6	2.7	3.7	1.2	41.8	6.2	12.3	1.8	137	14	50.8	4.5	241	17	58.4	5.5	529	30	125.0	9.6	10208	647	290	25
Andesite enclave (MLX)																																				
z1	1002	28	487	13	2.8	1.4	51.8	3.3	1.1	1.3	9.9	2.5	12.7	2.9	4.4	1.7	40.3	4.8	9.5	1.7	87.3	6.0	28.2	2.6	131.4	7.2	31.4	2.4	322	14	81.9	3.8	11127	199	241.2	8.6
z2	3070	75	488	20	-	-	132.9	5.2	0.5	1.1	9.7	2.6	16.5	3.2	6.8	1.6	76.0	5.6	23.5	2.0	283	11	104.2	6.2	490	18	109.6	6.1	953	30	196.6	6.1	9471	267	894	30
z3	5431	106	488	9	-	-	443	10	0.89	0.65	19.3	2.9	35.0	3.2	14.5	1.6	156.2	5.3	44.6	1.8	485	10	172.2	4.7	775	17	166.0	4.2	1424	26	281.8	4.9	9470	144	4559	90
z4	2277	48	488	7	-	-	71.0	4.4	0.1	1.3	7.1	2.7	11.4	3.3	4.0	1.8	61.5	5.7	18.3	2.4	208.3	7.5	75.0	3.8	341	11	71.8	3.3	616	15	127.6	4.5	9480	176	271.4	6.4
z5	2026	32	487	8	0.13	0.62	67.2	2.9	0.28	0.66	5.9	1.7	10.1	2.0	3.6	1.0	50.8	3.9	15.3	1.2	174.7	7.1	65.7	2.4	309.0	7.4	67.4	2.1	604	17	131.5	3.6	10517	153	260.9	6.6
z6	2581	56	489	10	-	-	75.8	4.2	0.30	0.92	9.5	2.1	16.0	2.9	6.5	1.4	75.0	6.5	21.7	1.9	242.4	9.2	85.4	4.2	382	13	80.5	3.2	679	19	140.1	4.5	8862	206	340.4	9.1
z7	1455	30	488	10	-	-	46.3	1.6	0.13	0.43	4.4	1.0	7.7	1.4	2.7	0.6	36.7	2.6	11.3	0.9	129.6	5.6	47.5	1.7	219.3	5.9	47.0	1.5	413	10	87.0	2.5	9277	201	152.1	4.2
z8	1903	39	488	8	-	-	43.1	2.5	-	-	5.1	2.2	9.5	2.8	4.7	1.4	52.4	4.6	15.1	1.7	171.6	7.2	62.2	2.8	286.3	9.2	60.7	2.4	521	12	108.6	4.1	8953	129	222.9	7.0
z9	2097	44	487	8	-	-	62.4	2.1	0.30	0.40	7.3	1.2	12.1	1.4	4.4	0.7	56.0	2.8	16.7	1.1	188.3	5.8	68.8	2.0	313.9	6.7	67.7	2.2	582	11	121.2	2.9	10201	183	236.0	5.1
z10	1451	28	486	10	1.18	0.26	60.5	1.2	0.37	0.22	3.9	0.6	5.7	0.8	1.8	0.4	28.6	1.5	9.1	0.4	135.1	2.9	43.8	1.0	222.4	4.9	53.0	1.0	513	10	118.7	2.1	11570	146	292.4	6.8
z11	1097	56	488	19	0.01	0.32	54.4	2.6	0.09	0.33	3.1	0.8	5.8	1.2	2.0	0.5	30.0	1.9	9.4	1.0	114.2	6.0	43.2	2.0	207.5	8.7	45.6	2.5	395	18	82.4	3.7	9532	398	121.5	5.9
z12	3181	83	487	12	0.42	0.82	75.7	3.5	0.30	0.81	8.3	2.0	14.4	2.5	5.9	1.4	71.0	6.2	23.0	1.6	271.9	7.8	103.4	3.2	492	14	108.9	3.9	980	27	214.5	6.8	10211	237	291.1	7.9
z13	1638	85	487	27	-	-	69.6	5.8	-	-	10.5	4.3	14.6	4.9	5.4	2.5	55.3	8.8	15.0	3.4	175	13	60.9	5.2	292	16	64.8	4.8	600	28	130.2	9.0	10653	404	361	19
z14	1714	74	487	21	0.12	0.67	68.3	3.4	0.23	0.68	6.9	1.6	11.2	2.1	3.7	1.0	51.3	4.9	15.3	1.3	185.1	9.2	66.9	3.4	317	14	69.8	3.2	610	27	127.4	7.1	10474	382	230	12
z15	1342	46	486	23	-	-	78.8	5.5	-	-	3.7	2.0	6.4	2.3	1.7	1.1	32.2	4.6	9.9	1.6	143.5	7.3	48.0	3.4	247	11	58.9	3.5	557	24	124.0	6.6	11507	494	325	16
z16	1221	42	486	36	2.3	3.7	66.5	7.9	0.3	3.2	7.5	5.3	7.0	4.7	1.8	2.9	32	10	9.4	4.1	117	14	44.9	7.5	229	20	52.0	7.5	484	45	109	12	10237	988	184	22
z17	3254	155	488	23	-	-	145	10	0.7	2.3	17.2	4.9	28.3	7.3	10.7	3.1	122	12	32.6	4.3	376	25	130.7	9.3	568	31	117.1	7.0	958	66	191	14	9709	534	599	40
z18	2382	118	487	25	-	-	167	15	-	-	9.4	6.7	15.8	7.6	5.5	4.5	69	14	20.2	5.7	238	21	89.9	9.8	420	29	91.2	9.2	801	54	169	13	10708	456	906	65
z19	2521	137	488	25	-	-	167	11	0.6	1.1	11.2	3.2	17.4	3.4	6.9	1.7	73.6	8.4	21.6	2.6	254	20	94.0	7.1	445	24	99.1	6.6	859	51	179	12	10014	657	982	68
average total procedural blank n=18 (d)	ppt	2SD	ppb	2SD	ppt	2SD	ppt	2SD	ppt	2SD	ppt	2SD	ppt	2SD	ppt	2SD	ppt	2SD	ppt	2SD	ppt	2SD	ppt	2SD	ppt	2SD	ppt	2SD	ppt	2SD	ppt	2SD	ppt	2SD	ppt	2SD
	5.1	6.2	0.12	0.15	0.51	0.51	0.0	1.2	0.30	0.26	-0.23	0.91	-0.70	0.66	-1.23	0.32	-0.7	1.0	-1.30	0.32	1.2	1.2	0.08	0.57	0.61	0.80	-0.31	0.31	3.2	1.2	2.42	0.59	66	191	4.7	2.1

Notes: Sc, Ti, Nb and Ta are not reported. ^{45}Sc was affected by $^{90}Zr^{2+}$ interferences. Nb and Ta were found in variable amounts in the U-Pb fraction of standard solutions put through column chemistry. Ti was below detection limit in most solutions.

(a) concentrations normalized to Zr+Hf = 497464 ppm in stoichiometric zircon.

(b) all data were corrected for blank contribution using the average blank ± 2SD reported at the bottom of the table. Uncertainties on concentrations were propagated using uncertainty propagation techniques described in Schoene et al. (2010) and are reported at the 2s confidence level.

(c) "-" indicates that concentrations in respective solutions were at or below the detection limit, given the magnitude of the blank correction.

(d) average total procedural blank given as unnormalized concentrations in blank solutions.

A2.1). Prior to dissolution, all crystals were annealed by heating to 900 °C for 48 h in a muffle furnace, transferred into 3 ml savillex beakers and chemically abraded in HF + trace HNO_3 at 180 °C for 15 h in parr bombs (Mattinson et al., 2005). Subsequently, zircons were rinsed with water, fluxed for several hours in 6N HCl and ultrasonically cleaned with water, acetone and 3N HNO_3. Single crystals were loaded in 200 μl Savillex capsules, spiked with ~3-5 mg of the EARTHTIME ^{202}Pb-^{205}Pb-^{233}U-^{235}U tracer solution (http://www.earth-time.org/) and dissolved in ~70 μl HF at 210 °C for 48 h in Parr bombs. After dissolution, samples were dried down and redissolved in 6N HCl at 180 °C overnight, dried down again and redissolved in 3N HCl. U and Pb were separated using a modified HCl-based single-column anion exchange chemistry (Krogh, 1973). The Zr, Hf, and trace element fractions ("wash") were collected for trace element and Hf isotope analyses (see below). The U-Pb fraction was loaded on outgassed Re filaments with a Si-Gel emitter (Gerstenberger and Haase, 1997). U and Pb isotopic measurements were performed on a Thermo TRITON thermal ionization mass spectrometer. Pb was measured in dynamic mode on a MasCom secondary electron multiplier. Analyses employing the ET2535 tracer were corrected using the fractionation factor derived from the measured $^{202}Pb/^{205}Pb$ ratio assuming a true value of 0.99924. U was measured as U-oxide in static mode on Faraday cups equipped with 10^{12} Ω resistors. Measured isotopic ratios were corrected for interferences of $^{233}U^{18}O^{16}O$ on $^{235}U^{16}O_2$ using an $^{18}O/^{16}O$ of 0.00205, measured on large U500 loads, and for mass fractionation using the measured $^{233}U/^{235}U$ ratio relative to a value of 0.99506 of the tracer. All common Pb in the zircon analyses was assumed to be procedural blank. U-Pb ratios and dates were calculated relative to a $^{235}U/^{205}Pb$ ratio of 100.23 ± 0.023% (1σ) and raw data were reduced using Tripoli and U-Pb_Redux software (Bowring et al., 2011) that employs algorithms of McLean et al. (2011). All uncertainties are reported at the 95% confidence level and exclude systematic uncertainties associated with tracer calibration and decay constants unless otherwise indicated.

Zircon trace element analyses: Trace elements in U-Pb dated zircons were analyzed following the approach of Schoene et al. (2010; Tab. A2.2). After column chemistry, the washes were dried down, redissolved in ~750 μl 0.5 M HNO_3 + 0.1 M HF doped with 1 ppb Ir, and transferred into pre-cleaned auto sampler microtubes. Trace element measurements were performed at ETH Zurich on an ICP-SF-MS (ELEMENT2, Thermo Fisher Scientific, Bremen, Germany) using an Aridus I desolvation nebulizer (CETAC, Omaha, USA) as sample introduction system and an autosampler (ASX-100, CETAC, Omaha, USA) for automated analysis. The instrumental parameters (gas flows, RF-power and ion lenses) were optimized for sensitivity (typically 1.4 x 10^6 cps/ppb In in medium resolution), low oxide rate (typically UO+/U+ below 0.03%) and low doubly charged rate (typically $^{137}Ba^{2+}/^{137}Ba^{+}$ 5%). The system was operated at medium resolu-

Table A2.3 *Lu-Hf isotopic data of U-Pb dated zircons analyzed by MC-ICPMS*

	$^{176}Yb/^{177}Hf$ (a)	±2σ	$^{176}Lu/^{177}Hf$ (a)	±2σ	$^{178}Hf/^{177}Hf$	$^{180}Hf/^{177}Hf$	SigHf [V] (b)	$^{176}Hf/^{177}Hf$	±2σ (c)	$^{176}Hf/^{177}Hf_t$ (d)	εHf_t (d)	±2σ (c)
Fish Canyon Tuff (FCT)												
z1	0.1665	133	0.00591	35	1.46713	1.88665	23	0.282573	10	0.282570	-7.00	0.36
z2	0.0531	43	0.00199	12	1.46714	1.88662	12	0.282547	11	0.282546	-7.82	0.38
z3	0.0444	36	0.00183	11	1.46713	1.88666	17	0.282531	11	0.282530	-8.39	0.40
z4	0.0608	49	0.00226	14	1.46714	1.88662	44	0.282526	8	0.282525	-8.59	0.29
z5	0.0443	35	0.00152	9	1.46713	1.88658	83	0.282513	8	0.282512	-9.02	0.28
z6	0.0515	41	0.00207	12	1.46714	1.88665	31	0.282544	9	0.282543	-7.95	0.33
z7	0.0665	53	0.00258	16	1.46712	1.88655	19	0.282567	10	0.282566	-7.12	0.34
z8	0.0507	41	0.00191	11	1.46715	1.88657	19	0.282527	10	0.282526	-8.55	0.34
z9	0.0585	47	0.00223	13	1.46713	1.88660	10	0.282519	14	0.282518	-8.84	0.51
z10	0.0219	18	0.00097	6	1.46715	1.88660	20	0.282543	9	0.282542	-7.97	0.33
z11	0.0305	24	0.00108	7	1.46714	1.88665	49	0.282531	8	0.282530	-8.39	0.30
z12	0.0490	39	0.00185	11	1.46715	1.88670	6	0.282585	19	0.282584	-6.49	0.67
z13	0.0648	52	0.00258	16	1.46718	1.88668	5	0.282522	20	0.282521	-8.73	0.70
z14	0.0424	34	0.00180	11	1.46713	1.88663	18	0.282528	11	0.282527	-8.51	0.38
z15	0.0419	34	0.00170	10	1.46712	1.88670	10	0.282520	14	0.282519	-8.78	0.50
z16	0.0526	42	0.00195	12	1.46711	1.88668	12	0.282539	11	0.282538	-8.13	0.38
z17	0.0426	34	0.00180	11	1.46714	1.88662	19	0.282537	10	0.282536	-8.19	0.35
z18	0.0438	35	0.00172	10	1.46714	1.88668	11	0.282525	13	0.282525	-8.59	0.47
z19	0.0546	44	0.00208	13	1.46714	1.88668	11	0.282549	14	0.282548	-7.78	0.51
Andesite enclave (MLX)												
z1	0.1040	83	0.00338	20	1.467	1.88661	16	0.282526	11	0.282524	-8.62	0.41
z2	0.0448	36	0.00144	9	1.467	1.88665	78	0.282537	8	0.282537	-8.16	0.30
z3	0.0474	38	0.00183	11	1.467	1.88666	31	0.282530	9	0.282530	-8.41	0.31
z4	0.0673	55	0.00247	15	1.467	1.88662	27	0.282555	11	0.282554	-7.56	0.38
z5	0.0606	48	0.00222	13	1.467	1.88669	14	0.282545	11	0.282544	-7.92	0.38
z6	0.0547	44	0.00196	12	1.467	1.88667	26	0.282532	10	0.282531	-8.37	0.34
z7	0.0980	78	0.00330	20	1.467	1.88660	12	0.282539	13	0.282537	-8.13	0.45
z8	0.0522	42	0.00195	12	1.467	1.88663	24	0.282529	13	0.282528	-8.47	0.45
z9	0.0832	67	0.00283	17	1.467	1.88668	8	0.282531	20	0.282530	-8.40	0.71
z10	0.0571	46	0.00216	13	1.467	1.88663	17	0.282529	12	0.282527	-8.49	0.41
JMC475 (n=21)	-	-	-	-	1.46718	1.88666	10	0.282148	5	0.282148	-22.52	0.18

Quoted uncertainties (absolute) relate to the last quoted figure. Accuracy and reproducibilty was checked by repeated analyses (n = 21) of 10 ppb solutions of JMC475.

(a) $^{176}Yb/^{177}Hf = (^{176}Yb/^{173}Yb)$true x $(^{173}Yb/^{177}Hf)$meas x (M173(Yb)/M177(Hf))b(Hf), b(Hf) = $\ln(^{179}Hf/^{177}Hf)$true / $(^{179}Hf/^{177}Hf)_{meas}$ / ln (M179(Hf)/M177(Hf)), M=mass of respective isotope. The $^{176}Lu/^{177}Hf$ were calculated in a similar way by using the $^{175}Lu/^{177}Hf$ and b(Yb).

(b) Mean Hf signal in volt.

(c) Uncertainties are quadratic additions of the within-run precision and the daily reproducibility of the 10ppb-JMC475 solution. Uncertainties for the JMC475 quoted at 2SD (2 standard deviation).

(d) Initial $^{176}Hf/^{177}Hf$ and eHf calculated using the apparent U-Pb age determined by ID-TIMS (see Table A2.1), and the CHUR parameters: $^{176}Lu/^{177}Hf = 0.0336$, and $^{176}Hf/^{177}Hf = 0.282785$ (Bouvier et al., 2008).

tion (typically m/Δm=4000) with a 10% mass window, 100 samples per peak with a dwell time of 10 ms each and 40 replicates per measurement. Instrumental blanks (HF-HNO_3 solution doped with Ir), procedural blanks, calibration standards and samples were introduced into the Aridus desolvation system using a self-aspirating, micro-concentric PFA nebuliser (PFA-ST, Elemental Scientific, Omaha, USA) with a nominal uptake rate of 50 μL min-1 and a typical sample and auxiliary gas flow of 0.9 L min-1 and 0.82 L min-1 respectively. The

Aridus desolvation system provides very low oxide rates using an Ar sweep gas of typically 2.50 L min-1 and a N_2 gas addition of 30 mL min-1. The low oxide rates allow to measure all elements in medium resolution, even the HREE, which suffer under wet sample introduction from oxide interference by the LREE. In order to provide matrix-matched calibration, synthetic zircon solutions were prepared from single element ICP-MS standards. Iridium was used as internal standard for all solutions. Zr, Hf, Y, Sc, Nb, Ta, U, Th, Pb, Ti and REEs were mixed gravimetrically in the approximate proportions expected in natural zircons. The stock solutions (1000 mg/kg) were diluted into nine calibration solutions containing the elements from 5 ng/kg – 900 ng/kg, except for Hf (from 20 ng/g – 180 μg/kg) and Zr (from 50 μg/kg – 10 mg/kg), each calibration standard contained 1 μg/kg Ir. A typical measurement sequence consisted of measurements of the calibration standards, followed by an instrumental and a procedural blank. Subsequently 4 – 12 zircon samples were measured. In-between the samples the system was washed with a HF-HNO3 solution for 7 minutes. After every 4 - 12 zircon samples one of the calibration standards (centre concentration) was re-measured together with a procedural blank. In each measurement session typical 24 zircon samples were analysed and a session lasted for approximately 18 h, followed by a retuning (if necessary) of the instrument and start of a new measurement session.

Zircon Hf isotope analyses: Lutetium-Hafnium isotopes of a subset of U-Pb dated zircons were analyzed employing a Thermo NEPTUNE multi collector–ICP-MS at Goethe-University Frankfurt (Tab. A2.3). Solutions remaining after trace element analyses were introduced into the plasma employing an Aridus desolvation nebulizer with a nominal uptake rate of 100 μl/min. Isotopic ratios were measured in static mode on Faraday detectors equipped with 1010 (for mass 180) or 10^{11} Ω (all other masses) resistors. ^{172}Yb, ^{173}Yb and ^{175}Lu were measured to correct for isobaric interferences of Yb and Lu on mass 176 assuming a ^{176}Yb/^{173}Yb ratio of 0.79502 and a ^{176}Lu/^{175}Lu ratio of 0.02656. Yb and Hf isotopic ratios were corrected for mass fractionation by normalizing to ^{172}Yb/^{173}Yb of 1.35351 and ^{179}Hf/^{177}Hf of 0.7325 using an exponential law. Mass fractionation of Lu was assumed to follow that of Yb (Gerdes and Zeh, 2006). Accuracy and reproducibility of this protocol were assessed by repeat analyses of 10 ppb JMC 475 standard solutions (^{176}Hf/^{177}Hf=0.282148 ± 5, 2SD, n=21) bracketing unknowns. Initial ^{176}Hf/^{177}Hf ratios and εHf were calculated using the ^{206}Pb/^{238}U date of the respective crystal and the CHUR parameters of Bouvier et al. (2008; ^{176}Lu/^{177}Hf=0.0336; ^{176}Hf/^{177}Hf=0.282785). All uncertainties are given at the 2σ level and include the reproducibility of the JMC 475 solution propagated by quadratic addition.

REFERENCES CITED

Annen, C., Blundy, J.D., and Sparks, R.S.J., 2006. The genesis of intermediate and silicic magmas in deep crustal hot zones. J. Petrol., v. 47, p. 505–539, doi:10.1093/petrology/egi084.

Bachmann, O., and Bergantz, G.W., 2003. Rejuvenation of the Fish Canyon magma body: A window into the evolution of large-volume silicic magma systems. Geology, v. 31, p. 789–792, doi:10.1130/G19764.1.

Bachmann, O., Dungan, M.A., and Lipman, P.W., 2002. The Fish Canyon magma body, San Juan Volcanic Field, Colorado: Rejuvenation and eruption of an upper-crustal batholith. J. Petrol., v. 43, p. 1469–1503, doi:10.1093/petrology/43.8.1469.

Bachmann, O., Dungan, M.A., and Bussy, F., 2005. Insights into shallow magmatic processes in large silicic magma bodies: The trace element record in the Fish Canyon magma body, Colorado. Contrib. Mineral. Petrol., v. 149, p. 338–349, doi:10.1007/s00410-005-0653-z.

Bachmann, O., Oberli, F., Dungan, M.A., Meier, M., Mundil, R., and Fischer, H., 2007. $^{40}Ar/^{39}Ar$ and U-Pb dating of the Fish Canyon magmatic system, San Juan volcanic field, Colorado: Evidence for an extended crystallization history. Chem. Geol., v. 236, p. 134–166, doi:10.1016/j.chemgeo.2006.09.005.

Bouvier, A., Vervoort, J.D., and Patchett, P.J., 2008. The Lu-Hf and Sm-Nd isotopic composition of CHUR: Constraints from unequilibrated chondrites and implications for the bulk composition of terrestrial planets. Earth Planet. Sci. Lett., v. 273, p. 48–57.

Bowring, J.F., McLean, N.M., and Bowring, S.A., 2011. Engineering cyber intrastructure for U-Pb geochronology: Tripoli and U-Pb_Redux. Geochem. Geophys. Geosyst., v. 12 (6), doi: 10.1029/2010GC003479.

Burgisser, A., and Bergantz, G.W., 2011. A rapid mechanism to remobilize and homogenize highly crystalline magma bodies. Nature, v. 471, p. 212–215, doi:10.1038/nature09799.

Channell, J.E.T., Hodell, D.A., Singer, B.S., and Xuan, C., 2010. Reconciling astrochronological and $^{40}Ar/^{39}Ar$ ages for the Matuyama-Brunhes boundary and late Matuyama Chron. Geochem. Geophys. Geosyst., v. 11, Q0AA12, doi:10.1029/2010GC003203.

Christensen, J.N., and DePaolo, D.J., 1993. Time scales of large volume silicic magma systems: Sr isotopic systematics of phenocrysts and glass from the Bishop Tuff, Long Valley, California. Contrib. Mineral. Petrol., v. 113, p. 100–114, doi:10.1007/BF00320834.

Claiborne, L.L., Miller, C.F., Flanagan, D.M., Clynne, M.A., and Wooden, J.L., 2010. Zircon reveals protracted magma storage and recycling beneath Mount St. Helens. Geology, v. 38, p. 1011–1014, doi:10.1130/G31285.1.

Gerdes, A. and Zeh, A., 2006. Combined U-Pb and Hf isotope LA-(MC-) ICP-MS analyses of detrital zircons: Comparison with SHRIMP and new constraints for the provenance and age of an Armorican metasediment in Central Germany. Earth Planet. Sci. Lett., v. 249, p. 47–62.

Gerstenberger, H. and Haase, G., 1997. A highly effective emitter substance for mass spectrometric Pb isotope ratio determinations. Chem. Geol., v. 136, p. 309–312.

Halliday, A.N., Mahood, G.A., Holden, P., Metz, J.M., Dempster, T.J., and Davidson, J.P., 1989. Evidence for long residence times of rhyolitic magma in the Long Valley magmatic system: the isotopic record in precaldera lavas of Glass Mountain. Earth Planet. Sci. Lett., v. 94, p. 274–290, doi:10.1016/0012-821X(89)90146-5.

Hildreth, W., and Moorbath, S., 1988. Crustal contribution to arc magmatism in the Andes of central Chile. Contrib. Mineral. Petrol., v. 98, p. 455–489, doi:10.1007/BF00372365.

Huber, C., Bachmann, O., and Dufek, J.,

2011. Thermo-mechanical reactivation of locked crystal mushes: Melting-induced internal fracturing and assimilation processes in magmas. Earth Planet. Sci. Lett., v. 304, p. 443–454, doi:10.1016/j.epsl.2011.02.022.

Jaffey, A.H., Flynn, K.F., Glendenin, L.E., Bentley, W.C., and Essling, A.M., 1971. Precision measurement of half-lives and specific activities of ^{235}U and ^{238}U. Phys. Rev., v. C4 (5), p. 1889–1906.

Klemetti, E.W., Deering, C.D., Cooper, K.M., and Roeske, S.M., 2011. Magmatic perturbations in the Okataina Volcanic Complex, New Zealand at thousand-year timescales recorded in single zircon crystals. Earth Planet. Sci. Lett., v. 305, p. 185–194, doi:10.1016/j.epsl.2011.02.054.

Krogh, T.E., 1973. A low contamination method for hydrothermal decomposition of zircon and extraction of U and Pb for isotopic age determination. Geochim. Cosmochim. Acta, v. 37, p. 485–494.

Kuiper, K.F., Deino, A., Hilgen, F.J., Krijgsman, W., Renne, P.R., and Wijbrans, J.R., 2008. Synchronizing rock clocks of earth history. Science, v. 320, p. 500–504, doi:10.1126/science.1154339.

Lipman, P.W., Doe, B.R., Hedge, C.E., and Steven, T.A., 1978. Petrologic evolution of the San Juan volcanic field, southwestern Colorado: Pb and Sr isotope evidence. GSA Bulletin, v. 89, p. 59–82, doi:10.1130/0016-7606-(1978)89<59:PEOTSJ>2.0.CO;2.

Mahood, G.A., 1990. Evidence for long residence times of rhyolitic magma in the Long Valley magmatic system: The isotopic record in precaldera lavas of Glass Mountain: Second reply. Earth Planet. Sci. Lett., v. 99, p. 395–399, doi:10.1016/0012-821X(90)90145-N.

Mattinson, J.M., 2005. Zircon U-Pb chemical abrasion ("CA-TIMS") method: Combined annealing and multi-step partial dissolution analysis for improved precision and accuracy of zircon ages. Chem. Geol., v. 220, p. 47–66.

McLean, N.M., Bowring, J.F., and Bowring, S.A., 2011. An algorithm for U-Pb isotope dilution data reduction and uncertainty propagation.Geochem.Geophys.Geosyst., v. 12 (6), doi: 10.1029/2010GC003478.

Reid, M.R., 2008. How long does it take to supersize an eruption? Elements, v. 4, p. 23–28, doi:10.2113/GSELEMENTS.4.1.23.

Reid, M.R., and Coath, C.D., 2000. In situ U-Pb ages of zircons from the Bishop Tuff: No evidence for long crystal residence times. Geology, p. 28, v. 443–446, doi:10.1130/0091-7613-(2000)28<443:ISUAOZ>2.0.CO;2.

Renne, P.R., Mundil, R., Balco, G., Min, K., and Ludwig, K.R., 2010. Joint determination of ^{40}K decay constants and $^{40}Ar^*/^{40}K$ for the Fish Canyon sanidine standard, and improved accuracy for $^{40}Ar/^{39}Ar$ geochronology. Geochim. Cosmochim. Acta, p. 74, v. 5349–5367, doi:10.1016/j.gca.2010.06.017.

Renne, P.R., Balco, G., Ludwig, K.R., Mundil, R., and Min, K., 2011. Response to the comment by W.H. Schwarz et al. on "Joint determination of ^{40}K decay constants and $^{40}Ar^*/^{40}K$ for the Fish Canyon sanidine standard, and improved accuracy for $^{40}Ar/^{39}Ar$ geochronology by Renne et al. (2010). Geochim. Cosmochim. Acta, p. 75, v. 5097–5100, doi:10.1016/j.gca.2011.06.021.

Rivera, T.A., Storey, M., Zeeden, C., Hilgen, F.J., and Kuiper, K., 2011. A refined astronomical calibrated $^{40}Ar/^{39}Ar$ age for Fish Canyon sanidine. Earth Planet. Sci. Lett., v. 311, p. 420–426, doi:10.1016/j.epsl.2011.09.017.

Rubatto, D., and Hermann, J., 2007. Experimental zircon/melt and zircon/garnet trace element partitioning and implications for the geochronology of crustal rocks. Chem.

Geol., v. 241, p. 38–61, doi:10.1016/j.chemgeo.2007.01.027.

Schmitz, M.D., and Bowring, S.A., 2001. U-Pb zircon and titanite systematics of the Fish Canyon Tuff: An assessment of high-precision U-Pb geochronology and its application to young volcanic rocks. Geochim. Cosmochim. Acta, v. 65, p. 2571–2587, doi:10.1016/S0016-7037-(01)00616-0.

Schoene, B., Latkoczy, C., Schaltegger, U., and Günther, D., 2010. A new method integrating high-precision U-Pb geochronology with zircon trace element analysis (U-Pb TIMS-TEA). Geochim. Cosmochim. Acta, v. 74, p. 7144–7159, doi:10.1016/j.gca.2010.09.016.

Schoene, B., Schaltegger, U., Brack, P., Latkoczy, C., Stracke, A., and Günther, D., 2012. Rates of magma differentiation and emplacement in a ballooning pluton recorded by U-Pb TIMS-TEA, Adamello batholith, Italy. Earth Planet. Sci. Lett., v. 355–356, p. 162–173, doi:10.1016/j.epsl.2012.08.019.

Vazquez, J.A., and Reid, M.A., 2004. Probing the accumulation history of the voluminous Toba magma. Science, v. 305, p. 991–994, doi:10.1126/science.1096994.

Westerhold, T., Röhl, U., and Laskar, J., 2012. Time-scale controversy: Accurate orbital calibration of the early Paleogene. Geochem. Geophys. Geosyst., v. 13, Q06015, doi:10.1029/2012GC004096.

***

Chapter 3

Reservoir assembly and eruption trigger mechanism at Yellowstone-type supervolcanoes: Isotopic and geochronologic insights from the 4.5 Ma Kilgore Tuff, Heise volcanic field, Idaho

J.F. Wotzlaw, I.N. Bindeman, K.E. Watts, A.K. Schmitt, L. Caricchi, U. Schaltegger

Keywords:
Kilgore Tuff
supereruption
reservoir assembly
zircon
oxygen isotopes
U-Pb geochronology

ABSTRACT

Large-volume caldera forming eruptions of silicic magmatic systems, often referred to as supereruptions, are among the most devastating natural disasters. The most voluminous eruption ever experienced by modern civilizations, the 1815 Tambora eruption, was more than an order of magnitude smaller than the largest-volume eruptions known from the geological record. Perhaps nowhere on Earth are deposits of supereruptions more prominent than in the Snake River Plain-Yellowstone Plateau (SRP-YP) volcanic province. The Heise volcanic field in eastern Idaho contains the youngest complete caldera cycle in the SRP-YP and culminated about 4.5 million years ago in the eruption of the low-$\delta^{18}O$, ~1800 km^3 Kilgore Tuff. Accessory zircons in the Kilgore Tuff display remarkable inter- and intracrystalline oxygen isotopic heterogeneity with a total range of ~8 ‰ in $\delta^{18}O$ suggesting that they crystallized from isotopically distinct and isolated reservoirs that were assembled and homogenized prior to eruption. In striking contrast to the oxygen isotopic heterogeneity, twenty-four of these zircons yielded indistinguishable crystallization ages with a Th-corrected weighted mean $^{206}Pb/^{238}U$ date of 4.4876 ± 0.0023 Ma that is indistinguishable from the eruption age. This requires that shallow magma generation and subsequent assembly of isolated magma batches occured within the resolution of our geochronology and thus is an extremely rapid process. This crystal scale image of the configuration of the pre-eruptive reservoir, with several isolated magma batches, is very similar to

the reservoir configurations imaged seismically beneath active supervolcanoes. The connection of magma batches vertically distributed over several kilometers would cause a substantial increase of buoyancy-related overpressure, providing an eruption trigger mechanism which is the direct consequence of the reservoir assembly process.

3.1 INTRODUCTION

Large-volume caldera forming eruptions are significantly more frequent than other extreme events of similar energy yield such as meteorite impacts (e.g., Mason et al., 2004). The most voluminous of these supereruptions release 100s to 1000s of cubic kilometers of pyroclastic material probably within several days (Hildreth, 1981). Such events cause severe devastation on a regional scale by pyroclastic flows and ash falls and release volcanic gases that affect Earth's radiation budget, atmospheric circulation patterns, cause stratospheric ozone depletion and ultimately global climate perturbations (Rampino and Self, 1992; Self, 2006; Bindeman et al., 2007a; Self and Blake, 2008; Martin and Bindeman, 2009). Understanding the time-scales and mechanisms of assembly and storage of large magma reservoirs that feed supereruptions as well as the mechanisms that ultimately trigger such eruptions is important for interpreting geodetic and seismic signals at active supervolcanoes and assessing the probability of future eruptions (Lowenstern et al., 2006). Seismic tomography of large active systems such as Yellowstone and Toba reveal complex spatial configurations of sub-caldera volcanic storage regions with isolated or connected sub-chambers (Miller and Smith, 1999; Husen et al., 2004; Stankiewicz et al., 2010; Fig. 3.1). If such complex reservoir configurations are common prior to caldera forming eruptions, evidence of chemically or isotopically diverse magma batches might be recorded in the crystal cargo of ancient eruptive products.

Here we take advantage of recent developments in high-precision U-Pb geochronology by isotope dilution thermal ionization mass spectrometry (ID-TIMS) that allow dating of accessory zircon with uncertainties at the permil level. This is one to almost two orders of magnitude more precise than what is achievable with in-situ methods and translates into absolute uncertainties of thousands of years for young volcanic units thus providing insights into the time scales of magma chamber processes preceding eruptions (Crowley et al., 2007; Wotzlaw et al., 2013; Rivera et al., 2013). We combine this technique with high spatial resolution oxygen isotope analyses of the same zircon crystals employing secondary ion mass spectrometry (SIMS) to track the rapid shallow magma segregation and batch assembly processes that led to one of the largest ignimbrite units in the world - the Kilgore Tuff of the Heise volcanic field in eastern Idaho. We further show that the crystal scale record of the pre-eruptive reservoir configuration beneath the Heise volcanic field is

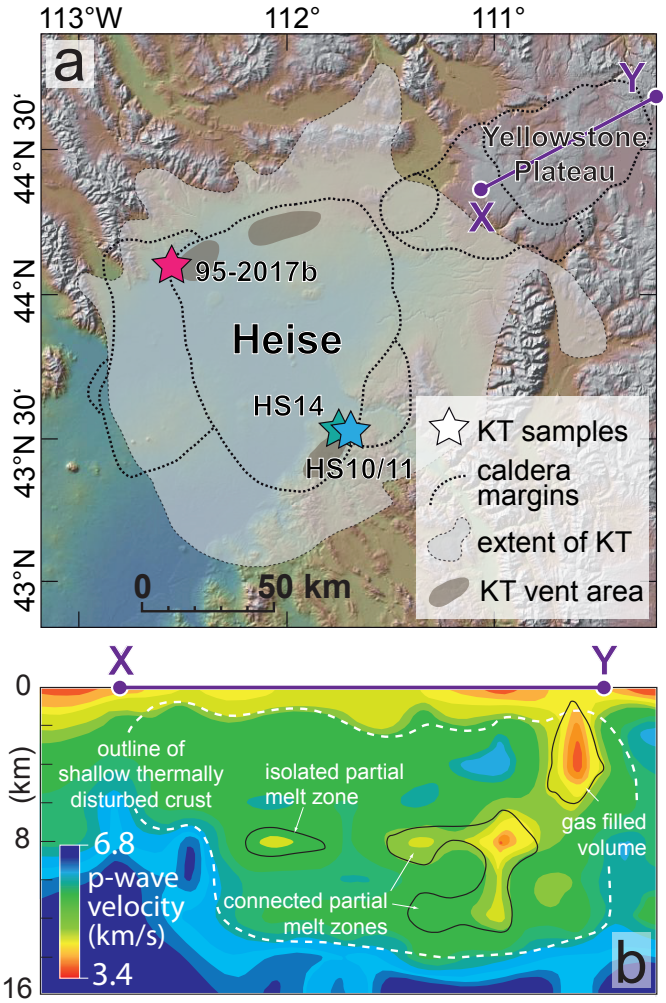

FIGURE 3.1 Caldera map of the Heise and Yellowstone Plateau volcanic fields and subsurface seismic tomography image of the present day Yellostone caldera. (a) Caldera map overlayn over digital elevation model showing the mapped caldera margins of the Heise and Yellowstone Plateau volcanic fields. Also shown are inferred vent areas from which the Kilgore Tuff was erupted and the extent of Kilgore Tuff deposits (after Morgan and McIntosh, 2005) as well as sample localities for samples analyzed in this study. X-Y line referres to the subsurface profile shown in (b). (b) Subsurface seismic tomography image of present day Yellowstone caldera (modified from Miller and Smith, 1999). Color contours refer to p-wave velocities. P-wave velocities outline the shallow thermal anomaly and the presence of pockets of partially molten material below Yellowstone caldera (see text for further discussion).

very similar to reservoirs imaged seismically beneath active supervolcanoes. We further speculate about the mechanim that triggered the Kilgore Tuff eruption and describe a new concept in which the eruption trigger is the direct consequence of the assembly process.

3.2 GEOLOGICAL SETTING AND PREVIOUS MODELS OF SHALLOW MAGMA GENESIS IN THE SNAKE RIVER PLAIN

The Heise volcanic field is a nested caldera complex in the eastern Snake River Plain - Yellowstone Plateau (SRP-YP) volcanic province. The SRP-YP is the manifestation of interaction of plume-derived magmas with the overriding North American continental crust (e.g., Humphreys et al., 2000; Pierce and Morgan, 2009; Schmandt et al., 2012). An important feature of SRP-YP volcanism is the abundance (~10,000 km^3 cumulative volume) of 18-oxygen depleted (i.e., low-$\delta^{18}O$) eruptive products. These ignimbrites and lavas often contain popu-

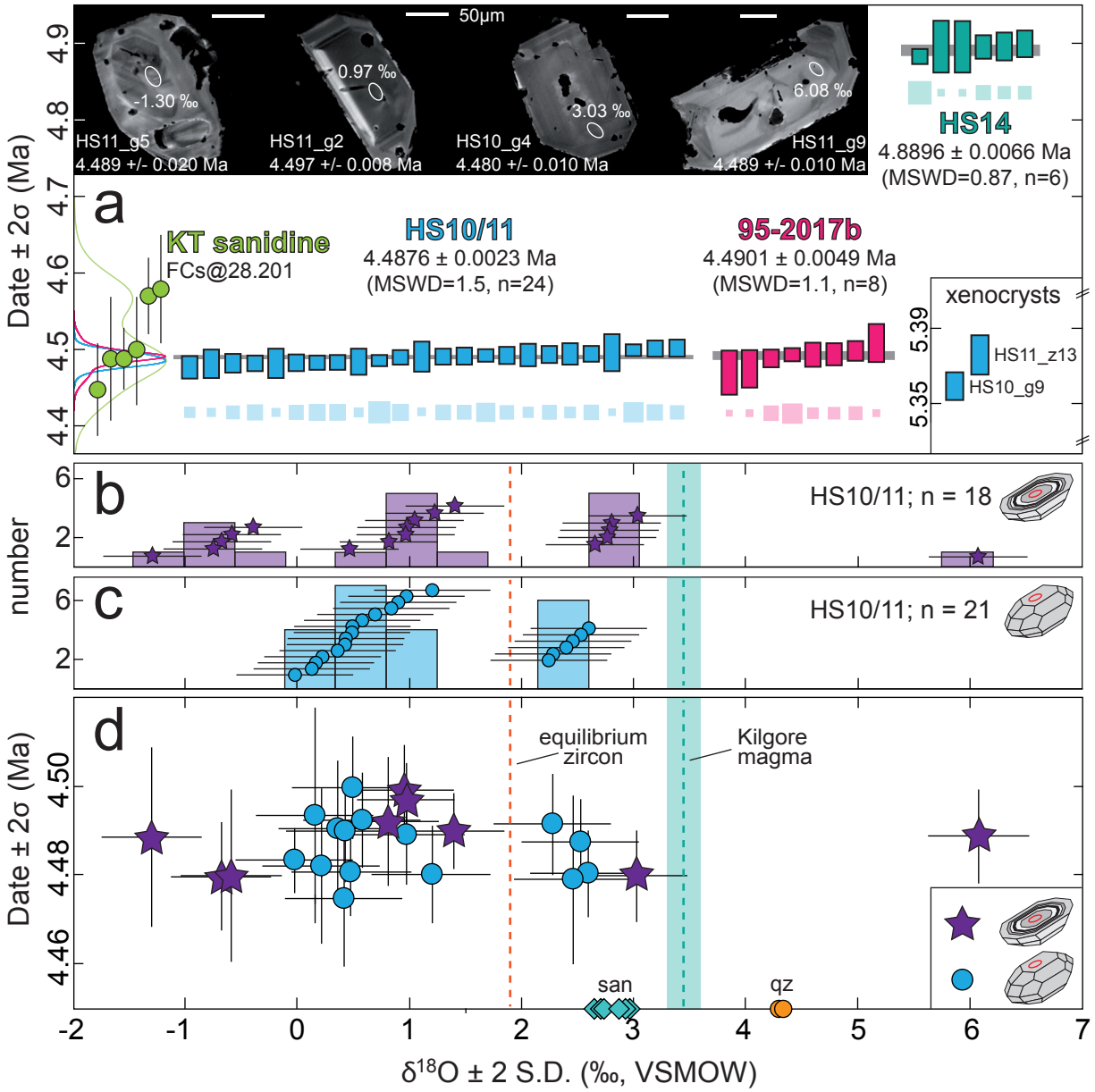

FIGURE 3.2 Oxygen isotope geochemistry and high-precision U-Pb geochronology of Kilgore Tuff zircons. (a) Ranked $^{206}Pb/^{238}U$ zircon dates corrected for initial ^{230}Th disequilibrium. Bars display 2σ analytical uncertainties. Horizontal grey bars display the weighted mean dates and shaded squares below individual dates represent the inverse variance corresponding to the weight each date contributes to the weighted mean date. Also shown are sanidine $^{40}Ar/^{39}Ar$ dates for various Kilgore Tuff samples reported by Morgan and McIntosh (2005) recalculated using the calibration of Kuiper et al. (2008; Fish Canyon sanidine of 28.201 Ma and Min et al. (2000) decay constant). (b-d) Oxygen isotope geochemistry of Kilgore zircons. All values are $\delta^{18}O$ in ‰ relative to Vienna Standard Mean Ocean Water (VSMOW) (b,c) Ion microprobe oxygen isotope ratios for zircon cores (b) and outermost zircon crystal faces (c). (d) Oxygen isotopic composition as a function of $^{206}Pb/^{238}U$ date. Also shown are the oxygen isotopic compositions of Kilgore sanidine and quartz reported by Watts et al. (2011).

lations of accessory zircons with diverse $\delta^{18}O$ values suggesting shallow crustal magma genesis by cannibalization (i.e., remelting) of buried and hydrothermally-altered tuffs from previous eruptive cycles (Bindeman and Valley, 2000; 2001; Bindeman et al., 2007b; 2008; Watts et al., 2011). At the Yellowstone, Heise and Picabo caldera clusters, progressively lower $\delta^{18}O$ values of eruptive products and greater diversity in $\delta^{18}O$ of their zircon populations towards the youngest (and final) rhyolites, suggests that large scale remelting of buried material becomes progressively more important toward the end of caldera cluster evolution (Bindeman et al., 2008; Watts et al., 2011; Drew et al., 2013). Numerical models suggest that the time scales for shallow crustal remelting, batch assembly, magma mixing and homogenisation are relatively short for high-temperature rhyolites in nested caldera and rift environments (Simakin and Bindeman, 2012).

The Kilgore Tuff, the fourth, final and most voluminous in the sequence of the Heise volcanic field may be an analogue for current and future processes at Yellowstone (e.g., Watts et al., 2011; 2012). The young age (~4.5 Ma) of the Kilgore Tuff and its isotopically diverse zircon population (Watts et al., 2011) provide an ideal opportunity to quantify the time scales of the batch assembly and homogenisation of shallow magma reservoirs prior to eruption employing precise geochronological methods (Fig. 3.2 and 3.3).

3.3 OXYGEN ISOTOPIC HETEROGENEITY OF ZIRCONS: RECORDERS OF PROGRESSIVE AMALGAMATION OF MAGMA BATCHES

Interior domains of zircon crystals analyzed by SIMS are remarkably diverse with respect to their oxygen isotopic composition (Fig. 3.2; Tab. A3.1). Individual spot analyses range in $\delta^{18}O_{VSMOW}$ from -1.30 to +6.07 ‰ and can be grouped in four distinct populations (Fig. 3.2b) suggesting that zircon cores crystallized from various ($n \geq 4$) isolated and isotopically distinct magma batches. Analyses of outermost zircon crystal faces yielded less isotopic diversity ($\delta^{18}O$ = -0.02 to +2.60 ‰; Fig. 3.2c), with two distinct populations, recording progressive blending of magmas from distinct batches and the presence of two isolated sub-reservoirs at the time of crystallization of zircon rims.

Notably, none of the analyzed zircon interior domains or even the outermost zircon rims is in high-temperature oxygen isotopic equilibrium with sanidine and quartz phenocrysts that reflect the isotopic composition of the erupted magma ($\delta^{18}O_{magma}$ = +3.5 ‰; Fig. 3.2). High-temperature equilibrium of sanidine and quartz phenocrysts sampled from various locations, as well as whole rock homogeneity with respect to Sr and Nd isotopes (Watts et al., 2011) suggest large-scale convective homogenization of the batch-assembled Kilgore magma body prior to eruption. The fact that outermost zircon rims are not in equilibrium with the erupted magma indicates that the homogenized magma present before eruption was undersaturated with respect to zircon and zircons were dissolving and/or the time between final assembly and

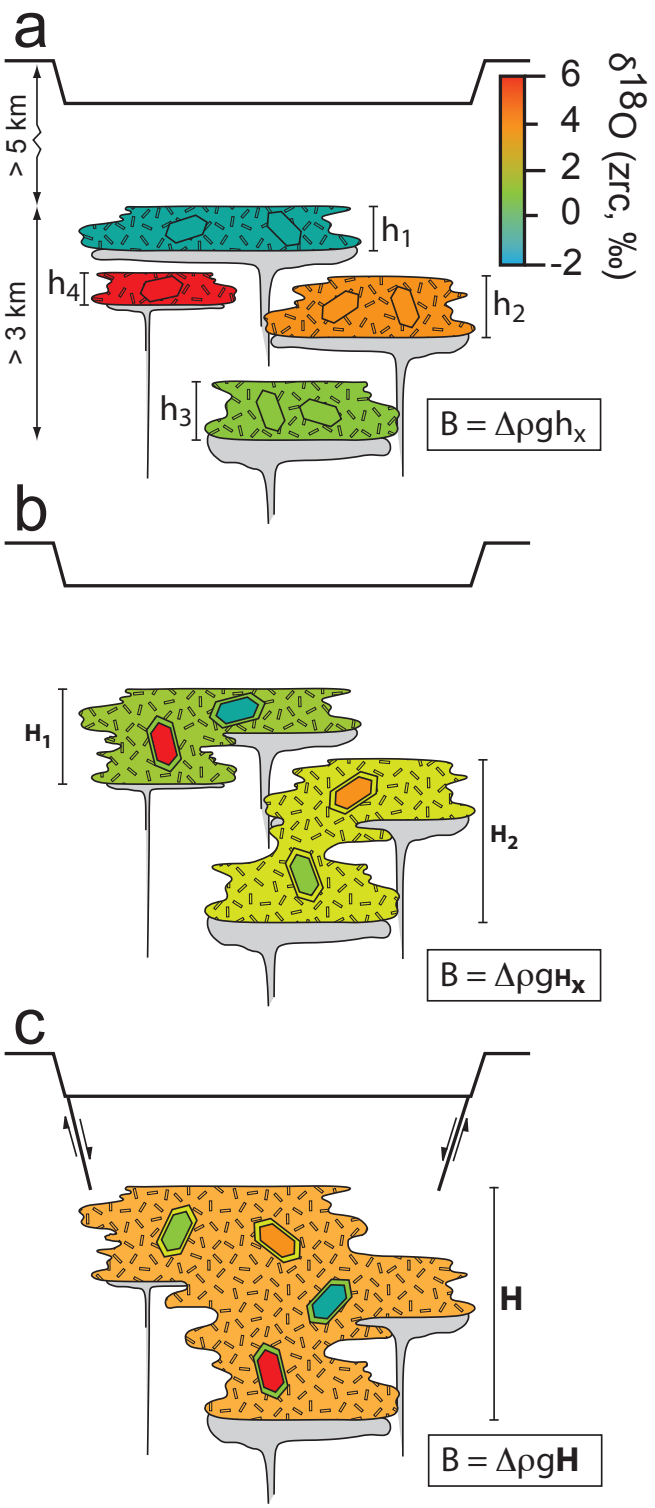

FIGURE 3.3 Conceptual cartoon illustrating the assembly process leading to accumulation of the Kilgore Tuff magma reservoir. Progressive amalgamation of isotopically distinct magma batches is recorded by isotopically diverse but age equivalent accessory zircon crystals. (a) Isolated, isotopically distinct magma batches are generated by remelting of intracaldera rocks that exchanged oxygen with meteoric water during hydrotheral alteration. Four magma batches are shown corresponding to the four zircon core populations with distinct oxygen isotopic composition. (b) Amalgamtion of isotopically distinct magma batches is inferred by the observation that zircon rims cluster in two distict populations with respect to their oxygen isotopic composition. (c) Progressive amalgamation and homogenisation of the magma reservoir prior to eruption. Sanidine and quartz are in isotopic equilibrium with the erupted magma (Watts et al., 2011) and the Kilgore Tuff is homogeneous on a caldera-wide scale requiring homogenisation prior to eruption. The color of individual magma batches referres to the zircon oxygen isotopic composition. Illustrated is also how the increase in thickness of the assembled magma batches (h, **H**, **H**) lead to an increase in buoyancy (B).

eruption was too short to isotopically equilibrate zircon rims diffusively. The lack of isotopic equilibration provides mineral diffusive time scales for the time interval between assembly and eruption on the order of 100s to 1000s of years (see model calculations of Bindeman and Valley, 2001; Bindeman et al., 2006; Bindeman, 2008).

3.4 ZIRCON U-PB GEOCHRONOLOGY AND THE DURATION OF RESERVOIR ASSEMBLY

To place additional constraints on the time-scales over which the shal-

low crustal reservoir was assembled, we dated zircons with diverse oxygen isotopic compositions employing high-precision chemical abrasion ID-TIMS techniques (see *supplementary methods*; Tab. A3.1). Twenty-four analyses of zircons previously analyzed by SIMS for oxygen isotopes, yielded indistinguishable initial ^{238}U-^{230}Th disequilibrium corrected $^{206}Pb/^{238}U$ dates, with a weighted mean of 4.4876 ± 0.0023 Ma (HS10/11; MSWD=1.5; Fig. 3.2a and 3.2d). Additional U-Pb analyses of zircons from a sample collected 80 km north-west (sample 95-2017b; Fig. 3.1) yielded an indistinguishable weighted mean of 4.4901 ± 0.0049 Ma (n=8; MSWD=1.1; Fig. 3.2).

Age-equivalent but isotopically diverse zircons suggest that the generation and subsequent progressive amalgamation, mixing and homogenization of isotopically distinct magma batches occured within the resolution of our geochronology (Fig. 3.3). During different stages of reservoir assembly several isotopically distinct sub-chambers co-existed in the sub-caldera storage region (Fig. 3.3), resulting in a pre-eruption Kilgore magma reservoir configuration that resembles the reservoir configuration imaged seismically beneath Yellowstone and Toba (Fig. 3.1 and 3.3; Miller and Smith, 1999; Stankiewicz et al., 2010).

All individual zircon $^{206}Pb/^{238}U$ dates overlap within their uncertainties with the mean sanidine $^{40}Ar/^{39}Ar$ date reported by Morgan and McIntosh (2005; recalculated using the Kuiper et al., 2008, calibration of the Fish Canyon Tuff sanidine standard). If this $^{40}Ar/^{39}Ar$ date (4.51 ± 0.05 Ma) is taken as the eruption age of the Kilgore Tuff, then isotopically diverse zircons crystallized shortly before eruption. This is remarkably consistent with mineral diffusive time-scales derived from oxygen isotopic heterogeneities in zircon (Bindeman and Valley, 2001; Bindeman et al., 2006; Bindeman, 2008).

The presence of two xenocrystic zircons with crystallization ages corresponding to one of the previous caldera forming eruptions that produced the Conant Creek Tuff, is additional evidence that magma generation was governed by remelting of intra-caldera rocks associated with previous eruptions. This is also consistent with the homogeneity of zircons with respect to their hafnium (Hf) isotopic composition compared to their significant oxygen isotopic heterogeneities (Fig. 3.4; Tab. A3.2). The homogeneous mixture of crustal and mantle derived Hf in Kilgore zircons is likely due to long-term hybridization and homogenization of the sub-caldera crust throughout the Heise caldera cycle. Meteoric-hydrothermal alteration of the sub-caldera crust creates oxygen isotopic heterogeneities but does not affect Hf.

3.5 BATCH ASSEMBLY AS A MECHANISM TO TRIGGER SUPERERUPTIONS

Our results suggest that the eruption occurred relatively soon after the connection and chemical blending of the magmas from different sub-reservoirs. It is unlikely that this is a coincidence and it is more probable that the merging of different reservoirs cause the system to evolve to a critical state that eventually culminated in the Kilgore Tuff eruption.

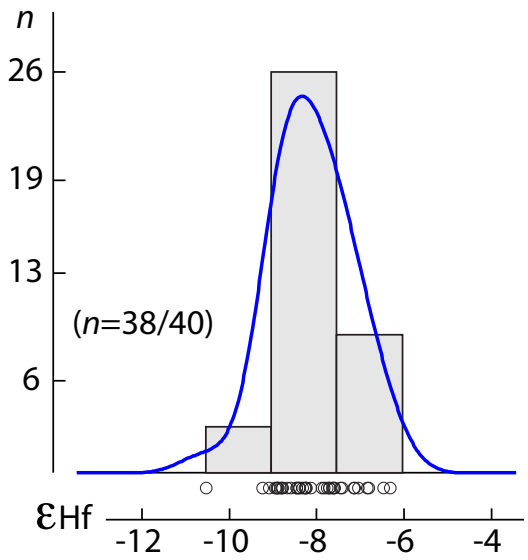

FIGURE 3.4 Histogram and Kernel density estimate (blue curve) of Hf isotopic compositions of U-Pb dated Kilgore zircons (Vermeesch, 2012). Individual data points are shown along the x-axis. Kilgore Tuff (samples HS10/11 and 95-2017b) and pre-Kilgore Tuff (HS14) zircon Hf data were combinded (see Tab. A3.2). Two zircons yielded significantly more negative εHf values (-13.4 and -17.3) and are not shown. Note that Kilgore zircons are significantly more homogeneous with respect to their Hf isotopic compositions compared to their oxygen isotopic compositions. See text for discussion.

Geophysical measurements of the Yellowstone and Toba magmatic system show that several, laterally extended, reservoirs, containing potentially eruptible magma, are present over a vertical distance of few kilometers (Miller and Smith, 1999; Husen et al., 2004; Stankiewicz et al., 2010; Fig. 3.1b). Magma in such reservoirs is less dense than the surrounding solid rock and it is therefore buoyant. Buoyancy (B) is a function of the vertical thickness of these magma chambers and is equal to $\Delta\rho gh$, where $\Delta\rho$ is the average difference in density between magma and the rocks around the reservoir, g is gravity and h is the thickness of the buoyant magma in each reservoir (Fig. 3.3). As long as the reservoirs are separated, their overpressure are essentially equal to the their respective buoyancy. To generate sufficient overpressure to trigger eruption in reservoirs that are comparable in size to the one that fed the Kilgore Tuff, extremely high magma injection rates are required if the surrounding crust is relatively hot and thus has a low viscosity (Jellinek and DePaolo, 2003; Rubin, 1995). However, if isolated reservoirs connect over a vertical distance H, the overpressure in the connected magmatic system increases rapidly to $\Delta\rho gH$ (Fig. 3.3). In the simplified assumption of two identical reservoirs arranged vertically (Fig. 3.3), their merging would rapidly double the overpressure potentially being sufficient to trigger an eruption.

The process of sub-reservoir amalgamation and thus the eruption trigger mechanism that we propose on the basis of the isotopic data could be monitored at active supervolcanoes using geophysical methods.

3.6 SUMMARY & CONCLUSIONS

Isotopically heterogeneous but age-equivalent zircons in the Kilgore Tuff suggest that the magma reservoir that fed

the eruption was assembled by progressive amalgamation, mixing and homogenization of isotopically distinct magma batches. Prior to eruption, several isolated batches were present in the subcaldera storage region. This pre-eruption reservoir configuration inferred for the Kilgore Tuff is very similar to reservoirs imaged seismically beneath active supervolcanoes. The short time scale between crystallization of isotopically diverse zircons, recording the co-existence of distinct magma batches and eruption suggests that such reservoir configurations are not indicative for repose episodes but may exist until shortly before eruption. The assembly process itself may in fact trigger the eruption, if the different magma batches are distributed over several kilometers vertical distance.

APPENDIX

SUPPLEMENTARY METHODS

Zircons were extracted using standard mineral separation techniques. For oxygen isotope analyses, one subset of zircons was mounted in epoxy resin and crystals were polished to expose crystal interior domains (see Watts et al., 2011; Fig. A-3.1). A second subset of zircons was pressed in indium metal to analyze outermost crystal faces. All oxygen isotope analyses were performed employing a CAMECA ims 1270 secondary ion mass spectrometer at the Department of Earth and Space Sciences of the University of California, Los Angeles (UCLA). Instrumental calibration and analytical methods were identical to those of Bindeman et al. (2010). Uncertainties were estimated from the reproducibility of repeat analyses of standard zircons AS3 and KIM measured during the respective analytical session. After SIMS analyses, selected individual zircon crystals were extracted from the grain mounts for high-precision U-Pb geochronology by isotope dilution thermal ionization mass spectrometry U-Pb geochronology. All ID-TIMS analyses were performed at the Radiogenic Isotope Laboratory of the Department of Earth Sciences, University of Geneva. Chemical and analytical procedures follow established and well documented protocols (Schoene et al., 2010a; 2010b; 2012; Wotzlaw et al., 2012; 2013). All $^{206}Pb/^{238}U$ dates were corrected for initial ^{238}U-^{230}Th disequilibrium using the whole rock Th/U reported by Watts et al. (2011; average 4.06 ± 0.74, 2 S.D.) as a proxy for the melt in equlibrium with zircon during crystallization. This appears reasonable in case of the crystal-poor (~5% crystals) Kilgore Tuff that has near liquidus zircon saturation temperatures (~850°C).

Hf isotope analyses of U-Pb dated crystals were partly performed at the University of Frankfurt and partly at the University of Geneva following protocols outlined in Wotzlaw et al. (2012; 2013) and Chelle-Michou et al. (submitted).

Oxygen and U-Pb isotopic data are given in Tab. A3.1 and Hf isotopic data are given in Tab. A3.2. All uncertainties are given at the 2σ level of confidence unless otherwise indicated.

REFERENCES CITED

Bindeman, I.N., and Valley, J.W., 2000. The

formation of low-$\delta^{18}O$ rhyolites after caldera collapse at Yellowstone. Geology, v. 28, p. 719–722.

Bindeman, I.N., and Valley, J.W., 2001. Low-low-$\delta^{18}O$ rhyolites from Yellowstone: Magmatic evolution based on analyses of zircon and individual phenocrysts. J. Petrol., v. 42, p. 1491–1517.

Bindeman, I.N., Schmitt, A.K., and Valley, J.W., 2006. U-Pb zircon geochronology of silicic tuffs from the Timber Mt/Oasis Valley caldera complex, Nevada: rapid generation of large-volume magmas by shallow-level remelting. Contrib. Mineral. Petrol., v. 152, p. 649–665.

Bindeman, I.N., Eiler, J.M., Wing, B., and Farquhar, J., 2007a. Rare sulfur and triple oxygen isotope geochemistry of volcanogenic sulfate aerosols. Geochim. Cosmochim. Acta, v. 71, p. 2326–2343.

Bindeman, I.N., Watts, K.E., Schmitt, A.K., Morgan, L.A., and Shanks, P.W.C., 2007b. Voluminous low-$\delta^{18}O$ magmas in the late Miocene Heise volcanic field, Idaho: Implications for the fate of Yellowstone hotspot calderas. Geology, v. 35, p. 1019–1022.

Bindeman, I.N., Fu, B., Kita, N., and Valley, J.W., 2008. Origin and evolution of Yellowstone silicic magmatism based on ion microprobe analysis of isotopically-zoned zircons. J. Petrol., v. 49, p. 163–193.

Bindeman, I.N., 2008. Oxygen isotopes in mantle and crustal magmas as revealed by single crystal analysis. Rev. Mineral. Geochem., v. 69, p. 445–478.

Bindeman, I.N., Schmitt, A.K., and Evans, D.A.D., 2010. Limits of hydrosphere-lithosphere interaction: origin of the lowest $\delta^{18}O$ silicate rock on Earth in the Paleoproterozoic Karelian rift. Geology, v. 38, p. 631–634.

Chelle-Michou, C., Chiaradia, M., Ovtcharova, M., Ulyanov, A., and Wotzlaw, J.W., Zircon reveals the temporal link between porphyry systems and the magmatic evolution of their plutonic roots (The Eocene Coroccohuayco deposit, Peru). *Submitted to Lithos*.

Crowley, J.L., Schoene, B., and Bowring, S.A., 2007. U-Pb dating of zircon in the Bishop Tuff at the millennial scale. Geology, v. 35, p. 1123–1126.

Drew, D.L., Bindeman, I.N., Watts, K., Schmitt, A.K., Fu, B., and McCurry, M., 2013. Crustal scale recycling in caldera complexes and rift zones of the Snake River Plain: O and Hf isotopic evidence in diverse zircons from low-$\delta^{18}O$ rhyolites of the Picabo volcanic field, Idaho. Earth Planet. Sci. Lett. (in press).

Hildreth, W., 1981. Gradients in silicic magma chambers: Implications for lithospheric magmatism. J. Geophys. Res., v. 86, p. 10153–10192.

Humphreys, E., Dueker, K., Schutt, D., and Smith R., 2000. Beneath Yellowstone: Evaluating plume and nonplume models using teleseismic images of the upper mantle. GSA Today, v. 10, p. 1–7.

Husen, S., Smith, R.B., and Waite, G.P., 2004. Evidence for gas and magmatic sources beneath the Yellowstone volcanic field from seismic tomography imaging. J. Volcanol. Geotherm. Res., v. 131, p. 397–410.

Jaffey, A.H., Flynn, K.F., Glendenin, L.E., Bentley, W.C., and Essling, A.M., 1971. Precision measurement of half-lives and specific activities of ^{235}U and ^{238}U. Phys. Rev., v. C4 (5), p. 1889–1906.

Jellinek, A.M., and DePaolo, D.J., 2003. A model for the origin of large silicic magma chambers: precursors of caldera-forming eruptions. Bull. Volcanol., v. 65, p. 363–381.

Kuiper, K.F., Deino, A., Hilgen, F.J., Krijgsman, W., Renne, P.R., and Wijbrans, J.R., 2008. Synchronizing Rock Clocks of Earth History. Science, v. 320, p. 500–504.

Table A3.1 *Oxygen and U-Pb isotopic data for Kilgore Tuff zircons*

	Oxygen isotopes			Composition				Isotopic Ratios							Dates (Ma)		Th-corrected	
	$\delta^{18}O$	1 S.D.	core/rim	Th/	Pb*	Pb_c	Pb*/	$^{206}Pb/$	$^{206}Pb/$	±2σ	$^{207}Pb/$	±2σ	$^{207}Pb/$	±2σ	$^{206}Pb/$	±2σ	$^{206}Pb/$	±2σ
	(‰)	abs		U	(pg)	(pg)	Pb_c	^{204}Pb	^{238}U	%	^{235}U	%	^{206}Pb	%	^{238}U	abs	^{238}U	abs
Fraction	(*)	(†)	(‡)	(a)	(b)	(c)	(d)	(e)	(f)		(f)		(f)		(g)		(h)	
HS10/11																		
HS11_z10	0.42	0.26	r	0.70	0.66	0.65	1.00	76	0.00068028	0.35	0.004742	8.7	0.05058	8.4	4.384	0.015	4.475	0.015
HS11_z6	2.46	0.26	r	0.74	0.48	0.59	0.81	64	0.00068114	0.44	0.004749	10.9	0.05059	10.5	4.389	0.019	4.479	0.019
HS10_g7	-0.68	0.22	c	0.72	0.76	0.54	1.40	98	0.00068118	0.27	0.004561	6.7	0.04859	6.4	4.390	0.012	4.480	0.012
HS10_g4	3.03	0.22	c	0.63	0.88	0.57	1.56	108	0.00068082	0.23	0.004640	5.7	0.04945	5.5	4.387	0.010	4.480	0.010
HS10_g5	-0.59	0.22	c	0.67	0.67	0.68	0.99	75	0.00068099	0.45	0.004797	9.4	0.05111	9.1	4.388	0.020	4.480	0.019
HS11_z12	1.20	0.26	r	0.64	0.80	0.54	1.47	104	0.00068090	0.25	0.004707	5.9	0.05016	5.7	4.388	0.011	4.480	0.011
HS11_z22	2.60	0.26	r	0.64	0.90	0.49	1.83	125	0.00068094	0.21	0.004478	5.0	0.04771	4.8	4.388	0.009	4.480	0.010
HS11_z2	0.48	0.26	r	0.70	0.74	0.35	2.13	140	0.00068126	0.21	0.004466	4.7	0.04756	4.5	4.390	0.009	4.481	0.010
HS11_z11	0.22	0.26	r	0.69	0.44	0.49	0.90	70	0.00068141	0.40	0.004603	10.0	0.04902	9.7	4.391	0.018	4.482	0.017
HS11_z1	-0.02	0.26	r	0.70	1.60	0.48	3.32	209	0.00068164	0.15	0.004379	3.0	0.04662	2.9	4.393	0.007	4.483	0.007
HS11_z18	2.53	0.26	r	0.67	0.82	0.40	2.04	136	0.00068218	0.21	0.004529	4.7	0.04817	4.6	4.396	0.009	4.487	0.010
HS11_g5	-1.30	0.22	c	0.63	0.28	0.38	0.73	62	0.00068219	0.46	0.004769	6.9	0.05073	6.5	4.396	0.020	4.489	0.020
HS11_g9	6.08	0.22	c	0.75	0.94	0.36	2.65	168	0.00068268	0.23	0.004599	4.1	0.04888	3.9	4.399	0.010	4.489	0.010
HS11_z7	0.97	0.26	r	0.73	0.80	0.52	1.54	106	0.00068267	0.25	0.004722	5.9	0.05019	5.6	4.399	0.011	4.489	0.011
HS11_g10	1.40	0.22	c	0.70	0.73	0.31	2.35	155	0.00068266	0.18	0.004493	2.6	0.04776	2.4	4.399	0.008	4.490	0.008
HS11_z3	0.43	0.26	r	0.65	0.75	0.51	1.46	103	0.00068249	0.26	0.004719	6.1	0.05017	5.8	4.398	0.011	4.490	0.011
HS11_z16	0.36	0.26	r	0.70	0.42	0.35	1.19	86	0.00068273	0.35	0.004258	8.6	0.04525	8.3	4.400	0.015	4.490	0.015
HS11_z8	2.28	0.26	r	0.65	0.97	0.66	1.46	103	0.00068269	0.25	0.004765	6.0	0.05064	5.8	4.399	0.011	4.491	0.011
HS11_g6	0.81	0.22	c	0.72	0.48	0.34	1.41	100	0.00068309	0.32	0.004482	4.9	0.04761	4.7	4.402	0.014	4.492	0.014
HS11_z9	0.58	0.26	r	0.70	0.78	0.43	1.81	122	0.00068304	0.23	0.004708	5.0	0.05001	4.8	4.402	0.010	4.492	0.011
HS11_z5	0.16	0.26	r	0.65	0.42	0.67	0.62	54	0.00068301	0.56	0.004862	13.6	0.05165	13.1	4.401	0.025	4.493	0.024
HS10_g2	0.97	0.22	c	0.66	0.95	0.34	2.80	180	0.00068359	0.17	0.004568	3.6	0.04849	3.5	4.405	0.008	4.497	0.008
HS11_g7	0.96	0.22	c	0.71	0.52	0.31	1.66	115	0.00068418	0.22	0.004690	3.7	0.04974	3.5	4.409	0.010	4.499	0.010
HS11_z21	0.49	0.26	r	0.70	0.59	0.34	1.76	119	0.00068418	0.26	0.004656	5.4	0.04938	5.2	4.409	0.011	4.500	0.011
HS10_g9	1.22	0.22	c	0.67	1.82	0.43	4.27	268	0.00081751	0.13	0.005436	1.7	0.04825	1.6	5.268	0.007	5.359	0.007
HS11_z13	0.13	0.26	r	0.56	1.08	0.52	2.07	141	0.00081959	0.19	0.005464	4.4	0.04838	4.2	5.281	0.010	5.376	0.010
95-2017b																		
95-2017b_z5	-	-		0.73	0.49	0.82	0.60	52	0.00067940	0.68	0.005004	14.4	0.05344	13.8	4.378	0.030	4.468	0.029

(Table A3.1 continued)

95-2017b_z7	-	-	0.71	0.49	0.70	0.70	58	0.00068003	0.58	0.004896	13.1	0.05224	12.6	4.382	0.025	4.473	0.025
95-2017b_z11	-	-	0.75	0.70	0.35	2.00	131	0.00068230	0.26	0.004477	5.4	0.04761	5.2	4.397	0.011	4.486	0.012
95-2017b_z1	-	-	0.65	0.98	0.32	3.09	197	0.00068265	0.19	0.004533	3.5	0.04819	3.3	4.399	0.008	4.491	0.009
95-2017b_z3	-	-	0.70	0.41	0.33	1.25	90	0.00068286	0.36	0.004728	7.6	0.05024	7.3	4.400	0.016	4.491	0.016
95-2017b_z8	-	-	0.70	0.48	0.35	1.38	97	0.00068294	0.33	0.004640	7.1	0.04930	6.9	4.401	0.014	4.492	0.014
95-2017b_z10	-	-	0.71	0.58	0.41	1.42	99	0.00068366	0.29	0.004736	6.7	0.05026	6.4	4.406	0.013	4.496	0.013
95-2017b_z6	-	-	0.68	0.27	0.35	0.78	63	0.00068522	0.58	0.004652	12.8	0.04926	12.3	4.416	0.025	4.507	0.025
HS14																	
HS14_z2	-	-	0.89	0.64	0.26	2.46	153	0.00074439	0.19	0.004955	4.2	0.04830	4.0	4.797	0.009	4.882	0.010
HS14_z3	-	-	0.55	0.30	0.62	0.49	47	0.00074485	0.74	0.005484	16.9	0.05342	16.2	4.800	0.035	4.894	0.034
HS14_z5	-	-	0.60	0.21	0.37	0.57	51	0.00074510	0.71	0.004813	17.9	0.04687	17.3	4.801	0.034	4.895	0.033
HS14_z8	-	-	0.59	0.67	0.62	1.09	83	0.00074507	0.32	0.005101	4.8	0.04968	4.5	4.801	0.016	4.895	0.015
HS14_z6	-	-	0.59	0.79	0.63	1.27	93	0.00074511	0.38	0.005171	7.8	0.05036	7.4	4.801	0.018	4.895	0.018
HS14_z4	-	-	0.63	0.60	0.57	1.05	80	0.00074588	0.37	0.005105	8.6	0.04966	8.3	4.806	0.018	4.899	0.017

(*) Analyzed by ion microprobe prior to ID-TIMS analysis. Reported relative to Vienna Standard Mean Ocean Water (VSMOW).
(†) Uncertainty based on reproducibility of zircon standards AS3 and KIM analyzed during the respective analytical session.
(‡) *Rims* refers to analyses performed on outermost faces of crystals pressed in indium metal. *Cores* refers to analyses performed on interior domains of crystals mounted in epoxy resin.
a Th contents calculated from radiogenic 208Pb and the $^{207}Pb/^{206}Pb$ date of the sample, assuming concordance between U-Th and Pb systems.
b Total mass of radiogenic Pb.
c Total mass of common Pb.
d Ratio of radiogenic Pb (including ^{208}Pb) to common Pb.
e Measured ratio corrected for fractionation and spike contribution only.
f Measured ratios corrected for fractionation, tracer and blank.
g Isotopic dates calculated using the decay constants $\lambda_{238} = 1.55125E^{-10}$ and $\lambda_{235} = 9.8485E^{-10}$ (Jaffey et al., 1971).
h Corrected for initial Th/U disequilibrium using radiogenic ^{208}Pb and $Th/U_{[magma]} = 4.06 \pm 0.74$ (2 S.D.; whole rock Th/U of Watts et al., 2011).

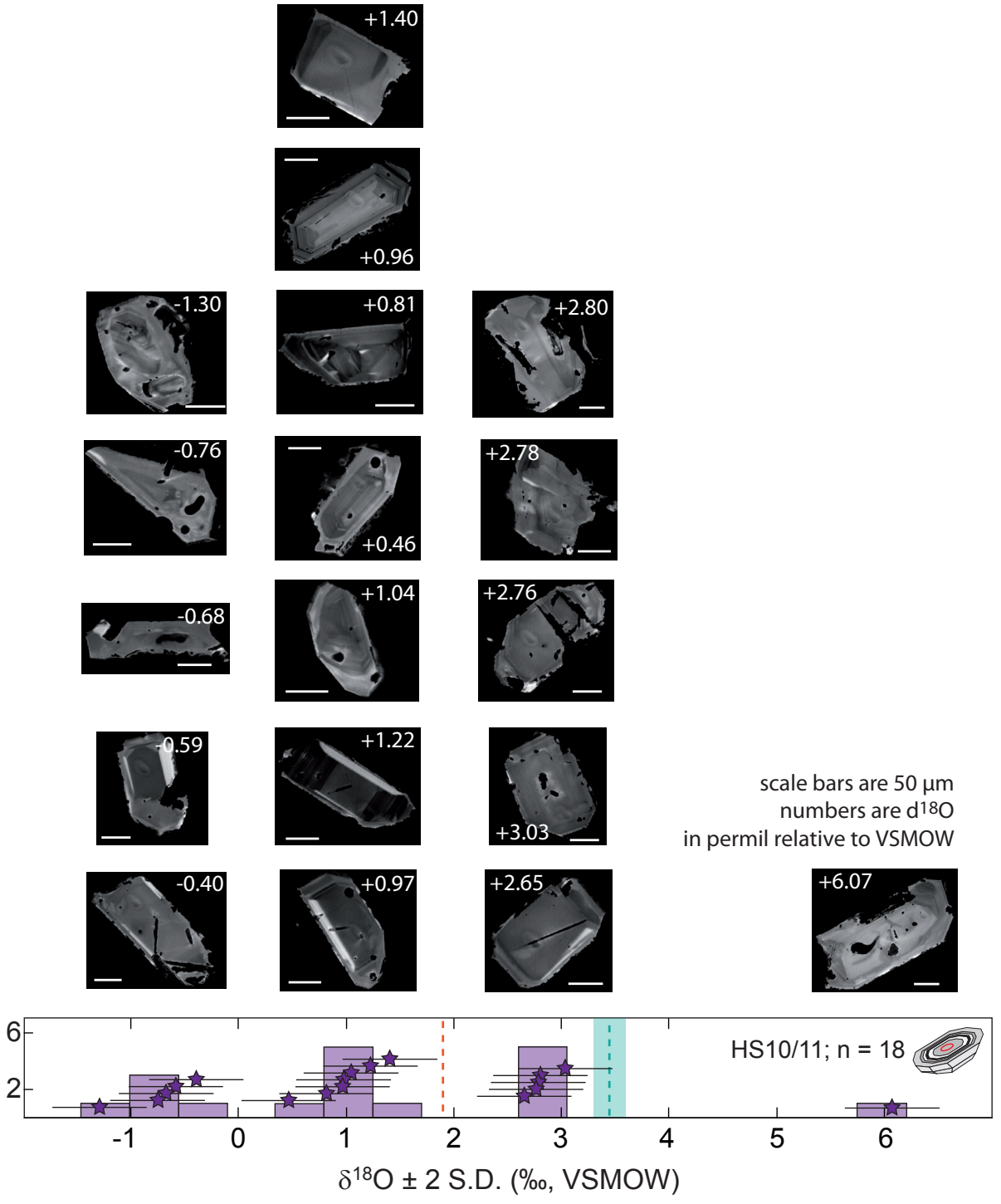

FIGURE A-3.1 Cathodoluminescence textures of Kilgore zircons. Zircons are grouped according to their oxygen isotopic composition. Most zircons show planar to weak oscillatory textures with superimposed sector zoning in some crystals. Note that there is no obvious relationship between CL texture and $\delta^{18}O$.

Table A3.2 *Lutetium-Hafnium isotopic data for Kilgore Tuff zircons*

	$^{176}Yb/^{177}Hf$ (a)	±2σ	$^{176}Lu/^{177}Hf$ (a)	±2σ	$^{178}Hf/^{177}Hf$	$^{180}Hf/^{177}Hf$	SigHf [V] (b)	$^{176}Hf/^{177}Hf$	±2σ (c)	$^{176}Hf/^{177}Hf_t$ (d)	εHf_t (d)	±2σ (c)
HS10/11												
HS11_z10	0.0352	28	0.00097	6	1.46718	1.88662	50	0.282537	27	0.282537	-8.7	0.2
HS11_z6	0.0350	28	0.00095	6	1.46717	1.88655	40	0.282530	6	0.282530	-8.9	0.2
HS10_g7	0.0342	27	0.00081	5	1.46725	1.88688	11	0.282571	12	0.282571	-7.5	0.4
HS10_g4	0.0364	29	0.00086	5	1.46724	1.88684	11	0.282549	11	0.282549	-8.3	0.4
HS10_g5	0.0415	33	0.00093	6	1.46726	1.88688	18	0.282484	11	0.282484	-10.5	0.4
HS11_z12	0.0329	26	0.00075	4	1.46728	1.88694	41	0.282521	9	0.282521	-9.2	0.3
HS11_z22	0.0319	26	0.00078	5	1.46725	1.88686	9	0.282539	12	0.282539	-8.6	0.4
HS11_z2	0.0417	33	0.00115	7	1.46718	1.88664	37	0.282529	7	0.282529	-8.9	0.2
HS11_z11	0.0404	32	0.00104	6	1.46728	1.88689	10	0.282573	12	0.282572	-7.4	0.4
HS11_z1	0.0431	34	0.00118	7	1.46717	1.88662	53	0.282525	7	0.282525	-9.1	0.2
HS11_z18	0.0370	30	0.00087	5	1.46724	1.88683	11	0.282561	13	0.282561	-7.8	0.5
HS11_g5	0.0345	28	0.00082	5	1.46723	1.88679	10	0.282552	12	0.282552	-8.1	0.4
HS11_g9	0.0323	26	0.00078	5	1.46727	1.88690	26	0.282292	10	0.282292	-17.3	0.3
HS11_z7	0.0420	34	0.00117	7	1.46717	1.88660	38	0.282533	12	0.282533	-8.8	0.2
HS11_g10	0.0341	27	0.00078	5	1.46725	1.88691	20	0.282532	10	0.282532	-8.8	0.4
HS11_z3	0.0350	28	0.00095	6	1.46717	1.88656	41	0.282531	8	0.282531	-8.9	0.2
HS11_z16	0.0436	35	0.00110	7	1.46723	1.88684	6	0.282564	15	0.282564	-7.7	0.5
HS11_z8	0.0329	26	0.00089	5	1.46719	1.88659	58	0.282534	17	0.282534	-8.8	0.2
HS11_g6	0.0418	33	0.00116	7	1.46718	1.88665	34	0.282545	13	0.282545	-8.4	0.2
HS11_z9	0.0408	33	0.00111	7	1.46718	1.88663	47	0.282543	15	0.282543	-8.5	0.2
HS11_z5	0.0301	24	0.00085	5	1.46716	1.88658	31	0.282544	8	0.282544	-8.4	0.2
HS10_g2	0.0485	39	0.00115	7	1.46724	1.88683	9	0.282543	12	0.282543	-8.5	0.4
HS11_g7	0.0438	35	0.00104	6	1.46724	1.88685	10	0.282549	12	0.282549	-8.2	0.4
HS11_z21	0.0439	35	0.00108	7	1.46722	1.88675	6	0.282564	15	0.282564	-7.7	0.5
HS10_g9	0.0482	39	0.00127	8	1.46722	1.88673	3	0.282599	17	0.282599	-6.5	0.6
HS11_z13	0.0364	29	0.00084	5	1.46726	1.88691	21	0.282567	10	0.282567	-7.6	0.4
95-2017b												
95-2017b_z5	0.0412	33	0.00094	6	1.46724	1.88690	22	0.282547	10	0.282547	-8.3	0.4
95-2017b_z7	0.0446	36	0.00104	6	1.46725	1.88692	10	0.282548	11	0.282548	-8.3	0.4
95-2017b_z11	0.0499	40	0.00120	7	1.46726	1.88691	6	0.282563	13	0.282563	-7.8	0.4
95-2017b_z1	0.0440	35	0.00103	6	1.46723	1.88689	9	0.282580	14	0.282580	-7.1	0.5
95-2017b_z3	0.0407	33	0.00102	6	1.46723	1.88682	7	0.282580	13	0.282580	-7.2	0.5
95-2017b_z8	0.0515	41	0.00125	8	1.46726	1.88688	8	0.282590	12	0.282590	-6.8	0.4
95-2017b_z10	0.0447	36	0.00106	6	1.46725	1.88683	9	0.282559	13	0.282559	-7.9	0.5
95-2017b_z6	0.0724	58	0.00183	11	1.46721	1.88677	6	0.282603	13	0.282603	-6.3	0.5
HS14												
HS14_z2	0.0310	25	0.00076	5	1.46727	1.88691	8	0.282531	11	0.282531	-8.9	0.4
HS14_z3	0.0470	38	0.00108	6	1.46725	1.88686	13	0.282566	11	0.282566	-7.6	0.4
HS14_z5	0.0258	21	0.00060	4	1.46726	1.88697	23	0.282583	11	0.282583	-7.1	0.4
HS14_z8	0.0621	50	0.00143	9	1.46722	1.88686	9	0.282404	11	0.282404	-13.4	0.4
HS14_z6	0.0264	21	0.00062	4	1.46725	1.88693	16	0.282589	10	0.282589	-6.8	0.4
HS14_z4	0.0478	38	0.00110	7	1.46725	1.88691	10	0.282568	12	0.282568	-7.6	0.4

Quoted uncertainties (absolute) relate to the last quoted figure. Accuracy and reproducibilty was checked by repeated analyses of 10-40 ppb solutions of JMC475.

(a) $^{176}Yb/^{177}Hf = (^{176}Yb/^{173}Yb)true \times (^{173}Yb/^{177}Hf)meas \times (M173(Yb)/M177(Hf))b(Hf)$, $b(Hf) = \ln(^{179}Hf/^{177}Hf)true / (^{179}Hf/^{177}Hf)_{meas} / \ln(M179(Hf)/M177(Hf))$, M=mass of respective isotope. The $^{176}Lu/^{177}Hf$ were calculated in a similar way by using the $^{175}Lu/^{177}Hf$ and b(Yb).

(b) Mean Hf signal in volt.

(c) Uncertainties are quadratic additions of the within-run precision and the daily reproducibility of the 10ppb-JMC475 solution. Uncertainties for the JMC475 quoted at 2SD (2 standard deviation).

(d) Initial $^{176}Hf/^{177}Hf$ and eHf calculated using the apparent U-Pb age determined by ID-TIMS (see Table A2.1), and the CHUR parameters: $^{176}Lu/^{177}Hf = 0.0336$, and $^{176}Hf/^{177}Hf = 0.282785$ (Bouvier et al., 2008).

Lowenstern, J.B., Smith, R.B., and Hill, D.P., 2006. Monitoring super-volcanoes: geophysical and geochemical signals at Yellowstone and other large caldera systems. Phil. Trans. R. Soc. A, v. 364, p. 2055–2072.

Martin, E., and Bindeman, I.N., 2009. Mass-independent isotopic signatures of volcanic sulfate from three supereruption ash deposits in Lake Tecopa, California. Earth Planet. Sci. Lett., v. 282, p. 102–114.

Mason, B.G., Pyle, D.M., and Oppenheimer, C., 2004. The size and frequency of the largest explosive eruptions on Earth. Bull. Volcanol., v. 66, p. 735–748.

Miller, D.S., and Smith, R.B., 1999. P and S velocity structure of the Yellowstone volcanic field from local earthquake and controlled-source tomography. J. Geophys. Res., v. 104, p. 15105–15121.

Morgan, L.A., and McIntosh, W.C., 2005. Timing and development of the Heise volcanic field, Snake River Plain, Idaho, western USA. GSA Bulletin, v. 117, p. 288–306.

Pierce, K.L., and Morgan, L.A., 2009. Is the track of the Yellowstone hotspot driven by a deep mantle plume? Review of volcanism, faulting, and uplift in light of new data. J. Volcanol. Geotherm. Res., v. 188, p. 1–25.

Rampino, M.R., and Self, S., 1992. Volcanic winter and accelerated glaciation following the Toba super-eruption. Nature, v. 359, p. 50–52.

Rivera, T.A., Storey, M., Schmitz, M.D., and Crowley, J.L., 2013. Age intercalibration of $^{40}Ar/^{39}Ar$ sanidine and chemically distinct U/Pb zircon populations from the Alder Creek rhyolite quaternary geochronology standard. Chem. Geol., v. 345, p. 87–98.

Rubin, A. M., 1995. Getting granite dikes out of the source region. J. Geophys. Res., v. 100, p. 5911–5929.

Schmandt, B., Dueker, K., Humphreys, E., and Hansen, S., 2012. Hot mantle upwelling across the 660 beneath Yellowstone. Earth Planet. Sci. Lett., v. 331–332, p. 224–236.

Schoene, B., Guex, J., Bartolini, A., Schaltegger, U., and Blackburn, T.J., 2010a. Correlating the end-Triassic mass extinction and flood basalt volcanism at the 100 ka level. Geology, v. 38, p. 387–390.

Schoene, B., Latkoczy, C., Schaltegger, U., and Günther, D., 2010b, A new method integrating high-precision U-Pb geochronology with zircon trace element analysis (U-Pb TIMS-TEA): Geochimica et Cosmochimica Acta, v. 74, p. 7144–7159, doi:10.1016/j.gca.2010.09.016.

Schoene, B., Schaltegger, U., Brack, P., Latkoczy, C., Stracke, A., and Günther, D., 2012, Rates of magma differentiation and emplacement in a ballooning pluton recorded by U-Pb TIMS-TEA, Adamello batholith, Italy: Earth and Planetary Science Letters, v. 355–356, p. 162–173, doi:10.1016/j.epsl.2012.08.019.

Self, S., 2006. The effects and consequences of very large explosive volcanic eruptions. Phil. Trans. R. Soc. A, v. 364, p. 2073–2097.

Self, S., and Blake, S., 2008. Consequences of explosive supereruptions. Elements, v. 4, p. 41–46.

Simakin A.G., and Bindeman I.N., 2012. Remelting in caldera and rift environments and the genesis of hot, "recycled" rhyolites. Earth Planet. Sci. Lett., v. 337-338, p. 224–235.

Stankiewicz, J., Ryberg, T., Haberland, C., Fauzi, and Natawidjaja, D., 2010. Lake Toba volcano magma chamber imaged by ambient seismic noise tomography. Geophys. Res. Lett., v. 37, p. L17306.

Vermeesch, P., 2012. On the visualisation of detrital age distributions. Chem. Geol., v. 312–313, p. 190–194.

Watts K.E., Bindeman I.N., and Schmitt A.K., 2011. Large-volume Rhyolite Genesis in Caldera Complexes of the Snake River Plain: Insights from the Kilgore Tuff of the Heise Volcanic Field, Idaho, with Comparison to Yellowstone and Bruneau-Jarbidge Rhyolites. J. Petrol., v. 52, p. 857–890.

Watts, K.E., Bindeman, I.N., and Schmitt, A.K., 2012. Crystal-scale anatomy of a dying supervolcano: An isotope and geochronology study of individual phenocrysts from voluminous rhyolites of the Yellowstone caldera. Contrib. Mineral. and Petrol., v. 164, p. 45–67.

Wotzlaw, J.F., Bindeman, I.N., Schaltegger, U., Brooks, C.K., and Naslund, H.R., 2012. High-resolution insights into episodes of crystallization, hydrothermal alteration and remelting in the Skaergaard intrusive complex. Earth Planet. Sci. Lett., v. 355-356, p. 199–212.

Wotzlaw, J.F., Schaltegger, U., Frick, D.A., Dungan, M.A., Gerdes, A., and Günther, D., 2013. Tracking the evolution of large-volume silicic magma reservoirs from assembly to supereruption. Geology, v. 41, p. 867–870.

***

Chapter 4

Testing the gold standard of geochronology against astronomical time: High-precision U-Pb geochronology of orbitally tuned ash beds from the Mediterranean Miocene

J.F. Wotzlaw, S.K. Hüsing, F.J. Hilgen, U. Schaltegger

Keywords:
U-Pb geochronology
astrochronology
intercalibration
zircon
^{230}Th disequilibrium
residence time

ABSTRACT

Several orbitally tuned Miocene sedimentary sequences around the Mediterranean contain abundant intercalated volcanic ash beds. These sequences provide the rare opportunity to intercalibrate radioisotopic dating methods with independent and accurate deposition ages derived from astrochronology. We present a large data set (N=17, n=175) of high precision zircon U-Pb dates for ash beds from an almost continuous orbitally tuned Messinian to Langhian (6.2-15.4 Ma) sedimentary sequence exposed along the Adriatic coast south of Ancona, Italy. We use this unique data set to evaluate (1) the accuracy of zircon U-Pb dates, (2) the significance of initial intermediate daughter product disequilibria for zircon U-Pb geochronology of young rocks, (3) the effect of prolonged pre-eruption zircon crystallization and zircon recycling on U-Pb derived ash bed deposition ages, and (4) discuss the implications for the intercalibration of radioisotope geochronometers and the calibration of the Geologic Time Scale.

4.1 INTRODUCTION

Uranium-lead geochronology by isotope – dilution thermal ionization mass spectrometry (ID-TIMS) is widely regarded as the most accurately calibrated radioisotopic dating method and is often referred to as the *gold standard* of geochronology. This stems from the unique dual decay of ^{238}U and ^{235}U aiding evaluation of closed system behaviour, precisely and accurately determined ^{238}U and ^{235}U decay constants (Jaffey et al., 1971; Schoene et al., 2006; Mattinson, 2010), gravimetrically calibrated reference and

tracer solutions (Condon et al., submitted; McLean et al., submitted) as well as decades of progressive improvements of analytical procedures, reducing laboratory contamination (e.g., Krogh, 1973; Bowring et al., 2006) and effectively reducing the influence of post-crystallization Pb-loss in the most commonly dated mineral zircon (e.g., Krogh, 1982; Mattinson, 2005).

These characteristics together with advances in thermal ionization mass spectrometry techniques allow the determination of parent-daughter isotopic ratios and dates with precision and accuracy at the permil level for the ^{238}U-^{206}Pb system. This level of precision and accuracy translates into absolute uncertainties of several thousand to tens of thousands of years when dating Cenozoic zircons. Such high temporal resolution may result in complex zircon age populations, reflecting prolonged zircon growth and magma residence, previously only resolvable by in-situ U-Th dating in Pleistocene magmatic systems (e.g., Schmitt, 2011). The potential of resolving the time-scales and rates of magmatic processes in pre-Pleistocene volcanic deposits and exhumed plutons, recently made ID-TIMS based zircon U-Pb geochronology a widely used tool in igneous petrology (e.g., Crowley et al., 2007; Schaltegger et al., 2009; Schoene et al., 2012; Wotzlaw et al., 2012, 2013; Rivera et al., 2013). When dealing with zircons from volcanic deposits, the prolonged magmatic history recorded by zircons, may somewhat systematically bias zircon U-Pb derived eruption/deposition ages. This is important for two reasons:

(1) Several isotopic systems are calibrated against the U-Pb system by dating two minerals of the same rock; one employing the U-Pb method (typically zircon) and another mineral using the radioisotopic system of interest (e.g., Lu-Hf, Scherer et al., 2001; Re-Os, Selby et al., 2007; Rb-Sr, Nebel et al., 2010; $^{40}Ar/^{39}Ar$, Renne et al., 2010, 2011). This approach is based on the a priori assumption that a given pair of radioisotopic dates of a pair of minerals (e.g., zircon U-Pb and sanidine $^{40}Ar/^{39}Ar$) date the exact same event (e.g., the eruption). If this assumption can be validated, systematic offsets between the two dates can be used to re-calibrate the system of interest. However, the prolonged crystallization history recorded by zircons has been suggested to contribute to the systematic offset between sanidine $^{40}Ar/^{39}Ar$ and zircon U-Pb dates (e.g., Simon et al., 2008; Renne et al., 2010; Renne et al., submitted) but may potentially also influence other intercalibrations (e.g., zircon U-Pb vs. molybdenite Re-Os; Chelle-Michou et al., in prep.).

(2) The high precision and accuracy achievable by zircon U-Pb geochronology also made it the method of choice for the numerical calibration of large parts of the Geologic Time Scale (GTS; e.g., Gradstein et al., 2012). In the GTS2012, U-Pb dates of volcanic ash beds intercalated with fossil-bearing marine sediments underpin much of the Palaeozoic and Mesozoic numerical time scales (Gradstein et al, 2012). Several recent studies reported significant complexities in ziron populations of Paleozoic and Mesozoic ash beds resembling those from younger

volcanic deposits that were related to prolonged pre-eruption zircon crystallization. Such data-sets require new data interpretation strategies (e.g., Schoene et al., 2010, Meyers et al., 2012; Guex et al., 2012). The larger absolute uncertainties associated with U-Pb dates of older zircons may also mask complexities especially in lower precision data-sets. In such cases, statistical methods to reduce uncertainty, such as the calculation of a weighted mean date of a population of zircons, may yield inaccurate results. These aspects have been suggested to significantly compromise chronostratigraphic applications of zircon U-Pb geochronology (e.g., Simon et al., 2008) and need thorough evaluation.

In contrary to the Paleozoic and Mesozoic, the numerical calibration of the Neogene period is entirely independent of the U-Pb system but instead relies on astrochronology (e.g., Hinnov and Hilgen, 2012; Hilgen et al., 2012). Astrochronology is based on cyclic sedimentary sequences that record periodic variations in the quantity of insolation the Earth receives from the sun. These periodic changes in insolation quantity are related to periodic variations in the ellipticity of the Earth's orbit (*eccentricity*), Earth's axial tilt (*obliquity*) and the orientation of the Earth's axis relative to the sun (*precession*). These parameters change as a function of time with specific periodicities. Main periodicities affecting Earth climate are 400,000 and 100,000 years for eccentricity, 41,000 years for obliquity and 19,000 and 23,000 for precession. The combined effects of these parameters can be modeled as a function of time, resulting in long-term numerical solutions for the insolation quantity of the Earth (*astronomical solution*; see Laskar et al., 2004; 2011 for the most recent models). These variations in insolation result in variations in Earth climate that may be recorded in cyclic patterns in lithology, geochemistry and/or isotopic composition of sedimentary sequences. These cyclic patterns in sedimentary records can be correlated with the astronomical solution (*orbital tuning*) resulting in numerically calibrated sedimentary records completely independent of radioisotopic dating methods.

Several Neogene sedimentary sequences around the Mediterranean Sea (e.g., Spain, Greece, Italy, Morocco) display precession controlled cyclic patterns that can be tuned to the astronomical solution of Laskar et al. (2004). Many of them serve as reference sections for large parts of the Miocene, Pliocene and Pleistocene epochs (Hilgen et al., 2012; Pillans and Gibbard, 2012). Some of these sequences contain intercalated volcanic ash beds derived from subduction-related volcanic systems in the Mediterranean (e.g., the Betic-Rif subduction system; the Tyrrhenian Sea; Aegean arc etc.). These ash beds provide the opportunity to directly intercalibrate radioisotopic dating methods with astrochronology. Sanidine crystals of some of these astronomically dated ash beds have previously been analyzed by the $^{40}Ar/^{39}Ar$ method in order to calibrate various dating standards relative to the astronomical age of the ash beds (e.g., Hilgen et al., 1997; Kuiper et al., 2004; 2005; 2008; Rivera et al., 2011; 2013).

We here employ ID-TIMS techniques to obtain high-precision zircon U-Pb dates from ash beds intercalated with orbitally tuned Langhian to Messinian sediments exposed along the Adriatic coast south of Ancona, Italy (Fig. 4.1; Hilgen et al., 2003; Hüsing et al., 2007; 2009; 2010). With this intercalibration study we independently test the accuracy of the U-Pb system, evaluate data interpretation strategies, and discuss some of the fundamental limitations of the zircon U-Pb method arising from pre-eruption crystallization and isotopic closure as well as initial intermediate daughter product disequilibria. The latter two aspects become increasingly more significant with decreasing age, but the general implications also apply to older zircons. We further discuss the implications for the calibration of sedimentary records and the intercalibration of radioisotopic geochronometers.

4.2 STRATIGRAPHIC FRAMEWORK, ASTROCHRONOLOGY AND PREVIOUS RADIOISOTOPIC DATING OF ASH BEDS

Miocene-Pliocene sedimentary deposits of the Mediterranean basin attracted considerable attention as high-resolution paleoclimate and paleoenvironmental archives. Much of the research focused on the timing, progression and causes of the Messinian salinity crisis that is marked by cyclic evaporite deposition related to isolation of the Mediterranean basin from the Atlantic ocean at ~6 Ma (e.g., Krijgsman et al., 1999; Hilgen et al., 2007). In an effort to extend Mediterranean paleoenvironmental records far into the Middle Miocene, detailed integrated stratigraphy work has been carried out for along the coastal cliff of Monte Còrnero, south-east of Ancona, Italy (Fig. 4.1). The marine sedimentary sequence exposed along the cliffs is essentially continuous from the Aquitanian to Messinian (Montanari et

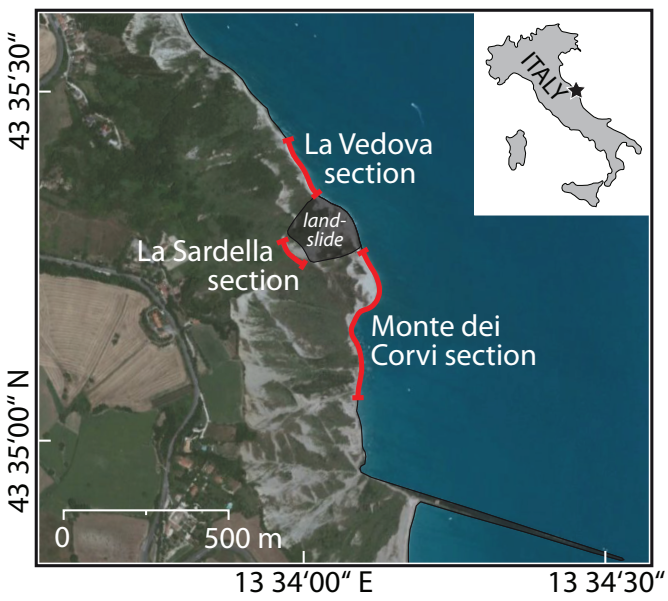

FIGURE 4.1 Map of the study area south of Ancona, Italy. Red lines show the location of studied sections along the beach (La Vedova and Monte dei Corvi sections) and cliff (La Sardella section). Indicated is also the landslide that covered parts of the section until 2011. Inset shows location of the study area at the Adriatic coast of Italy.

al., 1997; Hilgen et al., 2003). A series of studies throughout the last 10 years led to the construction of an almost complete Langhian to Messinian astrochronology (Hilgen et al., 2003; Hüsing et al., 2007; 2009; 2010; Mourik et al., 2011).

The Langhian interval, referred to as the La Vedova section (Fig. 4.1; Montanari et al., 1997; Mader et al., 2001; 2004; Hüsing et al., 2010) consists of a cyclic alternation of homogeneous dark marls and indurated marly limestones (Fig. 4.2). The first independent age constraints were reported by Mader et al. (2001) who dated biotites from a volcanic ash layer, referred to as the Aldo ash,

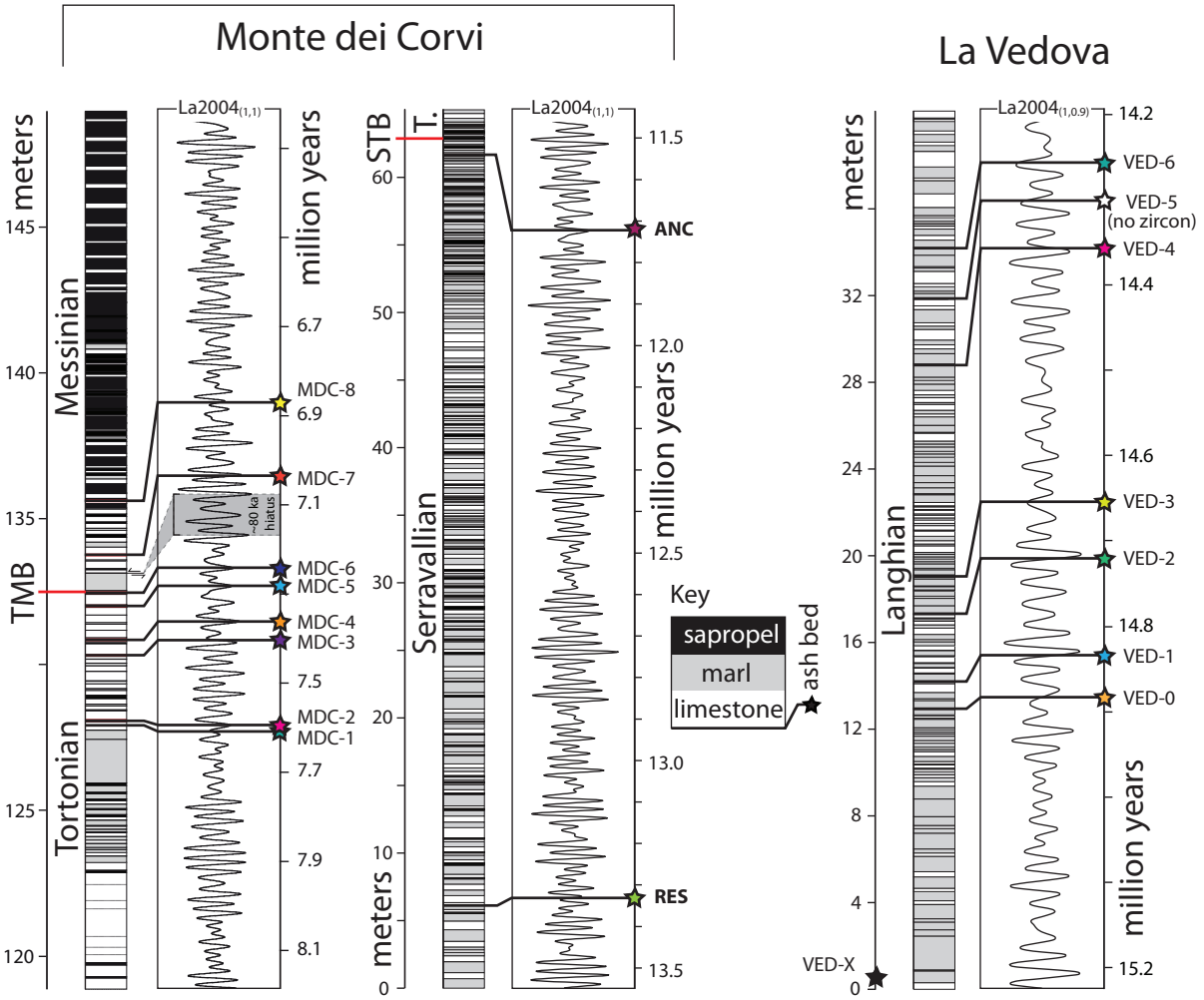

FIGURE 4.2 Stratigraphy and astrochronology of the Monte dei Corvi and La Vedova sections. Simplified lithologic logs show the cyclic alternations of ±sapropels, marls and limestones. Intercalated ash beds are shown with correlation to the astronomical solution of Laskar et al. (2004). The solutions used for tuning the Monte dei Corvi section use present-day values for tidal dissipation and dynamic ellipticity, while the solution used for tuning the La Vedova section uses a value of 0.9 for tidal dissipation (relative to present day tidal dissipation of 1.0; Hüsing et al., 2010). See text for further details.

employing the $^{40}Ar/^{39}Ar$ method. Mader et al. (2001; 2004) further established a preliminary astronomical tuning for an interval covering ~340 ka (~14.7-15.1 Ma). More recently, Hüsing et al. (2010) reported high resolution bio-, magneto- and cyclostratigraphic data as well as feldspar $^{40}Ar/^{39}Ar$ dates for two ash layers and established a robust astronomical tuning supported by geochemical proxy records for the interval between 15.3 and 14.1 Ma (Fig. 4.2). This interval contains a total of eight volcanic ash layers.

The slightly younger Monte dei Corvi section comprises the upper Serravallian, the entire Tortonian with the formally ratified Tortonian GSSP (Hilgen et al., 2003; 2005; 2012), and the lowermost Messinian. A robust astronomical tuning of this part of the sequence, in conjunction with high resolution bio- and magnetostratigraphy, was established and refined in a series of papers (Hilgen et al., 2003; Hüsing et al., 2007; 2009). The sedimentary succession consists of cyclic alternations of marls, limestones and sapropels. The Serravallian to Middle Tortonian part of the section displays a cyclic pattern consisting of couplets of marls and marly limestones with clusters of intercalated sapropels (Hilgen et al., 2003; Fig. 4.2). In the upper Tortonian to Messinian part of the sequence the cycle patterns change significantly (Hüsing et al., 2009); riplets of brown indurated marls, sapropels and softer greyish marls in the late Tortonian, followed by couplets of limestones and sapropels or limestones and grey marls, and couplets of thick sapropels and marly limestones in the Messinian "Euxinic Shales Interval" (Montanari et al., 1997; Hüsing et al., 2007). These precession controlled small scale cycle patterns allow a straightforward astronomical tuning. A small hiatus is present in the lowermost Messinian part of the section that was estimated to encompass four precession cycles (~80 ka; Fig. 4.2) using biostratigraphic arguments (Hüsing et al., 2009). The Monte dei Corvi section contains a total of ten ash layers; two within the upper Serravallian interval, referred to as the Respighi and Ancona ash beds (RES and ANC, respectively, in Fig. 4.2), the latter just below the Serravallian-Tortonian boundary, and eight in the uppermost Tortonian to lowermost Messinian interval (Fig. 4.2).

Biotite and feldspar $^{40}Ar/^{39}Ar$ dates have previously been reported for the Serravallian Ancona and Respighi ash beds (Montanari et al., 1997; Kuiper et al., 2005). Hüsing (2008) also reported feldspar $^{40}Ar/^{39}Ar$ dates for some of the uppermost Tortonian ashes and correlative beds from the Monte dei Casino section in the Northern Appennines. These $^{40}Ar/^{39}Ar$ dates do not show the systematic offset relative to the astronomical ages as reported by Kuiper et al. (2008) and Rivera et al. (2011) from other Mediterranean sections. This was attributed to the less favorable material for $^{40}Ar/^{39}Ar$ dating recovered from these ash beds (i.e., biotite and multigrain feldspar fractions) and not to inaccuracies in the tuning. The robust astronomical tuning of the La Vedova and Monte dei Corvi sections thus provides precise and accurate deposition ages for the intercalated ash beds that are entirely independent of radioisotopic age constraints.

4.3 SAMPLES AND ANALYTICAL METHODS

We sampled all 17 previously identified ash beds from the La Vedova and Monte dei Corvi sections (Fig. 4.2), 16 of them contained accessory zircon suitable for high-precision U-Pb geochronology. Additionally, a newly identified ash bed at the base of the La Vedova section (VED-X) also contained suitable zircon. The Respighi (RES) and all La Vedova (VED) ash beds are 5-10 cm thick clay layers. The Ancona ash bed (ANC) is a 20 cm thick limestone layer strongly enriched in volcaniclastic material, particularly biotite. The younger ash beds in the upper part of the Monte dei Corvi section (MDC) are similar to ANC, but are much thinner volcaniclastic layers in limestones and marls (Fig. 4.2).

To separate zircons, samples of the clay-rich ashes were carefully disintegrated in water and the clay was decanted leaving a coarse grained residuum. The limy samples were first wrapped in plastic foil, carefully crushed using a hammer and the resulting chips and powder were placed in cold 10% acetic acid for several hours/days to dissolve carbonates. In both cases, the residual clastic material was sieved to <200 μm using disposable nylon sieves. Zircons were separated from the <200 μm fraction using Methylene Iodide heavy liquid.

A total of 175 zircons were analyzed as single grains employing chemical abrasion ID-TIMS techniques at the University of Geneva following established procedures (e.g., Schoene et al., 2010; 2012; Wotzlaw et al., 2012; 2013). Prior to dissolution, all crystals were annealed by heating to 900°C for 48 h in a muffle furnace. Individual crystals were subsequently selected under a binocular microscope, transferred into 3 ml Savillex beakers, rinsed with 3 N HNO_3 and loaded into 200 μl Savillex microcapsules for partial dissolution (i.e., *"chemically abraded"*; Mattinson, 2005) in HF + trace HNO_3 at 180°C for 15 h in Parr bombs. After partial dissolution, residual crystals/crystal fragments were transferred back into 3 ml Savillex beakers, rinsed with water, fluxed for several hours in 6 N HCl and ultrasonically cleaned by alternating water and 3 N HNO_3. Zircons were then reloaded into their respective 200 μl microcapsules, spiked with 3-5 mg of the EARTHTIME ($\pm^{202}$Pb-)^{205}Pb-^{233}U-^{235}U tracer solution (hereafter referred to as ET535 and ET2535; tracer calibration v. 3.0; http://www.earth-time.org/; Condon et al., submitted; McLean et al., submitted) and dissolved in 70 μl HF at 210°C for 48 h in Parr bombs. After dissolution, samples were dried down and redissolved in 6 N HCl at 180°C overnight, dried down again and redissolved in 3 N HCl. U and Pb were then separated using a modified HCl-based single-column anion exchange chemistry (Krogh, 1973). The U-Pb fractions were dried down with a microdrop of 0.035 M H_3PO_4 and loaded on outgassed single Re-filaments with a Si-Gel emitter modified from Gerstenberger and Haase (1997). U and Pb isotopic measurements were performed on a Thermo TRITON thermal ionization mass spectrometer. Pb was measured in dynamic mode on a MasCom secondary electron multiplier. Analyses of ET2535-spiked samples

were corrected for instrumental mass fractionation using the fractionation factor derived from the measured $^{202}Pb/^{205}Pb$ ratio relative to a true value of 0.99924. ET535-spiked samples were corrected for 0.13 ± 0.03 %/amu mass fractionation which is the average value of measurements employing the ET2535 tracer over the course of this study ($n > 200$). U was measured as U-oxide in static mode on Faraday cups equipped with 10^{12} Ω resistors. Measured isotopic ratios were corrected for isobaric interferences of $^{233}U^{18}O^{16}O$ on $^{235}U^{16}O_2$ using an $^{18}O/^{16}O$ of 0.00205 and for mass fractionation using the measured $^{233}U/^{235}U$ ratio relative to a value of 0.99506 for both tracers and a sample $^{238}U/^{235}U$ of 137.818 ± 0.045 (2σ; Hiess et al., 2012). All common Pb in zircon analyses (Tab. 4.1) was assumed to be procedural blank and corrected using the long-term average composition of total procedural blank measurements (see footnote in Tab. 4.1). Data reduction was performed using Tripoli and U-Pb_Redux software (Bowring et al., 2011) that employs algorithms of McLean et al. (2011). U-Pb ratios and dates were calculated relative to a $^{235}U/^{205}Pb$ ratio of 100.23 ± 0.046% (2σ).

$^{206}Pb/^{238}U$ and $^{207}Pb/^{206}Pb$ dates were corrected for initial ^{238}U-^{230}Th disequilibrium in the ^{238}U-^{206}Pb decay chain arising from preferential exclusion of Th relative to U during zircon crystallization (e.g., Schärer, 1984). We here use a model correction assuming that variations in Th/U of analyzed zircons are due to variations in the Th/U of the magma in equilibrium with the respective zircon during crystallization and not due to variations in relative partitioning between Th and U (i.e., D_{Th}/D_U remains constant). We tentatively use a partition coefficient ratio D_{Th}/D_U of 0.2 with a conservative uncertainty of ± 0.1 (2σ) that covers the range of most empirically and experimentally determined partition coefficient ratios (e.g., Bindemann et al., 2006; Thomas et al., 2002; Rubatto and Hermann, 2007; Schmitt, 2011). This correction results in a constant increase of $^{206}Pb/^{238}U$ dates by 87 ± 11 ka. Uncertainties associated with the calculated Th/U_{magma} were propagated into the uncertainty of $^{206}Pb/^{238}U$ dates following Crowley et al. (2007) and McLean et al. (2011).

All uncertainties are reported at the 95% confidence level. Systematic uncertainties associated with the tracer isotopic composition and the ^{238}U decay constant were propagated following McLean et al. (2011; submitted) for comparison with astronomical ages and $^{40}Ar/^{39}Ar$ dates.

4.4 ZIRCON U-PB SYSTEMATICS

Analyzed ash bed zircons show some common features with respect to their U-Pb systematics, i.e., the relationship between the ^{238}U-^{206}Pb and ^{235}U-^{207}Pb systems (Tab. 4.1; Fig. 4.3) and the relationship between U-Pb dates and astronomical ages of individual ashes (Tab. 4.2; Fig. 4.4).

After correcting the $^{206}Pb/^{238}U$ ratios for ^{206}Pb deficit resulting from initial ^{238}U-^{230}Th disequilibrium, the majority of zircon analyses is concordant within uncertainty with some analyses showing minor but resolvable residual normal discordance (i.e., higher $^{207}Pb/^{235}U$ relative to concordia; samples MDC-4 to MDC-8

Table 4.1 *U-Pb isotopic data for zircons from astronomically tuned Miocene ash beds*

	Dates (Ma)						Composition				Isotopic Ratios					
Fraction	$^{206}Pb/^{238}U$ (a)	±2σ abs	$^{206}Pb/^{238}U$ (a,b)	±2σ abs	$^{207}Pb/^{235}U$ (a)	±2σ abs	Th/U (c)	Pb* (pg) (d)	Pb_c (pg) (e)	Pb*/Pb_c (f)	$^{206}Pb/^{204}Pb$ (h)	$^{206}Pb/^{238}U$ (i)	±2σ %	$^{207}Pb/^{235}U$ (i)	±2σ %	Corr. coef.
VED-X																
z8	15.232	0.019	15.319	0.022	15.35	0.26	0.47	2.80	0.41	6.84	437	0.0023657	0.13	0.015230	1.73	0.760
z6	15.233	0.010	15.320	0.015	15.31	0.11	0.49	7.41	0.40	18.35	1136	0.0023658	0.06	0.015196	0.73	0.682
z2	15.244	0.013	15.331	0.017	15.44	0.15	0.44	6.46	0.50	12.93	816	0.0023675	0.09	0.015319	0.96	0.719
z3	15.246	0.018	15.333	0.021	15.44	0.24	0.46	2.90	0.39	7.50	478	0.0023678	0.12	0.015318	1.58	0.746
z1	15.250	0.016	15.337	0.019	15.43	0.20	0.51	4.08	0.43	9.50	594	0.0023685	0.10	0.015317	1.29	0.747
z4	15.251	0.047	15.338	0.048	15.54	0.70	0.46	1.26	0.49	2.55	175	0.0023685	0.31	0.015426	4.57	0.759
z5	15.263	0.022	15.350	0.024	15.60	0.30	0.44	2.93	0.50	5.81	377	0.0023704	0.14	0.015482	1.97	0.750
z7	15.273	0.012	15.360	0.016	15.43	0.16	0.43	4.10	0.37	11.00	699	0.0023721	0.08	0.015316	1.07	0.741
z9	15.277	0.030	15.364	0.032	15.86	0.45	0.54	1.62	0.35	4.60	294	0.0023727	0.20	0.015739	2.86	0.745
VED-0																
z3	14.786	0.027	14.874	0.029	15.01	0.39	0.59	3.57	0.77	4.62	292	0.0022964	0.19	0.014893	2.62	0.760
z19	14.794	0.016	14.881	0.020	14.88	0.13	0.66	5.80	0.36	16.08	954	0.0022975	0.11	0.014759	0.85	0.733
z21	14.802	0.028	14.889	0.029	14.94	0.39	0.59	3.35	0.73	4.58	290	0.0022988	0.19	0.014818	2.65	0.746
z23	14.811	0.020	14.898	0.023	14.82	0.27	0.57	4.71	0.67	7.07	439	0.0023002	0.14	0.014705	1.82	0.746
z1	14.823	0.015	14.910	0.018	15.04	0.21	0.51	6.84	0.79	8.65	542	0.0023020	0.10	0.014921	1.42	0.689
z22	14.823	0.012	14.910	0.016	14.94	0.14	0.50	7.04	0.51	13.89	861	0.0023020	0.08	0.014822	0.92	0.651
z25	14.827	0.011	14.914	0.016	15.02	0.12	0.47	9.70	0.67	14.55	908	0.0023027	0.07	0.014900	0.84	0.665
z4	14.827	0.025	14.914	0.027	15.01	0.36	0.54	5.22	1.06	4.91	313	0.0023027	0.17	0.014897	2.40	0.741
z20	14.830	0.015	14.917	0.018	14.93	0.18	0.62	5.54	0.52	10.72	649	0.0023031	0.10	0.014811	1.22	0.670
z18	14.831	0.029	14.918	0.031	14.93	0.39	0.48	2.58	0.49	5.29	341	0.0023033	0.20	0.014810	2.60	0.758
z16	14.834	0.017	14.921	0.020	14.98	0.19	0.61	7.52	0.70	10.73	650	0.0023038	0.11	0.014863	1.26	0.713
z17	14.834	0.021	14.921	0.023	15.24	0.27	0.51	4.51	0.66	6.80	429	0.0023038	0.14	0.015123	1.79	0.729
z24	16.048	0.029	16.135	0.031	16.30	0.37	0.56	4.74	0.86	5.50	347	0.0024925	0.18	0.016180	2.26	0.771
VED-1																
z1	14.849	0.047	14.936	0.048	14.22	0.79	1.14	1.73	0.53	3.25	187	0.0023062	0.31	0.014106	5.56	0.723
z12	14.923	0.089	15.010	0.089	15.01	1.33	0.90	1.02	0.67	1.51	102	0.0023176	0.60	0.014893	8.95	0.770
z7	14.937	0.066	15.024	0.067	14.67	0.99	0.99	1.57	0.75	2.11	131	0.0023198	0.44	0.014555	6.80	0.771
z8	14.944	0.055	15.031	0.056	14.90	0.82	0.78	1.86	0.78	2.39	153	0.0023209	0.37	0.014780	5.58	0.759
z2	14.968	0.050	15.055	0.051	14.98	0.70	0.76	2.18	0.75	2.90	183	0.0023246	0.34	0.014859	4.70	0.791
z10	14.997	0.031	15.084	0.032	14.96	0.44	0.89	2.92	0.61	4.81	283	0.0023291	0.21	0.014846	2.93	0.776

(Table 4.1 continued)

z4	15.050	0.103	15.137	0.103	15.79	1.58	0.82	0.82	0.64	1.27	89	0.0023374	0.68	0.015676	10.07	0.763
z3	16.231	0.037	16.318	0.038	16.55	0.54	0.84	2.08	0.52	3.97	239	0.0025210	0.23	0.016429	3.30	0.754
z11	16.237	0.038	16.324	0.039	16.52	0.54	0.73	2.26	0.56	4.08	251	0.0025219	0.23	0.016406	3.29	0.721
z6	16.247	0.092	16.334	0.092	16.67	1.39	0.79	1.39	0.91	1.53	104	0.0025235	0.57	0.016553	8.42	0.765
VED-2																
z8	14.637	0.084	14.724	0.084	14.84	1.24	0.41	1.62	1.13	1.44	108	0.0022732	0.58	0.014718	8.44	0.756
z12	14.637	0.099	14.724	0.098	14.96	1.42	0.49	1.36	1.08	1.26	95	0.0022732	0.68	0.014843	9.57	0.747
z16	14.669	0.080	14.756	0.079	14.65	1.20	0.40	1.14	0.80	1.42	107	0.0022781	0.54	0.014535	8.25	0.758
z5	14.669	0.056	14.756	0.056	14.94	0.63	0.50	2.67	0.93	2.88	193	0.0022781	0.38	0.014821	4.27	0.638
z1	14.671	0.062	14.759	0.062	15.27	0.91	0.58	0.91	0.45	2.03	139	0.0022785	0.42	0.015149	6.04	0.758
z2	14.673	0.060	14.760	0.060	15.23	0.93	0.48	1.45	0.74	1.96	138	0.0022787	0.41	0.015114	6.13	0.749
z11	14.675	0.072	14.762	0.072	15.13	1.02	0.68	1.31	0.70	1.86	126	0.0022790	0.49	0.015012	6.79	0.760
z9	14.679	0.054	14.766	0.054	14.81	0.77	0.67	3.32	1.39	2.39	157	0.0022797	0.37	0.014697	5.24	0.756
z15	14.696	0.015	14.783	0.018	14.82	0.15	0.54	8.17	0.67	12.12	745	0.0022823	0.10	0.014701	1.04	0.628
z7	14.699	0.062	14.786	0.063	15.24	0.87	0.51	1.62	0.78	2.08	144	0.0022827	0.42	0.015121	5.78	0.767
z14	14.703	0.046	14.790	0.047	15.19	0.66	0.63	1.42	0.51	2.78	181	0.0022833	0.32	0.015075	4.39	0.779
z10	14.716	0.065	14.803	0.065	14.86	0.95	0.42	1.53	0.84	1.83	132	0.0022854	0.44	0.014747	6.44	0.752
z17	14.722	0.014	14.809	0.018	14.82	0.18	0.65	9.99	0.92	10.91	655	0.0022864	0.10	0.014707	1.19	0.677
z4	14.755	0.033	14.842	0.034	15.14	0.47	0.47	2.89	0.75	3.88	255	0.0022915	0.22	0.015020	3.10	0.733
z6	14.787	0.078	14.874	0.078	15.69	1.17	0.57	1.27	0.75	1.69	119	0.0022965	0.53	0.015569	7.51	0.772
VED-3																
z4	14.539	0.051	14.626	0.052	14.49	0.79	0.52	1.04	0.45	2.29	156	0.0022579	0.35	0.014372	5.46	0.747
z9	14.539	0.053	14.626	0.053	14.56	0.81	0.56	1.40	0.56	2.51	167	0.0022580	0.36	0.014443	5.58	0.771
z7	14.549	0.055	14.636	0.056	14.62	0.82	0.61	1.46	0.60	2.42	159	0.0022595	0.38	0.014502	5.63	0.785
z5	14.560	0.084	14.647	0.084	15.25	1.23	0.54	0.95	0.65	1.46	106	0.0022612	0.58	0.015135	8.11	0.774
z3	14.568	0.083	14.655	0.082	15.17	1.27	0.55	0.75	0.51	1.47	105	0.0022624	0.57	0.015056	8.45	0.773
z1	14.568	0.059	14.655	0.059	15.36	0.86	0.62	1.30	0.59	2.20	148	0.0022624	0.41	0.015244	5.63	0.773
z6	14.579	0.047	14.666	0.047	15.04	0.68	0.57	1.44	0.51	2.84	186	0.0022641	0.32	0.014926	4.58	0.784
z2	14.580	0.084	14.667	0.084	15.67	1.26	0.57	1.02	0.71	1.44	104	0.0022642	0.57	0.015556	8.09	0.772
z8	14.586	0.059	14.673	0.059	15.30	0.88	0.58	1.11	0.52	2.15	145	0.0022652	0.40	0.015183	5.82	0.779
VED-4																
z13	14.230	0.044	14.318	0.045	14.44	0.64	0.40	4.82	1.95	2.47	173	0.0022099	0.31	0.014319	4.48	0.743
z9	14.256	0.043	14.343	0.044	14.59	0.63	0.61	2.06	0.70	2.93	191	0.0022139	0.30	0.014472	4.34	0.760
z1	14.272	0.032	14.359	0.033	14.51	0.47	0.55	3.10	0.83	3.72	241	0.0022164	0.22	0.014390	3.28	0.709
z7	14.276	0.022	14.364	0.024	14.50	0.27	0.36	18.61	3.06	6.07	402	0.0022171	0.15	0.014385	1.88	0.670

(Table 4.1 continued)

z4	14.281	0.056	14.368	0.056	14.40	0.81	0.52	1.81	0.82	2.20	151	0.0022178	0.39	0.014282	5.65	0.751
z14	14.289	0.019	14.376	0.022	14.59	0.27	0.34	6.22	1.01	6.16	408	0.0022190	0.14	0.014474	1.89	0.697
z6	14.292	0.019	14.379	0.021	14.35	0.23	0.38	5.22	0.60	8.69	564	0.0022194	0.13	0.014229	1.61	0.526
z10	14.296	0.027	14.383	0.029	14.40	0.37	0.47	3.80	0.70	5.43	351	0.0022201	0.19	0.014279	2.58	0.729
z5	14.324	0.028	14.411	0.030	14.56	0.32	0.42	4.63	0.87	5.35	350	0.0022245	0.20	0.014439	2.24	0.645
z3	14.324	0.025	14.411	0.027	14.57	0.14	0.37	11.75	0.93	12.68	816	0.0022245	0.18	0.014456	0.96	0.456
z2	14.325	0.018	14.412	0.021	14.51	0.19	0.52	7.55	0.81	9.37	585	0.0022246	0.13	0.014390	1.35	0.683
z15	14.361	0.028	14.448	0.030	14.41	0.45	0.39	4.02	1.06	3.81	257	0.0022302	0.20	0.014293	3.12	0.700
z12	14.407	0.063	14.494	0.063	14.62	0.92	0.47	1.66	0.87	1.89	134	0.0022374	0.44	0.014500	6.35	0.757
z11	14.447	0.028	14.534	0.030	14.57	0.33	0.49	5.81	1.06	5.48	352	0.0022436	0.19	0.014456	2.31	0.678
VED-6																
z2	14.168	0.026	14.255	0.028	14.26	0.36	0.46	2.69	0.58	4.66	304	0.0022002	0.19	0.014145	2.57	0.741
z17	14.169	0.030	14.256	0.032	14.01	0.42	0.49	2.93	0.73	4.02	263	0.0022003	0.21	0.013891	3.02	0.755
z5	14.171	0.055	14.259	0.055	14.15	0.82	0.68	1.85	0.81	2.28	150	0.0022008	0.39	0.014037	5.81	0.770
z1	14.182	0.041	14.269	0.042	14.43	0.59	0.44	1.71	0.60	2.88	196	0.0022023	0.29	0.014317	4.10	0.772
z8	14.188	0.035	14.275	0.036	14.43	0.51	0.49	2.37	0.63	3.76	248	0.0022034	0.25	0.014314	3.57	0.769
z4	14.200	0.026	14.287	0.028	14.13	0.30	0.48	5.38	0.75	7.18	456	0.0022052	0.18	0.014010	2.17	0.609
z7	14.203	0.030	14.290	0.031	14.73	0.42	0.48	3.65	0.87	4.18	273	0.0022056	0.21	0.014613	2.85	0.769
z3	14.206	0.027	14.293	0.029	14.44	0.41	0.60	3.46	0.74	4.67	294	0.0022061	0.19	0.014325	2.86	0.680
z6	14.247	0.030	14.334	0.031	14.63	0.43	0.67	4.24	0.99	4.29	267	0.0022126	0.21	0.014517	2.97	0.756
RES																
z5	13.219	0.063	13.306	0.063	13.18	0.94	0.46	2.49	1.42	1.75	126	0.0020527	0.48	0.013061	7.21	0.739
z12	13.230	0.036	13.317	0.037	13.38	0.54	0.48	4.08	1.45	2.81	190	0.0020543	0.27	0.013265	4.07	0.740
z6	13.231	0.029	13.318	0.031	13.13	0.42	0.45	2.56	0.68	3.76	250	0.0020545	0.22	0.013014	3.22	0.715
z8	13.237	0.025	13.324	0.027	13.25	0.37	0.41	3.82	0.90	4.22	281	0.0020554	0.19	0.013130	2.78	0.729
z10	13.243	0.027	13.330	0.029	13.36	0.40	0.50	2.76	0.70	3.92	256	0.0020564	0.20	0.013248	3.00	0.724
z2	13.245	0.026	13.333	0.028	13.39	0.38	0.45	3.58	0.85	4.21	277	0.0020568	0.20	0.013270	2.85	0.712
z4	13.248	0.053	13.336	0.053	13.57	0.77	0.48	1.60	0.78	2.06	144	0.0020573	0.40	0.013455	5.68	0.735
z15	13.266	0.017	13.353	0.020	13.37	0.24	0.59	3.53	0.50	7.01	434	0.0020600	0.13	0.013251	1.80	0.735
z9	13.272	0.022	13.359	0.025	13.49	0.31	0.64	3.92	0.72	5.43	335	0.0020609	0.17	0.013372	2.30	0.717
z14	13.277	0.026	13.364	0.027	13.35	0.38	0.39	1.94	0.43	4.53	302	0.0020617	0.19	0.013233	2.84	0.773
ANC																
z13	11.618	0.019	11.705	0.022	11.49	0.25	1.23	3.22	0.48	6.71	356	0.0018039	0.16	0.011381	2.22	0.724
z5	11.623	0.038	11.710	0.039	11.84	0.56	1.10	4.53	1.54	2.94	172	0.0018046	0.33	0.011732	4.72	0.734
z12	11.625	0.018	11.712	0.021	11.44	0.21	1.27	4.12	0.47	8.80	458	0.0018050	0.16	0.011333	1.86	0.610

(Table 4.1 continued)

z1	11.628	0.017	11.715	0.020	11.62	0.25	1.28	4.65	0.65	7.13	373	0.0018054	0.15	0.011507	2.14	0.703
z6	11.630	0.013	11.717	0.017	11.71	0.15	1.06	4.36	0.38	11.44	618	0.0018058	0.11	0.011603	1.33	0.596
z11	11.630	0.019	11.717	0.022	11.73	0.19	1.41	4.93	0.51	9.58	482	0.0018058	0.16	0.011616	1.61	0.555
z2	11.635	0.018	11.722	0.021	11.75	0.28	1.28	3.41	0.51	6.68	351	0.0018065	0.16	0.011638	2.39	0.722
z10	11.649	0.014	11.736	0.017	11.74	0.18	1.39	4.44	0.44	10.18	513	0.0018087	0.12	0.011634	1.51	0.616
z9	11.655	0.033	11.742	0.034	11.80	0.47	1.36	5.26	1.45	3.63	196	0.0018096	0.28	0.011692	3.99	0.714
z3	13.481	0.022	13.568	0.024	13.44	0.32	1.28	5.44	0.89	6.10	324	0.0020934	0.16	0.013324	2.37	0.726
MDC-1																
z4	7.501	0.020	7.588	0.023	7.63	0.31	0.57	1.26	0.41	3.05	200	0.0011643	0.27	0.007542	4.08	0.752
z5	7.507	0.020	7.594	0.022	7.69	0.29	0.58	1.46	0.44	3.32	215	0.0011652	0.26	0.007601	3.75	0.755
z8	7.508	0.021	7.595	0.023	7.77	0.30	0.55	0.93	0.29	3.25	213	0.0011654	0.27	0.007686	3.85	0.763
z6	7.517	0.026	7.604	0.027	7.81	0.38	0.61	1.16	0.48	2.41	160	0.0011668	0.34	0.007717	4.94	0.756
z2	7.521	0.016	7.608	0.020	7.62	0.24	0.74	2.61	0.66	3.95	243	0.0011673	0.22	0.007530	3.19	0.746
z3	7.524	0.014	7.611	0.018	7.59	0.20	0.85	2.45	0.48	5.10	301	0.0011678	0.19	0.007498	2.65	0.754
z7	7.530	0.030	7.617	0.031	7.72	0.45	0.75	0.87	0.40	2.17	142	0.0011688	0.39	0.007636	5.82	0.751
z1	7.561	0.010	7.648	0.015	7.62	0.13	0.69	3.36	0.46	7.34	441	0.0011736	0.13	0.007533	1.78	0.742
MDC-2																
z5	7.492	0.017	7.580	0.020	7.61	0.26	0.50	1.73	0.51	3.42	225	0.0011629	0.23	0.007519	3.43	0.755
z4	7.495	0.017	7.583	0.020	7.69	0.25	0.52	1.69	0.47	3.60	235	0.0011634	0.23	0.007598	3.28	0.774
z2	7.499	0.022	7.586	0.024	7.79	0.33	0.52	1.14	0.40	2.84	190	0.0011640	0.30	0.007701	4.29	0.779
z1	7.500	0.021	7.588	0.023	7.73	0.32	0.57	1.48	0.52	2.83	187	0.0011642	0.28	0.007640	4.13	0.748
z3	7.500	0.020	7.588	0.022	7.58	0.29	0.57	1.33	0.42	3.18	208	0.0011642	0.26	0.007494	3.83	0.759
z8	7.508	0.025	7.595	0.027	7.79	0.38	0.53	1.39	0.58	2.41	164	0.0011653	0.34	0.007706	4.87	0.765
z6	7.510	0.017	7.598	0.020	7.82	0.26	0.53	1.40	0.39	3.54	231	0.0011657	0.23	0.007729	3.32	0.739
z7	7.516	0.022	7.603	0.024	7.54	0.32	0.55	1.36	0.47	2.86	189	0.0011666	0.29	0.007454	4.31	0.753
MDC-3																
z14	7.340	0.013	7.427	0.017	7.49	0.19	0.46	2.75	0.61	4.47	292	0.0011392	0.18	0.007401	2.59	0.743
z3	7.344	0.006	7.431	0.012	7.39	0.07	0.36	6.81	0.59	11.57	747	0.0011399	0.09	0.007308	1.00	0.618
z11	7.348	0.005	7.435	0.012	7.46	0.04	0.30	17.04	0.70	24.19	1570	0.0011404	0.06	0.007376	0.49	0.582
z13	7.351	0.007	7.438	0.013	7.47	0.08	0.08	6.10	0.58	10.50	737	0.0011409	0.10	0.007384	1.08	0.753
z6	7.352	0.006	7.439	0.013	7.43	0.05	0.16	35.19	1.99	17.66	1199	0.0011411	0.09	0.007344	0.64	0.536
z10	7.355	0.021	7.442	0.023	7.29	0.30	0.23	2.12	0.80	2.65	192	0.0011416	0.28	0.007206	4.19	0.735
z15	7.360	0.011	7.447	0.015	7.53	0.16	0.21	4.36	0.84	5.21	361	0.0011423	0.15	0.007447	2.09	0.749
z5	7.361	0.005	7.448	0.012	7.53	0.05	0.13	8.90	0.59	15.06	1031	0.0011425	0.06	0.007442	0.73	0.719
z8	7.372	0.006	7.460	0.012	7.46	0.08	0.23	9.56	0.84	11.44	766	0.0011443	0.09	0.007376	1.02	0.631

(Table 4.1 continued)

z16	7.373	0.010	7.460	0.015	7.50	0.13	0.22	3.79	0.59	6.41	438	0.0011444	0.14	0.007416	1.76	0.773
z7	7.379	0.006	7.467	0.012	7.49	0.08	0.18	9.21	0.88	10.42	709	0.0011454	0.08	0.007400	1.04	0.655
z12	7.399	0.010	7.486	0.015	7.54	0.12	0.43	4.27	0.60	7.14	459	0.0011484	0.13	0.007456	1.66	0.772
z2	7.429	0.006	7.517	0.012	7.51	0.05	0.24	9.27	0.54	17.25	1144	0.0011532	0.08	0.007420	0.72	0.529
z9	7.642	0.026	7.729	0.027	7.86	0.39	0.22	3.41	1.62	2.10	156	0.0011861	0.34	0.007768	5.00	0.749
MDC-4																
z7	7.296	0.007	7.383	0.013	7.43	0.09	0.48	6.02	0.61	9.84	617	0.0011324	0.10	0.007346	1.22	0.695
z2	7.304	0.009	7.392	0.014	7.48	0.13	0.28	2.76	0.45	6.18	417	0.0011337	0.13	0.007394	1.78	0.763
z3	7.342	0.006	7.430	0.012	7.48	0.08	0.16	4.51	0.43	10.59	725	0.0011396	0.08	0.007398	1.07	0.765
z5	7.349	0.014	7.437	0.018	7.48	0.21	0.44	1.83	0.43	4.21	278	0.0011407	0.19	0.007392	2.83	0.761
z6	7.367	0.014	7.455	0.017	7.58	0.21	0.18	1.73	0.43	4.02	285	0.0011435	0.19	0.007492	2.75	0.769
z4	7.383	0.003	7.470	0.011	7.52	0.02	0.13	19.72	0.45	44.11	2985	0.0011460	0.04	0.007433	0.28	0.603
z1	7.401	0.003	7.488	0.011	7.55	0.03	0.15	11.05	0.43	25.57	1732	0.0011487	0.04	0.007461	0.43	0.694
MDC-5																
z4	7.279	0.012	7.367	0.016	7.49	0.18	0.22	1.99	0.45	4.40	307	0.0011298	0.17	0.007404	2.40	0.741
z8	7.305	0.003	7.392	0.011	7.44	0.04	0.21	8.14	0.38	21.56	1437	0.0011338	0.05	0.007357	0.54	0.640
z7	7.336	0.004	7.423	0.012	7.47	0.03	0.21	13.16	0.32	41.54	2754	0.0011386	0.05	0.007381	0.34	0.828
z3	7.378	0.007	7.465	0.013	7.61	0.09	0.31	4.21	0.43	9.87	648	0.0011452	0.09	0.007520	1.14	0.725
z9	7.400	0.007	7.488	0.013	7.51	0.10	0.13	3.54	0.43	8.25	575	0.0011487	0.10	0.007423	1.34	0.744
z2	7.425	0.006	7.512	0.012	7.55	0.06	0.24	7.07	0.44	16.22	1077	0.0011524	0.08	0.007462	0.81	0.745
z6	7.665	0.003	7.752	0.012	7.76	0.04	0.12	7.87	0.34	23.24	1589	0.0011898	0.04	0.007675	0.50	0.749
z11	7.848	0.011	7.936	0.016	8.02	0.11	0.21	4.16	0.50	8.27	563	0.0012182	0.14	0.007934	1.42	0.581
MDC-6																
z9	7.230	0.004	7.317	0.011	7.35	0.05	0.14	6.02	0.34	17.63	1203	0.0011221	0.05	0.007268	0.63	0.629
z2	7.231	0.007	7.319	0.013	7.39	0.07	0.23	3.89	0.33	11.76	787	0.0011224	0.09	0.007306	0.99	0.797
z6	7.235	0.003	7.322	0.011	7.36	0.04	0.32	10.20	0.45	22.75	1467	0.0011229	0.05	0.007279	0.52	0.723
z8	7.247	0.003	7.334	0.011	7.38	0.03	0.27	14.68	0.48	30.57	1992	0.0011248	0.04	0.007293	0.39	0.702
z12	7.248	0.003	7.335	0.011	7.37	0.04	0.28	8.81	0.37	23.93	1561	0.0011249	0.04	0.007287	0.49	0.695
z1	7.287	0.008	7.374	0.014	7.40	0.09	0.19	5.02	0.58	8.65	591	0.0011310	0.11	0.007319	1.25	0.653
z10	7.312	0.004	7.399	0.011	7.44	0.03	0.12	11.09	0.33	33.60	2286	0.0011349	0.05	0.007358	0.37	0.748
z7	7.323	0.003	7.410	0.011	7.47	0.04	0.12	8.77	0.39	22.31	1526	0.0011366	0.04	0.007386	0.49	0.640
z11	7.420	0.006	7.507	0.012	7.58	0.03	0.16	10.42	0.37	28.19	1899	0.0011517	0.08	0.007490	0.46	0.604
z5	7.441	0.005	7.528	0.012	7.58	0.04	0.13	6.88	0.37	18.39	1256	0.0011550	0.06	0.007495	0.59	0.665
z4	7.454	0.004	7.542	0.012	7.57	0.01	0.20	25.79	0.35	74.65	4938	0.0011570	0.05	0.007488	0.19	0.735
z3	7.516	0.004	7.604	0.012	7.63	0.01	0.17	28.77	0.39	74.29	4966	0.0011666	0.05	0.007548	0.19	0.696

(Table 4.1 continued)

MDC-7																
z7	7.109	0.005	7.197	0.012	7.29	0.07	0.21	3.98	0.35	11.46	772	0.0011034	0.08	0.007206	0.97	0.742
z3	7.122	0.005	7.210	0.012	7.30	0.06	0.21	5.27	0.36	14.65	981	0.0011055	0.06	0.007212	0.76	0.728
z1	7.131	0.008	7.218	0.013	7.23	0.11	0.11	3.63	0.52	7.00	492	0.0011068	0.11	0.007143	1.51	0.741
z9	7.142	0.007	7.229	0.013	7.30	0.10	0.52	4.04	0.45	9.03	563	0.0011086	0.10	0.007218	1.33	0.740
z5	7.146	0.004	7.234	0.012	7.31	0.05	0.14	5.92	0.35	16.85	1149	0.0011092	0.06	0.007227	0.68	0.726
z10	7.148	0.004	7.235	0.012	7.28	0.04	0.15	11.29	0.53	21.17	1435	0.0011094	0.05	0.007195	0.54	0.611
z8	7.158	0.004	7.245	0.012	7.30	0.05	0.42	5.87	0.34	17.41	1098	0.0011110	0.06	0.007217	0.71	0.755
z2	7.172	0.004	7.259	0.012	7.30	0.05	0.18	6.10	0.38	16.12	1086	0.0011131	0.06	0.007220	0.72	0.702
z6	7.183	0.008	7.270	0.013	7.35	0.12	0.26	2.55	0.37	6.86	463	0.0011149	0.11	0.007262	1.60	0.743
z4	7.218	0.005	7.305	0.012	7.39	0.05	0.14	6.09	0.39	15.67	1071	0.0011203	0.07	0.007306	0.74	0.710
MDC-8																
z6	6.939	0.010	7.027	0.014	7.21	0.15	0.20	2.08	0.39	5.32	369	0.0010770	0.14	0.007129	2.03	0.747
z7	6.943	0.004	7.030	0.012	7.07	0.05	0.22	7.13	0.42	16.95	1129	0.0010776	0.06	0.006991	0.67	0.735
z10	6.950	0.009	7.037	0.014	7.09	0.12	0.28	2.91	0.45	6.48	436	0.0010787	0.13	0.007004	1.77	0.778
z5	6.975	0.004	7.063	0.012	7.11	0.04	0.24	7.90	0.40	19.63	1299	0.0010826	0.05	0.007029	0.59	0.721
z8	7.076	0.004	7.163	0.011	7.25	0.04	0.11	8.22	0.37	22.17	1519	0.0010983	0.05	0.007164	0.49	0.657
z2	7.096	0.004	7.184	0.011	7.22	0.04	0.29	9.19	0.50	18.26	1193	0.0011014	0.05	0.007133	0.61	0.662
z1	7.224	0.006	7.311	0.013	7.37	0.08	0.18	4.23	0.45	9.40	642	0.0011212	0.08	0.007283	1.15	0.737
z9	7.226	0.006	7.314	0.012	7.39	0.08	0.13	4.59	0.44	10.32	714	0.0011216	0.08	0.007305	1.03	0.745
z4	7.294	0.005	7.382	0.012	7.36	0.06	0.26	7.64	0.54	14.01	928	0.0011322	0.07	0.007272	0.83	0.732

(a) Isotopic dates calculated using the decay constants $\lambda_{238} = 1.55125E^{-10}$ and $\lambda_{235} = 9.8485E^{-10}$ (Jaffey et al. 1971).
(b) Corrected for initial Th/U disequilibrium using radiogenic ^{208}Pb and Th/U[magma] specified.
(c) Th contents calculated from radiogenic 208Pb and the $^{207}Pb/^{206}Pb$ date of the sample, assuming concordance between U-Th and Pb systems.
(d) Total mass of radiogenic Pb.
(e) Total mass of common Pb.
(f) Ratio of radiogenic Pb (including ^{208}Pb) to common Pb.
(h) Measured ratio corrected for fractionation and spike contribution only.
(i) Measured ratios corrected for fractionation, tracer and blank. The composition of the laboratory blank was determined by measuring total procedural blanks spiked with either of the two EARTHTIME tracer solutions. 27 TPBs were measured during the course of this study yielding an average composition of $^{206}Pb/^{204}Pb = 18.469 \pm 0.229$; $^{207}Pb/^{204}Pb = 15.471 \pm 0.160$; $^{208}Pb/^{204}Pb = 38.011 \pm 0.484$ (uncertainties are given as 1 standard deviation).

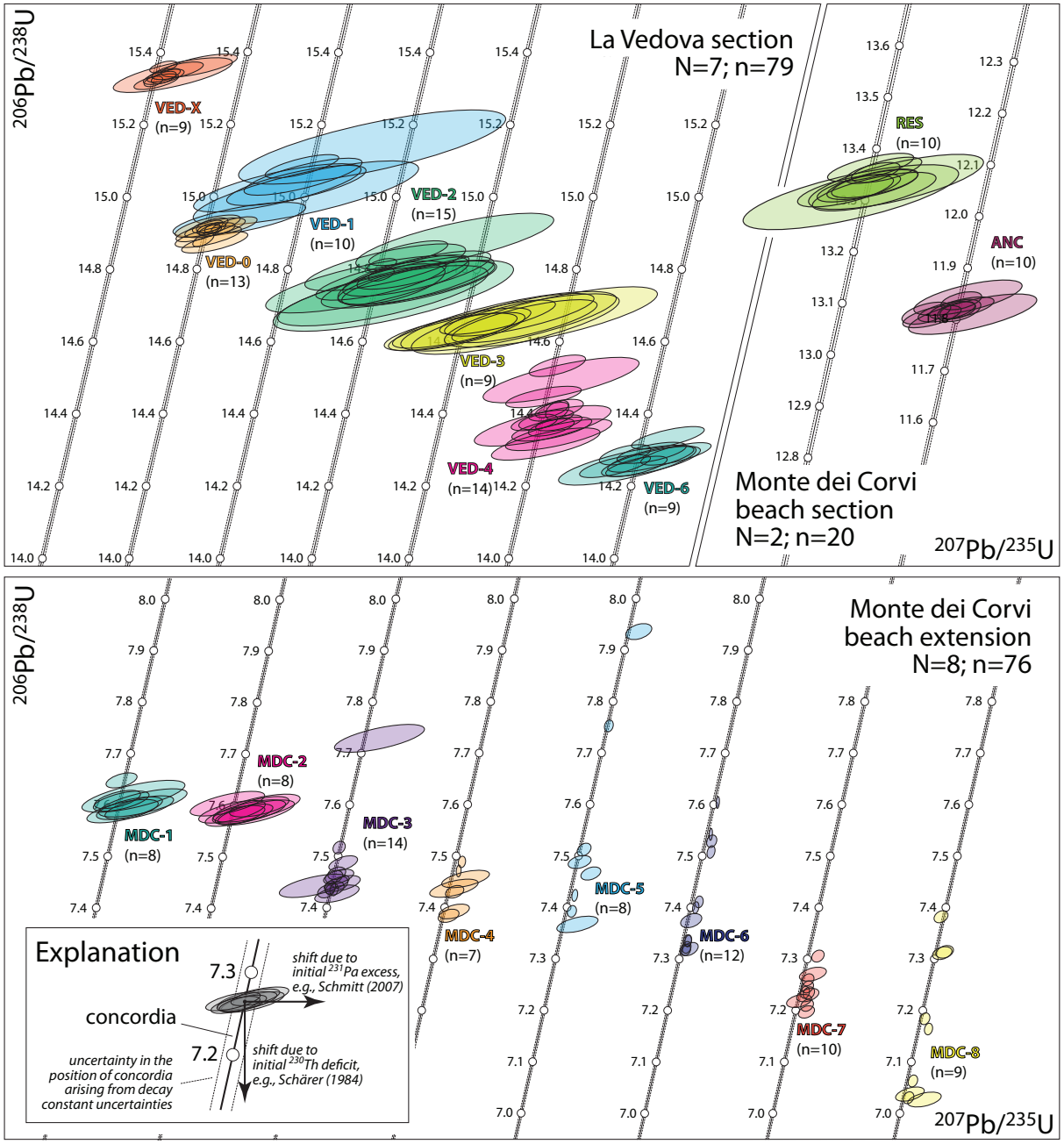

FIGURE 4.3 Zircon U-Pb isotope systematics of analyzed Miocene ash beds shown in concordia space. Shaded ellipses represent the 2σ or 86% confidence interval of individual zircon analyses. N = number of ash beds; n = number of analyzed zircons. Inset (bottom left) illustrates the effects of initial ^{230}Th deficit and ^{231}Pa excess in zircon on U-Pb systematics relative to the theoretical concordia. All analyses were corrected for initial ^{230}Th deficit assuming $D_{Th}/D_U = 0.2 \pm 0.1$ (see text for details) but are uncorrected for initial ^{231}Pa excess. The magnitude of the residual discordance is consistent with that expected from differential Pa-U paritioning during zircon crystallization (Schmitt, 2007; Schmitt, 2011; see text for further details).

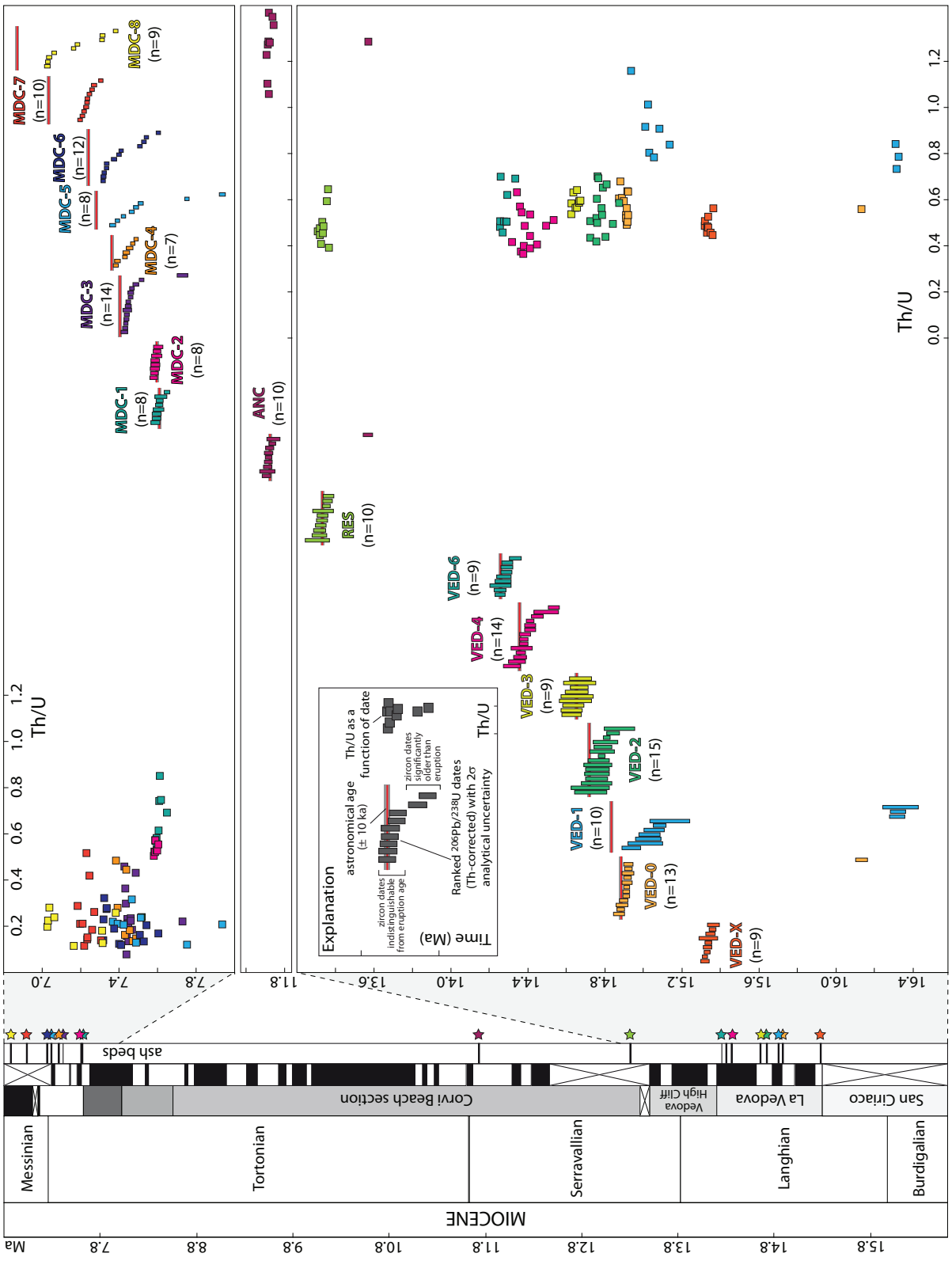
Ma
MIOCENE
Messinian
Tortonian
Serravallian
Langhian
Burdigalian
San Cirilaco
La Vedova
Vedova High Cliff
Corvi Beach section
ash beds
Th/U
MDC-1 (n=8)
MDC-2 (n=8)
MDC-3 (n=14)
MDC-4 (n=7)
MDC-5 (n=8)
MDC-6 (n=12)
MDC-7 (n=10)
MDC-8 (n=9)
ANC (n=10)
RES (n=10)
VED-6 (n=9)
VED-4 (n=14)
VED-3 (n=9)
VED-1 (n=10)
VED-2 (n=15)
VED-0 (n=13)
VED-X (n=9)
Time (Ma)
Explanation
astronomical age (± 10 ka)
Th/U as a function of date
zircon dates indistinguishable from eruption age
zircon dates significantly older than eruption
Ranked 206Pb/238U dates (Th-corrected) with 2σ analytical uncertainty

FIGURE 4.4 (previous page) Intercalibration of zircon U-Pb geochronology and astrochronology. Shown ia a summary of the stratigraphy, astrochronology and geochronology of the Monte dei Corvi and La Vedova sections. Stratigraphy is scaled to the astronomical age models (Hilgen et al., 2003; Hüsing et al., 2007; 2009; 2010; Mourik et al., 2010). Intercomparison of zircon $^{206}Pb/^{238}U$ dates (Th-corrected) and astronomical ages of analyzed ash beds shows single zircon dates with 2σ analytical uncertainty. Astronomical ages are shown as horizontal red bars with grey bars showing a ±10 ka uncertainty interval. Weighted mean dates for statistically equivalent zircon populations are not shown, but are given in Tab. 4.2. Also shown are the Th/U ratios of zircons as a function of $^{206}Pb/^{238}U$ date (see text for discussion).

in Fig. 4.3). The magnitude of the residual discordance is much larger than expected from inaccuracies in the U decay constants (Schoene et al., 2006; Mattinson et al., 2010) or U isotopic composition (Hiess et al., 2012) but is consistent with $^{207}Pb^*$ excess resulting from initial ^{235}U-^{231}Pa disequlibrium. Equivalent to inital ^{238}U-^{230}Th disequlibria, initial ^{235}U-^{231}Pa disequilibria mainly result from differential Pa-U partitioning during zircon crystallization (Schmitt, 2007; 2011) but may also partly be inherited from the $(^{235}U)/(^{231}Pa)$ of the magma. While the magnitude of the initial ^{230}Th deficit is constrained by complete exclusion of Th, translating into a maximum correction corresponding to a 110 ka increase of $^{206}Pb/^{238}U$ dates, the magnitude of ^{231}Pa excess is rather unconstrained and seems to vary significantly (Anczkiewicz et al., 2001; Parrish and Noble, 2003; Crowley et al., 2007; Schmitt, 2007; 2011). We thus only consider initial ^{230}Th deficit corrected $^{206}Pb/^{238}U$ dates for our intercomparison with astronomical ages.

The relationship between Th-corrected zircon $^{206}Pb/^{238}U$ dates and the respective astronomical ages is somewhat different between the La Vedova and Monte dei Corvi ash beds. A detailed comparison of U-Pb dates and astronomical ages is given in Fig. 4.4 and Tab. 4.2.

La Vedova: We dated a total of seventy-nine zircon crystals from six astronomically dated ash beds in the La Vedova section. Analytical uncertainties of single crystal $^{206}Pb/^{238}U$ dates range from 0.015 to 0.10 Ma (2σ; Tab. 4.1). All but one VED ash bed contain zircon populations that, with respect to their $^{206}Pb/^{238}U$ dates, show dispersion largely in excess of analytical scatter (i.e., many dates do not overlap within analytical uncertainty; MSWD >> 1; Tab. 4.2). VED-0 and VED-1 contain single crystals or small subpopulations that are way older than the main population (>16 Ma; Fig. 4.4). All ash beds except for VED-1 contain zircons with $^{206}Pb/^{238}U$ dates that overlap with the astronomical age (Fig. 4.4; Tab. 4.2). For ash beds that contain zircon subpopulations with more than four statistically equivalent single crystal dates including the youngest date, we calculated weighted mean $^{206}Pb/^{238}U$ dates (see summary in Tab. 4.2). Five of six ash beds contained such a population. In case of four ash beds the weighted mean dates overlap with the astronomical age. VED-2 contains a large population of statistically equivalent dates (n=13/15; MSWD = 1.2) with a weighted mean of 14.787 ± 0.019 Ma (analytical uncertainty/including systematic uncertainties). The weighted mean date is 67 ± 21 ka

Table 4.2 *Summary of intercomparison of zircon U-Pb geochronology and orbital tuning of the Monte dei Corvi and La Vedova sections*

Stratigraphy			Astronomical age (Ma)			Youngest $^{206}Pb/^{238}U$ date (Th-corrected)‡						Weighted mean $^{206}Pb/^{238}U$ date (Th-corrected)‡							
Section	Ash bed	Stratigraphic position (m)	Option 1*†	Option 2	Refs.	Date (Ma)	X	Y	Z	Δt (Ma)§	+/-	Date (Ma)	X	Y	Z	n	MSWD	Δt (Ma)§	+/-
La Vedova	VED-X	-	-	-	-	15.319	0.022	0.022	0.026	-	-	15.3298	0.0076	0.0095	0.019	7/9	1.0	-	-
	VED-0	12.95	14.884			14.874	0.029	0.029	0.033	-0.010	0.035	14.9025	0.0073	0.009	0.018	8/13	2.0	0.019	0.021
	VED-1	14.17	14.834			14.936	0.048	0.048	0.051	0.102	0.052	-	-	-	-	-	-	-	-
	VED-2	17.32	14.720			14.724	0.084	0.084	0.086	0.004	0.086	14.787	0.011	0.011	0.019	13/15	1.2	0.067	0.021
	VED-3	19.24	14.654		(1)	14.626	0.052	0.052	0.055	-0.028	0.056	14.649	0.020	0.021	0.029	9/9	0.4	-0.005	0.031
	VED-4	28.82	14.356			14.318	0.045	0.045	0.048	-0.038	0.049	14.368	0.010	0.011	0.019	8/14	1.4	0.012	0.021
	VED-5	31.85	14.300			-	-	-	-	-		-	-	-	-	-	-	-	-
	VED-6	34.20	14.257			14.255	0.028	0.028	0.032	-0.002	0.034	14.275	0.012	0.012	0.019	8/9	1.0	0.018	0.021
Monte dei Corvi	RES	~6.1	13.332	13.296	(2,#)	13.306	0.063	0.063	0.065	-0.026	0.065	13.3401	0.0093	0.011	0.018	10/10	1.5	0.008	0.021
	ANC	61.68	11.724	11.688	(2,4)	11.705	0.022	0.022	0.026	-0.019	0.027	11.7199	0.0072	0.0091	0.015	9/10	1.0	-0.004	0.018
	MDC-1	127.90	7.609	7.581		7.588	0.023	0.023	0.024	-0.021	0.026	7.6026	0.0084	0.0087	0.012	7/8	1.5	-0.006	0.010
	MDC-2	128.07	7.595			7.580	0.020	0.020	0.022	-0.015	0.024	7.5894	0.0079	0.0082	0.011	8/8	1.0	-0.006	0.015
	MDC-3	130.31	7.404	7.414, 7.426		7.427	0.017	0.017	0.019	0.023	0.021	7.4384	0.0049	0.0059	0.0098	8/14	1.1	0.034	0.014
	MDC-4	130.86	7.362	7.36	(3,4)	7.383	0.013	0.013	0.015	0.021	0.018	-	-	-	-	-	-	-	-
	MDC-5	131.95	7.282	7.308		7.367	0.016	0.016	0.018	0.085	0.021	-	-	-	-	-	-	-	-
	MDC-6	132.46	7.242	7.239		7.317	0.011	0.011	0.014	0.075	0.017	7.3256	0.0052	0.0056	0.0096	5/12	2.3	0.084	0.014
	MDC-7	133.77	7.035	7.04		7.197	0.012	0.012	0.014	0.162	0.018	-	-	-	-	-	-	-	-
	MDC-8	135.63	6.870	6.874		7.027	0.014	0.014	0.016	0.157	0.019	-	-	-	-	-	-	-	-

References: (1) Hüsing et al., 2010; (2) Hilgen et al., 2003; (3) Hüsing et al., 2009; (4) Lourens et al., 2004.

(*) Option 1 is the preferred astronomical age and is used for comparison with U-Pb dates throughout this chapter.

(†) Uncertainties on astronomical ages are conservatively estimated to be ± 10 ka which is treated as the 95% confidence interval.

(‡) Uncertainties of U-Pb dates are given at three levels of uncertainty propagation. X includes only analytical uncertainties, Y includes analytical and tracer calibration uncertainties and Z additionally includes the ^{238}U decay constant uncertainty.

(§) Δt denotes the absolute age difference between the U-Pb date and the astronomical age.

(#) Option 1 for RES uses the astronomical age of Hilgen et al. (2003; option 2) and assumes that the offset between the Hilgen et al. (2003) and the Hüsing et al. (2007) tuning is the same for RES and ANC.

older than the astronomical age although many of the single crystal dates are indistinguishable from the astronomical age. Most of the VED ash bed zircons have Th/U ratios ranging from 0.34 to 0.68; very common values for igneous zircon from felsic rocks (e.g., Hoskin and Schaltegger, 2003). Zircons of sample VED-1 have higher Th/U between 0.73 to 1.14 (Fig. 4.4). None of the zircon populations show a correlation between $^{206}Pb/^{238}U$ date and Th/U, but samples that show less dispersion with respect to date also show less dispersion with respect to Th/U.

Monte dei Corvi: Ninety-six zircon crystals from ten ash beds in the Monte dei Corvi section yielded $^{206}Pb/^{238}U$ dates with uncertainties ranging from 0.011 to 0.063 Ma. The two Serravallian ash beds (RES and ANC) yielded simple normally distributed populations of $^{206}Pb/^{238}U$ dates. The weighted mean dates of 13.340 ± 0.018 and 11.720 ± 0.015 Ma (including systematic uncertainties) are indistinguishable from the respective astronomical age. ANC also contains one xenocryst with a $^{206}Pb/^{238}U$ date of 13.568 ± 0.024 Ma. Th/U ratios of RES zircons range from 0.39 to 0.64, while ANC zircons have significantly higher Th/U ratios between 1.06-1.41.

Similar to the Serravallian ashes, the two oldest of the upper Tortonian/lower Messinian ash beds (MDC-1 and MDC-2; Fig 4.4) yielded large populations of statistically equivalent $^{206}Pb/^{238}U$ dates with weighted mean dates of 7.603 ± 0.012 and 7.589 ± 0.011 Ma, respectively (Tab. 4.2). These weighted mean dates are indistinguishable from the astronomical ages. MDC-1 contained one slightly older zircon that was excluded from the weighted mean calculation, and also has a larger range with respect to Th/U (0.55 to 0.85). MDC-2 zircons are chemically very homogeneous with Th/U between 0.50 and 0.57. The stratigraphically younger ashes are very distinct; (1) they yielded very complex zircon populations; (2) the majority of zircons have unusually low Th/U with an average of 0.22 but as low as 0.08 (Fig. 4.4); (3) the offset between the youngest zircon of a given ash bed and the respective astronomical age increases upsection, from 23 ± 21 and 21 ± 18 ka for MDC-3 and MDC-4, to 163 ± 18 and 157 ± 19 ka for MDC-7 and MDC-8 (Tab. 4.2).

4.5 DISCUSSION & CONCLUSIONS

4.5.1 Traceability of zircon U-Pb dates

Pb/U isotopic ratios and derived U-Pb dates determined in this study are traceable to the SI system of units. All Pb and U isotope abundance ratios of ash bed zircons and laboratory blanks as well as the magnitude of instrumental mass fractionation were measured against the EARTHTIME tracer solutions. Condon et al. (submitted) describe in detail the traceability of the calibration of these tracers. The counting experiments for the determination of the ^{238}U and ^{235}U decay constants are well documented in Jaffey et al. (1971) and the accuracy of these determinations has recently been evaluated using closed system zircons (Schoene et al., 2006; Mattinson et al., 2010). Hiess et al. (2012) measured the uranium isotopic composition of terres-

trial accessory minerals against the gravimetrically calibrated IRMM ^{233}U-^{236}U tracer (Richter et al., 2008; Verbruggen et al., 2008). These input parameters allow $^{206}Pb/^{238}U$, $^{207}Pb/^{235}U$ and $^{207}Pb/^{206}Pb$ dates to be traced back to the SI system of units (Condon et al., submitted). However, corrections for initial intermediate daughter product disequilibria add non-traceable parameters to the calculation of U-Pb dates. U-Pb dates that were corrected for initial intermediate daughter product disequilibria are thus not entirely traceable to the SI system of units. This is most relevant and significant for Th-corrected $^{206}Pb/^{238}U$ dates of young zircons where the magnitude of the correction is large relative to the date and uncertainty, but theoretically applies to zircons of any age and also to ^{231}Pa-corrected $^{207}Pb/^{235}U$ and $^{207}Pb/^{206}Pb$ dates corrected for both disequilibria. Most significant for our Messinian to Langhian zircons is the correction for initial ^{230}Th deficit that accounts for an increase of $^{206}Pb/^{238}U$ dates by 87 ± 11 ka, that is 0.5 to 1.5% of the dates.

4.5.2 Accuracy of zircon U-Pb dates

Despite being non-traceable, we consider our model correction for initial ^{238}U-^{230}Th disequilibrium to be accurate and thus our Th-corrected $^{206}Pb/^{238}U$ dates to be accurate within their quoted uncertainties. This can be tested using ash beds that have zircon populations with negligible pre-eruption residence times. For this purpose we here only consider ash beds with simple, normally distributed populations of $^{206}Pb/^{238}U$ dates, assuming that their pre-eruption residence times were short relative to their analytical uncertainties (Fig. 4.5). Th-uncorrected $^{206}Pb/^{238}U$ dates of these ashes are between 69 ± 33 to 115 ± 51 ka younger than the astronomical age of the respective ash bed. All Th-uncorrected dates of these ashes overlap within their uncertainties with the offset predicted from the Th-U partition coefficient ratio of 0.2 ± 0.1 used in our correction, that corresponds to 87 ± 11 ka. Notably, this is true for zircons with Th/U ranging from 0.39 to 1.41 (Fig. 4.5), suggesting that these chemical differences reflect variations in host magma composition and not variations in partition coefficient ratio. We thus conclude that our correction for initial ^{238}U-^{230}Th disequilibrium is accurate within associated uncertainties. Hence, we consider our ^{230}Th-corrected $^{206}Pb/^{238}U$ dates accurate within quoted uncertainties and attribute any offset relative to the respective astronomical ages to reflect true age differences between zircon crystallization and ash bed deposition.

In more general terms, the correction for initial ^{230}Th deficit has recently been considered by many geochronologists as a significant precision and accuracy limiting factor for U-Pb dating of young rocks. Our approach using a constant Th-U partition coefficient ratio with conservative uncertainty estimates, however, results in accurate dates for Miocene ash beds. The uncertainties associated with this correction are the dominant source of uncertainty for many of these Miocene zircons and limit the precision of single zircon dates to ± 11 ka. However, the magnitude of the correction using a constant $D_{Th/U}$ is equal for all zircons

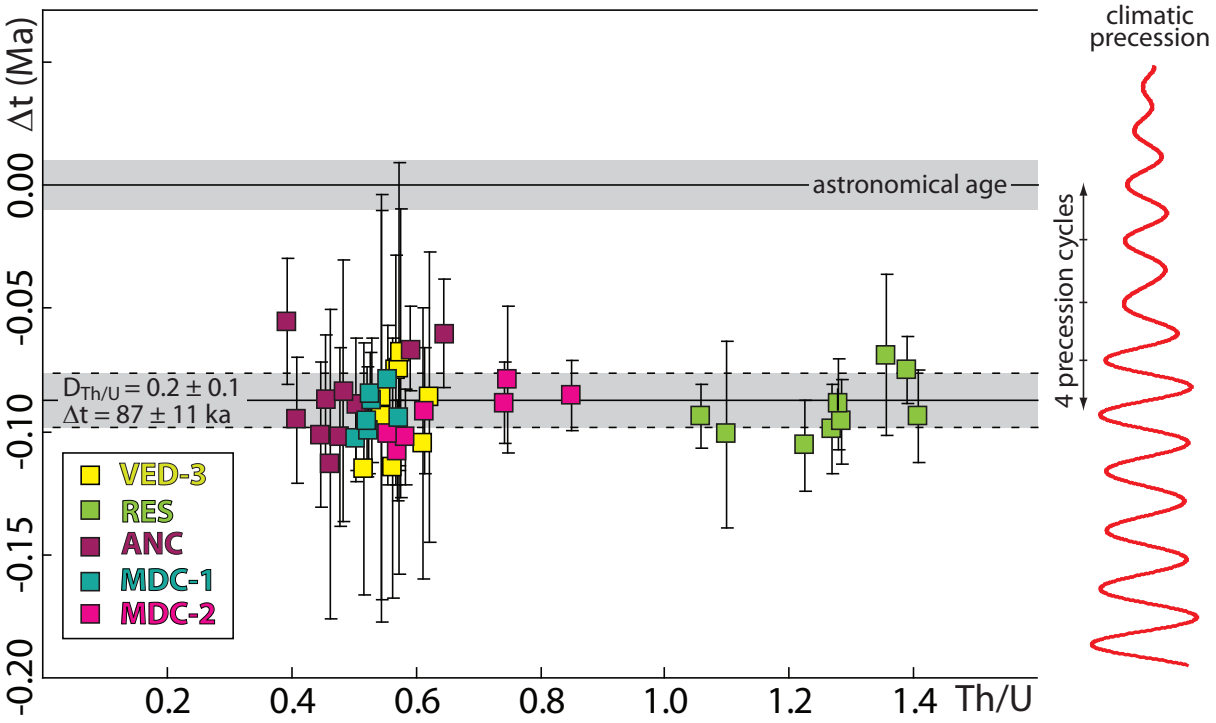

FIGURE 4.5 Evaluation of the initial ^{238}U-^{230}Th disequilibrium correction ("Th-correction") applied to Miocene zircons in this study. Shown is the absolute difference between the Th-uncorrected $^{206}Pb/^{238}U$ dates and the astronomical age as a function of Th/U for samples that yielded simple, normally distributed populations of zircon dates. A Th-U partition coefficient ratio ($D_{Th/U}$) of 0.2 ± 0.1 would result in an initial ^{230}Th deficit corresponding to 87 ± 11 ka. All displayed Th-uncorrected dates overlap with this theoretical offset relative to the astronomical age suggesting that our model correction is accurate within it's uncertainty. Note that the offset between uncorrected $^{206}Pb/^{238}U$ dates and astronomical age is constant over a wide range of zircon Th/U suggesting that variations in zircon Th/U result from variations in Th/U of the melt and not from variations in partition coefficients. Red curve at the right hand side schematically shows the climatic precession curve over ~260 ka. The magnitude of the Th-correction corresponds to approximately four climatic precession cycles, illustating the significance of this correction for the intercalibration of zircon U-Pb geochronology and astrochronology. See text for further details.

and thus associated uncertainties may be treated as systematic, equivalent to decay constant and tracer calibration uncertainties. Future efforts to determine zircon-melt partition coefficients for Th and U over a wide range of melt compositions will allow the U-Pb community to use a common and consistent set of values. In cases where it is feasible to directly measure Th/U of a reasonable proxy for melt composition (e.g., melt inclusions in quartz or zircon, matrix glass, bulk rock etc.), $^{206}Pb/^{238}U$ dates corrected using different approaches should be reported to assess the sensitivity of the dates and the corresponding interpretation to differences in the applied correction (e.g., Rioux et al., 2012).

4.5.3 Interpreting ash bed zircon U-Pb dates: Stratigraphic, geochemical and petrologic considerations

Zircon U-Pb dates accurately date zircon crystallization but depending on the pre-eruption evolution of the eruption-feeding magmatic system, zircon crystallization can significantly pre-date eruption and ash bed deposition. In our data set, many ash beds contain zircons that are 10s to 100s of ka older than the respective astronomical age, thus, significantly pre-dating deposition. However, most ash beds also contain zircons with U-Pb dates overlapping the respective astronomical age (Fig. 4.4), suggesting that these zircons crystallized close to eruption and accurately date ash bed deposition. A simple way to evaluate zircon U-Pb dates of ash beds in stratigraphic sequences is that they have to be consistent with the stratigraphic order, i.e., ash beds should progressively yield younger zircon U-Pb dates up section, if they date ash bed deposition. With the exception of VED-1, this is the case throughout the La Vedova and Monte dei Corvi sections. Considering only the youngest U-Pb date of a given ash bed to interpret ash bed deposition, results in excellent agreement with the astronomical age model for most of the sequence.

The youngest six upper Tortonian to lower Messinian ash beds yielded U-Pb dates that show an increasing offset between U-Pb dates and astronomical age up section but they do not violate stratigraphic order, when taking the youngest zircon date of a given ash bed as the deposition age. The close spacing between these ash beds, together with similarities in zircon morphology, Th/U and overlapping age distributions suggest that these ash beds were derived from repeatedly tapping a common magmatic source. These eruptions sample complex zircon populations reflecting the protracted growth and evolution of the eruption-feeding upper-crustal magmatic system. This example of the upper Tortonian to lower Messinian ash beds at Monte dei Corvi, nicely illustrates that stratigraphic consistency does not guarantee accuracy. It furthermore illustrates how the non-systematic nature of the bias induced by prolonged pre-eruption zircon growth impacts relative chronology and thus may result in inaccurate durations and process rates. This is of particular importance in high-resolution chronostratigraphic studies, e.g, across important stage boundaries that are marked by important events, such as mass extinctions. Geochemical proxies for ash bed provenance and ash bed petrology will significantly improve data interpretation confidence in such scenarios.

4.5.4 Implications for the intercalibration of radioisotope geochronometers

The difference between zircon crystallization and eruption ages may affect radioisotopic systems that were calibrated against the U-Pb system. However, this bias is most significant for young volcanic rocks. Most intercalibration efforts aim to calibrate fundamental parameters, such as decay constants, of the radioisotopic system of interest relative to the U-Pb system. For this purpose, significantly older rocks are usually used, for which the time scales of zircon crystalli-

zation are negligibly short relative to the absolute age (e.g., Scherer et al., 2001; Selby et al., 2007; Nebel et al., 2010). Hence, results of these studies are insensitive to small changes in U-Pb dates related to prolonged zircon crystallization.

One exception is the $^{40}Ar/^{39}Ar$ method for which Renne et al. (2010; 2011) reported a calibration based on data from counting experiments and pairs of sanidine $^{40}Ar/^{39}Ar$ and zircon U-Pb dates. For this calibration Renne et al. (2010; 2011) also employed Mesozoic and Cenozoic rocks, for which the age difference between zircon crystallization and eruption is potentially significant. These authors corrected zircon U-Pb dates for 90 ± 77 ka of pre-eruption residence time. As also discussed by Renne et al. (submitted) for their data set, this correction is significantly larger than the intercalibration of U-Pb dates and astrochronology for most ash beds herein implies. Recent studies suggest that the Renne et al. (2010; 2011) calibration yields erroneously old ages for Neogene rocks (e.g., Renne et al., submitted). If the correction for residence time employed by Renne et al. (2010; 2011) would be overestimated, $^{40}Ar/^{39}Ar$ dates calculated using this calibration would be too young; the opposite of what is suggested by recent intercalibration studies (Renne et al., submitted). However, given the non-systematic nature of the offset caused by prolonged pre-eruption zircon crystallization we can not exclude the possibility that some of the zircon dates employed by Renne et al. (2010; 2011) suffer from significantly longer pre-eruption residence times. This would explain why the Renne et al. (2010; 2011) calibration yields too old ages for young rocks.

Alternative calibrations of the $^{40}Ar/^{39}Ar$ system, such as those based on intercalibration of $^{40}Ar/^{39}Ar$ dates and orbital tuning (Kuiper et al., 2008; Rivera et al., 2011), may thus be favoured for calculating $^{40}Ar/^{39}Ar$ dates for young (i.e., Neogen) rocks.

4.5.5 Implications for zircon U-Pb calibrated geologic time scales

Much of the Paleozoic and Mesozoic geologic time scales is based on zircon U-Pb dates of ash beds intercalated with fossiliferous sediments. Assuming relative uncertainties of 0.05 to 0.1% for most of these dates, absolute uncertainties are on the order of 100,000 to 500,000 years. These absolute uncertainties are about an order of magnitude larger than uncertainties of our U-Pb dates reported herein. Hence, much of the complexities resulting from prolonged pre-eruptive zircon growth will be masked by the uncertainties. The complexities resolved herein will thus not significantly jeopardize the accuracy of ash bed deposition ages derived from these zircon U-Pb data sets. Many of the most recent data sets (e.g., Schoene et al., 2010; Davydov et al., 2010; Schmitz and Davydov, 2012; Guex et al., 2012; Wotzlaw et al., submitted), nevertheless, resolve complexities in excess of analytical scatter requiring careful data interpretation strategies, potentially guided by stratigraphic, geochemical, and petrologic constraints.

REFERENCES CITED

Anczkiewicz, R., Oberli, F., Burg, J.P., Villa,

I.M., Günther, D., and Meier, M., 2001. Timing of normal faulting along the Indus Suture in Pakistan Himalaya and a case of major $^{231}Pa/^{235}U$ initial disequilibrium in zircon. Earth Planet. Sci. Lett., v. 191, p. 101–114.

Bindeman, I.N., Schmitt, A.K., and Valley, J.W., 2006. U-Pb zircon geochronology of silicic tuffs from the Timber Mountain/ Oasis Valley caldera complex, Nevada: rapid generation of large volume magmas by shallow-level remelting. Contrib. Mineral. Petrol., v. 152, p. 649–665.

Bowring, J.F., McLean, N.M., and Bowring, S.A., 2011. Engineering cyber infrastructure for U-Pb geochronology: Tripoli and U-Pb_Redux. Geochem. Geophys. Geosyst., v. 12 (6), doi: 10.1029/2010GC003479.

Bowring, S. A., Schoene, B., Crowley, J.L., Ramezani, J., and Condon, D.J., 2006. High-precision U-Pb zircon geochronology and the stratigraphic record: progress and promise. The Paleontological Society Papers, v. 12, p. 25–46.

Condon, D.J., Schoene, B., McLean, N.M., Bowring, S.A., and Parrish, R.R., submitted. Metrology and traceability of U-Pb isotope dilution geochronology (EARTHTIME Tracer Calibration Part I). Submitted to Geochem. Geophys. Geosyst.

Crowley, J.L., Schoene, B., and Bowring, S.A., 2007. U-Pb dating of zircon in the Bishop Tuff at the millennial scale. Geology, v. 35, p. 1123–1126.

Davydov, V.I., Crowley, J.L., Schmitz, M.D., and Poletaev, V.I., 2010. High-precision U-Pb zircon age calibration of the global Carboniferous time scale and Milankovitch-band cyclicity in the Donets Basin, eastern Ukraine. Geochem. Geophys. Geosyst., v. 11 (1), doi:10.1029/2009GC002736.

Gerstenberger, H., and Haase, G., 1997. A highly effective emitter substance for mass spectrometric Pb isotope ratio determinations. Chem. Geol., v. 136, p. 309–312.

Gradstein, F.M, Ogg, J.G., Schmitz, M.D., and Ogg, G.M., (eds.), 2012. The Geologic Time Scale 2012. Elsevier, Oxford-Amsterdam-Waltham, 1144 pp.

Guex, J., Schoene, B., Bartolini, A., Spangenberg, J., Schaltegger, U., O'Dogherty, L., Taylor, D., Bucher, H., and Atudorei, V., 2012, Geochronological constraints on post-extinction recovery of the ammonoids and carbon cycle perturbations during the Early Jurassic. Palaeogeogr. Palaeoclimatol. Palaeoecol., v. 346–347, p. 1–11.

Hiess, J., Condon, D.J., McLean, N.M., and Noble, S.R., 2012. $^{238}U/^{235}U$ systematics in terrestrial uranium-bearing minerals. Science, v. 335, p. 1610–1614.

Hilgen, F.J., Krijgsman, W., and Wijbrans, J.R., 1997. Direct comparison of astronomical and $^{40}Ar/^{39}Ar$ ages of ash beds: Potential implications for the age of mineral dating standards. Geophys. Res. Lett., v. 24, p. 2043–2046.

Hilgen, F.J., Abdul Aziz, H., Krijgsman, W., Raffi, I., and Turco, E., 2003. Integrated stratigraphy and astronomical tuning of the Serravallian and lower Tortonian at Monte dei Corvi (Middle-Upper Miocene, northern Italy). Palaeogeogr. Palaeoclimatol. Palaeoecol., v. 199, p. 229–264.

Hilgen, F.J., Abdul Aziz, H., Bice, D., Iaccarino, S., Krijgsman, W., Kuiper, K.F., Montanari, A., Raffi, I., Turco, E., and Zachariasse, W.J., 2005. The Global Boundary Stratotype Section and Point (GSSP) of the Tortonian Stage (Upper Miocene) at Monte dei Corvi. Episodes, v. 28, p. 6–17.

Hilgen, F.J., Kuiper, K.F., Krijgsman, W., Snel, E., and Van der Laan, E., 2007. Astronomical tuning as the basis for high resolution chronostratigraphy: the intricate history of the Messinian Salinity Cri-

sis. Stratigraphy, v. 4, p. 231–238.
Hilgen, F.J., Lourens, L.J., Van Dam, J.A., Beu, A.G., Boyes, A.F., Cooper, R.A., Krijgsman, W., Ogg, J.G., Piller, W.E., and Wilson, D.S., 2012. The Neogene Period in Gradstein, F.M, Ogg, J.G., Schmitz, M.D., and Ogg, G.M., eds., The Geologic Time Scale 2012: Elsevier, Oxford-Amsterdam-Waltham, p. 681–730.
Hinnov, L.A., and Hilgen, F.J., 2012. Cyclostratigraphy and Astrochronology, in Gradstein, F.M, Ogg, J.G., Schmitz, M.D., and Ogg, G.M., eds., The Geologic Time Scale 2012. Elsevier, Oxford-Amsterdam-Waltham, p. 63–83.
Hoskin, P.W.O., and Schaltegger, U., 2003. The composition of zircon and igneous and metamorphic petrogenesis, in Hanchar, J.M. and Hoskin, P.W.O., eds., Zircon. Rev. Mineral. Geochem., v. 53, p. 27–62.
Hüsing, S.K., Hilgen, F.J., Abdul Aziz, H., and Krijgsman, W., 2007. Completing the Neogene geological time scale between 8.5 and 12.5 Ma. Earth Planet. Sci. Lett., v. 253, p. 340–358.
Hüsing, S.K., 2008. Astrochronology of the Mediterranean Miocene: Linking palaeoenvironmental changes to gateway dynamics. Ph.D. Thesis, Utrecht University, Geologica Ultraiectina, v. 295, 171 pp.
Hüsing, S.K., Kuiper, K.F., Link, W., Hilgen, F.J., and Krijgsman, W., 2009. The upper Tortonian-lower Messinian at Monte dei Corvi (Northern Apennines, Italy): Completing a Mediterranean reference section for the Tortonian Stage. Earth Planet. Sci. Lett., v. 282, p. 140–157.
Hüsing, S.K., Cascella, A., Hilgen, F.J., Krijgsman, W., Kuiper, K.F., Turco, E., and Wilson, D., 2010. Astrochronology of the Mediterranean Langhian between 15.29 and 14.17 Ma. Earth Planet. Sci. Lett., v. 290, p. 254–269.
Jaffey, A.H., Flynn, K.F., Glendenin, L.E., Bentley, W.C., and Essling, A.M., 1971. Precision measurement of half-lives and specific activities of ^{235}U and ^{238}U. Phys. Rev., v. C4 (5), p. 1889–1906.
Krijgsman, W., Hilgen, F.J., Raffi, I., Sierro, F.J., and Wilson, D., 1999. Chronology, causes and progression of the Messinian salinity crisis. Nature, v. 400, p. 652–655.
Krogh, T.E., 1973. A low contamination method for hydrothermal decomposition of zircon and extraction of U and Pb for isotopic age determination. Geochim. Cosmochim. Acta, v. 37, p. 485–494.
Krogh, T. E., 1982. Improved accuracy of U-Pb zircon ages by the creation of more concordant zircon systems using an air abrasion technique. Geochim. Cosmochim. Acta, v. 46, p. 637–649.
Kuiper, K.F., Hilgen, F.J., Steenbrink, J., and Wijbrans, J.R., 2004. $^{40}Ar/^{39}Ar$ ages of tephras intercalated in astronomical tuned Neogene sedimentary sequences in the eastern Mediterranean. Earth Planet. Sci. Lett., v. 222, p. 583–597.
Kuiper, K.F., Wijbrans, J.R., and Hilgen, F.J., 2005. Radioisotopic dating of the Tortonian Global Stratotype Section and Point; Implications for intercalibration of $^{40}Ar/^{39}Ar$ and astronomical dating methods. Terra Nova, v. 17, p. 385–398.
Kuiper, K.F., Deino, A., Hilgen, F.J., Krijgsman, W., Renne, P.R., and Wijbrans, J.R., 2008. Synchronizing Rock Clocks of Earth History. Science, v. 320, p. 500–504.
Laskar, J., Robutel, P., Joutel, F., Gastineau, M., Correia, A.C.M., and Levrard, B., 2004. A long-term numerical solution for the insolation quantities of the Earth: Astron. Astrophys., v. 428, p. 261–285.
Laskar, J., Fienga, A., Gastineau, M., and Manche, H., 2011. La2010: A new orbital solution for the long-term motion of the Earth. Astron. Astrophys., v. 532, p. A89.
Lourens, L.J., Hilgen, F.J., Shackleton, N.J., Laskar, J., and Wilson, D., 2004. The

Neogene Period, in Gradstein, F.M., Ogg, J.G., Smith, A.G., eds., A Geological Time Scale 2004. Cambridge University Press, Cambridge, p. 409–440.

Mader, D., Montanari, A., Gattacceca, J., Koeberl, C., Handler, R., and Coccioni, R., 2001. $^{40}Ar/^{39}Ar$ dating of a Langhian biotite-rich clay layer in the pelagic sequence of the Conero Riviera, Ancona, Italy. Earth Planet. Sci. Lett., v. 194, p. 111–126.

Mader, D., Cleaveland, L., Bice, D., Montanari, A., and Koeberl, C., 2004. High-resolution cyclostratigraphic analysis of multiple climate proxies from a short Langhian pelagic succession in the Conero Riviera, Ancona (Italy). Palaeogeogr. Palaeoclimatol. Palaeoecol., v. 211, p. 325–344.

Mattinson, J.M., 2005. Zircon U-Pb chemical abrasion ("CA-TIMS") method: combined annealing and multi-step partial dissolution analysis for improved precision and accuracy of zircon ages. Chem. Geol., v. 200, p. 47–66.

Mattinson, J. M., 2010. Analysis of the relative decay constants of 235U and 238U by multi-step CA-TIMS measurements of closed-system natural zircon samples. Chem. Geol., v. 275, p. 186–198.

McLean, N.M., Bowring, J.F., and Bowring, S.A., 2011. An algorithm for U-Pb isotope dilution data reduction and uncertainty propagation.Geochem.Geophys.Geosyst., v. 12 (6), doi: 10.1029/2010GC003478.

McLean, N.M., Condon, D.J., Schoene, B., and Bowring, S.A., submitted. Evaluating uncertainties in the calibration of isotopic reference materials and multi-element isotopic tracers (EARTHTIME Tracer Calibration Part II). Submitted to Geochem. Geophys. Geosyst.

Meyers, S.R., Siewert, S.E., Singer, B.S., Sageman, B.B., Condon, D.J., Obradovich, J.D., Jicha, B.R., and Sawyer, D.A., 2012. Intercalibration of radioisotopic and astrochronologic time scales for the Cenomanian-Turonian boundary interval, Western Interior Basin, USA. Geology, v. 40, p. 7–10.

Montanari, A., Beaudoin, B., Chan, L.S., Coccioni, R., Deino, A., De Paolo, D.J., Emmanuel, L., Fornaciari, E., Kruge, M., Lundblad, S., Mozzato, C., Portier, E., Renard, M., Rio, D., Sandroni, P., and Stankiewicz, A., 1997. Integrated stratigraphy of the Middle and Upper Miocene pelagic sequence of the Conero Riviera (Marche region, Italy), in Montanari, A., Odin, G.S., Coccioni, R., eds., Miocene Stratigraphy: An Integrated Approach. Volume Dev. Palaeontol. Stratigr., v. 15, Elsevier, p. 409–450.

Mourik, A.A., Bijkerk, J.F., Cascella, A., Hüsing, S.K., Hilgen, F.J., Lourens, L.J., and Turco, E., 2010. Astronomical tuning of the LaVedova High Cliff section (Ancona, Italy) - Implications of the Middle Miocene Climate Transition for Mediterranean sapropel formation. Earth Planet. Sci. Lett., v. 297, p. 249–261.

Nebel, O., Scherer, E., and Mezger, K., 2010. Evaluation of the ^{87}Rb decay constant by age comparison against the U-Pb system. Earth Planet. Sci. Lett., v. 301, p. 1–8.

Parrish, R.R., and Noble, S.R., 2003. Zircon U-Pb geochronology by isotope dilution–thermal ionisation mass spectrometry (ID-TIMS), in Hanchar, J.M. and Hoskin, P.W.O., eds., Zircon. Rev. Mineral. Geochem., v. 53, p. 183–213.

Pillans, B., and Gibbard, P., 2012. The Quaternary Period, in Gradstein, F.M, Ogg, J.G., Schmitz, M.D., and Ogg, G.M., eds., The Geologic Time Scale 2012. Elsevier, Oxford-Amsterdam-Waltham, p. 979–1010.

Renne, P.R., Mundil, R., Balco, G., Min, K.W., and Ludwig, K.R., 2010. Joint determination of ^{40}K decay constants and

$^{40}Ar^*/^{40}K$ for the Fish Canyon sanidine standard, and improved accuracy for $^{40}Ar/^{39}Ar$ geochronology. Geochim. Cosmochim. Acta, v. 74, p. 5349–5367.

Renne, P.R., Balco, G., Ludwig, K.R., Mundil, R., and Min, K., 2011. Response to the Comment by W.H. Schwarz et al. on "Joint determination of ^{40}K decay constants and $^{40}Ar^*/^{40}K$ for the Fish Canyon sanidine standard, and improved accuracy for $^{40}Ar/^{39}Ar$ geochronology" by P. R Renne et al. (2010). Geochim. Cosmochim. Acta, v. 75, p. 5097–5100.

Renne, P.R., Wotzlaw, J.F., Mark, D.A., Kuiper, K.F., and Schaltegger, U., submitted. $^{40}Ar/^{39}Ar$ and U/Pb dating of the Faneromeni A1 ash and implications for the intercalibration of Cenozoic geochronometers.

Richter, S., Alonso-Munoz, A., Eykens, R., Jacobsson, U., Kuehn, H., Verbruggen, A., Aregbe, Y., Wellum, R., and Keegan, E., 2008. The isotopic composition of natural uranium samples - measurements using the new $^{233}U/^{236}U$ double spike IRMM-3636. Int. J. Mass Spectr., v. 269, p. 145–148.

Rioux, M., Lissenberg, C.J., McLean, N.M., Bowring, S.A., MacLeod, C.J., Hellebrand, E., and Shimizu, N., 2012. Protracted timescales of lower crsutal growth at the fast-spreading East Pacific Rise. Nature Geoscience, v. 5, p. 275–278.

Rivera, T.A., Storey, M., Zeeden, C., Hilgen, F.J., and Kuiper, K., 2011. A refined astronomically calibrated $^{40}Ar/^{39}Ar$ age for Fish Canyon sanidine. Earth Planet. Sci. Lett., v. 311, p. 420–426.

Rivera, T.A., Storey, M., Schmitz, M.D., and Crowley, J.L., 2013. Age intercalibration of $^{40}Ar/^{39}Ar$ sanidine and chemically distinct U/Pb zircon populations from the Alder Creek rhyolite quaternary geochronology standard. Chem. Geol., v. 345, p. 87–98.

Rubatto, D., and Hermann, J., 2007. Experimental zircon/melt and zircon/garnet trace element partitioning and implications for the geochronology of crustal rocks. Chem. Geol., v. 241, p. 38–61.

Schärer, U., 1984. The effect of initial ^{230}Th disequilibrium on young U-Pb ages: the Makalu case, Himalaya. Earth. Planet. Sci. Lett., v. 67, p. 191–204.

Schaltegger, U., Brack, P., Ovtcharova, M., Peytcheva, I., Schoene, B., Stracke, A., Marocchi, M., and Bargossi, G.M., 2009. Zircon and titanite recording 1.5 million years of magma accretion, crystallization and initial cooling in a composite pluton (southern Adamello batholith, northern Italy). Earth Planet. Sci. Lett., v. 286, p. 208–218.

Scherer, E., Münker, C., and Mezger, K., 2001. Calibration of the Lutetium-Hafnium clock. Science, v. 293, p. 683–687.

Schmitt, A.K., 2007. Ion microprobe analysis of $(^{231}Pa)/(^{235}U)$ and an appraisal of protactinium partitioning in igneous zircon. Am. Mineral., v. 92, p. 691–694.

Schmitt, A.K., 2011. Uranium series accessory crystal dating of magmatic processes. Ann. Rev. Earth Planet. Sci., v. 39, p. 321–349.

Schmitz, M.D., and Davydov, V.I., 2012. Quantitative radiometric and biostratigraphic calibration of the Pennsylvanian-Early Permian (Cisuralian) time scale and pan-Euramerican chronostratigraphic correlation. GSA Bulletin, v. 127, p. 549–577.

Schoene, B., Crowley, J.L., Condon, D.C., Schmitz, M.D., and Bowring, S.A., 2006. Reassessing the uranium decay constants for geochronology using ID-TIMS U-Pb data. Geochim. Cosmochim. Acta, v. 70, p. 426–445.

Schoene, B., Guex, J., Bartolini, A., Schaltegger, U., and Blackburn, T.J., 2010. Correlating the end-Triassic mass extinction

and flood basalt volcanism at the 100 ka level. Geology, v. 38, p. 387–390.

Schoene, B., Schaltegger, U., Brack, P., Latkoczy, C., Stracke, A., and Günther, D., 2012. Rates of magma differentiation and emplacement in a ballooning pluton recorded by U-Pb TIMS-TEA, Adamello batholith, Italy. Earth Planet. Sci. Lett., v. 355–356, p. 162–173.

Selby, D., Creaser, R.A., Stein, H.J., Markey, R.S., and Hannah, J.L., 2007. Assessment of the ^{187}Re decay constant by cross calibration of Re-Os molybdenite and U-Pb zircon chronometers in magmatic ore systems. Geochim. Cosmochim. Acta, v. 71, p. 1999–2013.

Simon, J.I., Renne, P.R., and Mundil, R., 2008. Implications of pre-eruptive magmatic histories of zircons for U-Pb geochronology of silicic extrusions. Earth Planet. Sci. Lett., v. 266, p. 182–194.

Thomas, J.B., Bodnar, R.J., Shimizu, N., and Sinha, A.K., 2002. Determination of zircon/melt trace element partition coefficients from SIMS analysis of melt inclusions in zircon. Geochim. Cosmochim. Acta, v. 66, p. 2887–2901.

Verbruggen, A., Eykens, R., Kehoe, F., Kuhn, H., Richter, S., and Aregbe, Y., 2008. Preparation and certification of IRMM-3636, IRMM-3636a and IRMM-3636b. JRC Scientifc and Technical Report, Report EUR 23408 EN.

Wotzlaw, J.F., Bindeman, I.N., Schaltegger, U., Brooks, C.K., and Naslund, H.R., 2012. High-resolution insights into episodes of crystallization, hydrothermal alteration and remelting in the Skaergaard intrusive complex. Earth Planet. Sci. Lett., v. 355–356, p. 199–212.

Wotzlaw, J.F., Schaltegger, U., Frick, D.A., Dungan, M.A., Gerdes, A., and Günther, D., 2013. Tracking the evolution of large-volume silicic magma reservoirs from assembly to supereruption. Geology, v. 41, p. 867–870.

***

Chapter 5

Towards accurate numerical calibration of the Late Triassic: High-precision U-Pb geochronology constraints on the maximum duration of the Rhaetian

J.F. Wotzlaw, J. Guex, A. Bartolini, Y. Gallet, L. Krystyn, C. McRoberts, B. Schoene, D. Taylor, U. Schaltegger

Keywords:
Triassic time scale
Rhaetian
zircon
U-Pb geochronology
biostratigraphy
Newark APTS
mass extinction

ABSTRACT

Numerical calibration of the Late Triassic stages is arguably the most controversial issue in Mesozoic stratigraphy, despite its importance for assessing mechanisms of environmental perturbations and associated biologic consequences preceding the end-Triassic mass extinction. Here we report new CA-TIMS zircon U-Pb dates for volcanic ash beds within the Aramachay Formation of the Pucara Group in Northern Peru that place precise constraints on the maximum age of the Norian-Rhaetian boundary (NRB). The sampled ash bed bearing interval is located just above the last occurence of the bivalve *Monotis subcircularis* and contains horizons that contain the bivalves *Otapiria* aff. *O. norica* and *Oxytoma* cf. *O. inaequivalvis*. These bivalve assemblages clearly place this stratigraphic interval in the uppermost Norian but do not allow to precisely locate the NRB in this section. Zircon U-Pb dates of ash beds constrain the deposition age of this interval to be between 205.70 ± 0.15 Ma and 205.30 ± 0.14 Ma providing precise constraints on the maximum age of the NRB. We further recalibrate previously published zircon U-Pb dates for ash beds bracketing the Triassic-Jurassic boundary employing the most recent calibration of the EARTHTIME tracer solution, resulting in a duration of ~4 m.y. for the Rhaetian. This ends a prolonged controversy about the duration of this stage and has fundamental implications for the rates of paleoenvironmental deterioration that culminated in the end-Triassic mass extinction.

5.1 INTRODUCTION

The uppermost Triassic stage, the Rhaetian, is framed by two different biotic and environmental crises. At its top, the end Triassic-lower Jurassic crisis is marked by one of most severe mass extinctions of the Phanerozoic, followed by a highly perturbed recovery phase during the earliest Jurassic associated with important perturbations in the carbon cycle and strong climatic changes (Tanner et al., 2004; Guex et al., 2004; McElwain et al., 2009; Ruhl et al., 2011; Ruhl and Kürschner, 2011; Bartolini et al., 2012). These abiotic and biotic disturbances were likely driven by several pulses in volcanic activity during the emplacement of the Central Atlantic Magmatic Province (CAMP; Marzoli et al., 2004; Schoene et al., 2010; Blackburn et al., 2013). At its base (Norian-Rhaetian boundary, NRB), the Norian extinction is much less pronounced than the end Triassic extinction but it nevertheless affected a large proportion of the ammonoid genera and saw the near total disappearance of the bivalve *Monotis*, which was dominant in the Late Norian seas almost globally (Tanner et al., 2004; Ogg, 2012). Low paleolatitude conodont faunas of the Tethys ocean show a dramatic turnover from robust *Epigondolella*-dominated to fragile and tiny *Misikella* associations at the NRB, probably related to a major tropical warming during the earliest Rhaetian (Krystyn, 2008). Another major bio-event, which occurred just below the NRB, is the first appearance of coccolithophores, accompanied by a discernible increase in abundance of other calcareous nannofossils (e.g., *Prinsiosphaera triassic*) in the pelagic environments. This was accompanied by the massive development of scleractinian reefs, implying an environment very favourable to biocalcifying organisms during most of the Rhaetian, before their disappearance at the topmost Triassic (Gardin et al., 2012). The abiotic causes of the NRB crisis are still not well known, but the very end of the Norian is characterized by a worldwide regression, which induced important changes in marine lithofacies between the Norian and Rhaetian stages (Golebiowski, 1990).

This prelude to the Triassic-Jurassic biological crisis was marked by several extinction episodes and/or by a stepwise reduction in biodiversity. To better understand this complex biodiversity pattern and its relationship with abiotic mechanisms, absolute temporal constraints are of critical importance. However, the duration of the Rhaetian stage is strongly debated, leading to the concept of a short (~4 m.y.; Gallet et al., 2003; 2007; Lucas et al., 2012) versus long Rhaetian (up to ~10 m.y.; e.g., Olsen et al., 2010; Muttoni et al., 2010; Hüsing et al., 2011; for a synthesis see Ogg, 2012). These different estimates are primarily based on magnetostratigraphic correlations of biostratigraphically constrained marine sections and the continental Newark basin sequence. In this study, we present new high-precision zircon U-Pb dates obtained from volcanic ash beds intercalated with uppermost Norian marine sediments in Northern Peru. To our knowledge, this is the only locality worldwide, where the biostratigraphically defined NRB is associated with

zircon bearing volcanic ash beds. These data allow calculating the duration of the Rhaetian stage. The new data require the short option, which has important implications for the construction of a reliable Late Triassic geological time scale integrating marine (e.g., Tethys) and non-marine (Newark Basin) biostratigraphic and magnetostratigraphic data.

5.2 BIOSTRATIGRAPHIC DEFINITION OF THE NORIAN-RHAETIAN BOUNDARY AND THE SIGNIFICANCE OF BIVALVE BIOCHRONOLOGY IN THE PUCARA BASIN

The biostratigraphic definition of the NRB has been the subject of a long lasting and intense debate (e.g., Krystyn, 1980; Tozer, 1994). After a thorough discussion through the Subcommission on Triassic Stratigraphy (Krystyn, 2010), the base of the Rhaetian has been defined by the first occurrence (FO) of the conodont *Misikella posthernsteini*. This option appears as the most satisfactory because the NRB is then located just above the great Norian crises marked by the disappearance of most monotid bivalves (McRoberts et al., 2008) and by a significant turnover in ammonoid and low-paleolatitude conodont faunas (Krystyn and Kuerschner, 2005; Krystyn, 2008; Ogg, 2012).

Detailed biostratigraphic research has been carried out recently in the Utcubamba Valley (Northern Peru; Fig. 5.1) along a road section between Levanto and Maino. This section, hereafter referred to as the Lavanto section, preserves a complete marine sedimentary sequence from the Upper Norian to the Early Sinemurian (Schaltegger et al., 2008). The thickest sequence is located near Levanto

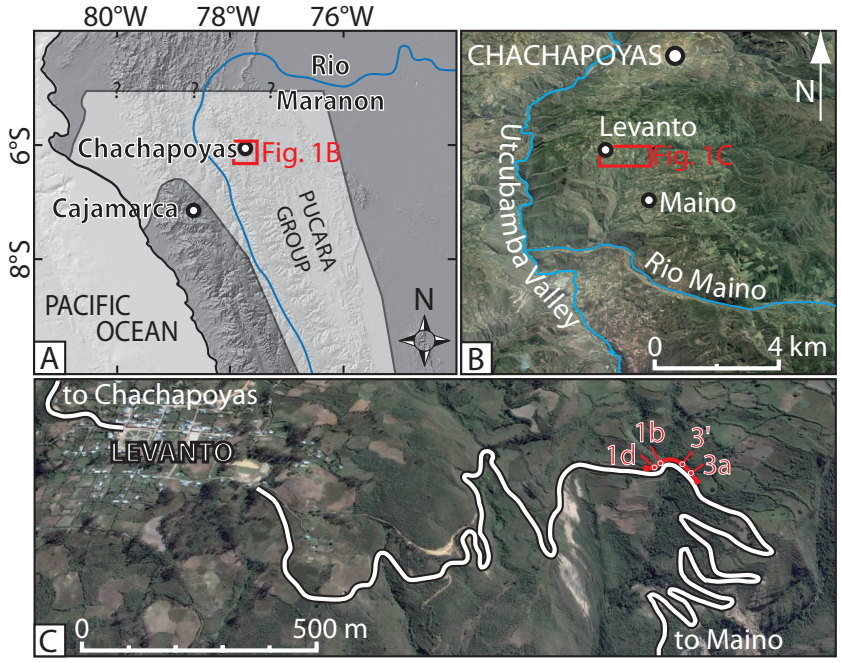

FIGURE 5.1 Geographical framework and geological setting of the study area. (A) Digital elevation model of northern and central Peru showing the location of the study area and the geographical extent of the Triassic-Jurassic Pucara Group. (B) Google EarthTM image with details of the study area to the east of the Utcubamba Valley. (C) Google EarthTM image of the study area along the road from Levanto to Maino with locations of the studied sequence with sampled fossiliferous horizons and volcanic ash beds. See text for details.

(Fig. 5.1B), consists of a thick monotonous sequence of soft brown siltstones alternating with slightly more calcareous silty beds. The Rhaetian of that sequence is poor in ammonites; the few collected specimens allow, however, a reliable correlation with the standard ammonoid zonations used in the Late Rhaetian and Early Jurassic. The base of the Jurassic and thus the TJB is marked by the first occurence of ammonite *Psiloceras spelae* (Fig. 5.2). The highest Rhaetian ammonite-bearing beds contain *Choristoceras crickmayi* and *C. marshi*, the lowest contain a rich Middle Rhaetian fauna with *Vandaites saximontanus*. Our correlation of the NRB is based on a characteristic uppermost Norian bivalve assemblage illustrated in Fig. 5.2 and Fig. A5.2.

Most significant for the definition of the NRB in the Levanto section, is the last occurence of large monotid bivalves, identified here as *Monotis subcircularis*. They are represented by hard gray and massive silty limestones at the base of the section. *Monotis subcircularis* and other large monotid bivalves underwent nearly complete extinction at the top of the Norian. Only two dwarf species that are remarkably different from the typical larger forms, occur in the lower Rhaetian, one crossing the NRB and the other first appearing in the basal Rhaetian (McRoberts, 2008). The extinction of large *Monotis* at the top of the Norian is correlative with the top of the *S. quinquepuncatus* ammonoid zone in the Tethys and the top of the *G. cordilleranus* ammonoid zone in the Americas. At the proposed GSSP at Steinbergkogel (Austria), *Monotis* shell beds are rare and disappear ~14 meters below the NRB with the latter being well defined by conodonts and ammonoids (Krystyn, 2008). The Steinbergkogel succession is entirely consistent with that from the classic Hernstein locality. The Hernstein succession contains many more *Monotis* beds with the last occuring ~1.7 meters below the first occurence of *M. posthernsteini* and some four meters below the first occurence of *Paracochloceras*, thus being closely associated with the NRB. There is some provinciality exhibited in *Monotis* distribution at the species level, with only few species, occuring in both Tethys and Panthalassa, compromising intercontinental correlations. However, our key species for the correlation of the NRB, *Monotis subcircularis*, is perhaps the most studied *Monotis* species anywhere in the world, it is among the largest and most widely distributed throughout both eastern and western Panthalassa. Significant occurences are known from North and South America (from Arctic Alaska to Chile), northern Russia, Japan, Timor and New Zealand (see Tozur, 1980 for a review), and at all these localities, is demonstrably upper Norian. In North America it is commonly associated with ammonoids and conodonts and usually does not survive to the very top of the *G. cordilleranus* zone (Silberling, 1985; Grant-Mackie and Silberling, 1990; Silberling et al., 1997; McRoberts, 2010; 2011). We thus argue that to the best of anyone's biochronologic ability, the uppermost Norian extinctions of large monotid bivalves and most ammonoids is synchronous.

The last occurence of *Monotis sub-*

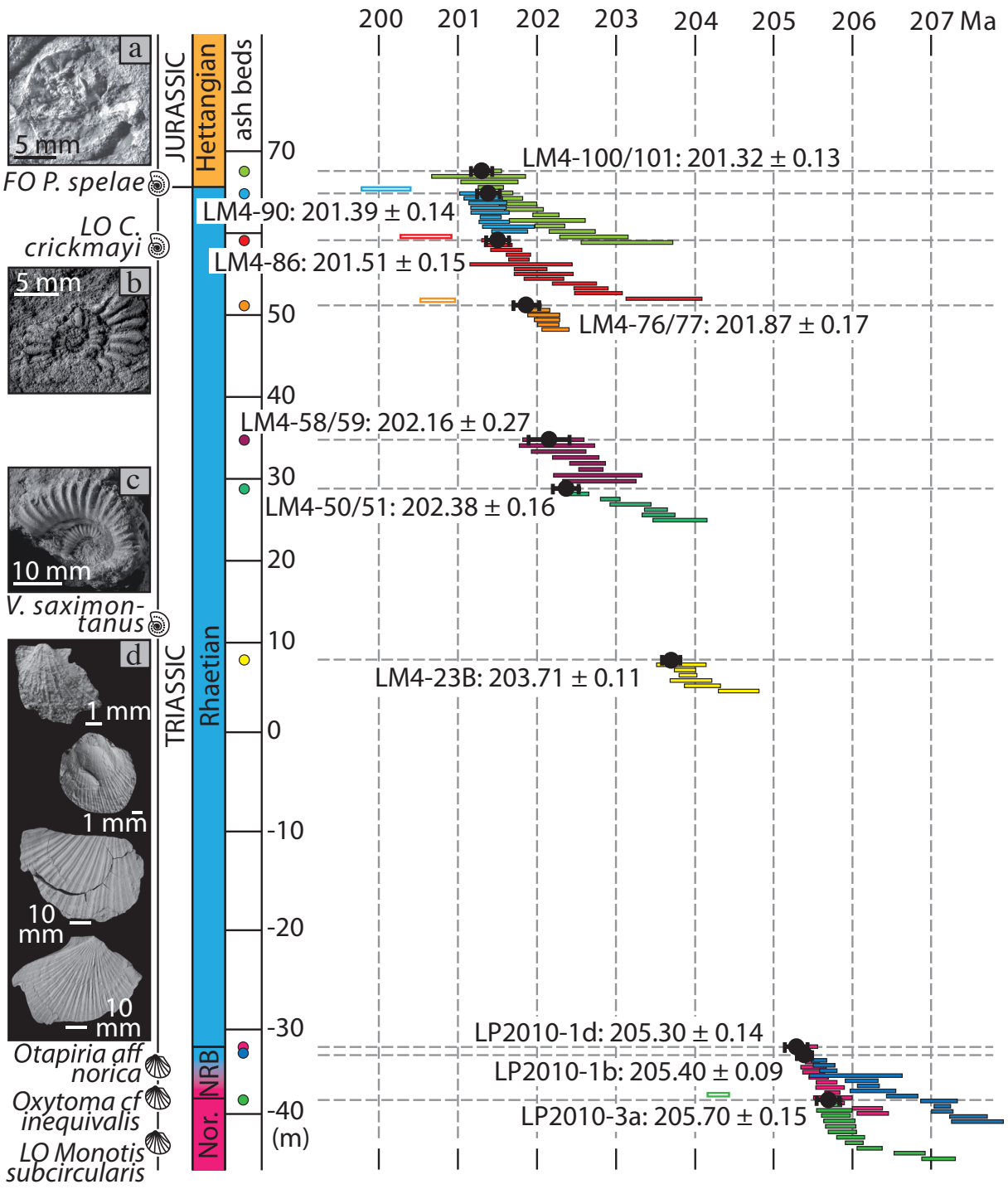
200
201
202
203
204
205
206
207 Ma
a
5 mm
JURASSIC
Hettangian
ash beds
70
FO P. spelae
LM4-100/101: 201.32 ± 0.13
LM4-90: 201.39 ± 0.14
LO C. crickmayi
LM4-86: 201.51 ± 0.15
5 mm
b
50
LM4-76/77: 201.87 ± 0.17
40
LM4-58/59: 202.16 ± 0.27
c
30
LM4-50/51: 202.38 ± 0.16
10 mm
20
V. saximon-tanus
10
LM4-23B: 203.71 ± 0.11
TRIASSIC
Rhaetian
d
1 mm
0
1 mm
-10
10 mm
-20
10 mm
-30
LP2010-1d: 205.30 ± 0.14
Otapiria aff norica
LP2010-1b: 205.40 ± 0.09
Oxytoma cf inequivalis
NRB
LP2010-3a: 205.70 ± 0.15
LO Monotis subcircularis
Nor.
-40
(m)

Figure 5.2 (previous page) Summary of biostratigraphy and U-Pb geochronology for the Upper Triassic of the Pucara Group, Northern Peru. The stratigraphic column shows the occurrences of characteristic ammonites and bivalves and the locations of U-Pb dated ash beds (colored dots). Photographs to the left of the stratigraphic column show representative specimen of collected ammonites and bivalves: (a) *Psiloceras spelae*, (b) *Choristoceras crickmayi*, (c) *Vandaites saximontanus*, (d; from top to bottom) *Oxytoma* cf. *O. inaequivalvis*, *Otapiria* aff. *O. norica*, two specimens of *Monotis subcircularis*. Previously published (Schoene et al., 2010; Guex et al., 2012) and new U–Pb ID-TIMS dates from single zircons are color coded to the corresponding ash bed with the width of the bar representing the 95% confidence level uncertainties. Ash bed deposition ages were computed employing a Monte Carlo based approach that enforces stratigraphic continuity (Guex et al., 2012; see text for details). The computed deposition ages are shown as black dots with uncertainty bar and are given next to the sample names (in Ma ± 2σ). Note that previously published zircon U-Pb dates were re-calculated employing the most recent calibration of the EARTHTIME tracer solution (see text further for details).

circularis in the Levanto section, thus, unequivocally places the overlying ~10 meter-thick stratigraphic interval, including the sampled intercalated volcanic ash beds, in the uppermost Norian. The sampled interval also contains horizons with different bivalves showing temporal and biogeographic affinities that provide additional support for an uppermost Norian and perhaps earliest Rhaetian age. One horizon (*sample 3a*) located some 5 meters above the last *Monotis* bed contains rare ($n = 5$) and largely fragmentary *Oxytoma* which are most similar to specimens illustrated by Ceconi and Westermann (1968) as *Oxytoma* cf. *O. inaequivalvis* from Late Norian strata at Los Molles in coastal Chile (see Appendix for further details). Approximately 5 meters further up-section another horizon (*sample 3'*) contains an abundant fauna (n >50) of poorly preserved *Otapiria*, which are closely related to *Otapiria norica* known from the late Norian (*Cordilleranus* ammonoid zone) of northeastern British Columbia, Canada (McRoberts, 2011; see Appendix for further details). In general, *Otapiria*, although known from as old as Carnian strata, is more common from Rhaetian to Hettangian strata.

Presented biochronologic constraints, particularly the last occurence of *Monotis subcircularis* beds, place the ash bed bearing stratigraphic interval in the uppermost Norian close to the NRB, possibly ranging into the lowermost Rhaetian. Zircon U-Pb dates of intercalated ash beds thus provide precise constraints for the maximum age of the NRB and the in combination with the previously reported age of the TJB (Schoene et al., 2010), constrain the maximum duration of the Rhaetian.

5.3 CA-ID-TIMS ZIRCON U-PB GEOCHRONOLOGY

To place numerical temporal constraints on the age of the NRB, here we report new high-precision zircon U-Pb dates obtained by chemical abrasion isotope dilution thermal ionization mass spectrometry (CA-ID-TIMS) from volcanic ash beds sampled from the 10-meter-thick stratigraphic interval above the highest *Monotis* beds (Fig. 5.2). All U-Pb dates were obtained from single zircon crystals employing CA-ID-TIMS techniques at the University of Geneva

(Schoene et al., 2010; see Appendix for details). Data reduction and uncertainty propagation follow those described in McLean et al. (2011) and were performed employing the U-Pb_Redux software (Bowring et al., 2011). U-Pb dates were calculated relative to the most recent calibration of the EARTHTIME ^{202}Pb-^{205}Pb-^{233}U-^{235}U tracer solution (v. 3.0; http://www.earth-time.org; Condon et al., submitted). Uncertainties are reported at the 95% confidence level and ignore systematic uncertainties associated with the tracer calibration and decay constants unless otherwise noted.

Zircon U-Pb data for sampled ash beds reveal complex zircon populations with the spread in single crystal $^{206}Pb/^{238}U$ dates largely exceeding analytical scatter. Similar complexities were observed by Schoene et al. (2010) and Guex et al. (2012) and we here follow their approach to estimate ash bed deposition from the youngest $^{206}Pb/^{238}U$ dates of the main zircon populations (Fig. 5.2, see Tab. A5.1 and Fig. A5.1 for further details). We further take advantage of the stratigraphic continuity to compute ash bed deposition ages employing a Monte Carlo based approach introduced by Guex et al. (2012). This approach takes the youngest $^{206}Pb/^{238}U$ dates of stratigraphically consecutive ash beds and their normally distributed uncertainties as the primary input parameters and computes a total of 10^6 random age models. Age models that violate stratigraphic superposition (i.e., the ash bed higher up in the sequence must be younger than the one below) are discarded before computing a new ash bed deposition age while constructing a stratigraphically consistent age models. Individual single crystal zircon $^{206}Pb/^{238}U$ dates and the computed deposition ages are plotted in Fig. 5.2 relative to the stratigraphic position of the respective ash bed.

5.4 THE NUMERICAL AGE OF THE NORIAN-RHAETIAN BOUNDARY AND THE DURATION OF THE RHAETIAN

Our calibration of the NRB based on bivalve biochronology and the new high-precision U-Pb dates constrain the maximum numerical age of the NRB to be between 205.70 ± 0.15 Ma and 205.30 ± 0.14 Ma (Fig. 5.2). Assuming that the NRB is located somewhere within the ash bed bearing stratigraphic interval above the last *Monotis* beds, the best estimate for the numerical age of this stage boundary is the mean age of 205.50 ± 0.35 Ma. This new age estimate can be combined with previously published U-Pb dates for the Middle Rhaetian to Lower Jurassic (Schoene et al., 2010; Guex et al., 2012) in order to estimate the maximum duration of the Rhaetian. All three reported U-Pb data sets were produced in the same laboratory using the same EARTHTIME tracer solution. However, the previous datasets (Schoene et al., 2010; Guex et al., 2012) were calculated relative to a previous working calibration of the EARTHTIME tracer. We thus recalculated the older data employing the new tracer calibration (v. 3.0; Condon et al., submitted), allowing comparison between all datasets while ignoring systematic uncertainties (Fig. 5.2). Most importantly for the discus-

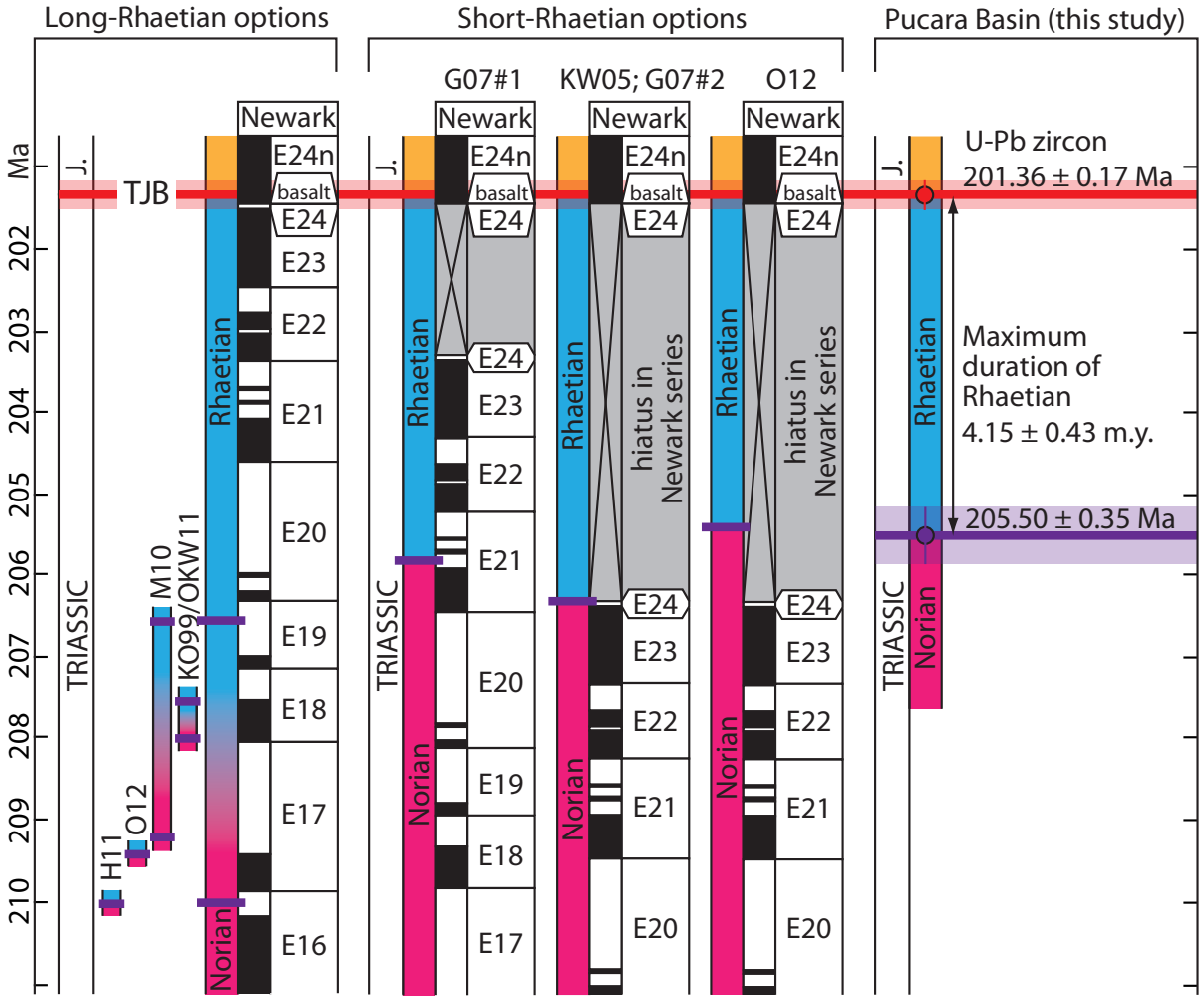

FIGURE 5.3 Comparison of various estimates for the numerical age of the Norian-Rhaetian boundary (NRB) and the duration of the Rhaetian. Shown are suggested correlations of Late Triassic sequences with the Newark basin and their resulting age of the NRB and duration of the Rhaetian (grouped in "long-Rhaetian" and "short-Rhaetian" options) in comparison to our radioisotopic constraints from the Pucara basin. Note that our radioisotopic constraints are in excellent agreement with the short options. Note furthermore that all short options require a hiatus in the Newark basin. Abbreviations: H11 - Hüsing et al. (2011); O12 - Ogg (2012); M10 - Muttoni et al. (2010); KO99 - Kent and Olsen (1999); OKW11 - Olsen et al. (2011); G07 - Gallet et al. 2007 (2 options are shown); KW05 - Kozur and Weems (2005); TJB - Triassic-Jurassic boundary.

sion of the duration of the Rhaetian, the age of the TJB reported by Schoene et al. (2010; 201.31 ± 0.18 Ma), becomes older by ~0.025%, that is 201.36 ± 0.17 Ma. Furthermore, the onset of the marine carbon isotope excursion, considered to reflect the onset of the end-Triassic Extinction (ETE) occurs just before 201.51 ± 0.15 Ma. This latter date is still equivalent to the recalculated age for the North Mountain Basalt (NMB) of 201.481 ± 0.021 Ma. The recently reported age of

201.566 ± 0.031 Ma for the same sample of NMB (Blackburn et al., 2013) does not overlap with our recalculated NMB date at the 95% confidence interval, despite being relative to the same calibration of the EARTHTIME tracer and despite using the same physical constants. This 0.03% systematic bias between the mean values of the two datasets does not affect the conclusions of either study, but remains a target for high-precision U-Pb intercalibration in future work. Using our new estimate for the maximum age of the NRB and the re-calibrated age for the TJB, we estimate the maximum duration of the Rhaetian to be 4.15 ± 0.43 m.y.

5.5 IMPLICATIONS FOR THE CORRELATION OF MARINE TETHYAN SECTIONS AND THE CONTINENTAL NEWARK BASIN

Our estimate for the duration of the Rhaetian helps to partly resolve previous debates about the durations of Late Triassic stages. During the last decade, numerous attempts were made to correlate different magnetostratigraphic datasets obtained from biostratigraphically well constrained marine Tethyan sections and the floating astrochronology of the continental Newark Basin sequence (eastern North America). However, published magnetic polarity data sets from Tethyan sections are inconsistent with each other and a unique correlation with the Newark sequence seems currently not attainable. Various correlation schemes broadly can be grouped in two options for the duration of the Rhaetian. Figure 3 compares the different options for the duration of the Rhaetian, derived from magnetostratigraphic correlations, with our U-Pb geochronologic constraints from the Pucara basin. Gallet et al. (2007) proposed a short duration of ~4.5 m.y. using the new biochronological Rhaetian definition. Other correlation schemes resulted in a significantly longer duration ("long Rhaetian") of up to 8-10 m.y. (for the most recent studies see Muttoni et al., 2010; Olsen et al., 2010; Hüsing et al., 2011; option #2 of Ogg, 2012; Fig. 5.3). Our new data strongly support a short duration of the Rhaetian as suggested by Gallet et al. (2007), although their magnetostratigraphic correlation scheme still requires further testing. A ~4 m.y. duration is furthermore in excellent agreement with other previously proposed Triassic time scales (e.g., Lucas et al., 2012; option #1 of Ogg, 2012). Regarding the now unsupported long Rhaetian option, it is worth stressing that the tentative correlations were performed assuming the fact that the entire Rhaetian was recorded in the Newark basin sequence. This assumption was however strongly questioned by several authors based on biostratigraphic arguments (Kozur and Weems, 2005, 2010; Lucas et al., 2012; Ogg, 2012). In contrary, as discussed in Ogg (2012), the option of a short Rhaetian that is strongly supported by our data, would imply an almost total lack of the Rhaetian in the Newark basin sequence (Fig. 5.3). However, Deenen et al. (2010; 2011) found the same sequence of magnetic reversals and sporomorph turnover below the oldest CAMP lavas in the Argana basin (Morocco) and Fundy basin (Canada). This would require that the same hiatus is present at exactly the same place in

three continental rift basins, despite very different accumulation rates. This is very unlikely, suggesting that there is no hiatus in the uppermost part of the Newark sequence but does not exclude hiatuses further down in the sequence. If there is no hiatus in the Newark sequence, our data require that the NRB is within the long reverse polarity interval of E20 at Newark. Our data certainly require a significant revision of the Late Triassic time-scale and re-evaluation of magnetostratigraphic correlations between marine sections in the Tethys and the continental Newark basin.

5.6 SUMMARY & CONCLUSIONS

We present high-precision zircon U-Pb dates from ash beds intercalated with Late Norian marine sediments in the Pucara basin, Northern Peru. The ash bed bearing interval is located just above the last occurence of *Monotis subcircularis* beds. The Late Norian extinction of these and other monotid bivalves is correlative with uppermost Norian ammonoid and conodont zones, thus, placing this stratigraphic interval into the uppermost Norian, but we can not unequivocally locate the NRB in this section. Zircon U-Pb dates of intercalated ash beds, thus, constrain the maximum age of the NRB and, in combination with previously reported dates from the TJB, the maximum duration of the Rhaetian to be 4.15 ± 0.43 m.y. These are the first zircon U-Pb dates from biochronologically constrained Late Norian strata anywhere in the world and support previously proposed correlations suggesting a short duration of the Rhaetian. They also provide independent constraints on the rates and durations of processes preceeding the end-Triassic mass extinction.

APPENDIX

ANALYTICAL METHODS AND SUPPLEMENTARY DISCUSSION OF NEW U-PB GEOCHRONOLOGY RESULTS

A total of 43 analyses (see Tab. A5.1) of single zircon crystals were performed employing chemical abrasion thermal ionization mass spectrometry techniques at the University of Geneva. Details of the analytical protocols are given in Schoene et al. (2010) and Wotzlaw et al. (2012; 2013). Analyses of 15 zircons from sample LP2010-3a yielded a main population with $^{206}Pb/^{238}U$ dates spreading over ~1.3 Ma. Two analyses returned significantly older and discordant U-Pb dates and one grain yielded a significantly younger date of 204.31 ± 0.13 Ma. In the main population, eight analyses are statistically equivalent with a weighted mean $^{206}Pb/^{238}U$ date of 205.797 ± 0.054/0.076/0.23 Ma (MSWD [mean square weighted deviation]=0.96; Fig. A5.1). The youngest zircon of the main population has a $^{206}Pb/^{238}U$ date of 205.70 ± 0.15/0.16/0.27 Ma. Zircons from sample LP2010-1b yielded the largest spread in $^{206}Pb/^{238}U$ dates of ~2.2 Ma and two distinct population with respect to Th/U (Fig. A5.1). We interpret this sample to be a composite ash bed or composed of reworked volcaniclastic material, rather than a primary air fall ash bed. Nevertheless, the $^{206}Pb/^{238}U$ date of the youngest zircon is consistent

Table A5.1 *U-Pb isotopic data for Upper Norian ash beds from the Pucara basin*

	Dates (Ma)								Composition				Isotopic Ratios							
	$^{206}Pb/^{238}U$	±2σ	$^{206}Pb/^{238}U$	±2σ	$^{207}Pb/^{235}U$	±2σ	$^{207}Pb/^{206}Pb$	±2σ	Th/	Pb*	Pb_c	Pb*/	$^{206}Pb/$	$^{206}Pb/$	±2σ	$^{207}Pb/$	±2σ	$^{207}Pb/$	±2σ	Corr.
		abs		abs		abs		abs	U	(pg)	(pg)	Pb_c	^{204}Pb	^{238}U	%	^{235}U	%	^{206}Pb	%	coef.
Fraction	(a)		(a,b)		(a)		(a)		(d)	(e)	(f)	(g)	(h)	(i)		(i)		(i)		
LP2010-1d																				
z6	205.26	0.19	205.35	0.19	204.5	1.4	195	17	0.57	4.27	0.28	15.27	920	0.0323532	0.10	0.223084	0.8	0.050032	0.7	0.525
z10	205.284	0.080	205.366	0.080	205.5	0.9	208	11	0.90	14.30	0.71	20.09	1111	0.0323572	0.04	0.224280	0.5	0.050294	0.5	0.595
z11	205.292	0.092	205.379	0.092	206.1	0.8	216	10	0.74	8.97	0.42	21.29	1223	0.0323585	0.05	0.225062	0.4	0.050467	0.4	0.487
z5	205.393	0.084	205.483	0.084	205.5	0.8	207	10	0.58	11.86	0.58	20.50	1227	0.0323745	0.04	0.224355	0.4	0.050284	0.4	0.557
z14	205.41	0.15	205.50	0.15	205.3	2.5	203	30	0.62	5.70	0.88	6.47	396	0.0323774	0.08	0.224027	1.4	0.050206	1.3	0.777
z9	205.41	0.13	205.50	0.13	205.5	1.2	207	14	0.70	8.45	0.53	16.08	936	0.0323781	0.07	0.224347	0.6	0.050276	0.6	0.635
z1	205.48	0.12	205.56	0.12	205.7	1.3	208	16	0.71	6.87	0.50	13.74	802	0.0323878	0.06	0.224583	0.7	0.050314	0.7	0.693
z7	205.57	0.13	205.66	0.13	206.4	1.4	216	17	0.64	7.24	0.58	12.57	747	0.0324035	0.06	0.225384	0.8	0.050469	0.7	0.678
z8	205.62	0.17	205.71	0.17	204.5	2.4	192	29	0.64	4.01	0.54	7.47	452	0.0324110	0.09	0.223108	1.3	0.049948	1.2	0.727
z4	205.657	0.090	205.740	0.090	205.9	0.9	209	11	0.87	11.99	0.57	20.97	1167	0.0324169	0.04	0.224858	0.5	0.050330	0.5	0.676
z2	205.66	0.24	205.74	0.24	208.2	3.1	237	36	0.73	3.76	0.61	6.20	370	0.0324167	0.12	0.227609	1.7	0.050947	1.6	0.680
z12	205.709	0.092	205.792	0.092	205.8	0.9	207	10	0.85	8.04	0.36	22.28	1244	0.0324252	0.05	0.224730	0.5	0.050289	0.4	0.652
z13	206.09	0.19	206.18	0.19	206.4	2.5	210	30	0.76	2.84	0.39	7.34	430	0.0324865	0.09	0.225383	1.4	0.050340	1.3	0.701
z3	206.16	0.20	206.25	0.20	205.3	1.6	196	18	0.59	6.59	0.56	11.72	704	0.0324973	0.10	0.224089	0.8	0.050034	0.8	0.585
LP2010-1b																				
z3	205.307	0.094	205.389	0.095	205.7	0.9	210	11	0.90	10.11	0.48	21.01	1161	0.0323609	0.05	0.224552	0.5	0.050349	0.5	0.429
z5	205.483	0.095	205.565	0.096	205.7	0.6	208	7	0.91	20.91	0.51	40.71	2230	0.0323891	0.05	0.224538	0.3	0.050302	0.3	0.608
z4	205.55	0.13	205.63	0.13	205.0	1.5	199	18	0.89	5.27	0.42	12.62	707	0.0323996	0.07	0.223717	0.8	0.050102	0.8	0.519
z14	205.59	0.10	205.68	0.10	205.3	1.1	201	13	0.63	9.14	0.55	16.52	980	0.0324068	0.05	0.224028	0.6	0.050160	0.6	0.423
z6	205.95	0.59	206.03	0.59	204.9	9.4	193	113	0.88	0.98	0.44	2.20	139	0.0324640	0.29	0.223599	5.1	0.049976	4.8	0.826
z15	206.03	0.21	206.11	0.21	205.9	2.7	205	32	0.95	3.29	0.45	7.35	414	0.0324765	0.10	0.224863	1.4	0.050239	1.4	0.664
z8	206.11	0.13	206.19	0.13	206.6	1.3	212	16	0.98	6.86	0.41	16.66	908	0.0324900	0.07	0.225677	0.7	0.050400	0.7	0.563
z12	206.17	0.29	206.25	0.29	206.5	3.7	211	44	0.81	2.69	0.54	4.95	293	0.0324987	0.14	0.225578	2.0	0.050364	1.9	0.607
z11	206.53	0.20	206.62	0.20	207.6	2.4	220	28	0.58	4.20	0.54	7.71	473	0.0325571	0.10	0.226850	1.3	0.050558	1.2	0.730
z9	207.01	0.23	207.09	0.23	206.2	2.2	197	26	0.92	3.68	0.37	9.98	559	0.0326337	0.11	0.225211	1.2	0.050075	1.1	0.492
z1	207.041	0.099	207.131	0.099	206.4	0.9	199	11	0.60	8.30	0.43	19.48	1162	0.0326385	0.05	0.225358	0.5	0.050100	0.5	0.540
z10	207.04	0.13	207.13	0.13	205.7	1.8	191	21	0.55	4.89	0.50	9.76	598	0.0326387	0.07	0.224611	1.0	0.049934	0.9	0.662
z7	207.38	0.23	207.47	0.23	208.9	3.9	227	45	0.62	2.97	0.67	4.44	277	0.0326923	0.11	0.228475	2.0	0.050709	2.0	0.783
z13	207.50	0.33	207.58	0.33	208.1	5.3	215	63	0.89	1.77	0.50	3.54	211	0.0327118	0.16	0.227487	2.8	0.050460	2.7	0.784

(Table A5.1 continued)

LP2010-3a

z1	204.23	0.13	204.31	0.13	203.7	1.2	197	14	0.69	11.43	0.78	14.74	864	0.0321879	0.06	0.222129	0.6	0.050073	0.6	0.587
z10	205.62	0.15	205.70	0.15	206.9	1.2	221	13	0.62	5.98	0.37	16.26	966	0.0324102	0.07	0.225970	0.6	0.050590	0.6	0.662
z3	205.673	0.088	205.763	0.088	205.7	0.9	206	11	0.61	10.09	0.52	19.46	1158	0.0324195	0.04	0.224520	0.5	0.050251	0.5	0.662
z11	205.68	0.22	205.77	0.22	207.0	2.6	222	30	0.65	3.89	0.50	7.83	469	0.0324201	0.11	0.226095	1.4	0.050602	1.3	0.649
z5	205.69	0.18	205.78	0.18	206.0	1.6	209	18	0.67	4.15	0.33	12.68	748	0.0324228	0.09	0.224904	0.8	0.050332	0.8	0.646
z4	205.74	0.20	205.83	0.20	206.7	2.3	218	28	0.70	3.40	0.45	7.51	447	0.0324301	0.10	0.225824	1.3	0.050526	1.2	0.627
z6	205.76	0.19	205.84	0.19	204.5	1.7	190	20	0.75	4.21	0.36	11.70	676	0.0324328	0.09	0.223095	0.9	0.049911	0.9	0.518
z8	205.77	0.17	205.86	0.17	206.2	2.2	211	27	0.69	3.11	0.39	7.95	473	0.0324356	0.09	0.225137	1.2	0.050364	1.1	0.682
z7	205.88	0.18	205.97	0.18	206.4	2.2	212	26	0.94	2.93	0.33	8.89	497	0.0324534	0.09	0.225364	1.2	0.050387	1.1	0.739
z14	205.93	0.12	206.02	0.12	206.2	1.0	209	11	0.85	5.87	0.28	20.89	1168	0.0324611	0.06	0.225140	0.5	0.050325	0.5	0.560
z13	206.13	0.16	206.21	0.16	205.9	1.2	203	14	0.93	6.49	0.34	19.10	1045	0.0324920	0.08	0.224766	0.7	0.050194	0.6	0.675
z9	206.61	0.19	206.70	0.19	206.9	1.4	210	16	0.59	5.02	0.32	15.63	937	0.0325700	0.10	0.226009	0.7	0.050350	0.7	0.470
z15	206.98	0.21	207.07	0.21	208.0	2.6	219	30	0.58	2.47	0.35	7.06	434	0.0326289	0.10	0.227291	1.4	0.050545	1.3	0.685
z12	477.51	1.16	477.60	1.16	524.1	5.5	733	27	0.45	2.36	0.36	6.58	416	0.0768860	0.25	0.675548	1.3	0.063753	1.3	0.431
z2	585.34	0.33	585.43	0.33	734.6	0.9	1222	3	0.29	14.58	0.35	41.67	2605	0.0950503	0.06	1.061663	0.2	0.081045	0.1	0.540

(a) Isotopic dates calculated using the decay constants $\lambda_{238} = 1.55125E^{-10}$ and $\lambda_{235} = 9.8485E^{-10}$ (Jaffey et al., 1971).
(b) Corrected for initial Th/U disequilibrium using radiogenic ^{208}Pb and $Th/U_{[magma]} = 4 \pm 1$.
(c) % discordance = 100 - (100 * ($^{206}Pb/^{238}U$ date) / ($^{207}Pb/^{206}Pb$ date))
(d) Th contents calculated from radiogenic ^{208}Pb and the $^{207}Pb/^{206}Pb$ date of the sample, assuming concordance between U-Th and Pb systems.
(e) Total mass of radiogenic Pb.
(f) Total mass of common Pb.
(g) Ratio of radiogenic Pb (including ^{208}Pb) to common Pb.
(h) Measured ratio corrected for fractionation and spike contribution only.
(i) Measured ratios corrected for fractionation, tracer and blank. The composition of the laboratory blank was determined by measuring total procedural blanks spiked with either of the two EARTHTIME tracer solutions. 27 TPBs were measured during the course of this study yielding an average composition of $^{206}Pb/^{204}Pb = 18.469 \pm 0.229$; $^{207}Pb/^{204}Pb = 15.471 \pm 0.160$; $^{208}Pb/^{204}Pb = 38.011 \pm 0.484$ (uncertainties are given as 1 S.D.).

with respect to its stratigraphic position relative the other two ash bed samples, giving a maximum deposition age of 205.389 ± 0.095/0.11/0.24 Ma. Fourteen analysed zircons from sample LP2010-1d gave $^{206}Pb/^{238}U$ dates with a total spread of ~0.9 Ma. The youngest six zircons have statistically equivalent $^{206}Pb/^{238}U$ dates with a weighted mean of 205.423 ± 0.043/0.68/0.23 Ma (MSWD=1.6; Fig. A5.1). The youngest zircon of this population yielded a $^{206}Pb/^{238}U$ date of 205.35 ± 0.19/0.20/0.30 Ma.

ADDITIONAL DETAILS OF BIVALVE BIOCHRONOLOGY

We here provide some additional details about the bivalves sampled above the last *Monotis subcircularis* beds. They provide some additional but support for an uppermost Norian and perhaps earliest Rhaetian for this stratigraphic interval.

Sample 3a: Located some 5 meters above the last Monotis bed, this horizon contains rare (n = 5) and largely fragmentary *Oxytoma*. The specimens are small and represented only by left valves. They are most similar to specimens illustrated by Ceconi and Westermann (1968) as *Oxytoma* cf. *O. inaequivalvis* from Upper Norian strata at Los Molles in coastal Chile, where they co-occur with the ammonoids *Arcestes* and *Cladiscites*, as well as by Chong and Hillebrandt (1985) from approximately the Norian-Rhaetian boundary at Quebrada Chaco, northern Chile, where they co-occur with a typical Late Norian early Rhaetian bivalve fauna. They are also closely similar to the *Oxytoma sp.* described and illustrated from the late Norian *Cordilleranus* ammonoid zone at Pine Pass, British Columbia, Canada (Westermann, 1966; McRoberts, 2011).

Sample 3': Approximately 5 metres further up section, this horizon contains an abundant fauna (*n* >50) of poorly preserved *Otapiria*. The *Otapiria* are very thin-shelled and likely represent a new species closely related to *Otapiria norica* known from the late Norian (*Cordilleranus* ammonoid zone) of northeastern British Columbia, Canada (McRoberts, 2011). The ornament and outlines are distinctively dissimilar to Rhaetian *Otapiria* from coastal Chile (e.g., *"Otapiria?* cf. *O. ussuriensis"* of Cecioni and Westermann, 1968) which occur some 40 m above the aforementioned *Oxytoma*, and from the Rhaetian of New Zealand (e.g., *O. dissimilis* of Marwick, 1953) or other Rhaetian *Otapiria* from the western Tethys (e.g., *O. marshalli alpina* of Zapfe, 1973). They are also distinctively dissimilar to Carnian-early Norian *Otapiria* such as those from southwest Japan or northeastern Russia (e.g., Ando, 1988; Kiparisova et al., 1966).

REFERENCES CITED

Blackburn, T.J., Olsen, P.E., Bowring, S.A., McLean, N.M., Kent, D.V., Puffer, J., McHone, G., Rasbury, E.T., and Et-Touhami, M., 2013, Zircon U-Pb geochronology links the End-Triassic extinction with the Central Atlantic Magmatic Province. Science, v. 340, p. 941–945.

Bowring, J.F., McLean, N.M., and Bowring, S.A., 2011. Engineering cyber infrastructure for U-Pb geochronology: Tripoli and U-Pb_Redux: Geochemistry, Geophysics, Geosystems, v. 12 (6), doi:

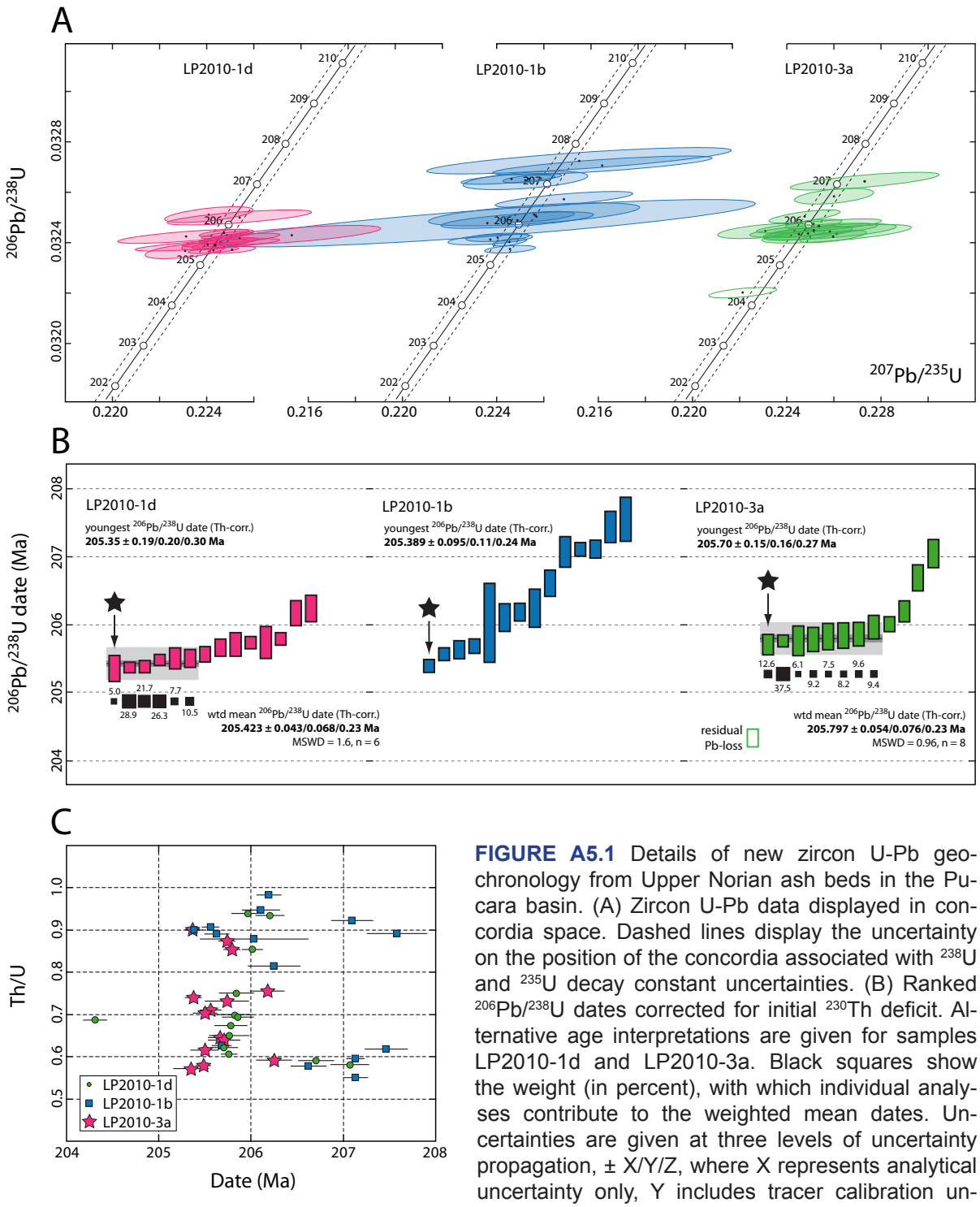

FIGURE A5.1 Details of new zircon U-Pb geochronology from Upper Norian ash beds in the Pucara basin. (A) Zircon U-Pb data displayed in concordia space. Dashed lines display the uncertainty on the position of the concordia associated with ^{238}U and ^{235}U decay constant uncertainties. (B) Ranked $^{206}Pb/^{238}U$ dates corrected for initial ^{230}Th deficit. Alternative age interpretations are given for samples LP2010-1d and LP2010-3a. Black squares show the weight (in percent), with which individual analyses contribute to the weighted mean dates. Uncertainties are given at three levels of uncertainty propagation, ± X/Y/Z, where X represents analytical uncertainty only, Y includes tracer calibration uncertainties, and Z includes tracer calibration and ^{238}U decay constant uncertainties. (C) Th/U as a function of $^{206}Pb/^{238}U$ dates for all samples. All uncertainties are given at the 2σ level of confidence.

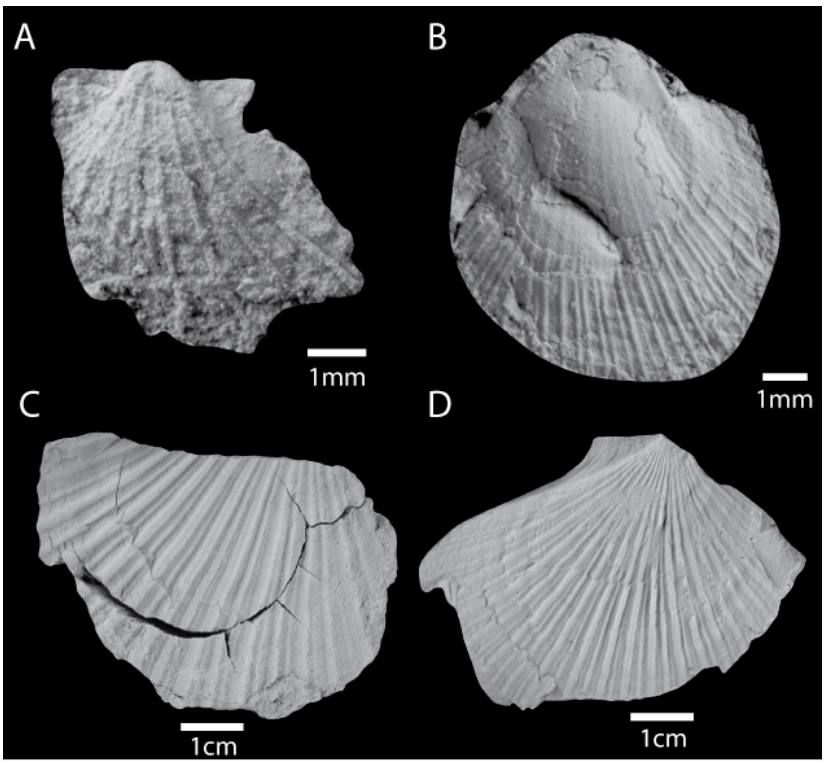

FIGURE A5.2 Photographs of characteristic bivalves from the Norian-Rhaetian boundary interval. (A) *Oxytoma sp.* cf. *O. inaequivalvis*, left valve, exterior (sample 3a). (B) *Otapiria n. sp.* aff. *O. norica*, left valve, exterior (sample 3'). (C-D) *Monotis subcircularis*.

10.1029/2010GC003479.

Cecioni, G., and Westermann, G.E.G., 1968, The Triassic/Jurassic marine transition of coastal Chile: Pacific Geology, v. 1, p. 41–75.

Condon, D.J., Schoene, B., McLean, N.M., Bowring, S.A., and Parrish, R.R., submitted. Metrology and traceability of U-Pb isotope dilution geochronology (EARTH-TIME Tracer Calibration Part I). Submitted to Geochem. Geophys. Geosyst.

Deenen, M.H.L., Ruhl, M., Bonis, N.R., Krijgsman, W., Kürschner, W.M., Reitsma, M., and van Bergen, M.J., 2010, A new chronology for the end-Triassic mass extinction: Earth and Planetary Science Letters, v. 291, p. 113–125.

Gallet, Y., Krystyn, L., Besse, J., and Marcoux, J., 2003, Improving the Upper Triassic numerical time scale from cross-correlation between Tethyan marine sections and the continental Newark basin sequence: Earth and Planetary Science Letters, v. 212, p. 255–261.

Gallet, Y., Krystyn, L., Marcoux, J., and Besse, J., 2007, New constraints on the End-Triassic (Upper Norian-Rhaetian) magnetostratigraphy: Earth and Planetary Science Letters, v. 255, p. 458–470.

Gardin, S., Krystyn, L., Richoz, S., Bartolini, A., and Galbrun, B., 2012. Where and when the earliest coccolithophores? Lethaia, v. 45 (4), p. 507–523.

Golebiowski, R., 1990, The Alpine Koessen Formation, a key for European topmost Triassic correlations; a sequence and ecostratigraphic contribution to the Norian-Rhaetian discussion: Albertiana, v. 8, p. 25–35.

Grant-Mackie, J.A., and Silberling, N.J., 1990. New data on the Upper Triassic bivalve Monotis in North America, and the new genus Pacimonotis. J. Paleontol., v. 64, p. 240–254.

Guex, J., Bartolini, A., Atudorei, V., and Taylor, D., 2004, High-resolution ammonite and carbon isotope stratigraphy across the Triassic–Jurassic boundary at New York Canyon (Nevada): Earth and Planetary Science Letters, v. 225, p. 29–41.

Guex, J., Schoene, B., Bartolini, A., Spangenberg, J., Schaltegger, U., O'Dogherty, L., Taylor, D., Bucher, H., and Atudorei, V., 2012, Geochronological constraints on post-extinction recovery of the ammonoids and carbon cycle perturbations during the Early Jurassic: Palaeogeography, Palaeoclimatology, Palaeoecology, v. 346-347, p. 1–11.

Hüsing, S.K., Deenen, M.H.L., Koopmans, J.G., and Krijgsman, W., 2011, Magnetostratigraphic dating of the proposed Rhaetian GSSP at Steinbergkogel (Upper Triassic, Austria): Implications for the Late Triassic time scale: Earth and Planetary Science Letters, v. 302, p. 203–216.

Jaffey, A.H., Flynn, K.F., Glendenin, L.E., Bentley, W.C., Essling, A.M., 1971. Precision measurement of half-lives and specific activities of ^{235}U and ^{238}U. Phys. Rev., v. C4 (5), p. 1889–1906.

Kozur, H.W., and Weems, R.E., 2005, Conchostracan evidence for a late Rhaetian to early Hettangian age for the CAMP volcanic event in the Newark Supergroup, and a Sevatian (late Norian) age for the immediately underlying beds: Hallesches Jahrbuch für Geowissenschaften. Reihe B: Geologie, Paläontologie, Mineralogie, v. 21, p. 21–51.

Kozur, H.W., and Weems, R.E., 2010, The biostratigraphic importance of conchostracans in the continental Triassic of the northern hemisphere, in S.G. Lucas (ed.), The Triassic Timescale, Geological Society, London, Special Publications, v. 334, p. 315–417.

Krystyn, L., 1980, Triassic conodont localities of the Salzkammergut region: Abhandlungen der Geologischen Bundesanstalt, v. 35, p. 61–98.

Krystyn, L., and Kuerschner, W., 2005, Biotic events around the Norian-Rhaetian boundary from a Tethyan perpective: Albertiana, v. 32, p. 17–20.

Krystyn, L., 2008, The Hallstatt pelagics - Norian and Rhaetian Fossillagerstaetten of Hallstatt. Berichte der Geologischen Bundesanstalt, v. 76, p. 81–98.

Krystyn, L., 2010, Decision report on the defining event for the base of the Rhaetian stage: Albertiana, v. 38, p. 11–12.

Lucas, S.G., Tanner, L.H., Kozur, H.W., Weems, R.E., and Heckert, A.B., 2012, The Late Triassic timescale: Age and correlation of the Carnian-Norian boundary: Earth-Science Reviews, v. 114, p. 1–18.

Marzoli, A., Bertrand, H., Knight, K.B., Cirilli, S., Buratti, N., Vérati, C., Nomade, S., Renne, P.R., Youbi, N., Martini, R., Allenbach, K., Neuwerth, R., Rapaille, C., Zaninetti, L., and Bellieni, G., 2004, Synchrony of the Central Atlantic magmatic province and the Triassic–Jurassic boundary climatic and biotic crisis: Geology, v. 32, p. 973–976.

McElwain, J.C., Wagner, P.J., and Hesselbo, S.P., 2009, Fossil plant relative abundances indicate sudden loss of Late Triassic biodiversity in East Greenland: Science, v. 324, p. 1554–1556.

McLean, N.M., Bowring, J.F., and Bowring, S.A., 2011, An algorithm for U-Pb isotope dilution data reduction and uncertainty propagation: Geochemistry, Geophysics, Geosystems, v. 12 (6), doi: 10.1029/2010GC003478.

McRoberts, C.A., Krystyn, L. and Shea, A., 2008, Rhaetian (Late Triassic) Monotis (Bivalvia: Pectinoida) from the eastern Northern Calcareous Alps (Austria) and the end-Norian crisis in pelagic faunas: Palaeontology, v. 51. p. 571–535.

McRoberts, C.A., 2010. Biochronology of

Triassic bivalves, in Lucas, S.G., ed., The Triassic Timescale, Geological Society, London, Special Publications, v. 334, p. 201–219.

McRoberts, C.A., 2011, Late Triassic Bivalvia (chiefly Halobiidae and Monotidae) from the Pardonet Formation,Williston Lake area, northeast British Columbia, Canada: Journal of Paleontology, v. 85, p. 615–666.

Muttoni, G., Kent, D.V., Jadoul, F., Olsen, P.E., and Rigo, M., 2010, Rhaetian magneto-biostratigraphy from the Southern Alps (Italy): Constraints on Triassic chronology: Palaeogeography, Palaeoclimatology, Palaeoecology, v. 285, p. 1–16.

Ogg, J.G., Ogg, G.M., and Gradstein, F.M., 2008, Triassic Period, in Ogg, J.G., Ogg, G.M., and Gradstein, F.M., eds., Concise Geologic Time Scale: Cambridge University Press, Cambridge, p. 95–106.

Ogg, J.G., 2012, Triassic, in Gradstein, F.M, Ogg, J.G., Schmitz, M.D., and Ogg, G.M., eds., The Geologic Time Scale 2012: Elsevier, Oxford-Amsterdam-Waltham, p. 681–730.

Olsen, P.E., Kent, D.V., and Whiteside, J.H., 2011, Implications of the Newark Supergroup-based astrochronology and geomagnetic polarity time scale (Newark-APTS) for the tempo and mode of the early diversification of the Dinosauria: Earth and Environmental Science Transactions of the Royal Society of Edinburgh, v. 101, p. 201–229.

Ruhl, M., Bonis, N.R., Reichart, G.J., Sinninghe Damsté, J.S., and Kürschner, W.M., 2011, Atmospheric carbon injection linked to end-Triassic mass extinction: Science, v. 333, p. 430–434.

Ruhl, M., and Kürschner, W.M., 2011, Multiple phases of carbon cycle disturbances from large igneous province formation at the Triassic-Jurassic transition: Geology, v. 39, p. 431–434.

Schaltegger, U., Guex, J., Bartolini, A., Schoene, B., and Ovtcharova, M., 2008, Precise U-Pb age constraints for end-Triassic mass extinction, it's correlation to volcanism and Hettangian post-extinction recovery: Earth and Planetary Science Letters, v. 267, p. 266–275.

Schoene, B., Guex, J., Bartolini, A., Schaltegger, U., and Blackburn, T.J., 2010, Correlating the end-Triassic mass extinction and flood basalt volcanism at the 100 ka level: Geology, v. 38, p. 387–390.

Silberling, N.J., 1985. Biogeographic significance of the Upper Triassic bivalve Monotis in circum-Pacific accreted terranes, in Howell, D.G., ed., Tectonostratigraphic terranes of the circum-Pacific region. Earth Science Series, Circum-Pacific Councel for Energy and Mineral Resources, p. 63–70.

Silberling, N.J., Grant-Mackie, J., and Nichols, K.M., 1997. The Late Triassic bivalve Monotis in accreted terranes of Alaska. U.S. Geological Survey Bulletin, v. 2151, p. 1–21.

Tanner, L.H., Lucas, S.G., and Chapman, M.G., 2004, Assessing the record and causes of Late Triassic extinctions: Earth Science Reviews, v. 65, p. 103–139.

Tozer, E.T., 1980. Latest Triassic (Upper Norian) ammonoid and Monotisfaunas and correlations Rivista Italiana Paleontologia e Stratigrafia, v. 85, p. 843-876.

Tozer, E.T., 1994, Canadian Triassic ammonoid faunas: Geological Survey of Canada Bulletin, v. 467, p. 1–663.

Wotzlaw, J.F., Bindeman, I.N., Schaltegger, U., Brooks, C.K., Naslund, H.R., 2012. High-resolution insights into episodes of crystallization, hydrothermal alteration and remelting in the Skaergaard intrusive complex. Earth Planet. Sci. Lett., v. 355–356, p. 199–212.

Wotzlaw, J.F., Schaltegger, U., Frick, D.A., Dungan, M.A., Gerdes, A., Günther, D.,

2013. Tracking the evolution of large-volume silicic magma reservoirs from assembly to supereruption. Geology, v. 41, p. 867–870.

***

Epilogue

The amount of geochemical information contained in μm-sized accessory zircons make these tiny crystals unique recorders of geological processes. Decoding the isotopic and chemical memory by means of mass spectrometry allows geochemists to obtain snapshots of the physical and chemical state of the crystallization environment at the time of zircon crystallization. This thesis documents the present state of the art and various applications of high-precision U-Pb geochronology by isotope dilution thermal ionization mass spectrometry.

Integrating high-precision U-Pb geochronology with isotopic and trace element analyses of the same zircon crystals to quantify the time scales of magmatic processes currently evolves into a new sub-discipline of igneous petrology that some researchers refer to as *zircon petrochronology*. Applications presented in this thesis largely focus on the thermal, chemical and physical evolution of upper crustal magmatic systems but also make first attemps to link the thermal evolution of such upper crustal systems to the evolution of their lower crustal roots. Quantifying the control of the lower crustal roots and the magma fluxes from the lower to upper crust will allow to construct crustal-scale models of continental magmatic systems.

This thesis, furthermore, makes first attempts and points out future directions that involve integrating *zircon petrochronology* with other radioisotope geochronometers, mineral diffusion timescales, thermo-mechanical models, and geophysical observations. Such a fully integrated approach will significanty improve our understanding of crustal magmatic systems and assist in quantifying the probability of future hazards related to large-volume volcanic eruptions that represent one of the major risks to modern civilisations.

Intercalibrating geochronometers is one of the major themes of this thesis and bringing sanidine $^{40}Ar/^{39}Ar$ dates and zircon U-Pb dates of volcanic rocks into agreement, remains one of the big challenges. Part of the difficulties arise from the fact that these two geochronometers ultimately date different events, i.e., volcanic eruption and zircon crystallization, respectively. Under favorable circumstances, there is a negligible time-lag between these two events and both chronometers should agree within their uncertainties. Integrating $^{40}Ar/^{39}Ar$ and U-Pb geochronology to calibrate Earth history will help to overcome some of the fundamental limitations inherent to both methods. Using these radioisotope geochronometers to anchor floating astrochronologies, based on the stable 400,000 years eccentricity frequency, will allow to calibrate Earth history at unprecedented temporal resolution for

most of the Phanerozoic eon and potentially even into the Precambrian.

Looking back on the remarkable progress made throughout the past century, there is little doubt that the following decades will lead to further tremendous advances in uranium-lead geochronology.

Acknowledgements

First and foremost I would like to thank *Urs Schaltegger* who took me on as a Ph.D. student as my supervisor but became a mentor and friend throughout the years. I especially thank him for allowing me to get involved in a variety of research projects that largely exceed the initial scope of my Ph.D. project.

I would like to express my gratitude to *Ilya N. Bindeman* (University of Oregon), who has been one of the biggest influences on my research. If he had not come to Geneva as a visiting Professor, my thesis would look significantly different. I always enjoyed our collaborations and thank him for agreeing to be part of my dissertation committee.

Frits Hilgen (Utrecht University) and *Othmar Müntener* (University of Lausanne) are also thanked for agreeing to be part of my dissertation committee. Both have been very influential.

I am extremely grateful to *Maria Ovtcharova* for introducing me to the work in the clean laboratory, for sharing an office with me and for always taking time to listen to my professional and personal problems.

Richard Spikings became one of my best friends and I thank him for all the evenings we spent together discussing science and other irritating aspects of life.

I also thank *Massimo Chiaradia* for sharing his analytical expertise, answering numerous questions related to mass spectrometry and his over all support as a friend.

I am grateful for the contributions of all my other collaborators and co-authors, many of which became friends: *Blair Schoene, Luca Caricchi, Silja Hüsing, Michael Dungan, Axel Gerdes, Jean Guex, Daniel Frick, Yves Gallet, Christopher McRoberts, Kent Brooks, Detlef Günther, Richard Naslund, Kathryn Watts, Annachiara Bartolini, Axel Schmitt, David Taylor, and Leopold Krystyn*.

I want to thank all my fellow PhD students, and all staff members of the Department of Earth Sciences in Geneva.

Lastly, I would like to express my sincere gratitude to my friends and family, especially my parents *Peter* and *Kerstin Wotzlaw* for always supporting and encouraging me in all my endeavours.

Annex

Annex A1: *Interlaboratory reproducibility of zircon standards AUSz2 and AUSz5 (Kennedy et al., submitted).*

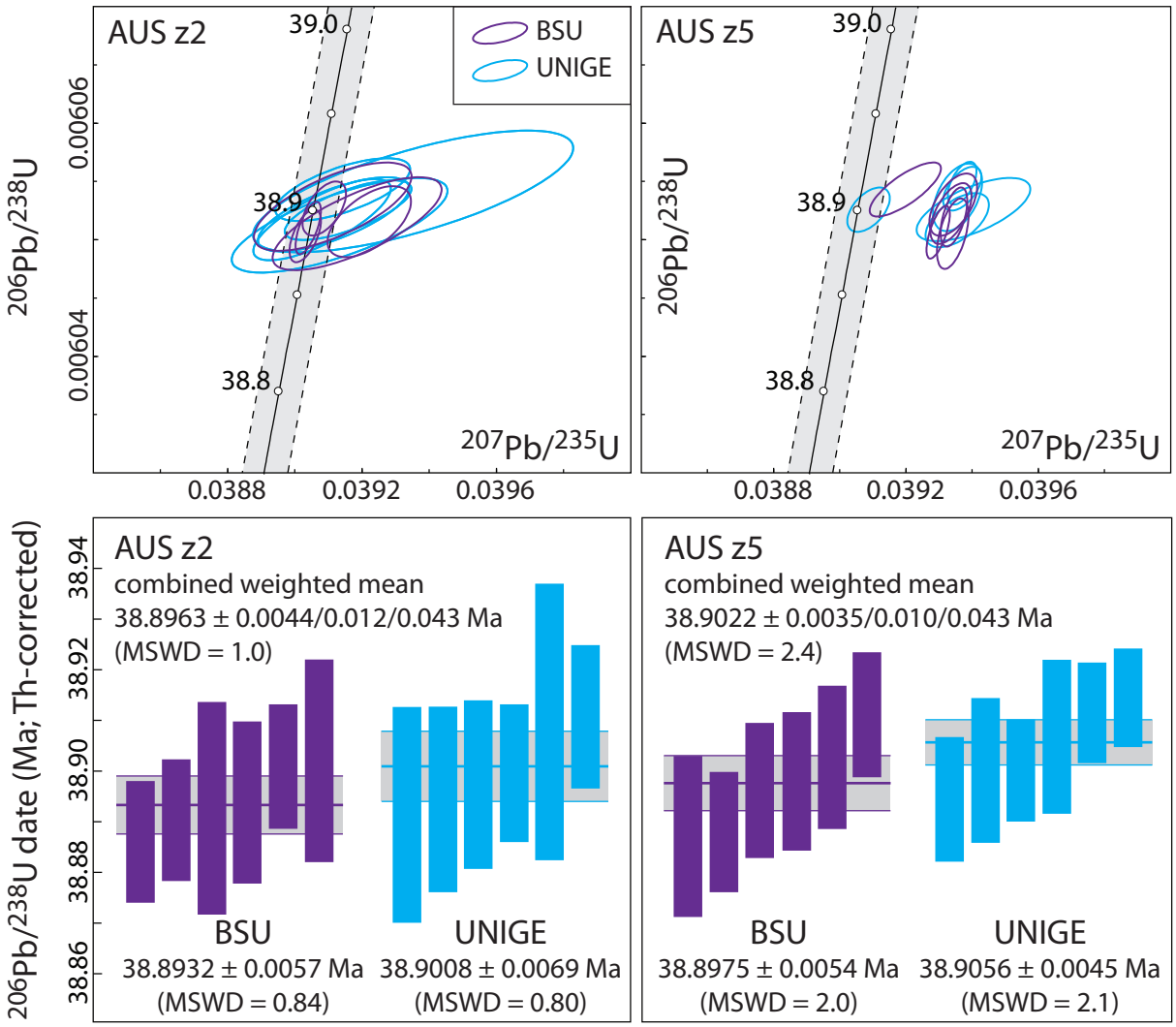

Supplementary Figure A1. Zircon U-Pb isotopic data for Eocene zircon standards AUSz2 and AUSz5 from two laboratories; BSU - Boise State University, UNIGE - University of Geneva (data from Kennedy et al., submitted). Top: Concordia diagrams showing concordance of AUSz2 zircon fragments, while 10 of 12 AUSz5 fragments are discordant. Bottom: Ranked Th-corrected $^{206}Pb/^{238}U$ dates displaying the remarkable interlaboratory reproducibility (<0.05%).

Annex A2: *Long-term reproducibility of analyses of the 100 Ma EARTHTIME synthetic U-Pb solution (Condon et al., 2008) at the University of Geneva.*

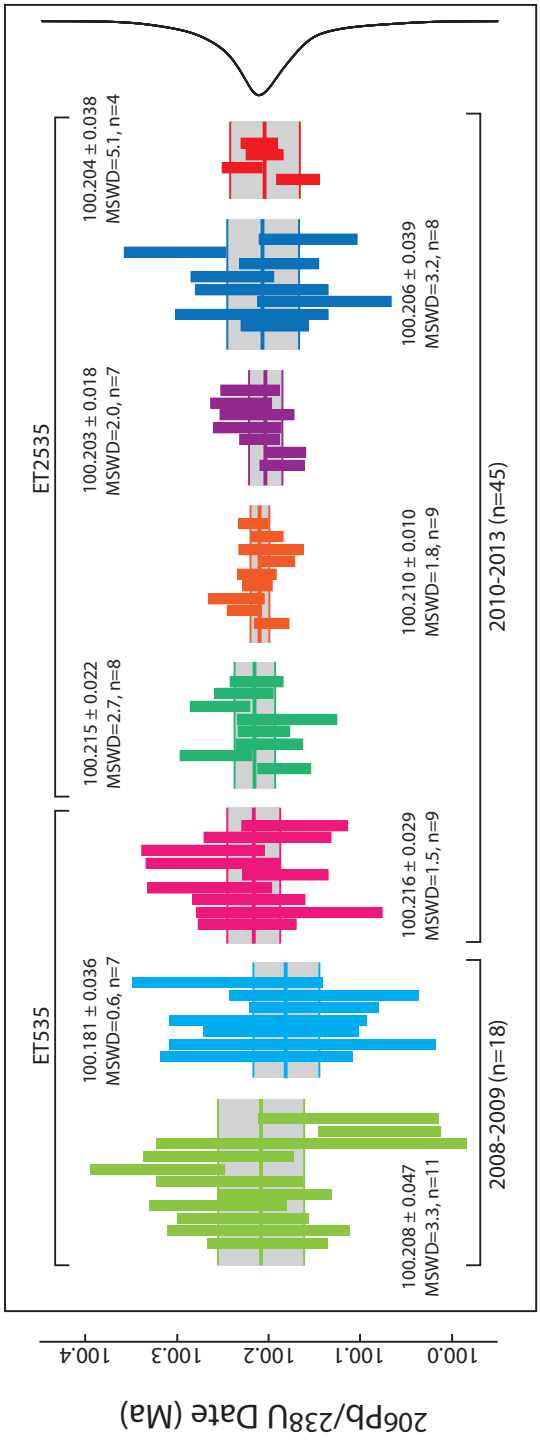

Supplementary Figure A2. U-Pb isotopic data for 100 Ma EARTHTIME synthetic solutions analyses at the University of Geneva between 2008 and 2013. Shown are $^{206}Pb/^{238}U$ dates. See Supplementary Table A1 for complete U-Pb isotopic data. Coloured bars represent 2σ analytical uncertainties of inidivual analyses. Grey bars with coloured lines represent 95% confidence intervals of weighted mean dates for blocks of analyses performed during short time intervals (i.e., several days to weeks). Probability density function includes all analyses (n=63). Variations in analytical precision largely arise from (1) uncertainties associated with external correction for instrumental mass fractionation for ET535 spiked samples compared to internal correction for ET2535 spiked samples and (2) variations in isotope ratio measurement precision due to variations in sample-spike ratio. These data suggest a long-term reproducibility of better than 0.05% for $^{206}Pb/^{238}U$ dates.

Supplementary Table A1. *U-Pb isotopic data for 100 Ma EARTHTIME solutions analysed at UNIGE between 2010 and 2013*

	Dates (Ma)						Composition				Isotopic Ratios							
	$^{206}Pb/^{238}U$	±2σ	$^{207}Pb/^{235}U$	±2σ	$^{207}Pb/^{206}Pb$	±2σ	Th/	Pb*	Pbc	Pb*/	$^{206}Pb/^{204}Pb$	$^{206}Pb/^{238}U$	±2σ	$^{207}Pb/^{235}U$	±2σ	$^{207}Pb/^{206}Pb$	±2σ	Corr.
Fraction	(a)	abs	(a)	abs	(a)	abs	U (c)	(pg) (d)	(pg) (e)	Pbc (f)	(g)	(h)	%	(h)	%	(h)	%	coef.
ET100 (run#)																		
8081	100.224	0.053	100.19	0.20	99.4	4.2	0.07	29.9	0.59	50.5	3455	0.015669	0.05	0.10371	0.21	0.04802	0.18	0.650
8082	100.177	0.101	100.22	0.21	101.3	4.4	0.07	52.2	0.71	73.3	5005	0.015661	0.10	0.10374	0.22	0.04806	0.18	0.555
8083	100.222	0.061	100.17	0.14	98.8	2.7	0.07	83.6	0.78	107.1	7313	0.015668	0.06	0.10368	0.14	0.04801	0.11	0.658
8084	100.265	0.068	100.56	0.33	107.6	7.5	0.07	21.5	0.64	33.3	2285	0.015675	0.07	0.10411	0.34	0.04819	0.32	0.421
8085	100.182	0.046	100.11	0.14	98.5	3.1	0.07	50.5	0.64	79.0	5397	0.015662	0.05	0.10362	0.14	0.04801	0.13	0.445
8086	100.261	0.073	100.27	0.12	100.4	2.3	0.07	80.8	0.73	110.2	7522	0.015675	0.07	0.10379	0.13	0.04804	0.09	0.688
8087	100.271	0.067	100.30	0.28	100.9	6.6	0.07	20.3	0.56	36.1	2478	0.015676	0.07	0.10382	0.29	0.04805	0.28	0.340
8428	100.201	0.069	100.09	0.14	97.5	2.7	0.07	65.3	0.66	98.8	6745	0.015665	0.07	0.10360	0.15	0.04799	0.11	0.689
8429	100.171	0.058	100.08	0.18	97.8	3.7	0.07	70.3	1.10	63.9	4368	0.015660	0.06	0.10358	0.19	0.04799	0.15	0.667
9454	100.183	0.029	99.81	0.12	91.0	2.7	0.07	76.3	0.87	87.6	5989	0.015662	0.03	0.10330	0.13	0.04785	0.11	0.520
9456	100.257	0.039	100.11	0.14	96.7	3.0	0.07	33.8	0.42	81.0	5535	0.015674	0.04	0.10362	0.14	0.04797	0.12	0.525
9457	100.199	0.037	100.13	0.12	98.6	2.6	0.07	60.4	0.64	93.9	6414	0.015665	0.04	0.10364	0.13	0.04801	0.11	0.609
9458	100.205	0.028	100.12	0.11	98.2	2.3	0.07	55.2	0.48	114.1	7786	0.015666	0.03	0.10363	0.11	0.04800	0.09	0.562
9459	100.180	0.054	100.14	0.15	99.2	3.1	0.07	47.1	0.47	100.2	6843	0.015662	0.05	0.10365	0.16	0.04802	0.13	0.680
9460	100.253	0.032	100.17	0.14	98.2	3.1	0.07	35.8	0.49	73.3	5007	0.015673	0.03	0.10368	0.15	0.04800	0.13	0.579
9461	100.227	0.032	100.14	0.12	98.2	2.6	0.07	56.8	0.70	81.3	5554	0.015669	0.03	0.10365	0.12	0.04800	0.11	0.400
9462	100.213	0.029	100.13	0.12	98.3	2.7	0.07	46.7	0.52	90.6	6187	0.015667	0.03	0.10364	0.12	0.04800	0.11	0.473
9525	100.197	0.018	100.16	0.10	99.3	2.2	0.07	59.6	0.56	106.9	7295	0.015664	0.02	0.10367	0.10	0.04802	0.09	0.410
9526	100.226	0.018	100.25	0.09	100.9	2.2	0.07	70.4	0.59	119.9	8183	0.015669	0.02	0.10377	0.10	0.04805	0.09	0.430
9527	100.235	0.030	100.23	0.14	100.2	3.0	0.07	55.2	0.54	101.3	6912	0.015671	0.03	0.10375	0.14	0.04804	0.12	0.688
9529	100.212	0.016	100.20	0.09	99.9	2.1	0.07	59.8	0.54	111.4	7600	0.015667	0.02	0.10371	0.09	0.04803	0.08	0.451
9530	100.213	0.021	100.17	0.09	99.1	2.0	0.07	97.4	0.76	128.1	8741	0.015667	0.02	0.10368	0.10	0.04802	0.08	0.679
9538	100.191	0.020	100.08	0.09	97.4	2.0	0.07	58.6	0.50	117.1	7989	0.015664	0.02	0.10358	0.09	0.04798	0.08	0.567
9539	100.197	0.035	100.19	0.18	100.0	3.4	0.07	61.2	0.51	120.6	8227	0.015665	0.04	0.10370	0.19	0.04804	0.14	1.108
9540	100.202	0.017	100.15	0.09	98.9	2.0	0.07	58.5	0.48	120.7	8235	0.015665	0.02	0.10366	0.09	0.04801	0.08	0.433
9541	100.216	0.016	100.14	0.09	98.4	2.0	0.07	55.2	0.52	106.0	7234	0.015668	0.02	0.10365	0.09	0.04800	0.08	0.387
10148	100.185	0.024	100.00	0.10	95.6	2.3	0.07	85.6	0.67	127.2	8679	0.015663	0.02	0.10350	0.11	0.04795	0.09	0.609
10149	100.181	0.021	99.95	0.09	94.4	2.1	0.07	88.6	0.71	124.1	8470	0.015662	0.02	0.10344	0.10	0.04792	0.08	0.437
10156	100.210	0.022	100.19	0.08	99.6	1.8	0.07	102.5	0.72	143.2	9770	0.015667	0.02	0.10370	0.09	0.04803	0.07	0.587
10215	100.223	0.037	100.04	0.13	95.6	2.9	0.07	72.6	0.61	118.4	8084	0.015669	0.04	0.10354	0.14	0.04795	0.12	0.497
10216	100.213	0.040	99.89	0.14	92.2	3.0	0.07	78.2	0.65	119.9	8187	0.015667	0.04	0.10338	0.14	0.04788	0.12	0.531
10217	100.230	0.033	100.04	0.11	95.6	2.5	0.07	68.4	0.55	123.8	8447	0.015670	0.03	0.10354	0.12	0.04795	0.10	0.518
10226	100.220	0.032	100.18	0.11	99.1	2.4	0.07	73.9	0.57	129.5	8836	0.015668	0.03	0.10369	0.11	0.04802	0.10	0.545
10355	100.193	0.037	99.96	0.11	94.4	2.4	0.07	103.0	0.87	118.9	8114	0.015664	0.04	0.10346	0.11	0.04792	0.10	0.431
10356	100.218	0.083	100.22	0.16	100.3	3.0	0.07	92.7	0.81	114.2	7794	0.015668	0.08	0.10374	0.16	0.04804	0.12	0.640
10357	100.139	0.073	99.93	0.13	95.0	1.6	0.07	95.9	0.77	124.2	8476	0.015655	0.07	0.10342	0.14	0.04793	0.06	0.953
10358	100.208	0.072	100.01	0.14	95.2	2.6	0.07	87.6	0.77	113.3	7732	0.015666	0.07	0.10351	0.15	0.04794	0.10	0.699

(Supplementary Table A1 continued)

10359	100.239	0.045	100.18	0.10	98.7	2.1	0.07	96.5	0.76	127.7	8714	0.015671	0.05	0.10369	0.10	0.04801	0.08	0.576
10360	100.189	0.043	100.15	0.12	99.2	2.5	0.07	93.6	0.77	122.1	8328	0.015663	0.04	0.10366	0.13	0.04802	0.10	0.588
10361	100.302	0.055	100.22	0.13	98.4	2.5	0.07	86.2	0.72	119.1	8131	0.015681	0.06	0.10374	0.13	0.04800	0.10	0.649
10362	100.157	0.053	100.15	0.09	99.9	1.9	0.07	92.0	0.74	124.0	8459	0.015658	0.05	0.10366	0.10	0.04803	0.07	0.597
10551	100.168	0.023	99.96	0.10	94.9	2.1	0.07	99.2	0.80	124.1	8470	0.015660	0.02	0.10345	0.10	0.04793	0.08	0.583
10552	100.229	0.022	100.23	0.11	100.4	2.4	0.07	93.3	0.86	108.8	7426	0.015669	0.02	0.10375	0.11	0.04804	0.09	0.554
10553	100.204	0.020	100.17	0.08	99.3	1.7	0.07	127.7	0.77	165.4	11282	0.015666	0.02	0.10368	0.08	0.04802	0.06	0.607
10554	100.210	0.020	100.06	0.09	96.4	2.0	0.07	94.6	0.72	131.0	8941	0.015667	0.02	0.10356	0.09	0.04796	0.08	0.551

a Isotopic dates calculated using the decay constants $\lambda_{238} = 1.55125E\text{-}10$ and $\lambda_{235} = 9.8485E\text{-}10$ (Jaffey et al. 1971).
b % discordance = 100 - (100 * ($^{206}Pb/^{238}U$ date) / ($^{207}Pb/^{206}Pb$ date))
c Th contents calculated from radiogenic ^{208}Pb and the $^{207}Pb/^{206}Pb$ date of the sample, assuming concordance between U-Th and Pb systems.
d Total mass of radiogenic Pb.
e Total mass of common Pb.
f Ratio of radiogenic Pb (including ^{208}Pb) to common Pb.
g Measured ratio corrected for fractionation and spike contribution only.
h Measured ratios corrected for fractionation, tracer and blank.

REFERENCES CITED

Condon, D.J., McLean, N., Schoene, B., Bowring, S., Parrish, R., Noble, S., 2008. Synthetic U-Pb 'standard' solutions for ID-TIMS geochronology. Geochim. Cosmochim. Acta, v. 72 (12S), p. A175.

Jaffey, A.H., Flynn, K.F., Glendenin, L.E., Bentley, W.C., Essling, A.M., 1971. Precision measurement of half-lives and specific activities of ^{235}U and ^{238}U. Phys. Rev., v. C4 (5), p. 1889–1906.

Kennedy, A.K., Wotzlaw, J.F., Crowley, J., Schmitz, M., Schaltegger, U., Eocene zircon reference materials for microanalysis of U-Th-Pb isotopes and trace elements. *Submitted to Am. Mineral.*